

UMTA-MA-06-0099-82-5
DOT-TSC-UMTA-82-57

PB83-218727



Control of Wheel/Rail Noise and Vibration

Paul J. Remington
Nicholas R. Dixon
Larry E. Wittig, et al.

Bolt Beranek and Newman, Inc.
50 Moulton Street
Cambridge MA 02238

April 1983
Final Report

This document is available to the public
through the National Technical Information
Service, Springfield, Virginia 22161.

REPRODUCED BY
**NATIONAL TECHNICAL
INFORMATION SERVICE**
U.S. DEPARTMENT OF COMMERCE
SPRINGFIELD, VA. 22161



U.S. Department of Transportation
Urban Mass Transportation
Administration

Office of Technical Assistance
Office of Systems Engineering
Washington DC 20590

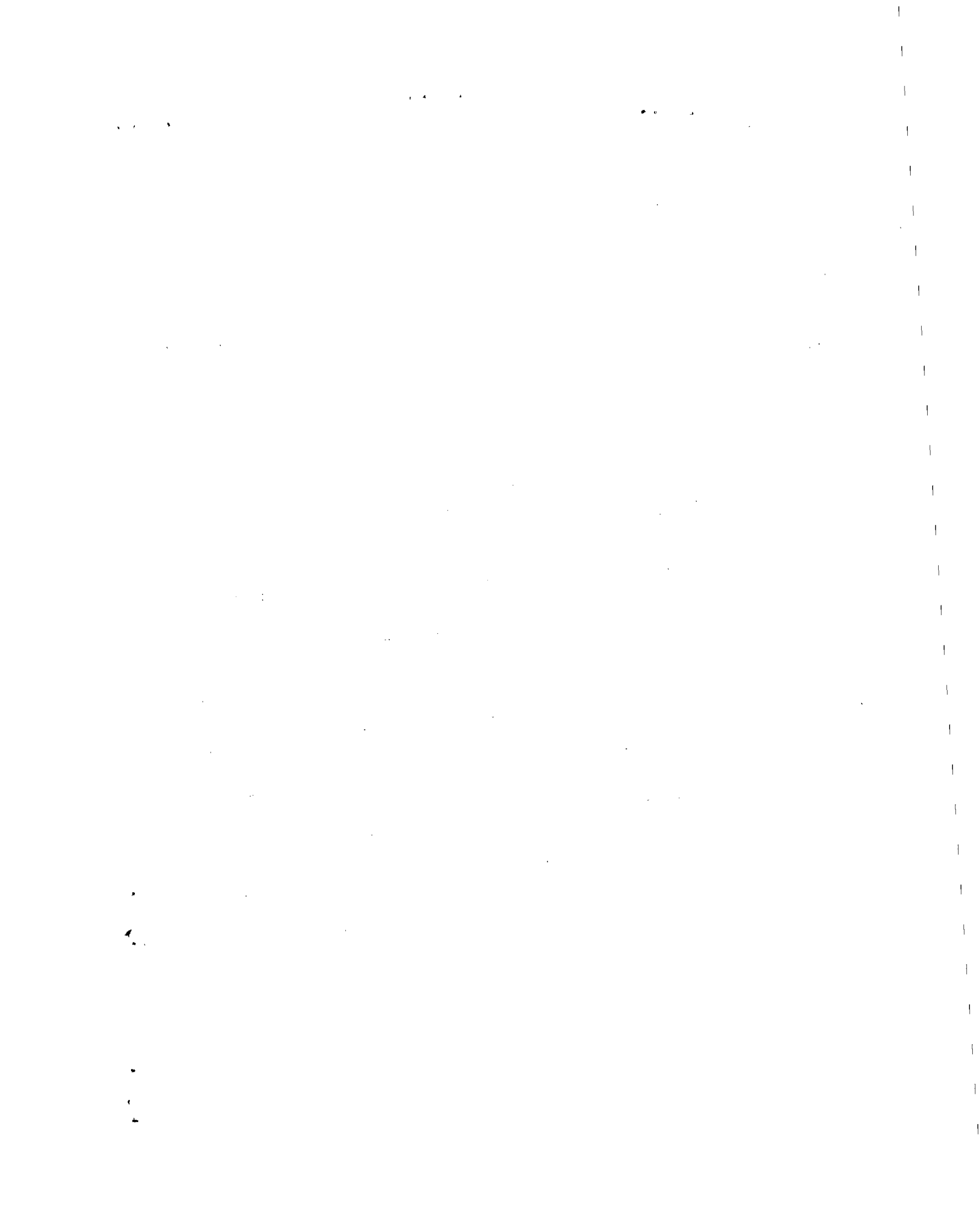
NOTICE

This document is disseminated under the sponsorship of the Department of Transportation in the interest of information exchange. The United States Government assumes no liability for its contents or use thereof.

NOTICE

The United States Government does not endorse products or manufacturers. Trade or manufacturers' names appear herein solely because they are considered essential to the object of this report.

1. Report No. UMTA-MA-06-0099-82-5		2. Government Accession No.		3. Recipient's Catalog No. PB83 218727	
4. Title and Subtitle Control of Wheel/Rail Noise and Vibration.				5. Report Date April 1983	
				6. Performing Organization Code DTS-77	
7. Author(s) P. J. Remington, N. R. Dixon, L. G. Kurzweil, C. W. Menge, J. D. Stahr, and L. E. Wittig				8. Performing Organization Report No. DOT-TSC-UMTA-82-57	
9. Performing Organization Name and Address Bolt Beranek and Newman, Inc.* 10 Moulton Street Cambridge, Massachusetts 02238				10. Work Unit No. (TRAIS) MA-06-0099(UM249/R2641)	
				11. Contract or Grant No. DOT-TSC-1768	
12. Sponsoring Agency Name and Address U.S. Department of Transportation Urban Mass Transportation Administration 400 Seventh Street, S.W. Washington, D. C. 20590				13. Type of Report and Period Covered Final Report Nov.79 - Feb.82	
				14. Sponsoring Agency Code URT-11	
15. Supplementary Notes *Under contract to:		U.S. Department of Transportation Research and Special Programs Administration Transportation Systems Center Cambridge, Massachusetts 02142			
16. Abstract This report presents the results of a program to develop and evaluate techniques for the control of wheel/rail noise in urban rail transit systems. The first part of the program included a literature review and a cost-benefit analysis to select, for further study, the most cost-effective wheel/rail control treatments. In this document, the focus is on the development, improvement, and validation of the analytical tools to be used in the design, development, and testing of those treatments. An analytical model of the generation of wheel/rail noise was developed and validated through an extensive series of field tests carried out at the Transportation Test Center in Pueblo, Colorado, using the State-of-the-Art-Car. A sensitivity analysis was performed using this analytical model. The analysis showed that wheel/rail noise is relatively insensitive to changes in most system parameter values, except wheel and rail roughness, contact area, and contact stiffness. The surface finish produced by most wheel truing and rail grinding machines was measured. A belt grinder used by the Toronto Transit Commission for wheel truing and a rail grinding block car used by the Chicago Transit Authority to grind rails were found to produce the quietest surface finishes, giving an estimated 12 dBA of noise reduction when compared with typical rapid transit wheels and rails in revenue service. A scale model of a new concept wheel employing a resilient tread was built and tested. Noise reductions of up to 8 dBA were achieved with tread stresses in the manageable range. The analytical model developed under this program was shown to agree reasonably well with field measurements of wheel/rail noise.					
17. Key Words Noise and Noise Control; Rail Grinding; Rapid Rail Transit Noise; Vibration; Wheel/Rail Noise; Wheel Truing			18. Distribution Statement Available to the Public through the National Technical Information Service, Springfield, Virginia 22161.		
19. Security Classif. (of this report) Unclassified		20. Security Classif. (of this page) Unclassified		21. No. of Pages 348	22. Price



PREFACE

This report presents the results of a program to develop and evaluate techniques for the control of wheel/rail noise in urban rail transit systems. The first part of the program, reported elsewhere [1], included a literature review and a cost-benefit analysis to select, for further study, the most cost-effective wheel/rail control treatments. In this document, we focus on the development, improvement, and validation of the analytical tools to be used in the design and assessment of noise control treatments and the design, development, and testing of those treatments.

Bolt Beranek and Newman Inc. (BBN) prepared this report under contract DOT-TSC-1768 as part of the Urban Rail Noise Abatement Program sponsored by the Urban Mass Transportation Administration's Office of Systems Engineering. Dr. Robert Kendig, Mr. Michael Dinning, and Mr. Robert Hinckley were technical coordinators of the work at the Transportation Systems Center.

Many people and organizations contributed to this project. In particular, we wish to thank Mr. Clifford Woodbury of Louis T. Klauder Associates; Mr. Paul Swanson of the Chicago Transit Authority; Mr. Alex Hunt of the Toronto Transit Commission; and Mr. Richard Otte of Raychem Corporation.

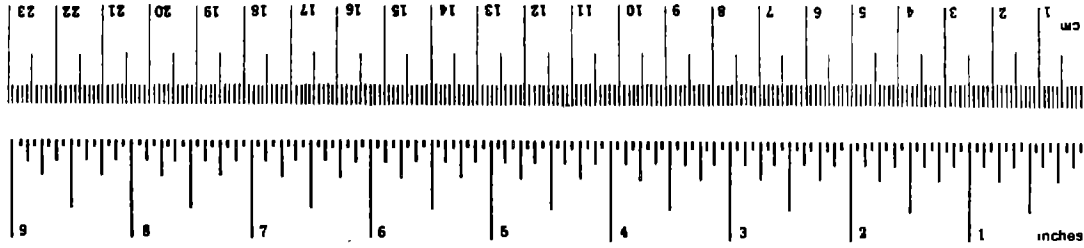
METRIC CONVERSION FACTORS

Approximate Conversions to Metric Measures

Symbol	When You Know	Multiply by	To Find	Symbol
LENGTH				
in	inches	2.5	centimeters	cm
ft	feet	30	centimeters	cm
yd	yards	0.9	meters	m
mi	miles	1.6	kilometers	km
AREA				
in ²	square inches	6.5	square centimeters	cm ²
ft ²	square feet	0.09	square meters	m ²
yd ²	square yards	0.8	square meters	m ²
mi ²	square miles	2.6	square kilometers	km ²
	acres	0.4	hectares	ha
MASS (weight)				
oz	ounces	28	grams	g
lb	pounds	0.45	kilograms	kg
	short tons (2000 lb)	0.9	tonnes	t
VOLUME				
tsp	teaspoons	5	milliliters	ml
Tbsp	tablespoons	15	milliliters	ml
fl oz	fluid ounces	30	milliliters	ml
c	cups	0.24	liters	l
pt	pints	0.47	liters	l
qt	quarts	0.95	liters	l
gal	gallons	3.8	liters	l
ft ³	cubic feet	0.03	cubic meters	m ³
yd ³	cubic yards	0.76	cubic meters	m ³
TEMPERATURE (exact)				
°F	Fahrenheit temperature	5/9 (after subtracting 32)	Celsius temperature	°C

Approximate Conversions from Metric Measures

Symbol	When You Know	Multiply by	To Find	Symbol
LENGTH				
mm	millimeters	0.04	inches	in
cm	centimeters	0.4	inches	in
m	meters	3.3	feet	ft
m	meters	1.1	yards	yd
km	kilometers	0.6	miles	mi
AREA				
cm ²	square centimeters	0.16	square inches	in ²
m ²	square meters	1.2	square yards	yd ²
km ²	square kilometers	0.4	square miles	mi ²
ha	hectares (10,000 m ²)	2.5	acres	acres
MASS (weight)				
g	grams	0.035	ounces	oz
kg	kilograms	2.2	pounds	lb
t	tonnes (1000 kg)	1.1	short tons	short tons
VOLUME				
ml	milliliters	0.03	fluid ounces	fl oz
l	liters	2.1	pints	pt
l	liters	1.06	quarts	qt
l	liters	0.26	gallons	gal
m ³	cubic meters	35	cubic feet	ft ³
m ³	cubic meters	1.3	cubic yards	yd ³
TEMPERATURE (exact)				
°C	Celsius temperature	9/5 (then add 32)	Fahrenheit temperature	°F



* 1 m = 2.54 (exactly). For other exact conversions and more detailed tables, see NBS Misc. Publ. 286, Units of Weights and Measures, Price \$2.25, SD Catalog No. C13.10:286.

TABLE OF CONTENTS

SECTION	PAGE
1. INTRODUCTION.....	1
1.1 Background.....	1
1.2 Overview.....	5
1.3 Organization of the Report.....	10
2. THEORETICAL ANALYSIS.....	11
2.1 Rolling Noise.....	11
2.1.1 Wheel/rail interaction.....	13
2.1.2 Sound radiation.....	64
2.2 Impact Noise.....	85
2.2.1 Rail joints.....	88
2.2.2 Wheel flats.....	96
2.2.3 Summary.....	103
2.3 Squeal Noise.....	104
2.3.1 Theoretical background.....	104
2.3.2 Lateral friction vs creep.....	108
2.3.3 Maximum curve radius for squeal...	113
2.3.4 Wheel damping to suppress squeal..	118
3. FIELD VALIDATION OF THE ANALYSIS.....	121
3.1 Test Site.....	121
3.2 Instrumentation.....	128
3.2.1 On-board instruments.....	128
3.2.2 Wayside instrumentation.....	134
3.2.3 Special instrumentation.....	141
3.3 Comparison of Measured and Predicted Rolling Noise.....	163

TABLE OF CONTENTS (Cont.)

SECTION	PAGE
3.4 Comparison of Measured and Predicted Impact Noise.....	174
3.4.1 Jointed rail.....	174
3.4.2 Wheel flats.....	192
3.5 Rail Response.....	197
4. SENSITIVITY ANALYSIS.....	203
4.1 Baseline System.....	203
4.2 Parameter Value Changes.....	206
5. TREATMENTS FOR THE CONTROL OF NOISE.....	229
5.1 Control of Squeal Noise.....	230
5.1.1 Hard-faced rails.....	230
5.1.2 Comparison of MBTA and CTA squeal noise occurrence.....	233
5.2 Impact and Rolling Noise.....	234
5.2.1 Wheel truing and rail grinding.....	234
5.2.2 Resiliently treaded wheels.....	270
6. CONCLUSIONS AND RECOMMENDATIONS.....	318
6.1 Conclusions.....	318
6.1.1 Analytical modeling.....	318
6.1.2 Noise control.....	318
6.2 Recommendations.....	319
6.2.1 Field testing.....	319
6.2.2 Analytical modeling.....	322
REFERENCES.....	R-1
APPENDIX: REPORT OF NEW TECHNOLOGY.....	A-1

LIST OF FIGURES

FIGURE	PAGE
1. The geometry of squeal noise excitation.....	3
2. The generation of impact and roar noise.....	4
3. The state-of-the-art car.....	7
4. Test sections at the Transportation Test Center, Pueblo, Colorado.....	8
5. Block diagram of the analytical model.....	12
6. Schematic drawing of wheel/rail interaction.....	14
7. The contact area wavenumber filter for $b =$ 0.20 in.....	23
8. Wheel/rail lateral response.....	26
9. Rail cross-impedance relating vertical force and horizontal response for 100 lb/yd rail on tie and ballast.....	30
10. Instrumentation for the rail cross-impedance measurements.....	31
11. Variables in the wheel radial response equations.	33
12. Modified first mode for the wheel radial impedance.....	36
13. Setup for measuring the radial impedance of the SOAC 30-in. wheel.....	39
14. The instrumentation chain for measuring wheel impedance.....	40
15. Comparison of measured and predicted radial impedance for the SOAC 30-in. wheel.....	41
16. Definition of axial displacement and twist of wheel tread.....	44
17. Comparison of measured and predicted axial wheel impedance for the SOAC wheel.....	46
18. Axial impedance measurement of the SOAC wheel....	47
19. Vertical impedance of 100 lb/yd rail on wood ties and ballast.....	49
20. Shaker positioned beneath rail at TTC (Pueblo) for rail impedance measurement.....	51

LIST OF FIGURES (Cont.)

FIGURE	PAGE
21. Vertical rail impedance amplitude for 119 lb/ yd rail on concrete ties and ballast at TTC (Pueblo).....	53
22. Horizontal rail impedance amplitude.....	54
23. Instrumentation for the rail impedance measurements at TTC (Pueblo).....	55
24. Vertical vibration spectra at various distances from the point of excitation.....	58
25. Horizontal vibration spectra at various distances from the point of excitation.....	59
26. Decay of vertical rail vibration in one-third octave bands with distances from the point of excitation.....	60
27. Rail loss factor for vertical vibration.....	62
28. Rail loss factor for horizontal vibration.....	63
29. Line source geometry.....	67
30. Geometrical parameters used in the ground effects model.....	70
31. Test site and sound source for the ground effect measurements.....	75
32. Test site geometry.....	76
33. Microphone at zero degree position; source at wheel height.....	77
34. Microphone at zero degree position; source at rail height.....	79
35. Direct and reflected ray paths from the wheel and rail.....	80
36. Four-angle average loudspeaker response; source at wheel height.....	81
37. Four-angle average loudspeaker response; source at rail height.....	82
38. Propagation model effect on wheel passby, using the TTC test site geometry.....	84
39. Rail joint geometry.....	90

LIST OF FIGURES (Cont.)

FIGURE	PAGE
40. Approximation to the rail joint equivalent roughness spectrum.....	94
41. Wheel flat impact geometry.....	97
42. Wheel flat equivalent roughness spectrum approximation.....	99
43. Comparison of equivalent roughness and measured data.....	101
44. Friction coefficient vs lateral creep.....	106
45. The Raychem roller rig.....	109
46. Schematic of the Raychem roller rig.....	110
47. Lateral creep data compared to Rudd's original model.....	112
48. Revised creep model.....	114
49. Field survey of curves on the MBTA where squeal noise occurs.....	117
50. Theoretical loss factor required to suppress squeal.....	119
51. The transit test track at the Transportation Test Center.....	122
52. Test site No. 1 - welded rail on concrete ties.....	123
53. Test site No. 2 - bolted rail on wooden ties.....	124
54. The SOAC on the screech loop at TTC (Pueblo) (TTC photos).....	126
55. Principal dimensions of the SOAC.....	127
56. On-board instrumentation system.....	129
57. Wheel accelerometer locations.....	130
58. Slip ring assembly used in the wheel vibration measurements (TTC photos).....	132
59. Car-mounted microphone.....	133
60. The speed and position sensor provided by the test center (TTC photo).....	133
61. Wayside instrumentation.....	135

LIST OF FIGURES (Cont.)

FIGURE	PAGE
62. The wayside instrumentation van.....	136
63. Rail accelerometer locations (TTC photo).....	138
64. Wayside microphone locations at test site No. 1.....	139
65. Spurious noise in the rail vibration recordings, vertical acceleration at the rail foot.....	140
66. Schematic of roughness measuring device.....	142
67. The test cart for measuring rail roughness.....	143
68. The measurement of roughness on both tangent and curved track (TTC photo).....	144
69. Technician guiding the cables from the roughness cart (TTC photo).....	146
70. The Hegenscheidt wheel-truing machine set up for measuring wheel roughness (TTC photos).....	147
71. Typical rail roughness acceleration spectrum - welded rail.....	148
72. Typical wheel acceleration spectrum.....	149
73. Probe transfer function.....	151
74. Rail roughness on the welded rail test section.....	153
75. Rail roughness spectra at three properties.....	154
76. Rail roughness spectra for three different track sections at TTC, Pueblo.....	155
77. Rail roughness spectra on the screech loop.....	156
78. Wheel roughness spectra on SOAC.....	157
79. Wheel roughness spectra from three cars.....	158
80. Measuring the wheel/rail contact area.....	161
81. SOAC wheel/rail contact imprints.....	162
82. Wheel/rail system component vibration for the SOAC passing by at 30 mph on welded rail; 4-sec averaging time.....	165

LIST OF FIGURES (Cont.)

FIGURE		PAGE
83.	Estimates of the contribution of each of the components of the wheel/rail system for the SOAC passing by at 30 mph on welded rail; 4-sec averaging time.....	167
84.	Comparison of predictions and measurements using measured wheel and rail roughness at 30 mph; 4-sec averaging time.....	169
85.	Wheel tread cross section showing possible errors in the measured radial acceleration.....	172
86.	Comparison of measured and predicted wheel/rail noise and vibration for the SOAC at 20 mph on welded rail; 4-sec averaging time.....	175
87.	Comparison of measured and predicted wheel/rail noise and vibration for the SOAC at 30 mph; 4-sec averaging time.....	177
88.	Comparison of measured and predicted wheel/rail noise and vibration for the SOAC at 45 mph; 4-sec averaging time.....	179
89.	Comparison of measured and predicted wheel/rail noise and vibration for the SOAC at 60 mph; 2-sec averaging time.....	181
90.	Comparison of measured and predicted wheel/rail noise and vibration for the SOAC at 80 mph; 2-sec averaging time.....	183
91.	Comparison of measured and predicted wayside noise at 25 ft; 4-sec averaging time.....	184
92.	Typical rail joint on the transit test track....	185
93.	Rail joint geometry at the test section.....	187
94.	Comparison of measured and predicted wayside noise at 25 ft on welded and jointed rail; 4-sec averaging time.....	188
95.	Wayside noise at 25 ft on welded and jointed rail; 4-sec averaging time.....	189
96.	Wayside noise at 25 ft on welded and jointed rail; 2-sec averaging time.....	190
97.	Comparison of wheel vibration on welded and jointed rail at 30 mph.....	191

LIST OF FIGURES (Cont.)

FIGURE	PAGE
98. Wheel flat geometry.....	193
99. Comparison of measured wayside noise at 25 ft for smooth and flatted wheels (normalized to a 4-sec averaging time).....	194
100. Rail roughness spectra at welded rail test site compared with equivalent roughness due to wheel flats.....	196
101. Comparison of noise and vibration with and without wheel flats.....	198
102. Rail vibration during passage of SOAC at 30 mph (normalized to a 4-sec averaging time).....	200
103. Baseline wheel and rail roughness.....	204
104. Baseline rail loss factor.....	205
105. Baseline system predictions of wheel/rail noise and vibration.....	207
106. Estimated effect of changes in wheel radius on wayside noise at 25 ft; two-car train at 30 mph	210
107. Estimated effect of wheel tread thickness changes on wayside noise at 25 ft; two-car train at 30 mph.....	211
108. Estimated effect of wheel web thickness on wayside noise at 25 ft; two-car train at 30 mph.....	212
109. Estimated effect of rail weight on wayside noise at 25 ft; two-car train at 30 mph.....	213
110. Estimated effect of wheel damping on wayside noise at 25 ft; two-car train at 30 mph.....	215
111. Estimated effect of wheel load on wayside noise at 25 ft; two-car train at 30 mph.....	216
112. Estimated effect of changing contact stiffness on wayside noise at 25 ft; two-car train at 30 mph.....	218
113. Estimated wheel sound radiation for various contact stiffnesses.....	219
114. Estimated effect of increasing contact area on wayside noise at 25 ft; two-car train at 30 mph.....	221

LIST OF FIGURES (Cont.)

FIGURE	PAGE
115.	Estimated noise levels after wheel and rail smoothing.....223
116.	Lower-bound wheel and rail roughness.....224
117.	Effect on noise of rail joints.....226
118.	Typical wheel flat.....227
119.	Effect on noise of wheel flats.....228
120.	Hard-faced rail.....231
121.	Test site in Hannover.....232
122.	Comparison of squeal occurrence on the MBTA and CTA.....235
123.	Stanray undercar milling machine.....238
124.	Wheel roughness after smoothing with the undercar milling machine.....240
125.	Wheel roughness after smoothing with an undercar lathe.....242
126.	Wheel roughness after turning on a wheelset lathe.....243
127.	The belt grinder at TTC (Toronto).....245
128.	The hydraulic jacks used to support the transit car on the belt grinder.....246
129.	The grinding operation.....247
130.	One-third octave band acceleration level obtained from surface roughness probe before and after belt grinding. (Wheel axle 3, track 3; wheel surface speed = 22.7 in./sec.).....250
131.	One-third octave band acceleration level obtained from surface roughness probe before and after belt grinding. (Wheel axle 1, track 3; wheel surface speed = 22.7 in./sec.).....251
132.	Wheel roughness before belt grinding, after belt grinding, and after 520 miles of service.....252
133.	Speno vertical axis rail grinder at SEPTA.....254

LIST OF FIGURES (Cont.)

FIGURE	PAGE
134.	The rail roughness measuring device in use on the screech loop at TTC (Pueblo).....255
135.	Rail roughness after use of the vertical axis rail grinder at TTC (Pueblo).....256
136.	The CTA rail grinding car.....258
137.	The grinding block arrangement under the trucks of the TTC (Toronto) rail grinding car.....259
138.	The CTA test site at Loyola Station on the Evanston line.....260
139.	CTA (Loyola Station) rail roughness before grinding and after 7 to 8 passes.....262
140.	Comparison of rail roughness at CTA (Loyola Station) before and after rail grinding. (Outside rail.).....263
141.	Comparison of rail roughness at CTA (Loyola Station) before and after rail grinding. (Inside rail.).....264
142.	Performance of the CTA rail grinder.....266
143.	The estimated reduction in noise from a two-car train at 25 ft, because of wheel truing and rail grinding.....267
144.	The reduction in noise achievable with the best wheel truing and rail grinding techniques.....269
145.	Rail wheel geometry.....273
146.	Dimensions of the three test wheels.....274
147.	BBN roughness measuring probe mounted on roller rig.....276
148.	Roughness spectra measured on roller rig.....277
149.	Contact patch areas for steel nitinol C wheels (shown actual size).....278
150.	Noise and vibration instrumentation.....280
151.	Slip ring assembly mounted on rail wheel (TTC photo).....281

LIST OF FIGURES (Cont.)

FIGURE	PAGE
152.	Comparison of rolling noise for steel and nitinol C wheels. (Raychem roller rig; load = 625 lb at 60 km/hr.).....284
153.	Comparison of rolling noise for steel and nitinol C wheels. (Raychem roller rig; load = 625 lb at 88 km/hr.).....285
154.	Rolling vibration for rail wheel. (Load = 625 lb at 88 km/hr.).....286
155.	Comparison of steel vs nitinol A rolling noise. (Raychem roller rig; 625 lb at 60 km/hr.).....288
156.	Schematic of a concept for a resiliently treaded wheel.....290
157.	Preliminary design.....292
158.	Estimated acoustic performance of the resiliently treaded wheel.....295
159.	Test wheels used on Raychem roller rig, scaled from CTA 28-in. rolled steel wheel.....296
160.	Surface roughness of test wheel after manufacture.....298
161.	Contact stiffness for standard and resilient test wheels.....299
162.	Approximate contact patch sizes measured on the test wheels for different loads.....301
163.	The two sets of strain gauges on the wheel tread.....303
164.	Orientation of the strain gauges.....305
165.	Typical traces of strain vs circumferential position.....307
166.	The standard steel wheel mounted in the Raychem roller rig.....308
167.	The resiliently treaded wheel mounted in the Raychem roller rig.....308
168.	Basic, uncorrected data one-third octave band spectra of standard wheel and resiliently treaded (thin rim) wheel. (Speed = 40 km/hr; load = 1000 lb.).....309

LIST OF FIGURES (Cont.)

FIGURE	PAGE
169. Background noise of rolling rig. (Speed = 40 km/hr; no contact between rail wheel and test wheel.).....	310
170. Comparison between the standard wheel and the resiliently treaded wheel. (Speed = 40 km/hr; load = 1000 lb; tread ring thickness = 0.16 in.).....	312
171. Comparison between the standard wheel and the resiliently treaded wheel. (Speed = 80 km/hr; load = 1000 lb; tread ring thickness = 0.16 in.).....	313
172. Comparison between the standard wheel and the resiliently treaded wheel. (Speed = 40 km/hr; load = 1500 lb; tread ring thickness = 0.16 in.).....	314
173. Comparison between the standard wheel and the resiliently treaded wheel. (Speed = 60 km/hr; load = 500 lb; tread ring thickness = 0.16 in.).....	315
174. Comparison of steel wheel with the resiliently treaded wheel with the 0.23-in. tread ring. (Speed = 40 km/hr; load = 1000 lb.).....	316

LIST OF TABLES

TABLE	PAGE
1. The quantity ξ in the equation for the Hertzian deflection.....	16
2. Parameters for the SOAC 30-in. wheel.....	38
3. Some resonant frequencies in Hz of a 2.5-ft segment of 119 lb/yd rail.....	56
4. Rolling noise model summary.....	86
5. The likelihood of squeal for curves on the MBTA with a ratio of curve radius to truck wheelbase greater or less than 100.....	118
6. Typical loss factors of damped wheels [23].....	120
7. SOAC wheel/rail contact areas.....	164
8. Incidence of squeal and lubrication on CTA curves.....	236
9. Percentage of lubricated and unlubricated curves that squeal.....	236
10. Nitinol alloy properties.....	275
11. Summary of nitinol C wheel test results scaled up to a 30-in. wheel.....	287
12. Preliminary design estimates for the resiliently treaded wheel.....	293
13. Contact stiffness (lb/in.).....	300
14. Contact patch dimensions for the 1000-lb scaled wheel load (9700-lb full scale).....	302
15. Principal stresses at the center of the 0.16-in.-thick tread.....	306
16. Stresses in the tread near the tread support for the 0.16-in.-thick tread.....	306
17. Summary of full-scale noise reductions achieved with resiliently treaded wheel with 0.16-in. tread ring.....	317

1. INTRODUCTION

1.1 Background

Flanged metal wheels on metal rails have been used to support, guide, and move heavy loads with minimum rolling resistance since 1805, when Richard Trevithick of England designed the first steam locomotive. For this locomotive, he used cast iron wheels with flanges on the outside which ran on cast iron "edge rails." These were rails with a head geometry similar to present-day rails but with no rail foot. Instead, the rail base rested in a cast iron chair mounted on a stone block.

In 1827, the United States entered railroading with the founding of the Baltimore and Ohio Railroad. American designers reversed the European style, however, building wheels with flanges on the inside. Soon, the tapered or conical wheel tread was introduced, and by 1831, the "T-rail" section still used today, was introduced by the Camden and Amboy Railroad. Shortly thereafter, the stone blocks used as rail supports were replaced by wooden railroad ties (a far-reaching change that stemmed from a shortage of stone during the development of the first New Jersey-New York railroad line). Consequently, by the early 1830s, the wheel/rail system looked essentially the same as it does today. Improvements made since that time have been primarily in the areas of metallurgy, manufacturing, and standardization.

There are a number of good reasons for the longevity of this seemingly simple system. It is durable and self-guiding, has low rolling resistance, and has high load-carrying capacity. But it has one major drawback for use in urban transportation vehicles - the intense noise generated by the interaction between the wheel and rail while the vehicle is in motion. This wheel/rail noise

is generally divided into three very general categories [2], squeal, impact, and roar.

Squeal is the term used to describe the intense noise, consisting of one or more tones, heard when rail cars round curves of small radius. As the transit car rounds the curve, its wheels cannot run tangent to the rails because they are constrained by the car's rigid truck - i.e., the axles cannot take up radial positions in the curve. As the car turns the curve, then, the wheels roll along the rail, but they also creep laterally across the rail head as shown in Fig. 1. If the lateral creep, defined as the wheel lateral velocity divided by the rolling velocity, is sufficiently large, a small transient excitation of the wheel will be reinforced by the friction forces at the wheel/rail interface. The wheel response will then grow until a stable amplitude is reached at one or more of the wheel natural frequencies. This intense wheel vibration is then radiated as the familiar squeal noise. In typical rapid transit systems, curves of 700 ft or less will generate squeal.

Impact noise and rolling noise are generated by the same source: irregularities on the wheel and rail running surfaces, as illustrated in Fig. 2. For impact noise, the irregularities are typically wheel flats and rail joints. For rolling noise, the small-scale roughness on the running surfaces of the wheel and rail generates the noise. In each case, when the wheel encounters the irregularity, it must either rise up over it, push the rail down out of the way, or do a little of each. In any event, the rapid change in vertical velocity of the wheel and/or rail results in a large force at the interface, which excites the wheel and rail and causes them to radiate sound.

Squeal, impact noise, and rolling noise have existed from the earliest days of rail transit. Surprisingly, 150 years

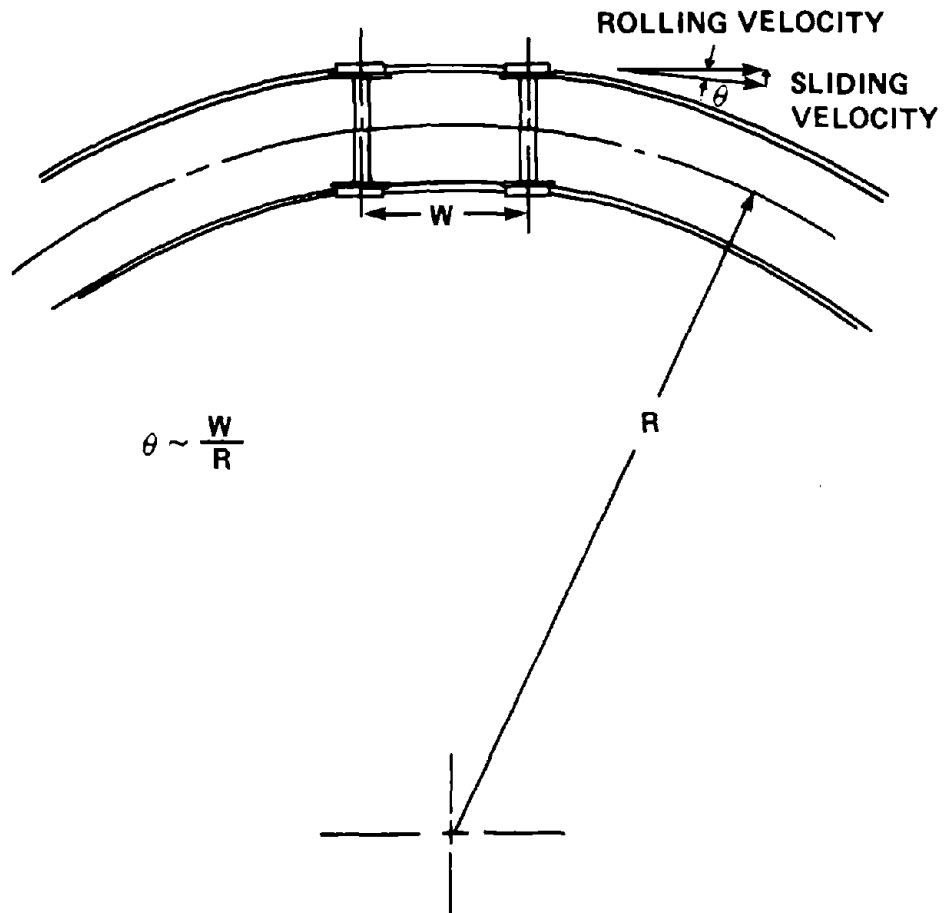


FIG. 1. THE GEOMETRY OF SQUEAL NOISE EXCITATION.

WHEEL/RAIL INTERACTION

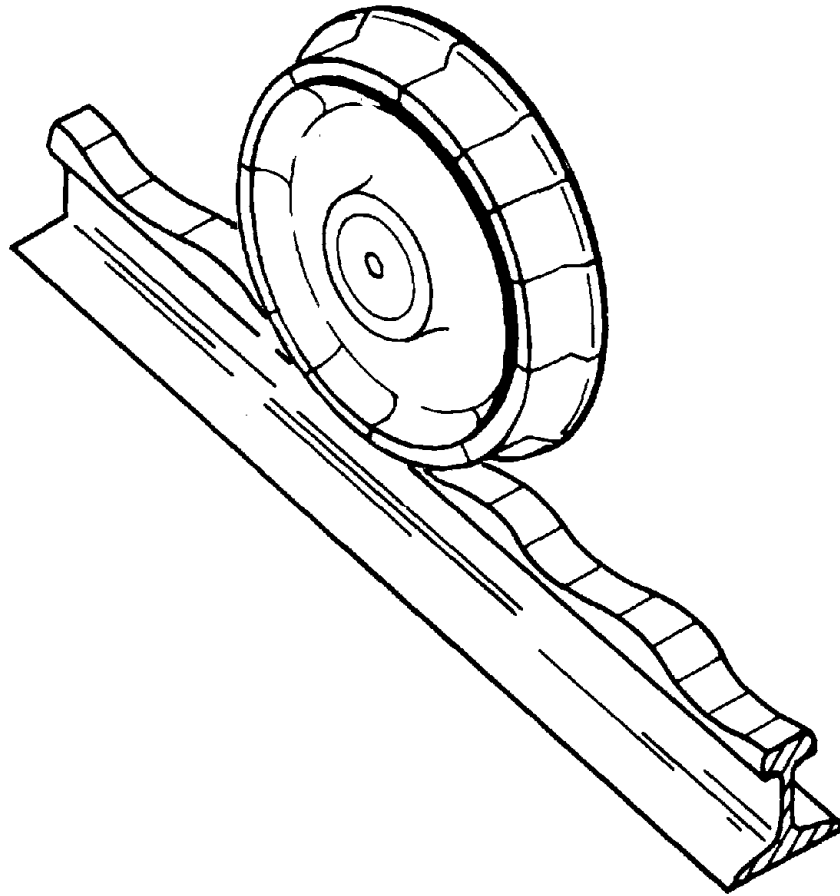


FIG. 2. THE GENERATION OF IMPACT AND ROAR NOISE.

later, there are still few treatments that can effectively reduce these noises in a manner compatible with the operation of rapid transit systems. In the 1970s, the Department of Transportation addressed this problem by initiating a study into the sources and mechanisms of wheel/rail noise [3]. The program described in this report builds on that earlier work, developing durable, compatible, cost-effective treatments to bring the rail industry closer to the goal of control of wheel/rail noise.

1.2 Overview

This program began with an intensive review of the open literature combined with extensive contacts with rapid transit and railroad equipment manufacturers, rapid transit operators, and researchers in the field of wheel/rail noise. The review critically evaluated the most cost-effective treatments for the control of wheel/rail noise. The results of this critical evaluation, published as U.S. DOT Report No. UMTA-MA-06-0099-81-1 [1], provided guidance for the remainder of the study.

Having identified and rank-ordered potential wheel/rail noise control treatments, we constructed a detailed analytical model of the generation of wheel/rail noise. The model was based on the work in the aforementioned DOT study on the sources and mechanisms of wheel/rail noise [3], but was substantially improved in a number of areas, including a more sophisticated wheel impedance model, modeling of the lateral wheel response, inclusion of contact stiffness effects, and a sophisticated sound propagation model that involved ground effects. The objective in developing the model was to provide a design and evaluation tool for the development of improved noise control treatments.

Before the analytical model could be used with confidence, it had to be validated. To do so, we carried out an extensive series of tests on the Transit Test Track (TTT) at the U.S.

Department of Transportation's Transportation Test Center (TTC) in Pueblo, Colorado. We used the State-of-the-Art Car (SOAC), a modern vehicle built by DOT around 1970 to demonstrate the latest state-of-the-art technology for rapid transit cars. Figure 3 shows the SOAC on the screech loop at TTC (Pueblo), and Fig. 4 shows the two tangent test sections used during the validation measurements. We measured noise, wheel and rail vibration, roughness, impedance, and contact area, and sound propagation effects. These data were then compared with the analytical model predictions to establish the validity of the analysis.

After validating the analytical model, we exercised it for a wheel/rail system typical of rapid transit systems throughout the United States to establish critical parameters in the generation of noise. Those results, together with the results of the critical evaluation, focused our efforts on a small number of noise control treatments. For squeal noise, we concentrated on site-specific treatments, such as rail lubrication and the use of a special antisqueal rail called a "hard-faced" rail. We also looked at the effect of curve radius on the likelihood of squeal occurring. For roar and impact noise, we focused on techniques for wheel and rail smoothing and resiliently treaded wheels, a new wheel design that takes advantage of the noise-reducing capabilities of reduced contact stiffness and increased contact area.

Hard-faced rails are being used experimentally in Europe. To examine their effectiveness at reducing squeal, we made measurements on a curve in Hannover, West Germany, that had both hard-faced and standard rails. We also requested information from the Frankfurt and Stuttgart transit systems on their operating experience. Rail lubrication, both oil and water spray, was examined on the screech loop at Pueblo. TTC personnel carried out a series of measurements at our direction to examine

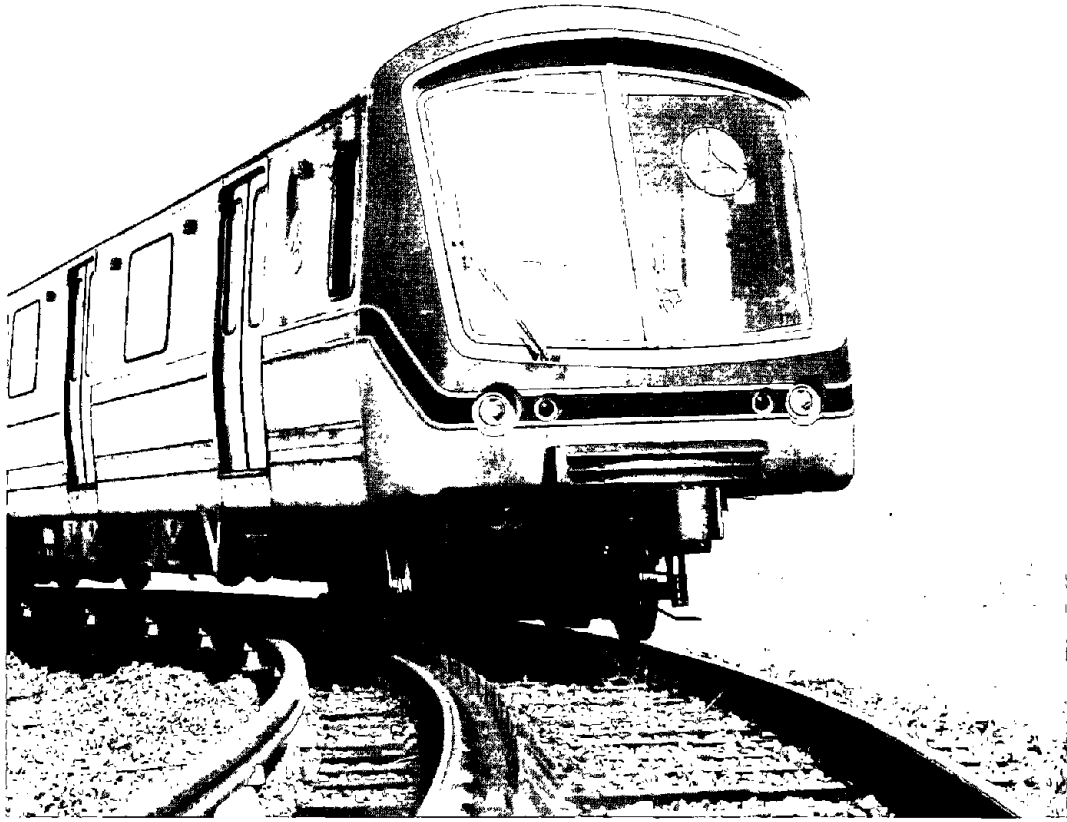
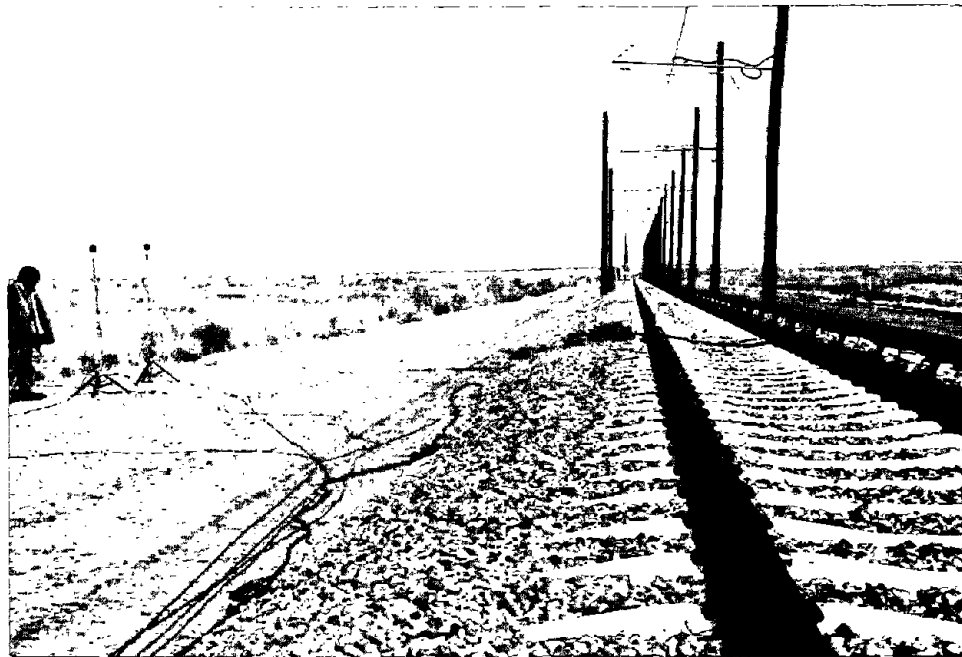


FIG. 3. THE STATE-OF-THE-ART CAR.



(a) Jointed Rail on Wood Ties.



(b) Welded Rail on Concrete Ties.

FIG. 4. TEST SECTIONS AT THE TRANSPORTATION TEST CENTER, PUEBLO, COLORADO.

the effectiveness of lubricating one rail or both rails. Tests were carried out with and without restraining rail. [These tests are not discussed in this report; they will be reported on separately by TSC personnel. We do, however, report on a comparison of squeal occurrence on two transit properties - one that uses rail lubrication on curves, the Chicago Transit Authority (CTA), and one that does not, the Massachusetts Bay Transportation Authority (MBTA).]

Using a specially developed device for measuring wheel and rail roughness, we measured wheel and rail running surface roughness after applying various wheel and rail smoothing techniques (such as rail grinding and wheel truing). The analytical model was then used to determine the anticipated reduction in noise resulting from the application of various combinations of these treatments.

Two resiliently treaded wheels were examined: a wheel with a nickel titanium tread and a wheel of new design that incorporates a thin, removable steel tread. Scale-model wheels of both types (1/3 to 1/4 scale) were tested on a roller rig (by using a large wheel to simulate a rail) to examine their acoustical effectiveness and mechanical integrity.

A preliminary examination of slip-slide prevention systems indicated that a major program would be required to determine the effectiveness of those systems in reducing the noise caused by wheel flats and to learn whether increased wheel truing or the use of slip-slide prevention systems would be the most cost-effective way to reduce wheel flat noise. Such a program was beyond our resources. Therefore, we simply provided the elements of a plan to address these issues. Other programs have also been suggested to develop further such noise control approaches as the

use of hard-faced rails, wheel and rail smoothing techniques, and resiliently treaded wheels.

1.3 Organization of the Report

Sections 2 and 3 of this report describe the development of the analytical model and its validation, respectively. In Sec. 4, we present the results of exercising the model to determine those parameters important to noise generation. Section 5 is a discussion of the development and evaluation of a number of wheel/rail noise control techniques, and Sec. 6 presents a number of plans for continuing research.

2. THEORETICAL ANALYSIS

2.1 Rolling Noise

The wheel/rail noise that predominates on tangent track in the absence of discontinuities on the wheel and rail running surface, such as wheel flats, rail joints, etc., is called "roar" or "rolling noise." An earlier DOT study [3] showed that this noise can be attributed to the small-scale roughness on the running surfaces of the wheel and rail exciting both into vibration. In turn, this vibration is radiated as wheel/rail noise.

That study also presented an analytical model that related the radiated sound to the wheel and rail roughness. Although that model showed reasonable agreement with measured data, it became apparent early in the program that the following modifications were necessary:

- Inclusion of the contact stiffness in the wheel/rail interaction model
- Improvement of the wheel/rail contact area filter model
- Improvement of the wheel impedance model
- Improvement in the prediction model for the wheel axial response
- Inclusion of ground effects in the sound propagation model
- Prediction of the average wayside noise during a train passby rather than the noise at a particular train position during the passby.

Figure 5 shows a block diagram of the analytical model after inclusion of the above modifications. The model is divided into two parts: wheel/rail interaction and sound radiation. In the

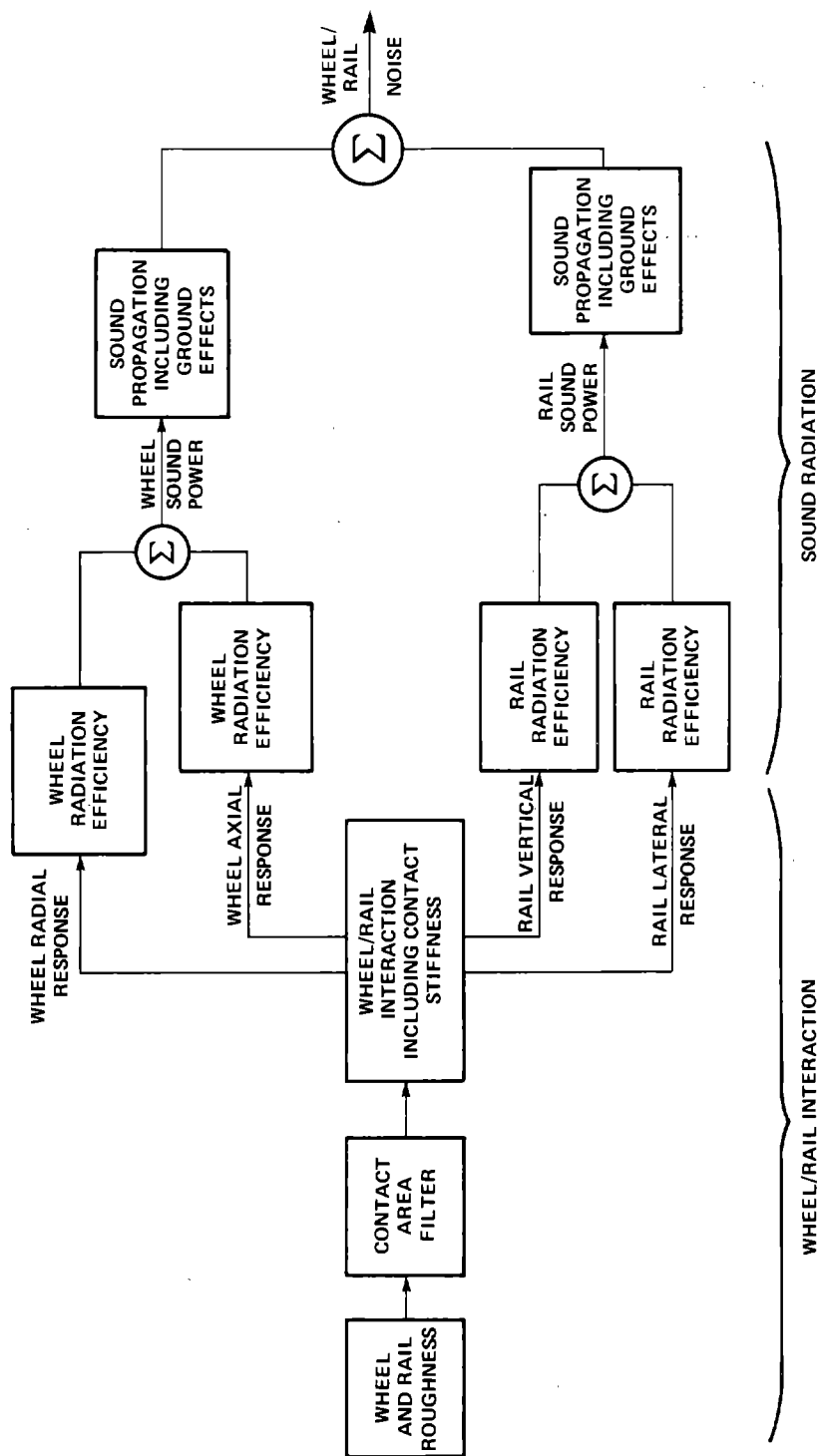


FIG. 5. BLOCK DIAGRAM OF THE ANALYTICAL MODEL.

next two sections, we discuss the modifications made to these two components of the model.

2.1.1 Wheel/rail interaction

Contact Stiffness

Figure 6 is a schematic drawing of the interaction between the wheel and rail. When the wheel and rail are pressed together under load, there is a small amount of local deformation. This local or Hertzian deformation is distinct from the gross bending deformation of the rail and the modal response of the wheel. To account for it, we have placed one small spring between the rough surface of the wheel and the reference circle and another between the rough surface of the rail and the rail reference line. Referring to Fig. 6, we can write

$$Y_{WR} = Y_{RV} + W - \frac{F_V}{K_{CW}} + r - \frac{F_V}{K_{CR}} \quad (1)$$

where F_V is the interaction force between the wheel and rail, W and r are roughness displacement on the surface of the wheel and rail respectively, and Y_W and Y_R are the wheel and rail gross deflections, as opposed to the local Hertzian deflections. Under the assumption of harmonic excitation of the form $e^{-j\omega t}$, we can take the derivative of both sides of Eq. (1) and obtain

$$\dot{Y}_{WR} = \dot{Y}_{RV} + \dot{W} + \frac{j\omega F_V}{K_{CW}} + \dot{r} + \frac{j\omega F_V}{K_{CR}} \quad (2)$$

where $(\dot{}) = \frac{d}{dt}$.

If the point impedance of the wheel in the radial direction is Z_{WR} and the point impedance of the rail in the vertical direction is Z_{RV} , the relationship between the interaction for F and the

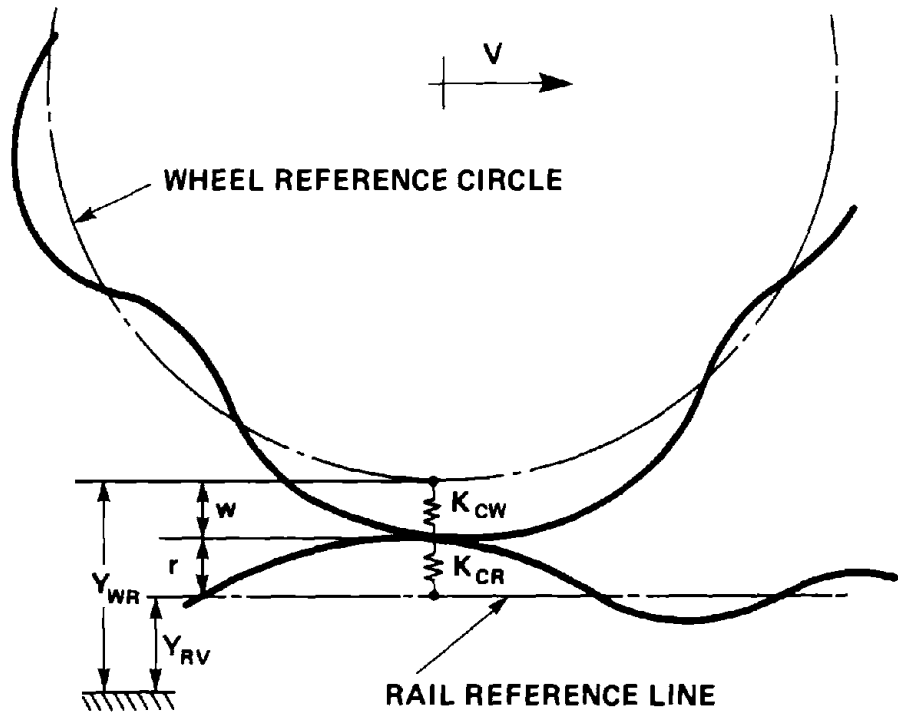


FIG. 6. SCHEMATIC DRAWING OF WHEEL/RAIL INTERACTION.

wheel and rail velocity is given by:

$$\begin{aligned}\dot{Y}_{WR} &= \frac{F_V}{Z_{WR}} \\ \dot{Y}_{RV} &= -\frac{F_V}{Z_{RV}}.\end{aligned}\quad (3)$$

Substituting Eqs. (3) into Eq. (2) and solving for F_V in terms of the roughness velocities \dot{W} and \dot{R} , we obtain

$$F_V = \frac{Z_{WR} Z_{RV} (\dot{w} + \dot{r})}{Z_{WR} + Z_{RV} - j\omega Z_{WR} Z_{RV} \left(\frac{1}{K_{CR}} + \frac{1}{K_{CW}} \right)}.\quad (4)$$

Substituting Eq. (4) into Eqs. (3), we obtain

$$\dot{Y}_{WR} = \frac{Z_{RV} (\dot{w} + \dot{r})}{Z_{WR} + Z_{RV} - j\omega Z_{WR} Z_{RV} \left(\frac{1}{K_{CR}} + \frac{1}{K_{CW}} \right)}.\quad (5)$$

$$\dot{Y}_{RV} = \frac{Z_{WR} (\dot{w} + \dot{r})}{Z_{WR} + Z_{RV} - j\omega Z_{WR} Z_{RV} \left(\frac{1}{K_{CR}} + \frac{1}{K_{CW}} \right)}.\quad (6)$$

If we define a stiffness R_C by

$$\frac{1}{R_C} = \frac{1}{K_{CR}} + \frac{1}{K_{CW}},\quad (7)$$

we can see immediately that R_C is the total stiffness of the two contact springs in series and is the total Hertzian contact stiffness between the wheel and rail. Analytical estimates of R_C are readily available in the literature [4]. For a new wheel rolling on a new rail, the vertical deflection α for a load P forcing the wheel against the rail is given by

$$\alpha' = \xi \sqrt[3]{\left(\frac{P}{\frac{4}{3} \frac{E}{1-\nu^2}}\right)^2 \frac{1}{4} \left(\frac{1}{R_W} + \frac{1}{R_R}\right)}, \quad (8)$$

where E is the modulus of the wheel and rail, R_W is the wheel radius, and R_R is the radius of curvature of the rail (usually 10 to 14 in.). The quantity ξ is given in Table 1 as a function of the angle θ , which is given by

$$\theta = \cos^{-1} \left\{ \frac{\left| \frac{1}{R_W} - \frac{1}{R_R} \right|}{\left(\frac{1}{R_W} + \frac{1}{R_R} \right)} \right\}. \quad (9)$$

TABLE 1. THE QUANTITY ξ IN THE EQUATION FOR THE HERTZIAN DEFLECTION [4].

θ (degrees)	ξ
1.453	30
1.637	40
1.772	50
1.875	60
1.944	70
1.985	80
2.000	90
1.985	100

Estimating K_C from the relationship

$$K_C = \frac{dP}{d\alpha},$$

we can rearrange Eq. (8), take the derivative of P with respect to α , and obtain

$$K_C = \frac{dP}{d\alpha} = \frac{3}{2\xi} \sqrt[3]{\left(\frac{4}{3} \frac{E}{1-\nu^2}\right)^2 P \left(\frac{4R_W R_R}{R_W + R_R}\right)} \quad (10)$$

We will use this expression to estimate the contact stiffness.

If the wheel and rail have random roughness on their running surfaces with wavenumber spectra $\phi_{RW}(k)$ and $\phi_{RR}(k)$, respectively, we can estimate the frequency spectrum of the wheel and rail velocity at the point of contact by

$$\begin{aligned} \phi_{\dot{Y}_{RV}}^{(pc)}(\omega) &= \left| \frac{Z_{WR}}{Z_{WR} + Z_{RV} - j\omega \frac{Z_{WR} Z_{RV}}{K_C}} \right|^2 \omega^2 |H(k)|^2 [\phi_{RW}(k) + \phi_{RR}(k)] \frac{dk}{d\omega} \\ \phi_{\dot{Y}_{WR}}^{(pc)}(\omega) &= \left| \frac{Z_{RV}}{Z_{WR} + Z_{RV} - j\omega \frac{Z_{WR} Z_{RV}}{K_C}} \right|^2 \omega^2 |H(k)|^2 [\phi_{RW}(k) + \phi_{RR}(k)] \frac{dk}{d\omega} \end{aligned} \quad (11)$$

where $k = \omega/V$. We have related the frequency spectrum of the roughness at train speed V by

$$\phi(\omega) = \phi(k) \frac{dk}{d\omega} \quad .$$

Note that we have included the quantity $|H(k)|^2$ to account for the fact that the components of roughness with very short

wavelengths are less efficient at exciting the wheel and rail. We will calculate this quantity later in this section.

In general, we are interested in one-third octave or octave band spectra rather than power spectra, as in Eq. (11). Consequently, we can write

$$\begin{aligned}
 S_{\dot{Y}_{RV}}^{(pc)}(\omega) &= \int_{\omega - \frac{\Delta\omega}{2}}^{\omega + \frac{\Delta\omega}{2}} \phi_{Y_R}^{(pc)}(\omega) d\omega \\
 &\approx \left| \frac{Z_{WR}}{Z_{WR} + Z_{RV} - \frac{j\omega Z_{WR} Z_{RV}}{K_C}} \right|^2 \omega^2 [S_{RW}(k) + S_{RR}(k)] |H(k)|^2 \\
 S_{\dot{Y}_{WR}}^{(pc)}(\omega) &= \int_{\omega - \frac{\Delta\omega}{2}}^{\omega + \frac{\Delta\omega}{2}} \phi_{Y_W}^{(pc)}(\omega) d\omega \\
 &\approx \left| \frac{Z_{RV}}{Z_{WR} + Z_{RV} - j\omega \frac{Z_{WR} Z_{RV}}{K_C}} \right|^2 \omega^2 [S_{RW}(k) + S_{RR}(k)] |H(k)|^2,
 \end{aligned} \tag{12}$$

where

$$\begin{aligned}
 S_{RW}(k) &= \int_{k - \frac{\Delta k}{2}}^{k + \frac{\Delta k}{2}} \phi_{RW}(k) dk \\
 S_{RR}(k) &= \int_{k - \frac{\Delta k}{2}}^{k + \frac{\Delta k}{2}} \phi_{RR}(k) dk
 \end{aligned} \tag{13}$$

and $\Delta k = \Delta\omega/V$.

In most of this report, $\Delta\omega$ will be a one-third octave band, and consequently the roughness spectra will also be in one-third octave bands in wavenumber.

In the next section, when we examine the calculation of the sound radiation, it will be convenient to have the rail vibration averaged over time T , where T is longer than the time it takes the train to pass. It has been shown [5] that the average rail response is related to the rail response at the point of contact by

$$S_{\dot{Y}_{RV}}^{(AVG)}(\omega) = \frac{N (1 - e^{-\eta_{RV} k_{RV} VT})}{2\eta_{RV} k_{RV} VT} S_{\dot{Y}_{RV}}^{(pc)}(\omega) , \quad (14)$$

where N is the number of axles in the passing train, η_{RV} is the rail loss factor, and k_{RV} is the bending wavenumber on the rail given by

$$k_{RV} = \left(\frac{\omega}{r_{RV} c_\ell} \right)^{1/2} , \quad (15)$$

where r_{RV} is the radius of gyration of the rail for bending in the vertical plane and c_ℓ is the longitudinal wavespeed in the rail. It is convenient for comparison with measurements to express the rail response in terms of the acceleration

$$S_{\ddot{Y}_{RV}}^{(AVG)}(\omega) = \frac{N\omega^4 (1 - e^{-\eta_{RV} k_{RV} VT})}{2\eta_{RV} k_{RV} VT} \times \left| \frac{z_{WR}}{z_{WR} + z_{RV} - j\omega \frac{z_{WR} z_{RV}}{K_C}} \right|^2 |H(k)|^2 [S_{RR}(k) + S_{WR}(k)] , \quad (16)$$

where the relationship between velocity and acceleration spectra, $S_{\dot{Y}}(\omega) = \omega^2 S_Y(\omega)$, has been used in Eq. (16).

As with the rail, it is also convenient when calculating the sound radiation from the wheel to have the average response on the wheel rather than the response at the point of contact. The wheel is a multimodal system. As we will see later, the amplitude of its response to a harmonic point force of amplitude F is given by

$$\dot{Y}_{WR} = \sum_n A_n \cos n\theta \quad ,$$

where θ is the angle measured from the point of application of the force and A_n is the modal admittance of the n th mode. The time averaged squared response at location θ is given by

$$\langle \dot{Y}_{WR}^2 \rangle = \frac{|F^2|}{2} \text{Re} \left\{ \sum_n \sum_m A_n A_m^* \cos n\theta \cos m\theta \right\} \quad , \quad (17)$$

where $*$ means complex conjugate. Consequently, at the point of contact, the time average response is

$$\langle (\dot{Y}_{WR}^{pc})^2 \rangle = \frac{|F^2|}{2} \left| \sum_n A_n \right|^2 \quad (18)$$

and the average squared response around the circumference of the wheel is

$$\langle (\dot{Y}_{WR}^{(AVG)})^2 \rangle = \frac{|F^2|}{2} \text{Re} \left\{ \sum_n \sum_m A_n A_m^* \frac{1}{2\pi} \int_0^{2\pi} \cos n\theta \cos m\theta d\theta \right\} \quad . \quad (19)$$

The integral on the right equals $1/2$ if n equals m and 0 if n does not equal m . Consequently, Eq. (19) simplifies to

$$\langle (\dot{Y}_{WR}^{(AVG)})^2 \rangle = \frac{|F^2|}{2} \sum_n |A_n|^2 \quad (20)$$

Therefore, if $S_{\dot{Y}_W}^{(AVG)}(\omega)$ is the spectrum of the wheel response averaged around the circumference of the wheel, we can write

$$S_{\dot{Y}_{WR}}^{(AVG)}(\omega) = \frac{\sum_n |A_n|^2}{|\sum_n A_n|^2} S_{\dot{Y}_{WR}}^{(pc)}(\omega) \quad (21)$$

Expressing the wheel response in terms of its acceleration, we obtain

$$S_{\ddot{Y}_{WR}}^{(AVG)}(\omega) = \omega^4 \left| \frac{\sum_n |A_n|^2}{|\sum_n A_n|^2} \frac{Z_{RV}}{Z_{RV} + Z_{WR} - j\omega \frac{Z_{RV} Z_{WR}}{K_C}} \right|^2 |H(k)|^2 [S_{RW}(k) + S_{RR}(k)] \quad (22)$$

We will calculate the values of A_n later in this section.

Contact Area Filter

When the wheel rests on the rail there is a small, generally elliptical, area about the size of a dime, in which the two are in intimate contact. Components of roughness on the surface of the wheel and rail with wavelengths much greater than the dimensions of this contact area are unaffected by it. Those components of roughness with wavelengths on the order of or less than the dimensions of the contact area tend to be averaged out and consequently are less effective in exciting the wheel and rail.

The quantity $H(k)$ in Eqs. (16) and (22) accounts for this averaging out of the short wavelength roughness. In an earlier study [3], an analytical estimate was made for $H(k)$ for circular contact areas given by

$$|H(k)|^2 = \frac{4}{\alpha} \frac{1}{(kb)^2} \int_0^{\tan^{-1} \alpha} J_1^2(kb \sec \chi) d\chi, \quad (23)$$

where b is the contact area radius, k is the roughness wave-number, and α is a measure of the degree of correlation of roughness across the wheel and rail running surfaces. If α is small, the roughness is highly correlated. If α is large, the roughness is poorly correlated. Since we have no data on the correlation effect, we will take the limit of Eq. (23) as α approaches zero, i.e., roughness well correlated across the width of the contact area. We obtain

$$|H(k)|^2 = 4 \left[\frac{J_1(kb)}{kb} \right]^2. \quad (24)$$

Note that for elliptically shaped areas we estimate b by

$$b = \sqrt{pq}, \quad (25)$$

where p and q are the major and minor axes of the ellipse.

This function is plotted in Fig. 7 for $b = 0.20$ in., a typical value for rapid transit systems, and it is referred to in the figure as uniform weighting, as Eq. (24) results from uniformly integrating the roughness over the contact area rather than weighting the integral highest where the stress is highest, for example.

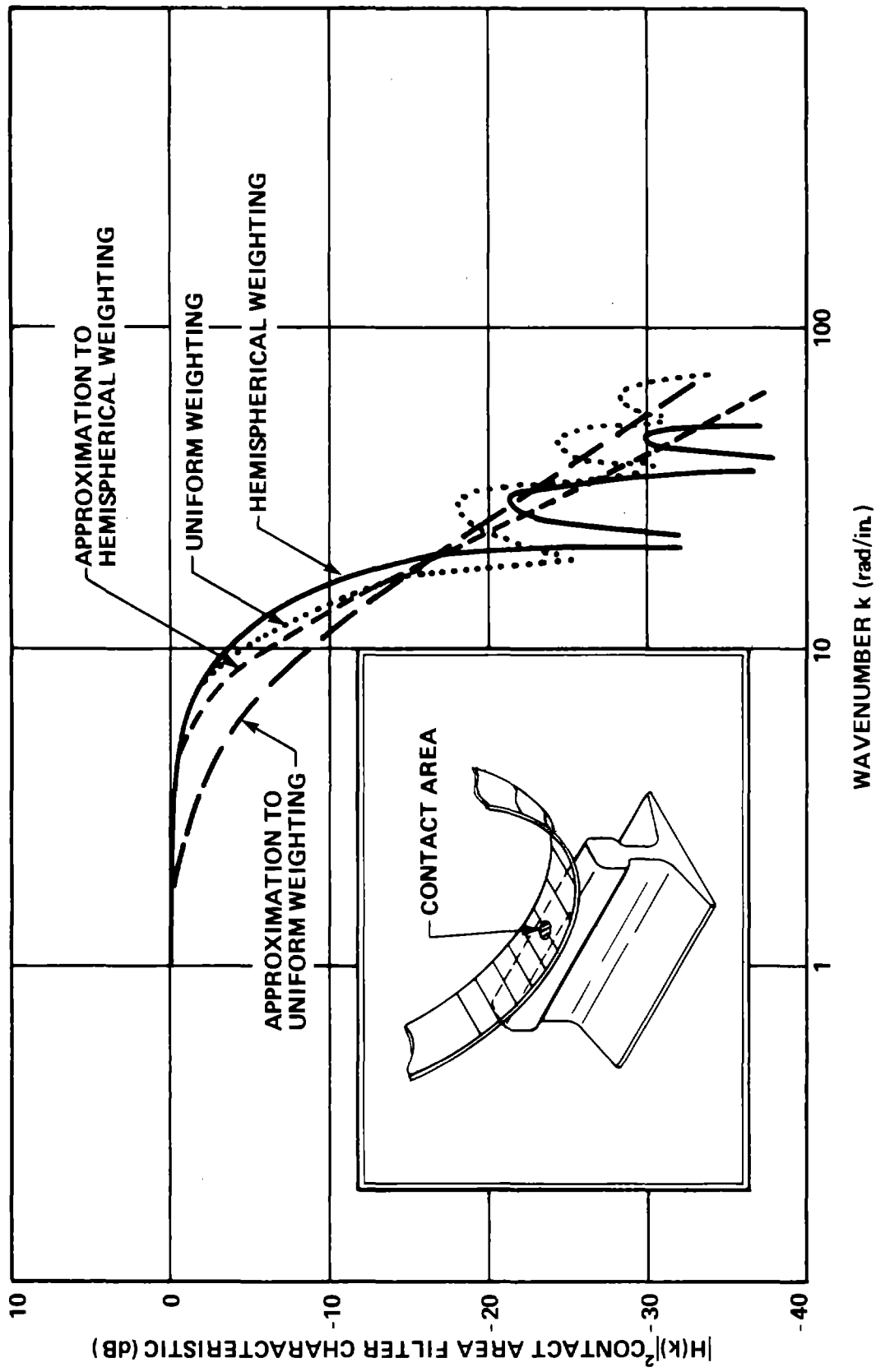


FIG. 7. THE CONTACT AREA WAVENUMBER FILTER FOR $b = 0.20$ in.

The function is very irregular for large k , and a smoothed average value at these high wavenumbers, approximating the filtering effect in octave or one-third octave band, would be useful. For large kb , $J_1^2(kb) \sim (2/\pi kb) \cos^2(kb + 3\pi/4)$, and the average value of this function is $1/(\pi kb)$. At low values of kb , Eq. (24) approaches 1. Consequently, a good smoothed estimate for Eq. (24) is

$$|H(k)|^2 = \frac{1}{1 + \frac{(kb)^3}{4/\pi}} \quad (26)$$

This equation is also plotted in Fig. 7 for comparison with the original function.

If the contact area is circular, the normal stress is distributed according to the form $(b^2 - r^2)^{1/2}$, where b is the contact area radius and r is the radial distance from the center to a point of interest in the circular area. Another approach to calculating the filtering effect of the contact area is to assume that the roughness is most effective in exciting the wheel and rail where the stress is highest. We then weight the integral over the contact area by the stress function. Using an approach similar to that in Remington, Rudd, and Ver [3] and assessing that the roughness is well correlated across the rail and wheel running surfaces, we obtain

$$H(k) = \frac{3}{2\pi b^3} \int_0^{2\pi} d\theta \int_0^b r dr (b^2 - r^2)^{1/2} e^{jkr \cos \theta} \quad (27)$$

Noting that $J_0(Z) = \frac{1}{2\pi} \int_0^{2\pi} d\phi e^{-jZ \cos \phi}$, we can write

$$H(k) = \frac{3}{b^3} \int_0^b (b^2 - r^2)^{1/2} J_0(kr) r dr \quad (28)$$

That integral has a closed form solution [6],

$$H(k) = 3\sqrt{2} \Gamma(1.5) \frac{J_{1.5}(kb)}{(kb)^{1.5}} = \frac{3}{(kb)^2} \left[\frac{\sin kb}{kb} - \cos kb \right] . \quad (29)$$

The absolute value squared of Eq. (29) is shown in Fig. 7. It too is very irregular for k large. Consequently, we have calculated a smoothed average value as for Eq. (24),

$$|H(k)|^2 \approx \frac{1}{1 + \frac{(kb)^4}{4.5}} . \quad (30)$$

Equation (30) is also plotted in Fig. 7. Either this equation or Eq. (26) would be appropriate in our analysis, and the differences between them are small in the wavenumber region of interest. We will use Eq. (26), uniform weighting, in the work to follow.

Wheel and Rail Lateral Response

In an earlier model of wheel/rail noise [3] it was assumed that the lateral or axial response of the wheel was equal to the radial response. That assumption was based on laboratory measurements of the wheel response to a point force applied radially at the tread. Since that time, measurements of wheel vibration on an operating transit car (see Sec. 3) have indicated that that assumption is inadequate. Here we derive a more complex model of both wheel and rail lateral response that correlates better with measured data.

Figure 8 shows the interacting wheel and rail with the forces and velocities at the point of contact. Since the wheel and rail are constrained to move together in the lateral direction, we have assumed that the vertical force F_v tends to

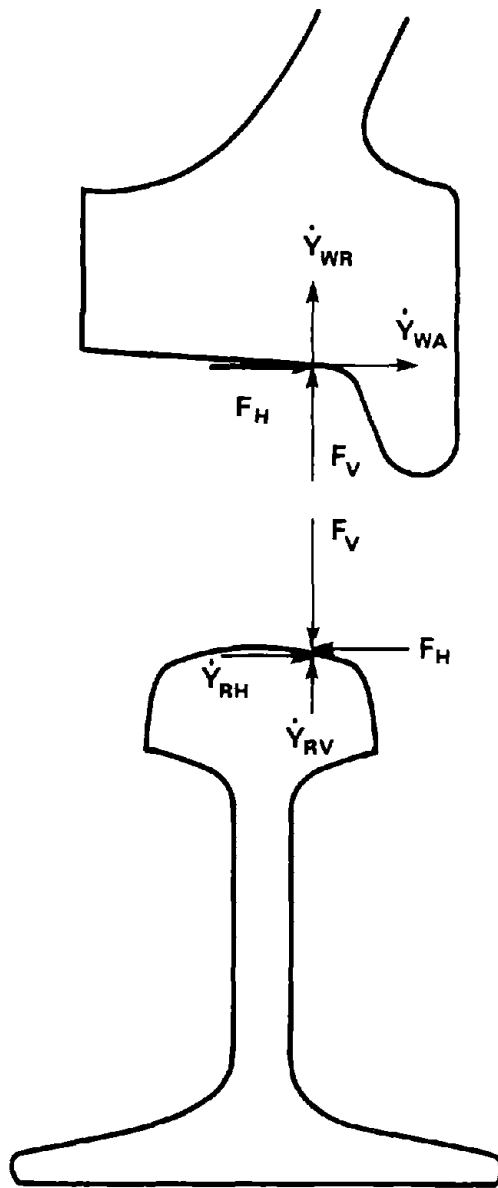


FIG. 8. WHEEL/RAIL LATERAL RESPONSE.

generate lateral motion in the wheel because it is a very asymmetric structure, and in the rail because the point of contact is rarely, if ever, at the centerline of the rail. In mathematical terms, we define two vertical force to horizontal response cross-impedances as follows:

$$\begin{aligned} F_V &= Z_{WVH} \dot{Y}_{WA} \\ F_V &= Z_{RVH} \dot{Y}_{RH} \end{aligned} \quad (31)$$

where \dot{Y}_{WA} is the axial wheel velocity and \dot{Y}_{RH} is the horizontal rail velocity. The lateral wheel and rail response in terms of the vertical and horizontal forces is given by

$$\begin{aligned} \dot{Y}_{WA} &= \frac{F_V}{Z_{WVH}} + \frac{F_H}{Z_{WA}} \\ \dot{Y}_{RH} &= \frac{F_V}{Z_{RVH}} - \frac{F_H}{Z_{RH}} \end{aligned} \quad (32)$$

where Z_{WA} is the axial wheel impedance and Z_{RH} is the horizontal rail impedance.

Noting that if no sliding occurs between the wheel and rail, $\dot{Y}_{RH} = \dot{Y}_{WA}$ at the point of contact, we can solve Eq. (24) for \dot{Y}_{WA} in terms of F_V .

$$\dot{Y}_{WA} = \dot{Y}_{RH} = \frac{F_V}{\left(1 + \frac{Z_{RH}}{Z_{WA}}\right)} \left[\frac{1}{Z_{WVH}} + \frac{1}{Z_{RVH}} \frac{Z_{RH}}{Z_{WA}} \right] \quad (33)$$

Both terms in the brackets would be expected to be large at the axial resonant frequencies of the wheel. We have data on Z_{RVH} , but unfortunately we have no data on Z_{WVH} . We would expect the latter to depend strongly on the details of wheel geometry, since Z_{WVH} would probably be very small at the wheel resonant

frequencies and very large at the wheel antiresonant frequencies. Consequently, measurements on one wheel would probably not be generalizable to wheels of different geometry. However, because the rail is not so resonant a structure as the wheel, measurements of Z_{RVH} on one rail should be reasonably generalizable to other rails, provided the size change is not too great. Consequently, we will rely only on the second term in the brackets of Eq. (33) to estimate the lateral wheel and rail response. As we will see in Sec. 3, this approximation provides reasonable predictions of the lateral wheel response. Using this simplified version of Eq. (33) and noting that $F_V = Z_{WR} \dot{Y}_{WR}$, we can write

$$S_{\dot{Y}_{WA}}^{(pc)}(\omega) = \left| \frac{Z_{RH}}{Z_{WA} + Z_{RH}} \right|^2 \frac{1}{|Z_{RVH}|^2} S_{\dot{Y}_{WR}}^{(pc)}(\omega), \quad (34)$$

where $S_{\dot{Y}_{WA}}^{(pc)}(\omega)$ is the frequency spectrum of the wheel axial response at the point of contact.

As before, we are interested in the spectrum of the average response around the circumference of the wheel, $S_{\dot{Y}_{WA}}^{(AVG)}(\omega)$. In a manner completely analogous to the derivation of Eq. (21) for the wheel radial response, we can show that

$$S_{\dot{Y}_{WA}}^{(AVG)}(\omega) = \frac{\sum_n |B_n|^2}{\left| \sum_n B_n \right|^2} S_{\dot{Y}_{WA}}^{(pc)}(\omega), \quad (35)$$

where the B_n are the wheel axial modal admittances. Combining Eqs. (34) and (35) and expressing the wheel response in terms of the spectrum of its acceleration, we obtain

$$S_{Y_{WA}}^{(AVG)}(\omega) = \omega^2 \frac{\sum_n |B_n^2|}{|\sum_n B_n|^2} \left| \frac{Z_{RH}}{Z_{WA} + Z_{RH}} \right|^2 \frac{1}{|Z_{RVH}|^2} S_{Y_{WR}}^{(pc)}(\omega) \quad (36)$$

Substituting Eq. (12) into this equation, we can express the average axial acceleration spectrum on the wheel in terms of the wheel and rail roughness spectra.

Figure 9 shows the measurements of Z_{RVH} for various forcing points on the rail head of a 100 lb/yd rail on wood ties. The measurements were made using the instrumentation system shown in Fig. 10. We will use these data in Eq. (36) to predict the wheel lateral response.

The rail lateral response at the point of contact is the same as that at the wheel. The average horizontal rail response can be estimated in a manner completely analogous to the average vertical rail velocity spectrum estimated in Eq. (14). Consequently, the horizontal rail velocity spectrum averaged over time T , where T is longer than the time it takes the train to pass at velocity V , is given by

$$S_{Y_{RH}}^{(AVG)}(\omega) = \frac{N \left(\frac{1 - e^{-\eta_{RH} k_{RH}}}{2 \eta_{RH} k_{RH}} \right) VT}{VT} S_{Y_{WA}}^{(pc)}(\omega) \quad (37)$$

where η_{RH} is the rail loss factor for horizontal rail vibration, k_{RH} is the bending wavenumber for horizontal vibration given by

$$k_{RH} = \left(\frac{\omega}{r_{RH} c_\ell} \right)^{1/2} \quad (38)$$

and r_{RH} is the radius of gyration of the rail for bending in the horizontal plane.

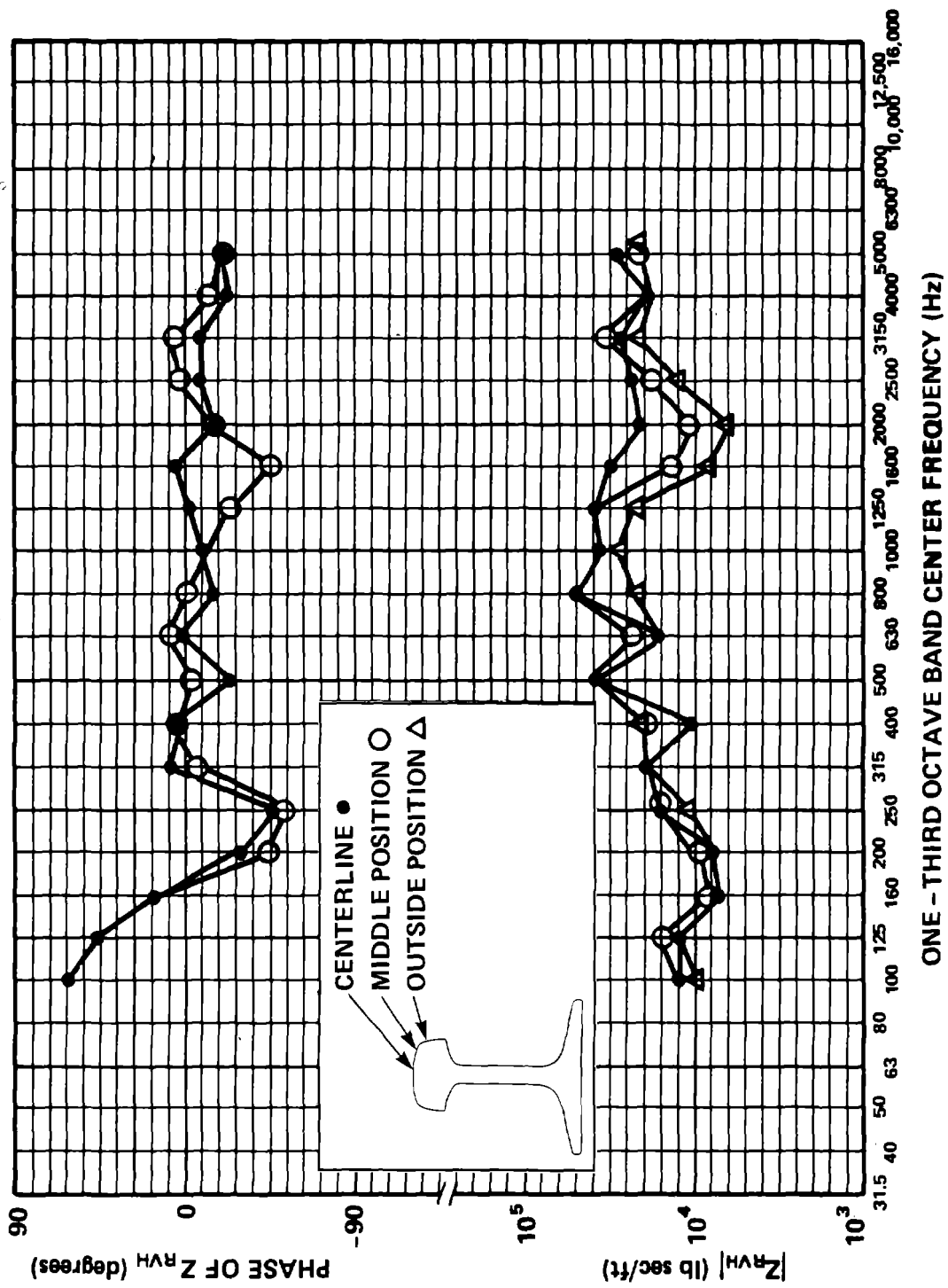


FIG. 9. RAIL CROSS-IMPEDANCE RELATING VERTICAL FORCE AND HORIZONTAL RESPONSE FOR 100 lb/yard RAIL ON TIE AND BALLAST.

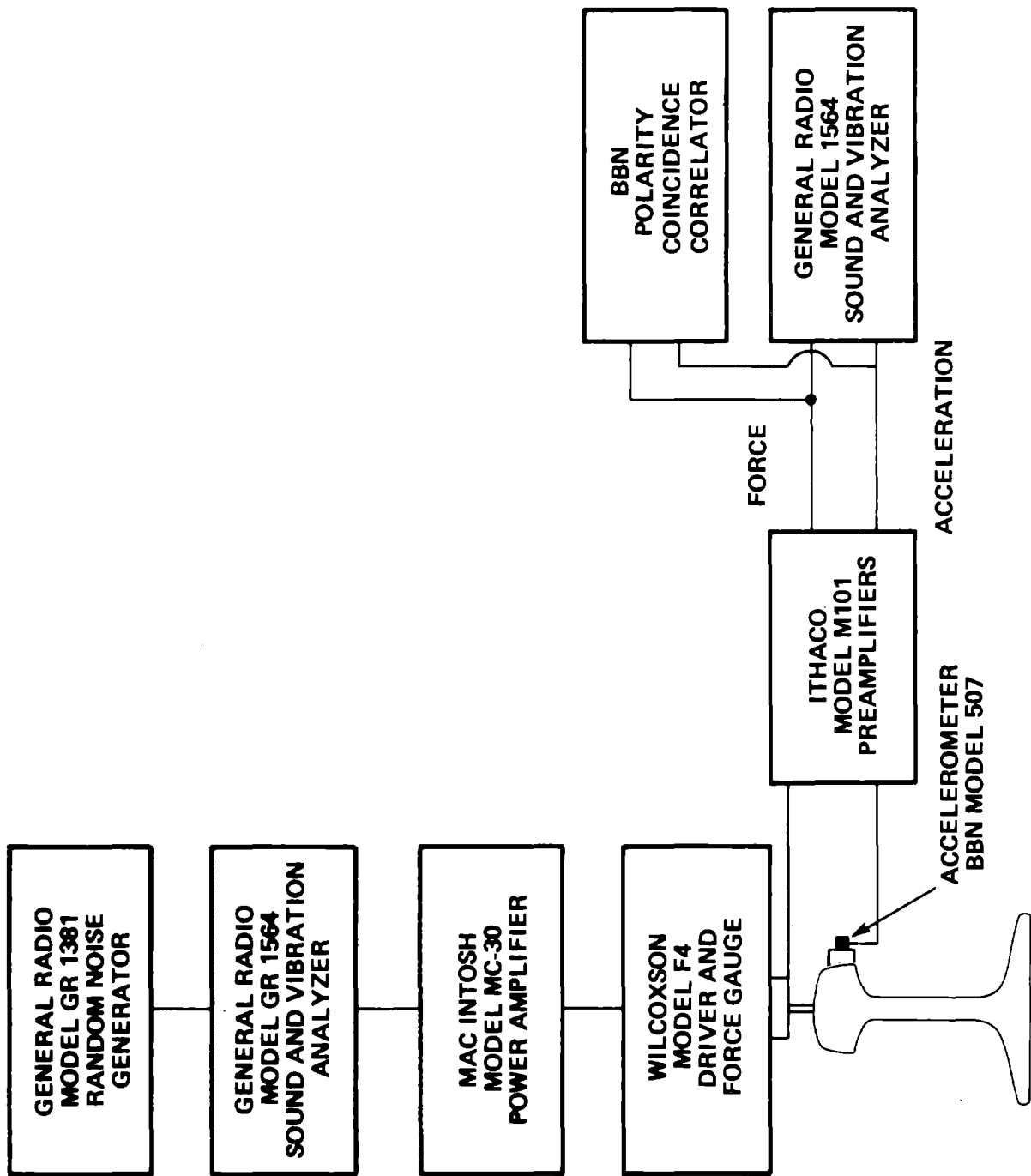


FIG. 10. INSTRUMENTATION FOR THE RAIL CROSS-IMPEDANCE MEASUREMENTS.

Wheel Radial Impedance

The wheel is a very complex structure; dealing with its dynamics in detail will probably require the use of finite element techniques and a digital computer. However, using normal mode techniques, we can make an estimate that is sufficiently accurate for our purposes.

Using Love's [7] equations for the in-plane vibration of a ring modified slightly to account for the stiffness in compression of the web, we obtain for the wheel

$$R_W K_1 u + \frac{\partial N}{\partial \theta} + T + X R_W = m R_W \frac{\partial^2 u}{\partial t^2}$$

$$- R_W K_2 w + \frac{\partial T}{\partial \theta} - N = m R_W \frac{\partial^2 w}{\partial t^2}$$

$$G' = \frac{E I_{WR}}{R_W^2} \left[\frac{\partial^2 u}{\partial \theta^2} + \frac{\partial w}{\partial \theta} \right]$$

$$\frac{\partial G'}{\partial \theta} + N R_W = 0 \quad , \quad (39)$$

where $E = \frac{E'}{1-\nu^2} (1-j\eta_W)$, E' is Young's modulus of the wheel, ν is Poisson's ratio, and η_W is the loss factor (damping), I_{WR} is the in-plane bending moment of inertia of the wheel tread, u is the radial displacement, and w the circumferential displacement of the tread, K_1 and K_2 are the radial and circumferential in-plane stiffnesses due to the wheel web, R_W is the wheel radius, m is the mass per unit length of the tread, and the last of Eqs. (39) results from neglecting rotary inertia. Other variables are defined in Fig. 11.

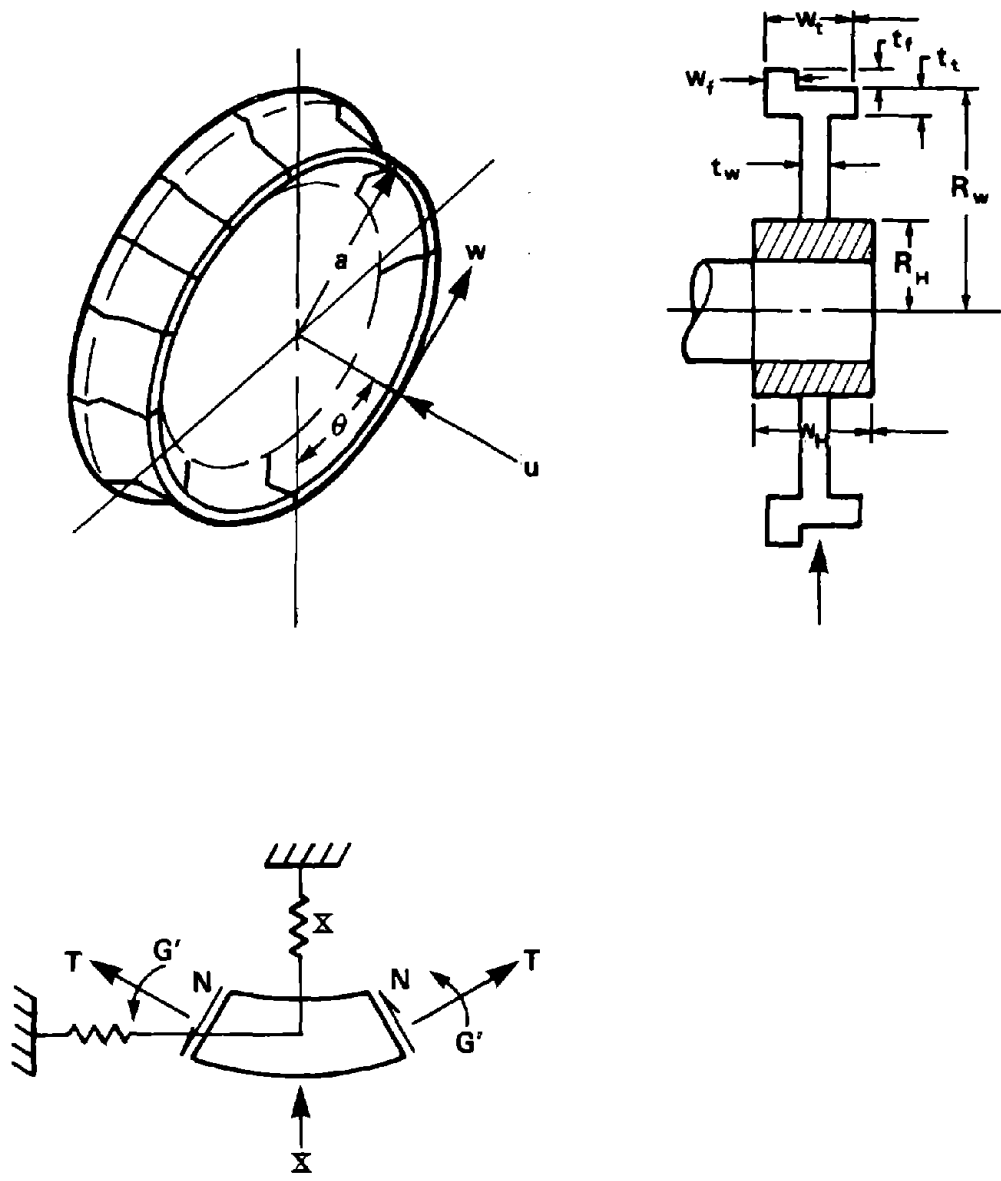


FIG. 11. VARIABLES IN THE WHEEL RADIAL RESPONSE EQUATIONS.

Using Love's assumption of no extension of the central line of the ring, we can further write that

$$u = \frac{\partial w}{\partial \theta} \quad . \quad (40)$$

If a harmonic point force of amplitude F is applied to the tread at $\theta=0$, the tread response will be in the form

$$u(\theta, t) = \sum_n A_n \cos n\theta e^{-j\omega t} \quad . \quad (41)$$

Substituting Eqs. (40) and (41) into Eq. (39) and solving for A_n , we obtain

$$A_n = \frac{X_n R_W^2 n^2}{\frac{EI_{WR}}{R_W^2} n^2 (n^2-1)^2 + R_W^2 (K_2 + n^2 K_1) - m R_W^2 \omega^2 (n^2+1)} \quad (42)$$

and $X_n = \frac{F}{\pi R_W}$,

from which the admittance $\frac{1}{Z_{WR}}$ can be easily obtained as

$$\frac{1}{Z_{WR}} = \sum_{n=1}^{\infty} \frac{\dot{u}_n}{F} = \sum_{n=1}^{\infty} \frac{-j\omega R_W n^2 / \pi}{\frac{EI_{WR}}{R_W^2} (n^2 (n^2-1)^2 + R_W^2 (K_1 n^2 + K_2) - m R_W^2 \omega^2 (n^2+1))} \quad . \quad (43)$$

The stiffnesses K_1 and K_2 due to the web are derived in Reference 5 as

$$K_1 = \frac{Et_n}{R_W}$$

$$K_2 = \frac{Et_W}{2R_W} n \quad , \quad (44)$$

where t is the average web thickness.

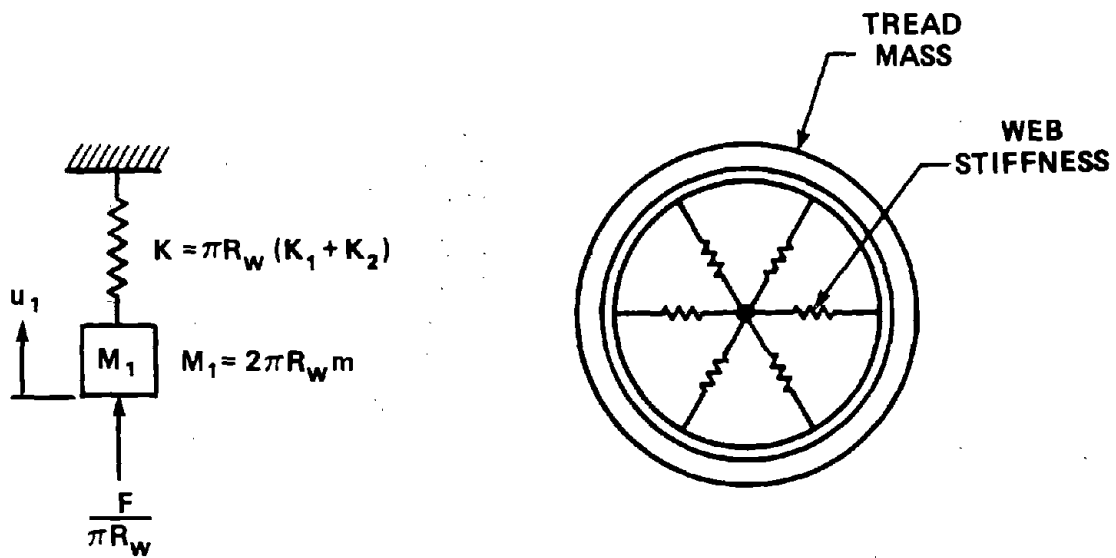
Equation (43) does not agree with measurements of wheel admittance at low frequency (below about 500 Hz). As we shall see below, measurements have shown that the radial admittance of a railroad wheel becomes mass-like at low frequency. However, Eq. (43) becomes spring-like at frequencies well below the first radial resonance. We can correct our model to make it more representative of measured data by modifying the first modal admittance term in Eq. (43), as illustrated in Fig. 12. The first mode is the rigid body displacement of the tread,

$$u(\theta, t) = A_1 \cos\theta e^{-j\omega t},$$

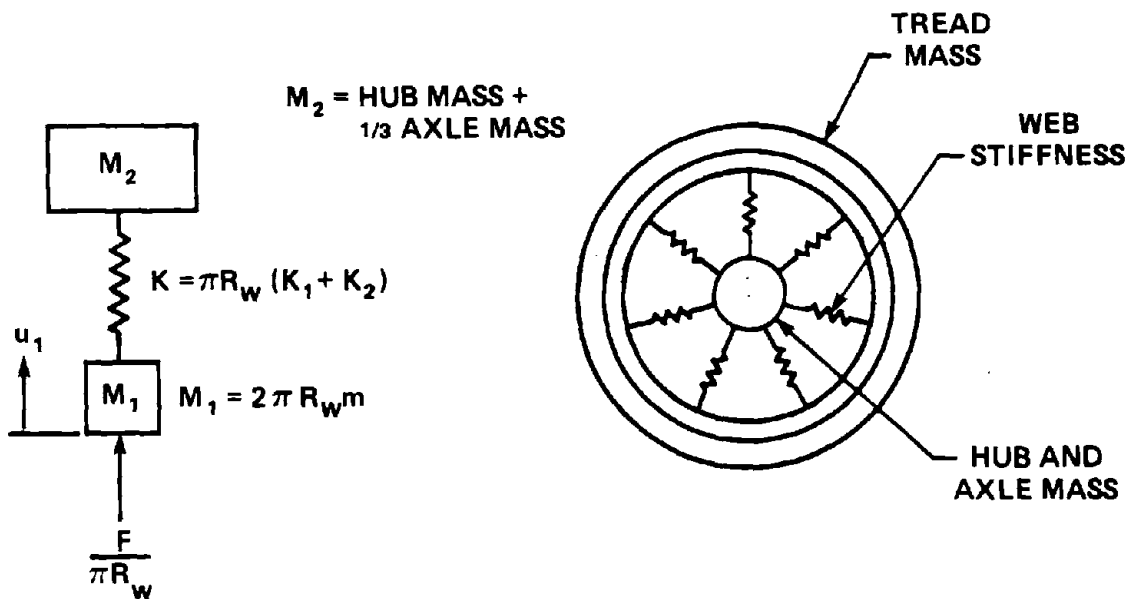
against the stiffness of the web.

In Eq. (33) the mass of the first mode is precisely the tread mass, and the stiffness of that mode is precisely the integrated stiffness of the wheel web for rigid body displacement of the tread. Figure 12a illustrates this relationship schematically and shows that the web stiffness is attached to ground. Such a model would be valid if the mass of the wheel hub and axle were very much larger than all other masses in the system. The model of the first mode in Fig. 12b is more correct, in that it shows that the web stiffness is attached to a mass representing the hub and one-third of the axle mass.* Substituting the model in Fig. 12b for the first mode in Eq. (33), we obtain for the amplitude of the first mode

*The axle is assumed to be pinned at its other end. Consequently, its effective inertia is only one-third of its mass.



(a) Original Model of the First Mode



(b) Modified First Mode

FIG. 12. MODIFIED FIRST MODE FOR THE WHEEL RADIAL IMPEDANCE.

$$A_1 = \frac{1 - (\omega/\omega_L)^2}{-j\omega M_W [1 - (\omega/\omega_H)^2]} \quad (45a)$$

and for the total admittance of the wheel

$$\frac{1}{Z_{WR}} = \frac{\dot{u}}{F} = \frac{1 - (\omega/\omega_L)^2}{-j\omega M_W (1 - (\omega/\omega_H)^2)} + \sum_{n=2}^{\infty} \frac{-j\omega R_W n^2 / \pi}{\frac{ETI_{WR}}{R_W^2} n^2 (n^2 - 1)^2 + \frac{Et_W R_W}{2} n(n^2 + 1) - m R_W^2 \omega^2 (n^2 + 1)}, \quad (45b)$$

where

$$\omega_L = \sqrt{\frac{K}{M_2}}$$

$$K = \pi Et$$

$$\omega_H = \sqrt{\frac{K(M_1 + M_2)}{M_1 M_2}}$$

$$M_1 = 2\pi R_W m$$

M_2 is the wheel hub mass plus one-third of the axle mass, and M_W is the entire wheel mass. To be strictly in agreement with the model of Fig. 12, M_W should be equal to the sum of M_1 and M_2 , but that would leave out the mass of the web, which does contribute to the admittance at low frequency when the wheel moves as a rigid body. Physically, we are including the mass of the web when the tread and hub are moving together in phase at low frequency but excluding the effect of the hub mass on the resonant frequency of the first mode.

Equation (45) provides fairly reasonable agreement with measurements of wheel impedance. Figure 13 shows an electromagnetic shaker set up in the field to obtain the radial impedance of the 30-in. wheel on the State-of-the-Art-Car (SOAC). Figure 14 shows the instrumentation chain, and Fig. 15 compares measurements with the predictions of Eq. (45). The parameters used in Eq. (45) to model the SOAC wheel are shown in Table 2.

Figure 15 shows that the measurements and predictions agree quite well. The one major exception is the strong peak in the predictions at approximately 800 Hz. That peak is missing in the measurements. In obtaining the measured data, we controlled the force amplitude and plotted the velocity while sweeping in frequency. Figure 15 is the inverse of that velocity. Consequently,

TABLE 2. PARAMETERS FOR THE SOAC 30-in. WHEEL.

Variable	Description	Value
R_W	wheel radius	15 in.
m	mass per unit length of tread	3.54 lb/in.
M_W	wheel mass plus one-third of axle mass	661 lb
M_2	hub mass plus one-third of axle mass	234.7
t_W	web thickness	1.0 in.
t_t	tread thickness	2.375 in.
w_t	tread width	5.0 in.
h_f	flange height	0.875 in.
t_f	flange width	1.0 in.
A_T	cross sectional area of the tread	12.75 in. ²
R_H	hub radius	4.625 in.
W_H	hub width	7.0 in.
I_{WR}	in-plane (radial) bending moment of inertia of tread	7.86 in. ⁴
I_{WA}	out-of-plane (axial) bending moment of inertia of tread	28.14 in. ⁴
J_W	polar moment of inertia of tread	36.0 in. ⁴

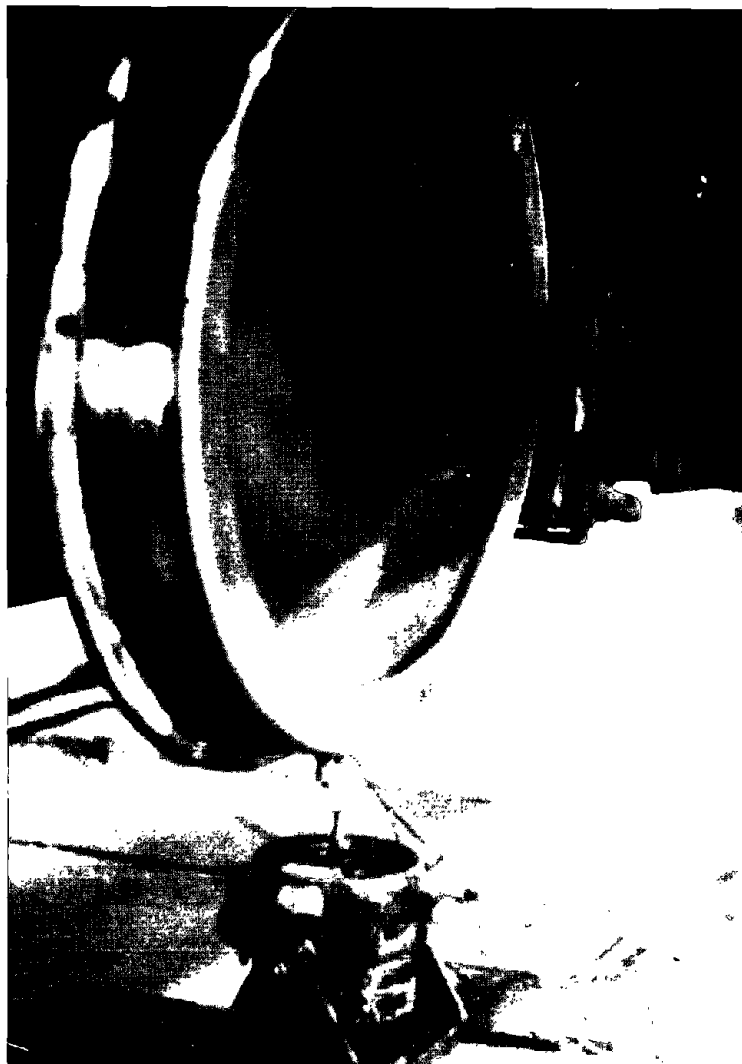


FIG. 13. SETUP FOR MEASURING THE RADIAL IMPEDANCE OF THE SOAC 30-in. WHEEL.

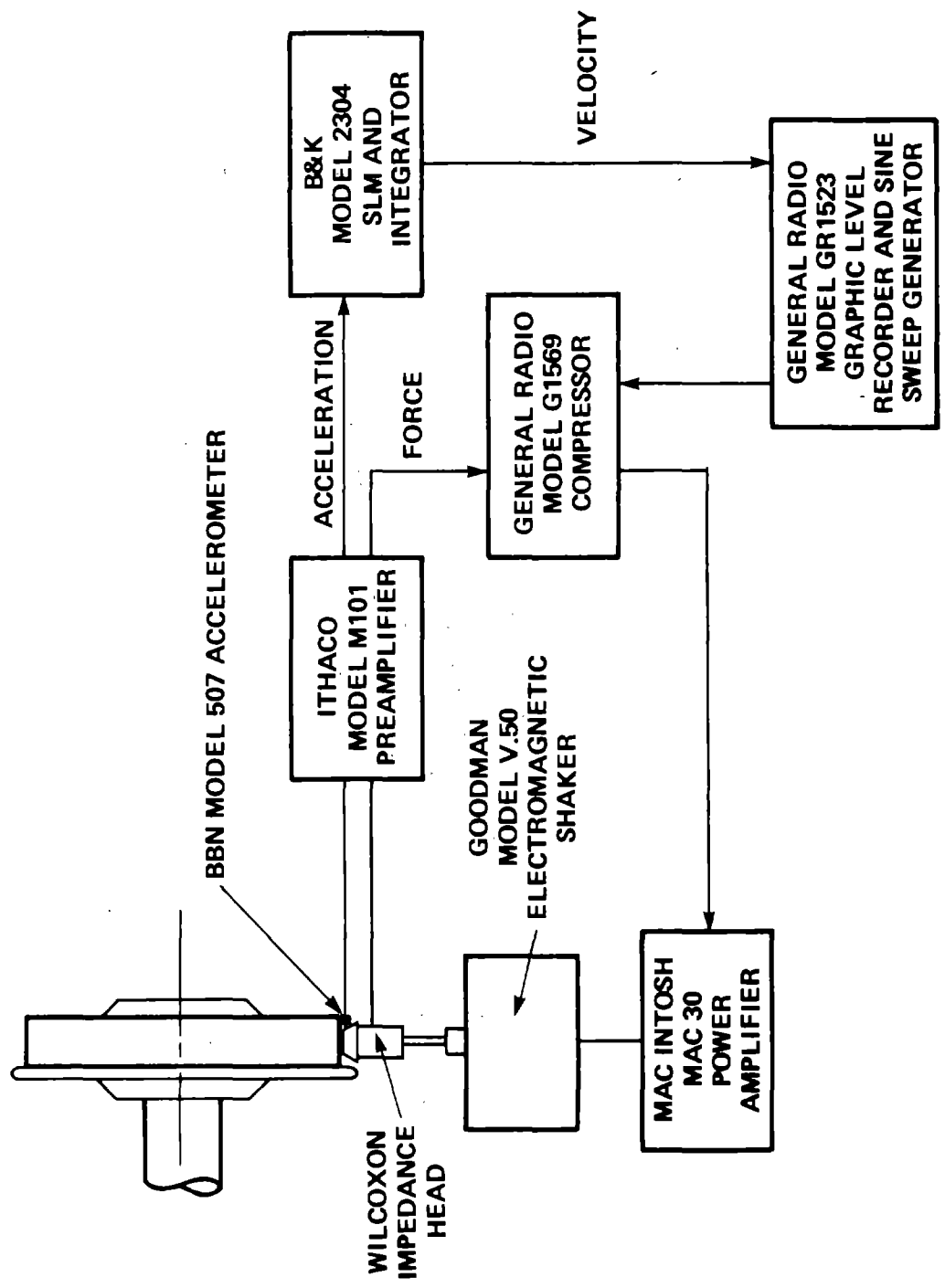


FIG. 14. THE INSTRUMENTATION CHAIN FOR MEASURING WHEEL IMPEDANCE.

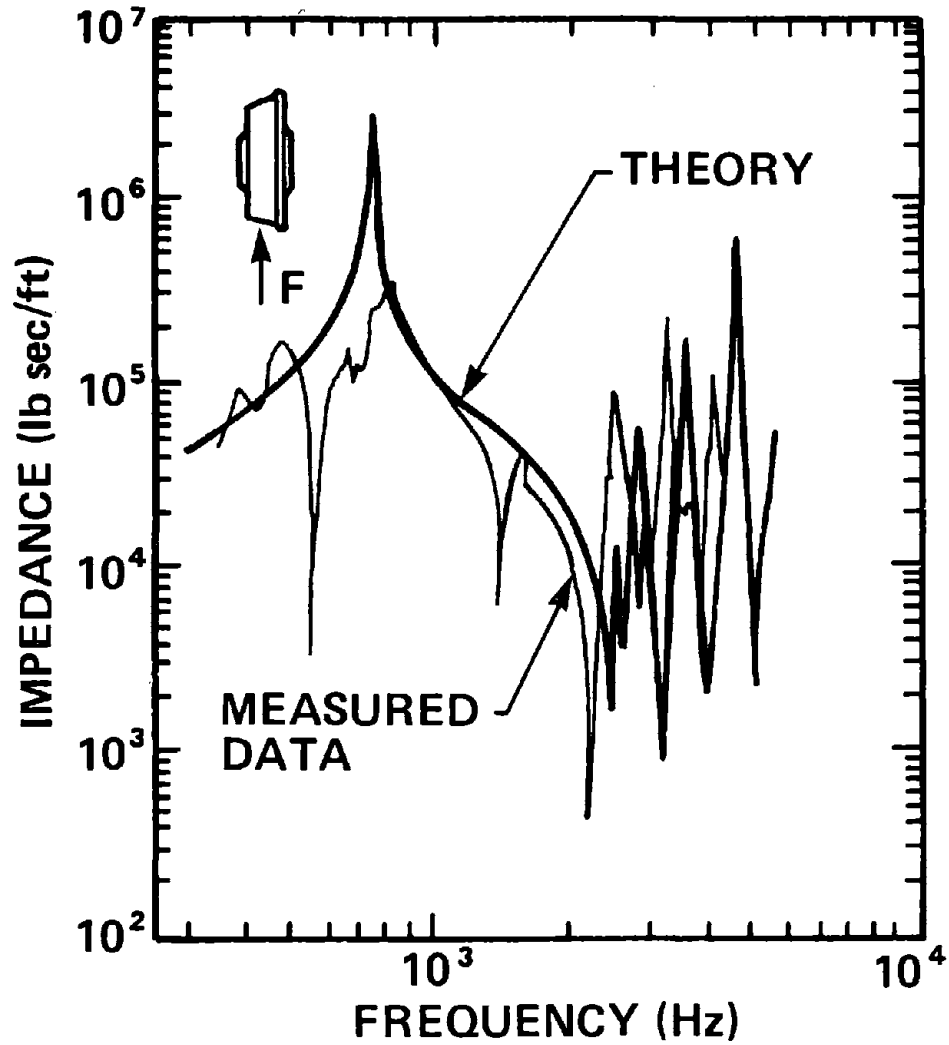


FIG. 15. COMPARISON OF MEASURED AND PREDICTED RADIAL IMPEDANCE FOR THE SOAC 30-in. WHEEL.

peaks in the impedance represent very low velocity. The fact that the measured impedance does not show the strong peak simply reveals that we ran into the noise floor of our instrumentation chain.

There are some errors on the order of 10 to 15% in the prediction of the natural frequencies. Since we are interested primarily in one-third octave band predictions, those discrepancies are acceptable. The deep valleys in the impedance data at approximately 550 Hz and 1320 Hz are associated with axial resonances of the wheel. They appear in the radial impedance data either because the twisting of the tread associated with its axial motion is sensed by the accelerometer on the tread or as a consequence of the 1-in-20 taper on the tread of the wheel.

Since both shaker and accelerometer were oriented perpendicular to the tread in the impedance measurements, there is a small component of force in the axial direction as a consequence of the tread taper. In addition, the accelerometer is weakly sensitive to axial motion of the wheel because of both its cross-axis sensitivity and its orientation on the tread.

When the wheel is rolling on the rail, the taper on the tread will not lead to any axial motion of the wheel, because the wheel and rail are constrained to move together in the lateral direction at the point of contact. On the other hand, any twist induced in the tread from the force of interaction being applied to one side or the other of the center of twist of the wheel tread will induce axial motion in the wheel. However, we are accounting for that induced axial motion by means of Eq. (45). Consequently, in this model of the wheel radial impedance, we are making no attempt to account for the axial resonances in the radial impedance data.

Axial Wheel Impedance

The modeling of the wheel axial impedance is somewhat simpler than that of the radial impedance, partly because the web of the wheel does not significantly affect the dynamics of tread for motion in the axial (out-of-plane) direction. Using Love's equations of motion for the out-of-plane vibration of a ring [7], we obtain

$$\begin{aligned} \frac{EI_{WA}}{R_W^2} \frac{\partial^4 v}{\partial \theta^4} + \frac{C}{R_W^2} \frac{\partial^2 v}{\partial \theta^2} - mR_W^2 \frac{\partial^2 v}{\partial t^2} + \rho I_{WA} \frac{\partial^4 v}{\partial t^2 \partial \theta^2} \\ + \frac{1}{R_W} (EI_{WA} + C) \frac{\partial^2 \beta}{\partial \theta^2} = - R_W Y \\ \frac{1}{R_W^2} (EI_{WA} + C) \frac{\partial^2 v}{\partial \theta^2} + \frac{C}{R_W} \frac{\partial^2 \beta}{\partial \theta^2} - \frac{EI_{WA}}{R_W} \beta - \rho J_W R_W \frac{\partial^2 \beta}{\partial t^2} = 0 \end{aligned} \quad (46)$$

where v is the out-of-plane displacement of the tread and β is the twist, as shown on Fig. 16, I_{WA} is the moment of inertia of the tread for bending out of the plane of the wheel, ρ is the density of the wheel material, Y is the force per unit length applied at the tread in the axial direction, and C is the torsional stiffness of the tread given by [8]

$$C \cong \frac{GA_T^4}{40J_W} .$$

If the wheel is excited by a harmonic point force of amplitude f in the axial direction at $\theta = 0$, the wheel response will be of the form

$$\begin{aligned} v(\theta, t) &= \sum_p B_p \cos p\theta e^{-j\omega t} \\ \beta(\theta, t) &= \sum_p C_p \cos p\theta e^{-j\omega t} \end{aligned} \quad (47)$$

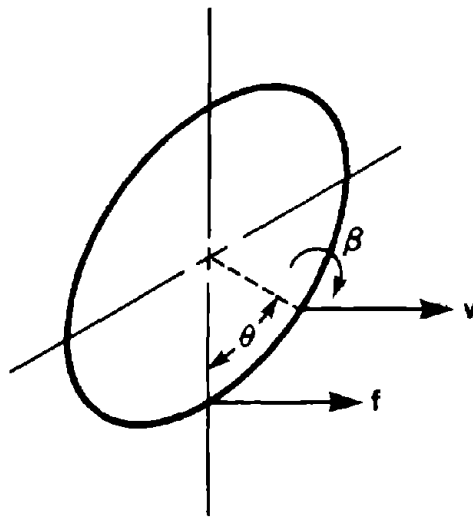


FIG. 16. DEFINITION OF AXIAL DISPLACEMENT AND TWIST OF WHEEL TREAD.

Substituting Eqs. (47) into Eq. (46) and solving for B_p , we obtain

$$B_p = \frac{[(C_p^2 + EI_{WA}) - \rho J_W R_W^2 \omega^2] Y_p}{R_W \left\{ p^4 \left(\frac{C + EI_{WA}}{R_W^2} \right)^2 + \left[\frac{EI_{WA} p^4 + C p^2}{R_W^2} - (m R_W^2 + \rho I_{WA} p^2) \omega^2 \right] \left[\frac{C_p^2 + EI_{WA}}{R_W^2} - \rho J_W \omega^2 \right] \right\}}, \quad (48)$$

where for a point force $Y_p = \frac{f}{\pi R_W}$.

Differentiating Eq. (48) and summing over all p to obtain the velocity at the point of forcing, we obtain for the wheel axial admittance

$$\begin{aligned} \frac{1}{Z_{WA}} &= \sum_p \frac{-j \omega B_p}{f} \\ &= \sum_p \frac{-j \omega [(C_p^2 + EI_{WA}) - \rho J_W R_W^2 \omega^2]}{R_W \left\{ -p^4 \left(\frac{C + EI_{WA}}{R_W^2} \right)^2 + \left[\frac{EI_{WA} p^4 + C p^2}{R_W^2} - (m R_W^2 + \rho I_{WA} p^2) \omega^2 \right] \left[\frac{C_p^2 + EI_{WA}}{R_W^2} - \rho J_W \omega^2 \right] \right\}} \end{aligned} \quad (49)$$

where Z_{WA} is the axial wheel impedance.

Figure 17 compares measured and predicted admittances. To make the predictions, we used the parameter values in Table 2. The axial admittance of the 30-in. SOAC wheel was measured in the field, as shown in Fig. 18. The instrumentation chain was the same as for the radial impedance measurements. Agreement between measured and predicted impedances is quite good except at low frequency, where our estimate of the first natural frequency of the tread is too low, and we do not predict many of the low-frequency resonances involving interaction between the wheel and axle.

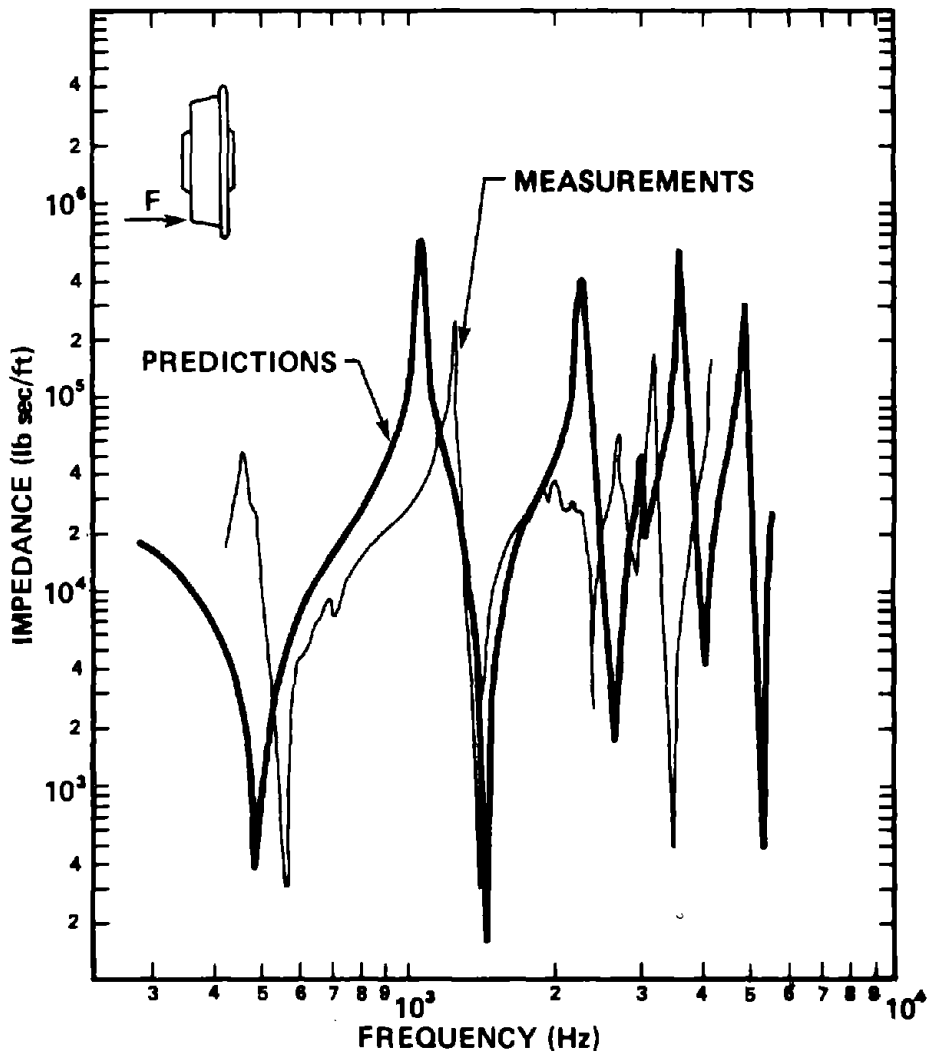


FIG. 17. COMPARISON OF MEASURED AND PREDICTED AXIAL WHEEL IMPEDANCE FOR THE SOAC WHEEL.

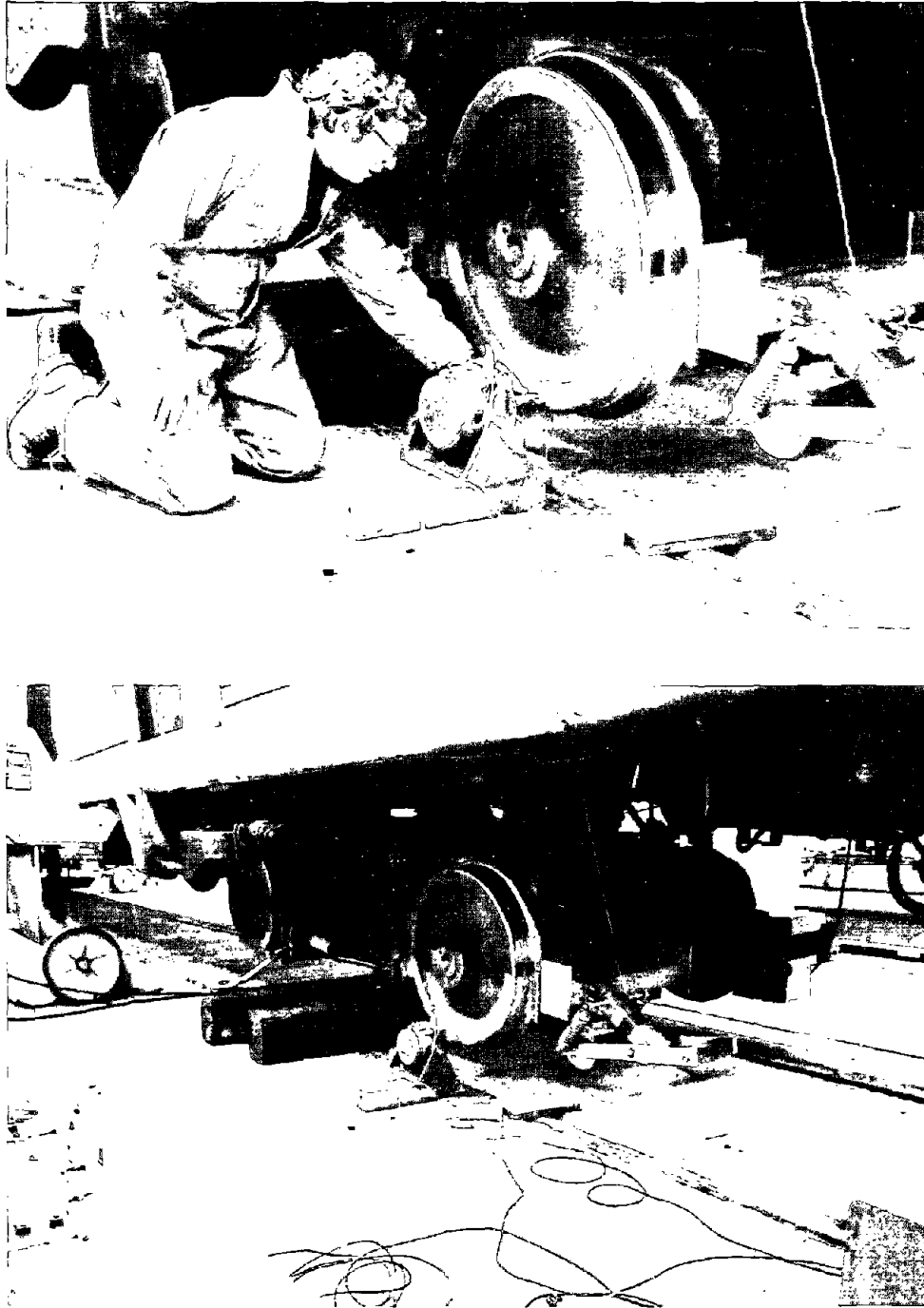


FIG. 18. AXIAL IMPEDANCE MEASUREMENT OF THE SOAC WHEEL.

Rail Impedance

An earlier study [3] showed that above approximately 250 Hz, both the vertical and lateral rail impedances could be well modeled by the impedance of an infinite beam having the same bending stiffness and mass per unit length as the rail, i.e.,

$$\begin{aligned} Z_{RV} &= 2\rho_R A_R (\omega r_{RV} c_\ell)^{1/2} (1-j) \\ Z_{RH} &= 2\rho_R A_R (\omega r_{RH} c_\ell)^{1/2} (1-j) \quad , \end{aligned} \quad (50)$$

where ρ_R is the density, A_R is the cross-sectional area, c_ℓ is the longitudinal wavespeed of the rail, r_{RV} is the radius of gyration for vertical bending, and r_{RH} is that radius for lateral bending. In Fig. 19, we compare the measured vertical impedance of 100 lb/yd rail on wood ties and ballast with the prediction of Eq. (51). The rail was on an old industrial siding with tie spacing varying between 22 1/4 in. and 25 1/4 in. The instrumentation used for the measurement was the same as that shown in Fig. 8 for the cross-impedance terms Z_{RVH} . The measurements were performed at three positions on the rail head: at the centerline of the rail, as close to the gauge side of the rail as possible, and in the middle, halfway between these two positions. This middle position is probably most representative of where the wheel rides on the rail, at least for new wheels and rails.

The predictions are seen to overestimate the impedance amplitude by a small amount, and the effect of measurement position is small, except at high frequency. Earlier measurements of both vertical and lateral rail impedance [3] at the rail centerline showed somewhat better agreement between measurements and predictions. In that case, the rail was 60 lb/yd and on relatively new ties and ballast. The discrepancy in Fig. 17 may be due in part to the presence of the ties in the older track bed. These act somewhat as periodic supports to the rail, and

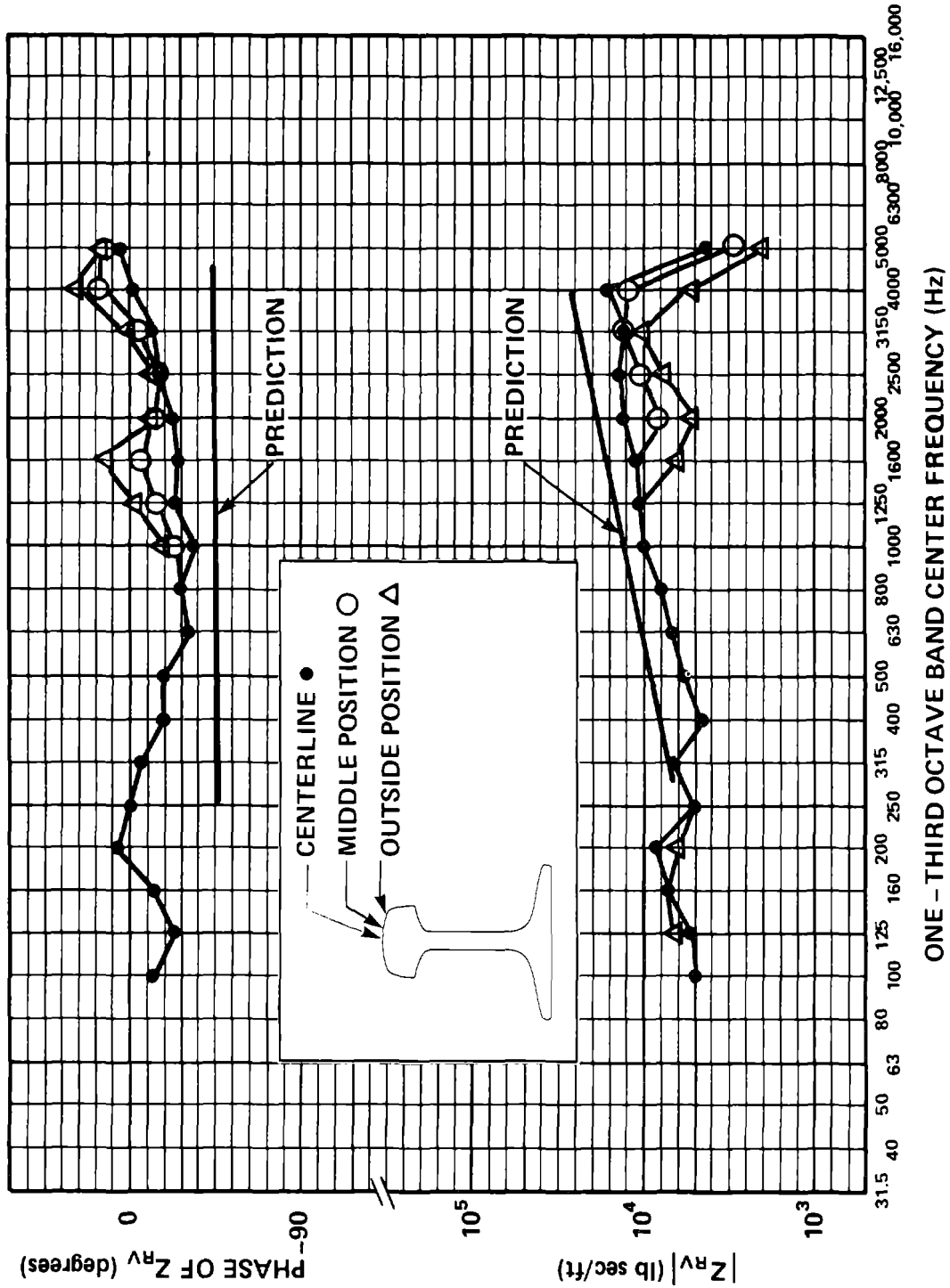


FIG. 19. VERTICAL IMPEDANCE OF 100 lb/yd RAIL ON WOOD TIES AND BALLAST.

their influence may be accentuated by the reduced flexibility of the old compacted track bed. Munjal and Heckl [9] have shown that the periodic support afforded the rail by the ties can lead to reduction in the impedance below that of an infinitely long beam in the 250-Hz to 2000-Hz range.

A more dramatic example of this reduction in the vertical rail impedance was obtained when we measured the vertical and lateral rail impedance on the Transit Test Track at the Transportation Test Center in Pueblo, Colorado. Part of that track is composed of continuously welded 119 lb/yard rail on concrete ties and ballast, with the ties spaced every 30 in. Figure 20 shows the shaker located under the rail between two ties. We placed the shaker beneath the rail rather than above it so that we could park the transit car wheel directly above the shaker, a position allowing us to measure the sum of the wheel and rail impedance. In an earlier model of wheel/rail noise [3], the equation for the response of the wheel and rail had just the sum of the wheel and rail impedance in the denominator. To measure that sum directly is very attractive because it eliminates the need for accurate measurement of the phase of both the wheel and rail impedance. However, as we later learned in this program, the contact stiffness between the wheel and rail plays a very important role in their interaction. As a consequence, the equation predicting the wheel and rail response [see Eq. (16)] does not have just the sum of the wheel and rail impedance in the denominator; rather, it has a term of the form

$$Z_{WR} + Z_{RV} - j\omega \frac{Z_{WR}Z_{RV}}{K_C} , \quad (51)$$

and the measurement of the rail impedance, as in Fig. 20 with the wheel parked directly over the shaker, does not measure this quantity. In fact, it is probably not possible to measure the combined impedances in Eq. (51) directly.

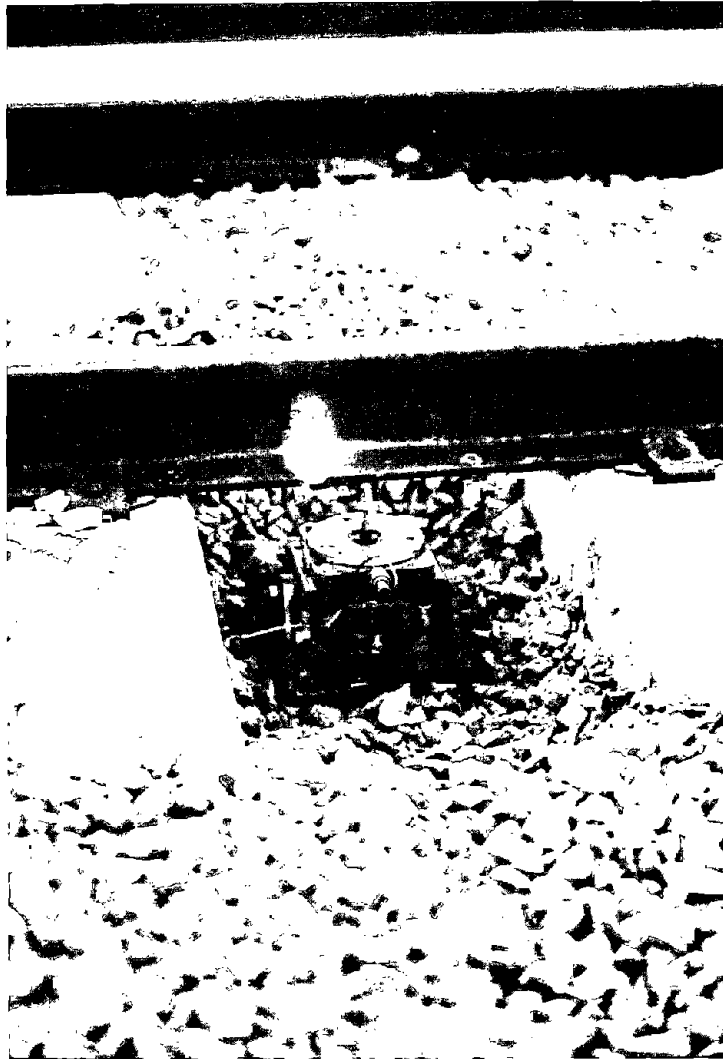


FIG. 20. SHAKER POSITIONED BENEATH RAIL AT TTC (PUEBLO) FOR RAIL IMPEDANCE MEASUREMENT.

In any event, when the rail impedance was excited as shown in Fig. 20, the resulting vertical rail impedance was that shown in Fig. 21. The horizontal rail impedance was measured similarly, by forcing the rail at the side of the rail head. The results of those measurements are shown in Fig. 22.

In both cases, the instrumentation chain shown in Fig. 23 was used. The one-third octave band spectra of force and velocity were obtained, and their ratios in each one-third octave band were used to obtain the impedance.

There is a dramatic drop in the Z_{RV} and Z_{RH} relative to the predicted impedances at 800 to 1250 Hz and 250 to 400 Hz, respectively. We believe that this drop is a consequence of the periodic support afforded the rail by the concrete ties. If one were to model the rail as an infinite beam on periodic simple supports, spaced the same distance apart as the ties, one would expect to see dips in the impedance below that of a free infinite beam. The dips would be expected to occur at frequencies corresponding to the resonant frequencies of a finite length of that beam, in which the length is equal to the spacing between supports and the ends are either both built-in or both simply supported. At other frequencies, the impedance would approach that of an infinite beam [10]. A few of the resonant frequencies of a 2.5-ft segment (the tie spacing) of 119 lb/yd rail are given in Table 3. The rail impedances in Figs. 21 and 22 correspond approximately to the characteristics of the above model. The dips in the impedance occur near the resonant frequencies of

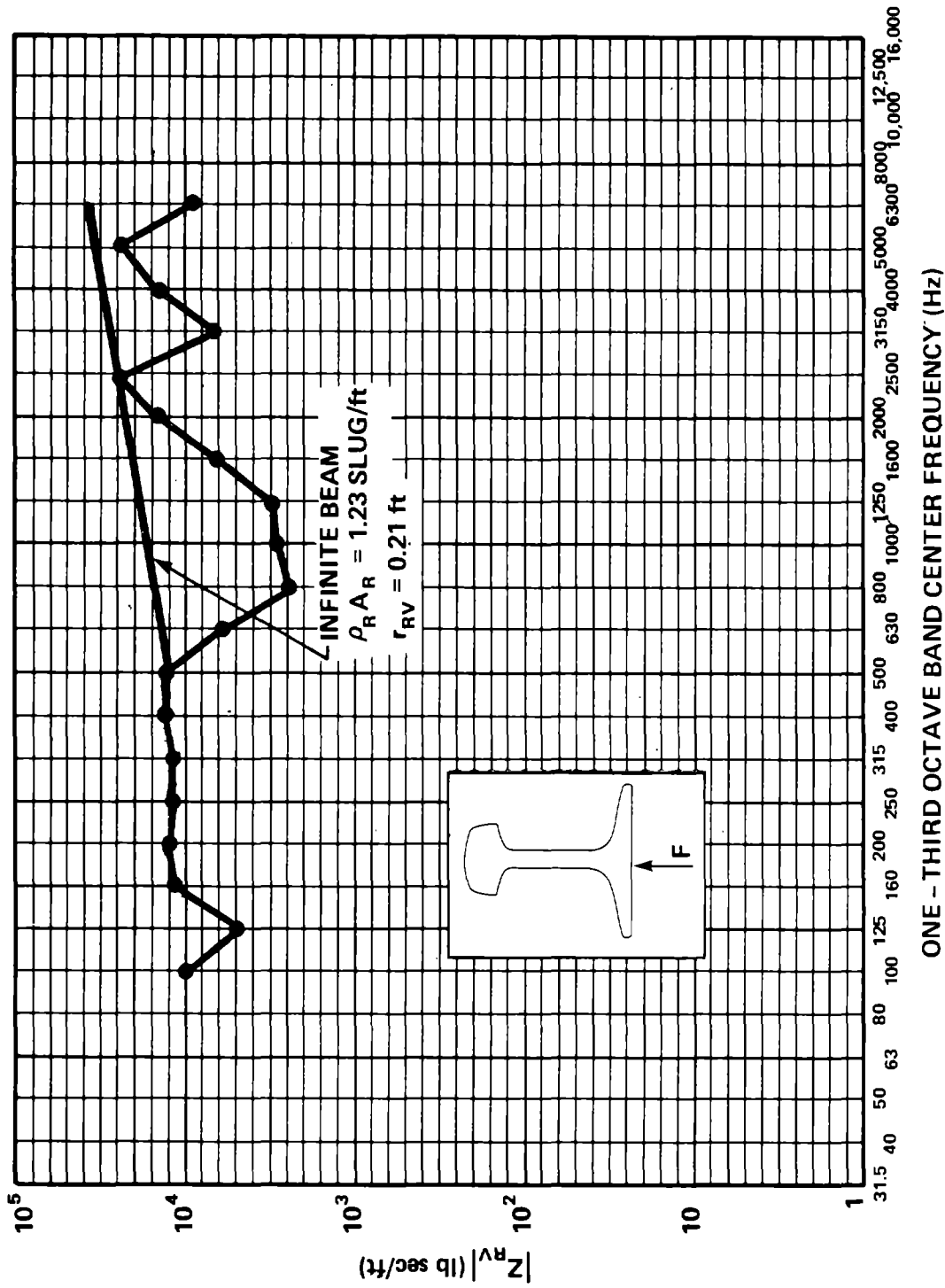


FIG. 21. VERTICAL RAIL IMPEDANCE AMPLITUDE FOR 119 lb/yd RAIL ON CONCRETE TIES AND BALLAST AT TTC (PUEBLO).

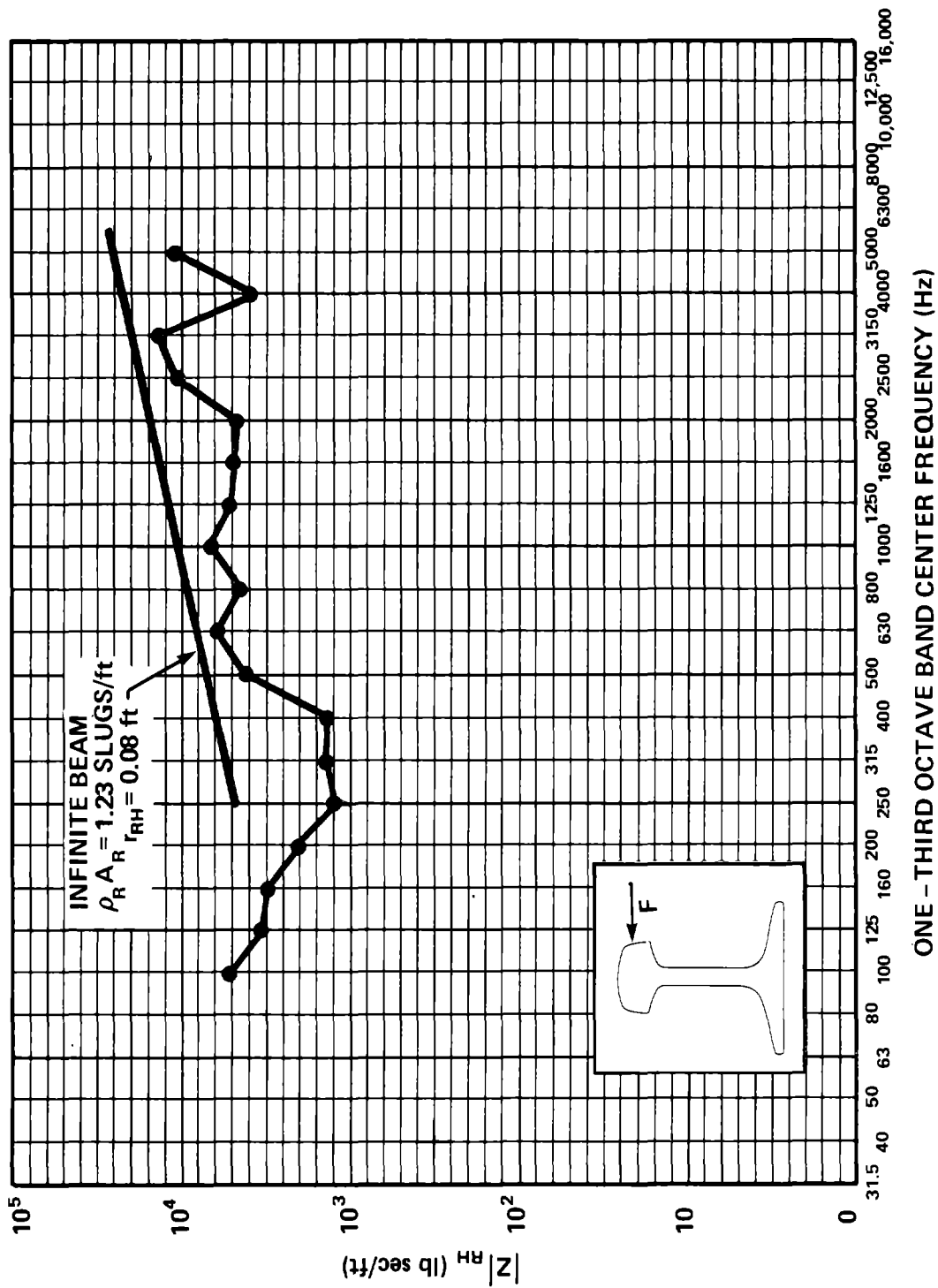


FIG. 22. HORIZONTAL RAIL IMPEDANCE AMPLITUDE.

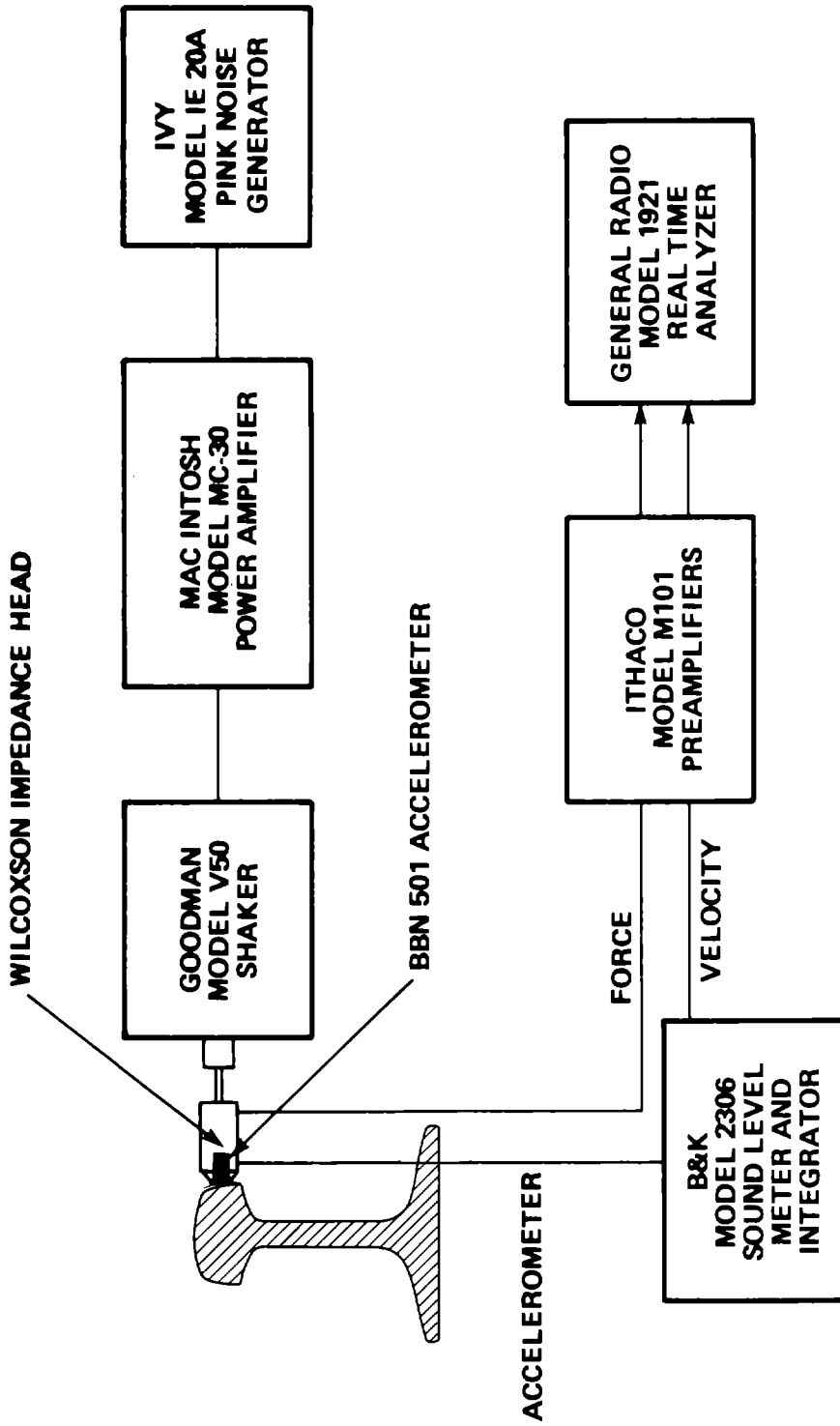


FIG. 23. INSTRUMENTATION FOR THE RAIL IMPEDANCE MEASUREMENTS AT TTC (PUEBLO).

Table 3; between the dips, the impedance approaches that of an infinite beam without supports.

TABLE 3. SOME RESONANT FREQUENCIES IN Hz OF A 2.5-FT SEGMENT OF 119 lb/yd RAIL.

Vertical		Horizontal	
Simply Supported	Clamped	Simply Supported	Clamped
897	2,018	342	769
3,589	5,556	1,367	2,136
8,075	10,988	3,076	4,187

The rail impedances measured at TTC are not typical of those found on most track structures in the United States. Typical construction is usually jointed rail on wooden ties and ballast. Whether the strong periodic structure effect on the TTC rail is due to the use of continuously welded rail, the presence of the concrete ties or the very precise and regular tie placement is not known. We make no attempt here to include the periodic support effects in our model of rail impedance but will continue to use Eq. (50).

Rail Loss Factor

The rate of decay of vibration along the length of rail affects the noise radiated by the rail. If the vibration decays very slowly, the length of rail that vibrates significantly and radiates sound is greater, and more sound power is radiated.

The rail loss factor for vertical vibration η_{RV} appears explicitly in Eq. (16) for the average vertical rail response, and the rail loss factor for horizontal vibration η_{RH} appears in

Eq. (37) for the average horizontal rail response. As the next section shows, this average rail response is used to predict the average sound level during a train passby.

At TTC (Pueblo), the decay of rail vibration was measured by exciting the rail with an impact hammer in the vertical and horizontal directions obtaining one-third octave band spectra of the corresponding vertical or horizontal vibration velocity at a number of distances from the point of excitation. Figures 24 and 25 show these spectra. These data were then replotted vs distance for each one-third octave band, as illustrated in Fig. 26. A straight line was fitted to the data points, and the loss factor was estimated from the slope of the straight line by means of the following two equations:

$$\eta_{RV} = \frac{-\Delta_V}{2k_{RV}(4.34)}$$

$$\eta_{RH} = \frac{-\Delta_H}{2k_{RH}4.34} \quad , \quad (52)$$

where Δ_V and Δ_H are the slopes in dB/ft for the decay of vertical and horizontal rail vibration with distance, respectively, and k_{RV} and k_{RH} are rail bending wavenumbers for vertical and horizontal vibration, respectively.

Note that in fitting a straight line to the data points in Fig. 26, the line intercepts -3 dB at the point of excitation, not at zero dB, because at the point of excitation the response is made up of two equal parts 90° out of phase: a near field confined to the vicinity of the point of excitation and a propagating component that carries vibration away from the point of excitation in both directions. It is the decay rate of this propagating component that we wish to estimate, and at the point of excitation its amplitude is 3 dB below the total response.

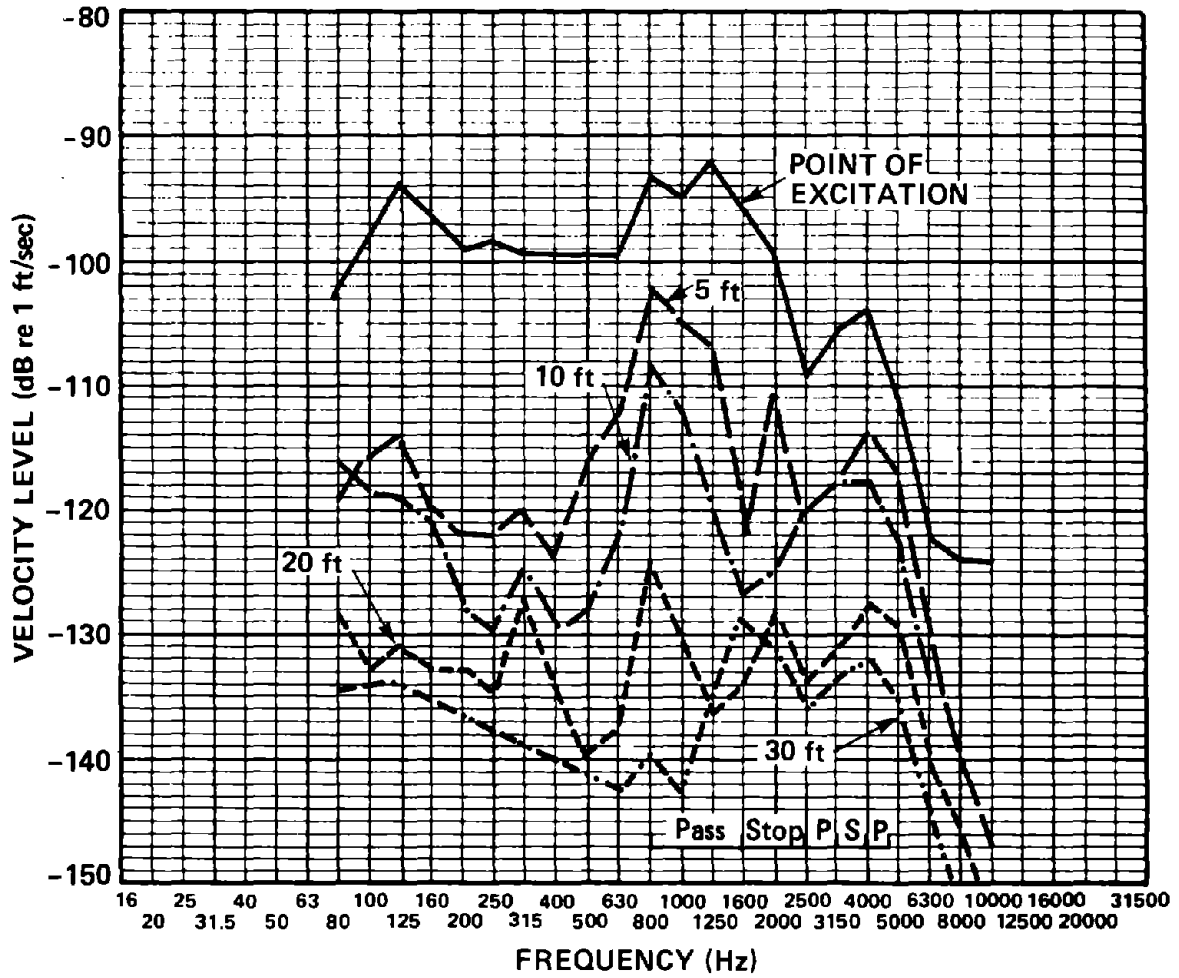


FIG. 24. VERTICAL VIBRATION SPECTRA AT VARIOUS DISTANCES FROM THE POINT OF EXCITATION.

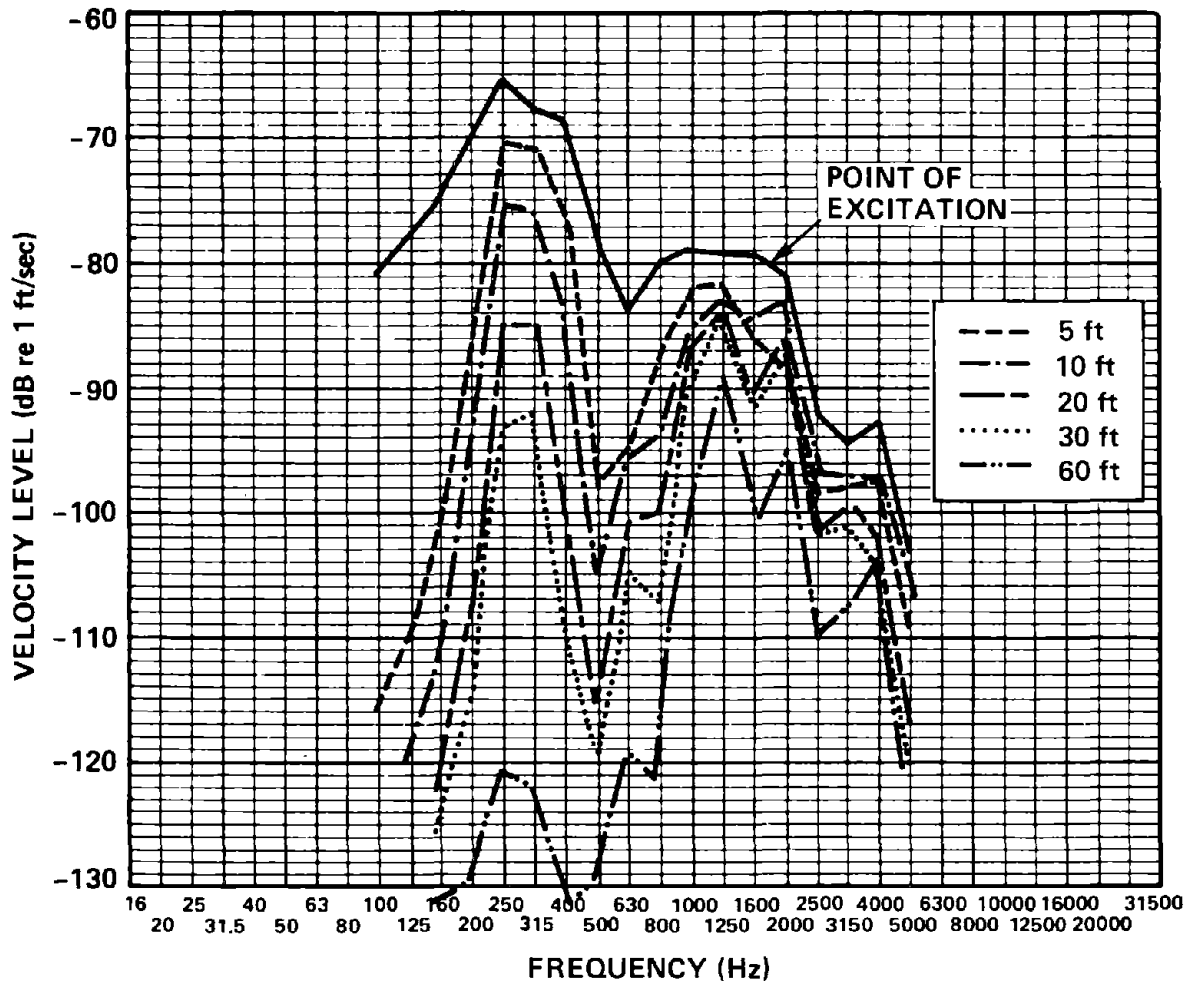


FIG. 25. HORIZONTAL VIBRATION SPECTRA AT VARIOUS DISTANCES FROM THE POINT OF EXCITATION.

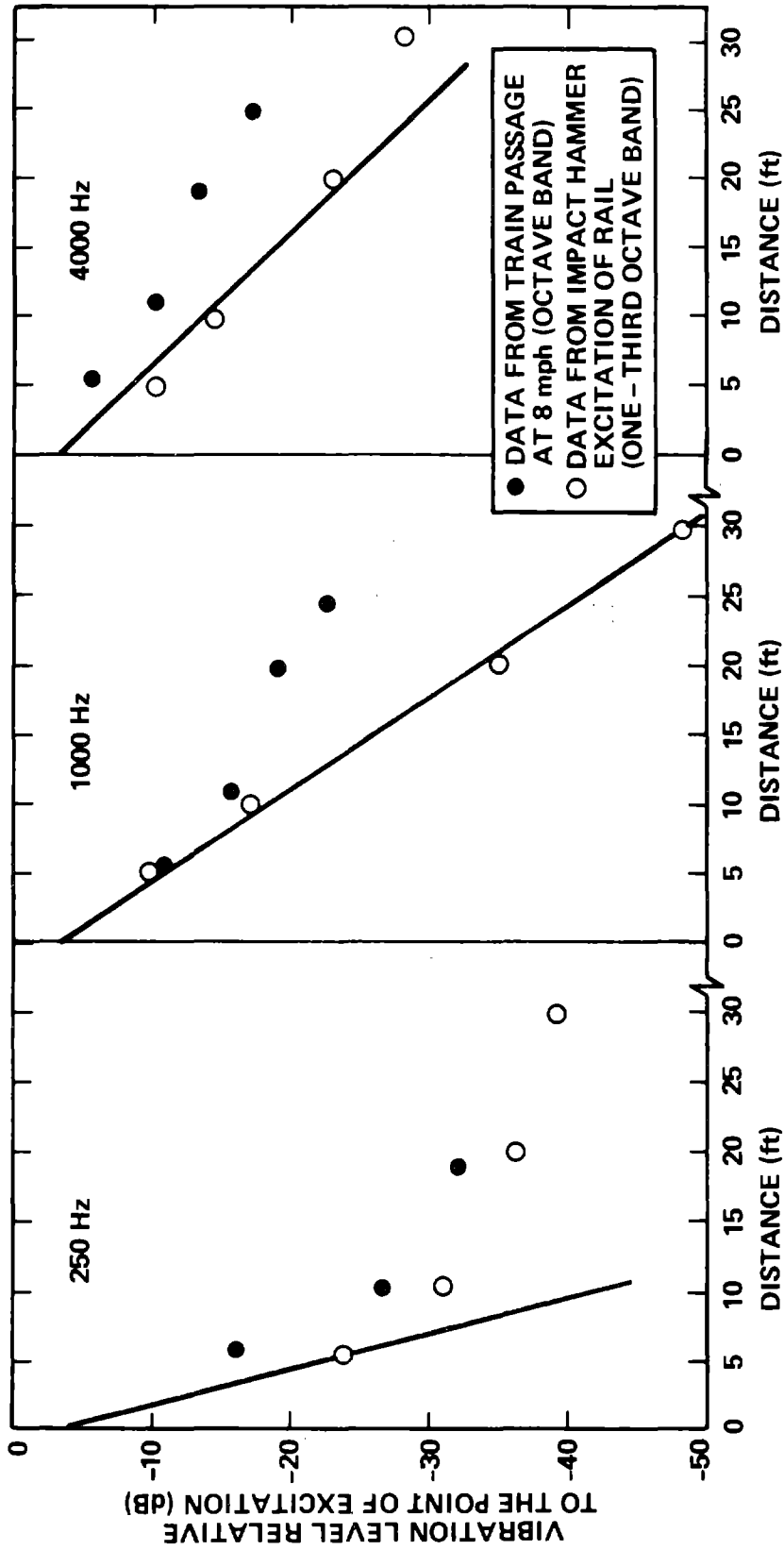


FIG. 26. DECAY OF VERTICAL RAIL VIBRATION IN ONE-THIRD OCTAVE BANDS WITH DISTANCES FROM THE POINT OF EXCITATION.

The resulting loss factors are plotted in Figs. 27 and 28 and compared with published data from Germany (Naake [11]) and data from the Pullman Standard Test Track [3]. The figures show that the rate of decay of rail vibration at TTC is much greater than that measured anywhere else.

For the most part, fitting a straight line to the data and identifying the slope, as in Fig. 26, presented little difficulty. The exception was at the very high decay rates. At 250 Hz in Fig. 26, for example, a single straight line cannot be fitted to the data points. At these very high decay rates, our model of the rail as an infinite beam is probably too simple. A more appropriate model would be a periodically supported infinite beam. Such a model would in fact predict the very high decay rates at low frequency that we have observed here. However, the complexity of such a rail model is not justified, since for most rail installations in the United States, these periodic structure effects seem to be much less significant than at TTC (Pueblo). Consequently, for the purposes of obtaining a first-order model of the rail response, we have estimated the rail loss factor by simply drawing a line between -3 dB at the origin and the data point at a distance of 5 ft. Since for these cases of rapid decay of vibration, the rail vibration is very low beyond 5 ft (20 dB or more below the vibration level at the point of excitation) and the details of how the vibration decays beyond 5 ft are important in estimating the average rail vibration.

To provide a check on these rail loss factor estimates, we analyzed strip charts of the rail vibration (filtered in octave bands) during the passage of the test train at a known speed. A photocell at the accelerometer position provided information on the wheel locations during the passby. From these strip charts, we estimated the decay of rail vibration with distance in front

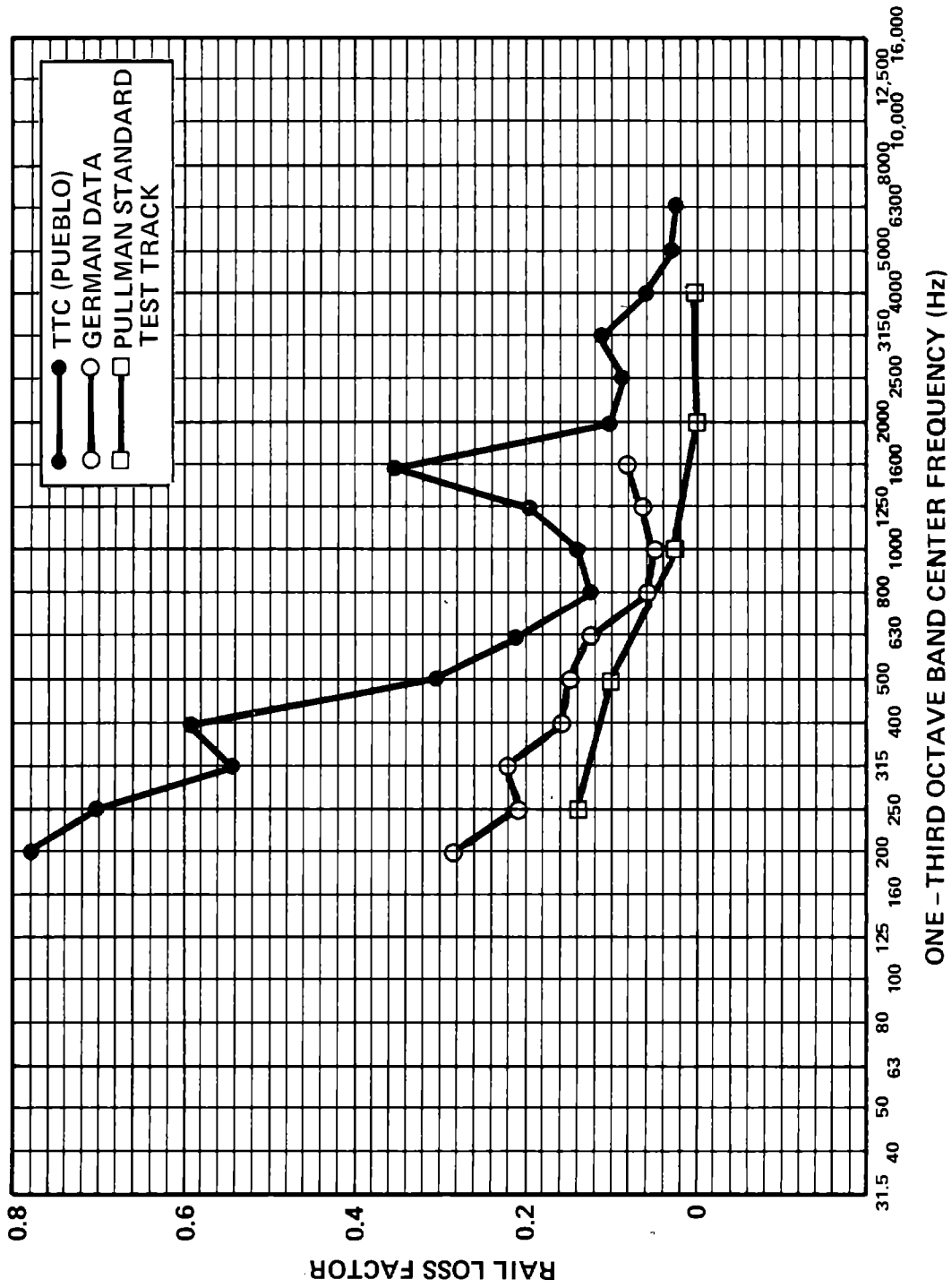


FIG. 27. RAIL LOSS FACTOR FOR VERTICAL VIBRATION.

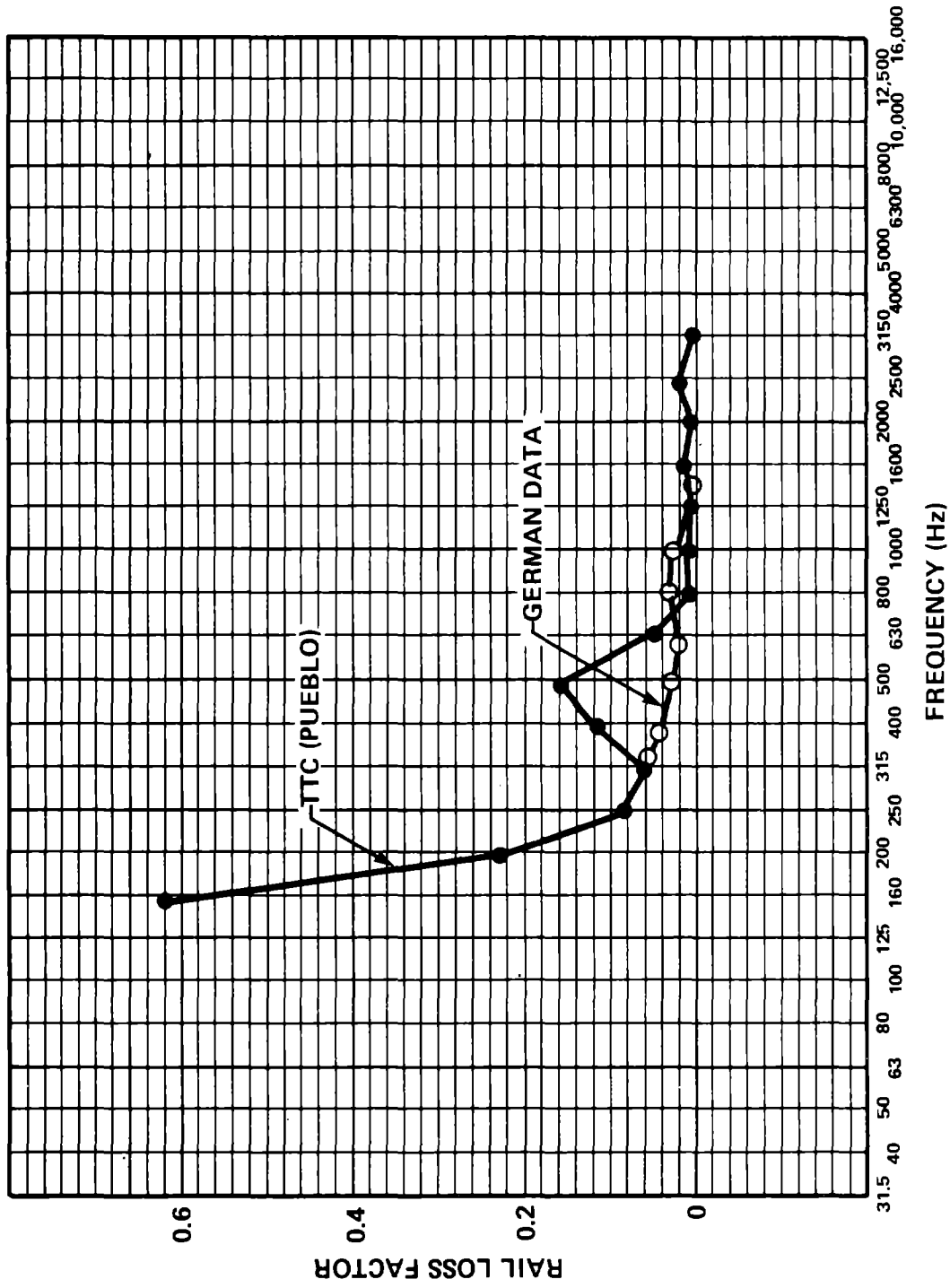


FIG. 28. RAIL LOSS FACTOR FOR HORIZONTAL VIBRATION.

of the first wheel and behind the last wheel of the train. The average of these two results is plotted in Fig. 26.

These results show a slightly lower decay rate near the point of excitation, but they generally confirm the results obtained with the impact hammer. At the greater distances from the point of excitation, the higher relative vibration levels at high frequency found during the train passage may be due in part to the cross axis sensitivity of the accelerometer. At these higher frequencies, the horizontal rail vibration decays more slowly than the vertical. Since the wheel excites both horizontal and vertical vibration at the point of contact, the horizontal rail vibration may dominate at these greater distances, and the accelerometer may sense the horizontal vibration through its cross-axis sensitivity.

2.1.2 Sound radiation

In this section, we derive the relationship between the wheel and rail vibration levels calculated in the previous section and the average sound levels at the wayside. Average sound level is the sound level at the wayside averaged over a time that is longer than the time for the train to pass the microphone. In terms of data analysis, this simply means that when analyzing the signal from a wayside microphone, one selects an averaging time on the one-third octave or narrowband analyzer that is longer than the time during which the signal is within about 10 dB of its maximum value. Using the average sound level has two major advantages: (1) the mathematics becomes simpler, and (2) the result is more easily translated into the equivalent sound level L_{eq} , or the day-night equivalent sound level L_{dn} , the most common measures for assessing noise impact.

An earlier study [5], showed that the sound pressure squared at the wayside averaged over time $T, \langle p^2 \rangle_T$, caused by radiation

from a single rail because of passage of a single wheel, is given by

$$\langle p^2 \rangle_T = \frac{\sigma_{RV}(r_F+r_H)(\rho c)^2}{4d} \langle \dot{Y}_{RV}^2 \rangle_T + \frac{\sigma_{RH}h_R(\rho c)^2}{4d} \langle \dot{Y}_{RH}^2 \rangle_T , \quad (53)$$

where σ_{RH} is the rail radiation efficiency for horizontal vibration, σ_{RV} is the rail radiation efficiency for vertical vibration, ρc is the acoustic impedance, d is the perpendicular distance of the observer from the rail, r_F and r_H are the rail foot and head widths, respectively, h_R is the rail height, and $\langle \dot{Y}_{RH}^2 \rangle_T$ and $\langle \dot{Y}_{RV}^2 \rangle_T$ are the horizontal and vertical rail velocity squared, respectively, at a point averaged over time T .

Similarly, for the wheel,

$$\langle p^2 \rangle_T = \frac{\sigma_{WR}A_{WR}}{4dVT} (\rho c)^2 \langle \dot{Y}_{WR}^2 \rangle + \frac{\sigma_{WA}A_{WA}}{4dVT} (\rho c)^2 \langle \dot{Y}_{WA}^2 \rangle , \quad (54)$$

where σ_{WR} and σ_{WA} are wheel radiation efficiencies for radial and axial vibration respectively, A_{WR} and A_{WA} are the radiating areas of the wheel for radial and axial vibration respectively, V is the train velocity, and $\langle \dot{Y}_{WR}^2 \rangle$ and $\langle \dot{Y}_{WA}^2 \rangle$ are the average vibration velocity on the wheel in the radial and axial directions, respectively.

The above equations assume freefield radiation and do not take into account reflections from the ground plane. If the change in the sound pressure squared at the wayside due to ground plane reflections is given by the function $R(r)$, where r is the source-receiver distance, the sound pressure squared at the wayside from a line source with a stationary distribution of sound radiation is given by

$$p^2(t) = \frac{\rho c}{4\pi} \int_{-\infty}^{\infty} R(r) \frac{W(\xi)d\xi}{r^2} , \quad (55)$$

where $W(\xi)d\xi$ is the power radiated by an element $d\xi$ of the line source. If the distribution of radiation from the line source moves by at velocity V , as shown in Fig. 29, the average sound pressure squared is given by

$$\langle p^2 \rangle_T = \frac{1}{T} \int_{-T/2}^{T/2} p^2(t) dt \approx \frac{1}{T} \int_{-\infty}^{\infty} p^2(t) dt = \frac{\rho c}{4\pi T} \int_{-\infty}^{\infty} \int_{-\infty}^{\infty} R(r) \frac{W(\xi)d\xi}{r^2} dt . \quad (56)$$

Defining the variable x as

$$x = Vt + \xi$$

and noting that

$$r^2 = x^2 + d^2 ,$$

we can rewrite Eq. (56) as

$$\langle p^2 \rangle_T = \frac{\rho c}{4\pi VT} \int_{-\infty}^{\infty} W(\xi)d\xi \int_{-\infty}^{\infty} \frac{dx R([d^2+x^2])^{1/2}}{(d^2+x^2)} \quad (57)$$

The first integral in Eq. (57) can be written

$$\frac{1}{VT} \int_{-\infty}^{\infty} W(\xi)d\xi = \frac{\sigma \rho c S}{VT} \int \dot{Y}^2(\xi)d\xi = \sigma \rho c S \langle \dot{Y}^2 \rangle_T , \quad (58)$$

where σ is the radiation efficiency, S is the radiating area per unit length, and $\dot{Y}^2(\xi)$ is the vibratory velocity of the line

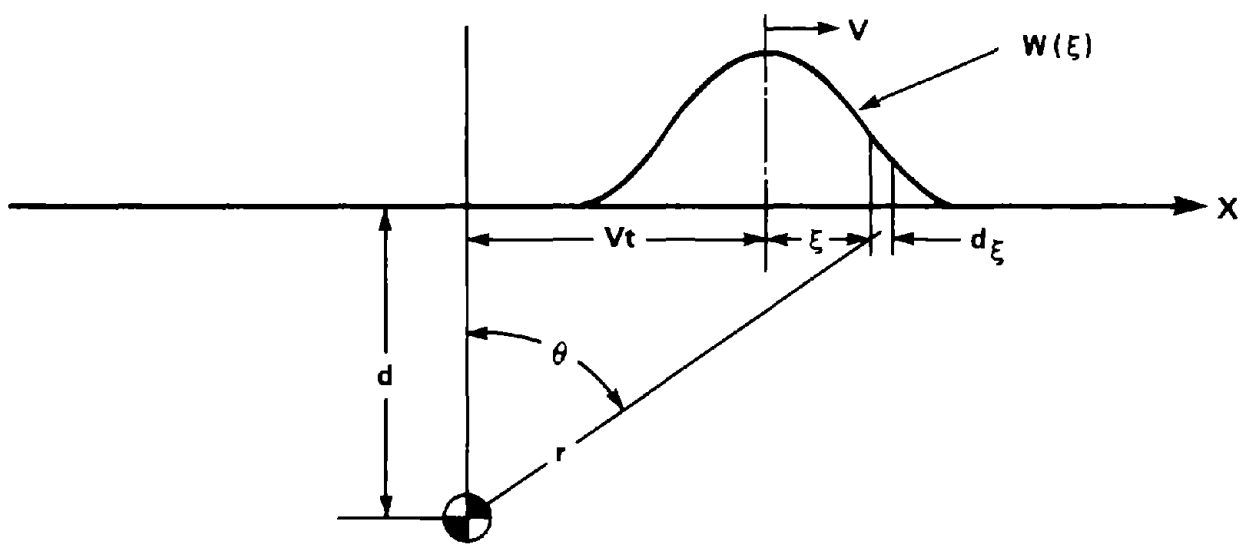


FIG. 29. LINE SOURCE GEOMETRY.

source, and where $\langle \dot{Y}^2 \rangle_T$ is the velocity squared at a point on the line source averaged over time T.

The second integral in Eq. (57) can also be simplified by expressing x and r in terms of the angle ψ defined in Fig. 28, i.e., $x = d \tan \psi$ and $r = d \sec \psi$. Making this simplification and substituting Eq. (58) into Eq. (57), we obtain

$$\langle p^2 \rangle_T = \frac{\sigma(\rho c)^2 S}{4d} \langle Y^2 \rangle_T \left[\frac{2}{\pi} \int_0^{\frac{\pi}{2}} R(d \sec \psi) d\psi \right]. \quad (59)$$

Equation (59) is essentially the same expression as Eq. (53), but multiplied by the integral in brackets. The average sound pressure squared from two rails excited by the passage of N axles then becomes

$$\langle p^2 \rangle_T = 2N \left\{ \frac{\sigma_{RV}(\rho c)^2 (r_F + r_H)}{4d} \langle \dot{Y}_{RV}^2 \rangle_T + \frac{\sigma_{RH}(\rho c)^2 h_R}{4d} \langle \dot{Y}_{RH}^2 \rangle_T \right\} D(\omega, d). \quad (60)$$

where

$$D(\omega, d) = \frac{2}{\pi} \int_0^{\frac{\pi}{2}} R(d \sec \psi) d\psi. \quad (61)$$

A similar derivation can be carried out for the wheel, which yields for the passage of N axles

$$\langle p^2 \rangle_T = 2N \left\{ \frac{\sigma_{WR} A_{WR} (\rho c)^2}{4dVT} \langle \dot{Y}_{WR}^2 \rangle + \frac{\sigma_{WA} A_{WA} (\rho c)^2}{4dVT} \langle \dot{Y}_{WA}^2 \rangle \right\} D(\omega, d). \quad (62)$$

Ground Effects

The quantity $D(\omega, d)$ contains the effects of the ground on the propagation of sound over it. The ground can be reasonably well modeled as a finite impedance plane. The model that we use here is based on some mathematics by Chessel [12], whose work represents a compilation and summary of several other studies [13-16].

The propagation of sound along a finite impedance boundary was originally studied by Ingard [13] and Rudnick [14], using different boundary conditions. Ingard assumed that the second medium (the ground, in our case) is locally reacting - that is, propagation in the second medium is ignored. Rudnick allowed for propagation in the second medium. Chessel [12] compared the excess attenuation results when using both assumptions under a wide range of geometrical and ground impedance conditions. He found that the differences were at most 0.3 dB; insignificant for our purposes. Using Ingard's equations and the variables defined in Fig. 30, we obtain for the function $F(r)$ in Eq. (55),

$$R(r) = 1 + \frac{1}{r'^2} |Q|^2 + \frac{2}{r'} |Q| \cos\left(\frac{2\pi\Delta r}{\lambda} + \theta\right), \quad (63)$$

where $r' = r_R/r$, $\Delta r = r_R - r$, and the phase lag of the reflected wave,

$$\theta = \tan^{-1} [\text{Im}(Q)/\text{Re}(Q)].$$

The quantity Q is the strength of the image source (see Fig. 30) given by

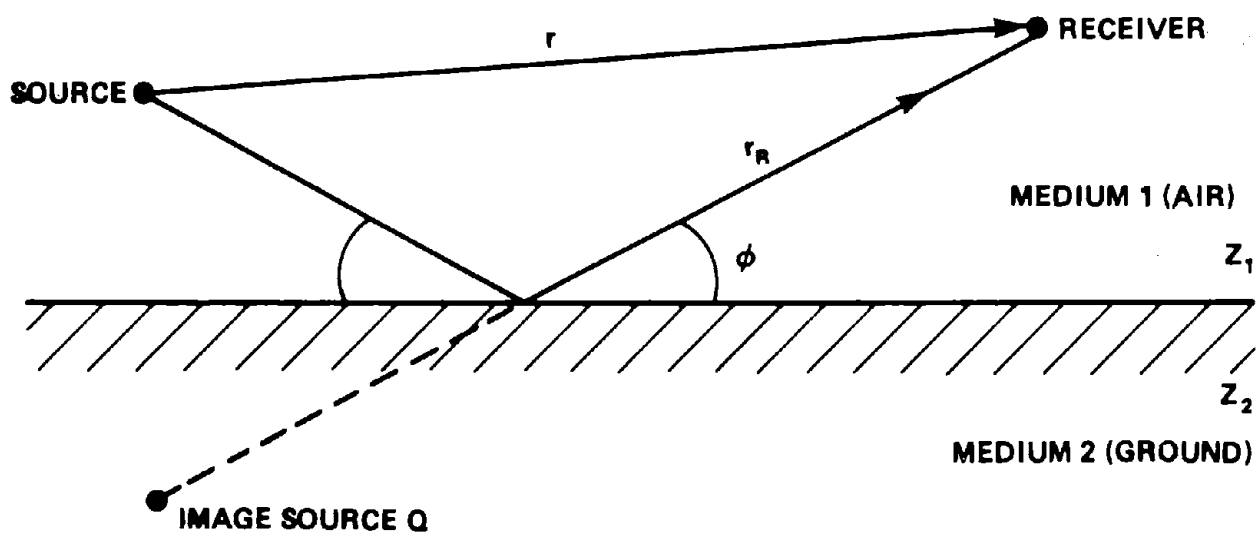


FIG. 30. GEOMETRICAL PARAMETERS USED IN THE GROUND EFFECTS MODEL.

$$Q = R_p + F(\tilde{w})(1-R_p) . \quad (64)$$

The reflection coefficient R_p , relating the amplitude and phase of the incident and reflected sound waves at the ground plane, is given by

$$R_p = \frac{\sin\phi - z_1/z_2}{\sin\phi + z_1/z_2} , \quad (65)$$

where ϕ , the reflection angle; z_1 , the characteristic impedance of medium 1 (air); and z_2 , the impedance of medium 2 (ground) are defined in Fig. 30. $F(\tilde{w})$, known as the boundary loss factor or the amplitude factor, describes the behavior of the ground and surface waves. \tilde{w} is often referred to as the "numerical distance." The following series expansions are used for the numerical evaluation of $F(\tilde{w})$.

$$F(\tilde{w}) = 1 + i(\pi\tilde{w})^{1/2} e^{(-\tilde{w})} - 2e^{(-\tilde{w})} \sum_{n=1}^{\infty} \frac{\tilde{w}^n}{(n-1)!(2n-1)}$$

for $|\tilde{w}| < 10$

$$F(\tilde{w}) = - \sum_{n=1}^{\infty} \frac{(2n)!}{2^n n! (2\tilde{w})^n}$$

for $|\tilde{w}| > 10$. (66)

For the locally reacting assumption, \tilde{w} is expressed as

$$\tilde{w} = (1/2)ik_1r_2 \frac{(\sin\phi + z_1/z_2)^2}{(1 + \sin\phi \cdot z_1/z_2)} . \quad (67)$$

k_1 is the wavenumber in air, and $i = \sqrt{-1}$.

The characteristic acoustic impedance for medium 2, the ground, is required for the evaluation of R_p , but has proven difficult to measure directly. Delaney and Bazley [15] measured the acoustic properties of a wide range of materials. The measured values of characteristic impedance were shown to normalize nicely as a function of frequency divided by specific flow resistance per unit thickness (σ_f).

Expressing the characteristic impedance z of the material as

$$z = R + iX ,$$

the experimentally determined functions are

$$\frac{R}{\rho_0 c_0} = 1 + 9.08(f/\sigma_f)^{-0.75}$$

$$\frac{X}{\rho_0 c_0} = 11.9(f/\sigma_f)^{-0.73} , \quad (68)$$

where $\rho_0 c_0$ is the characteristic impedance of air, f is frequency, and σ_f is in units of cgs rayls. Embleton [16] has used this model for characterizing the impedance of common types of ground with the single-parameter flow resistance, σ_f . Embleton's results were used for our estimation of σ for the TTC site.

Equation (63) can be expanded to apply to one-third octave band intervals. When one assumes a white noise spectrum, the expression becomes

$$R(r) = 1 + \frac{1}{r^2} |Q|^2 + \frac{2}{r} |Q| \sin\left(\frac{\mu \Delta r}{\lambda}\right) \frac{\cos(\eta \Delta r / \lambda + \theta)}{\mu \Delta r / \lambda} , \quad (69)$$

where

$$\mu = 2\pi \Delta f / 2f = 0.729$$

$$\eta = 2\pi[1 + (\Delta f/2f)^2]^{1/2} = 6.325$$

for one-third octave band intervals. The center frequency of the one-third octave bands is used for each band.

The expression for $D(\omega, d)$ can be obtained by substituting Eq. (69) into Eq. (61)

$$D(\omega, d) = \frac{2}{\pi} \int_0^{\frac{\pi}{2}} \left\{ 1 + \frac{|Q|^2}{(r')^2} + \frac{|Q|}{r'} \sin \left(\frac{\mu \Delta r}{\lambda} \right) \frac{\cos \left(\frac{n \Delta r}{\lambda} + \theta \right)}{\mu \Delta r / \lambda} \right\} d\psi, \quad (70)$$

where $r = d \sec \psi$.

This integral is generally evaluated numerically.

Equations (60) and (62), along with Eq. (70), constitute our formulas for predicting the average sound pressure at the wayside given the average vibration levels on the rails and wheels.

In order to build our confidence in the validity of the prediction of Eq. (67) and Eq. (70), we carried out a series of measurements at the Transportation Test Center in conjunction with the model validation measurements mentioned in the introduction and described more fully in Sec. 3. We selected a section of tangent track on the Transit Test Track that was also used for the measurements of rolling noise. The sound source used for the propagation measurements was a high-efficiency, 4-in.-diameter cone loudspeaker (JBL 2105) in a sealed enclosure. This small source was used so that it could be placed separately at the rail height and the wheel height. Therefore, any differences in the effect of the ground on the propagation from the rail could be separated from the effect from the wheel. The loudspeaker was calibrated in BBN's anechoic chamber for directivity and efficiency (output re input amplitude) as a function of frequency.

From the calibration, "freefield" sound levels were projected for the loudspeaker at the distances and angles used in the propagation measurements. These "freefield" levels were compared to the sound levels measured at the site to determine the effects of the ground on the propagation.

Figure 31 shows the test site and the speaker in position at rail height and at wheel height. The geometry of the test site and microphone locations are shown in Fig. 32. The geometry used as input to the model was the same as that shown in the figure. The specific flow resistance used for the ground was 1000 cgs rayls. This value was selected on the basis of Embleton's [16] descriptions of various types of ground and the associated flow resistivities. For all of the comparisons presented below, the microphone was positioned along a line 22.7 ft from the speaker (see Fig. 32). Also, the microphone was at a height 6.3 ft above the ground (4 ft above top-of-rail).

Figure 33 shows the curves for the measured and predicted loudspeaker response with the loudspeaker at the wheel height (wheel center 15 in. above the top of the rail) and the microphone at the zero degree (perpendicular) position, 22.7 ft from the speaker. It may be of interest to note that the agreement between measurement and theory in the low-frequency region (315 to 630 Hz) improved markedly when the source height in the prediction model was lowered by 0.5 ft. Since the predicted sound level at low frequencies is a strong function of site geometry, this improvement may be explained by unobserved terrain variation between the source and receiver.



(a) Test Site



(b) Speaker at Rail Height



(c) Speaker at Wheel Height

FIG. 31. TEST SITE AND SOUND SOURCE FOR THE GROUND EFFECT MEASUREMENTS.

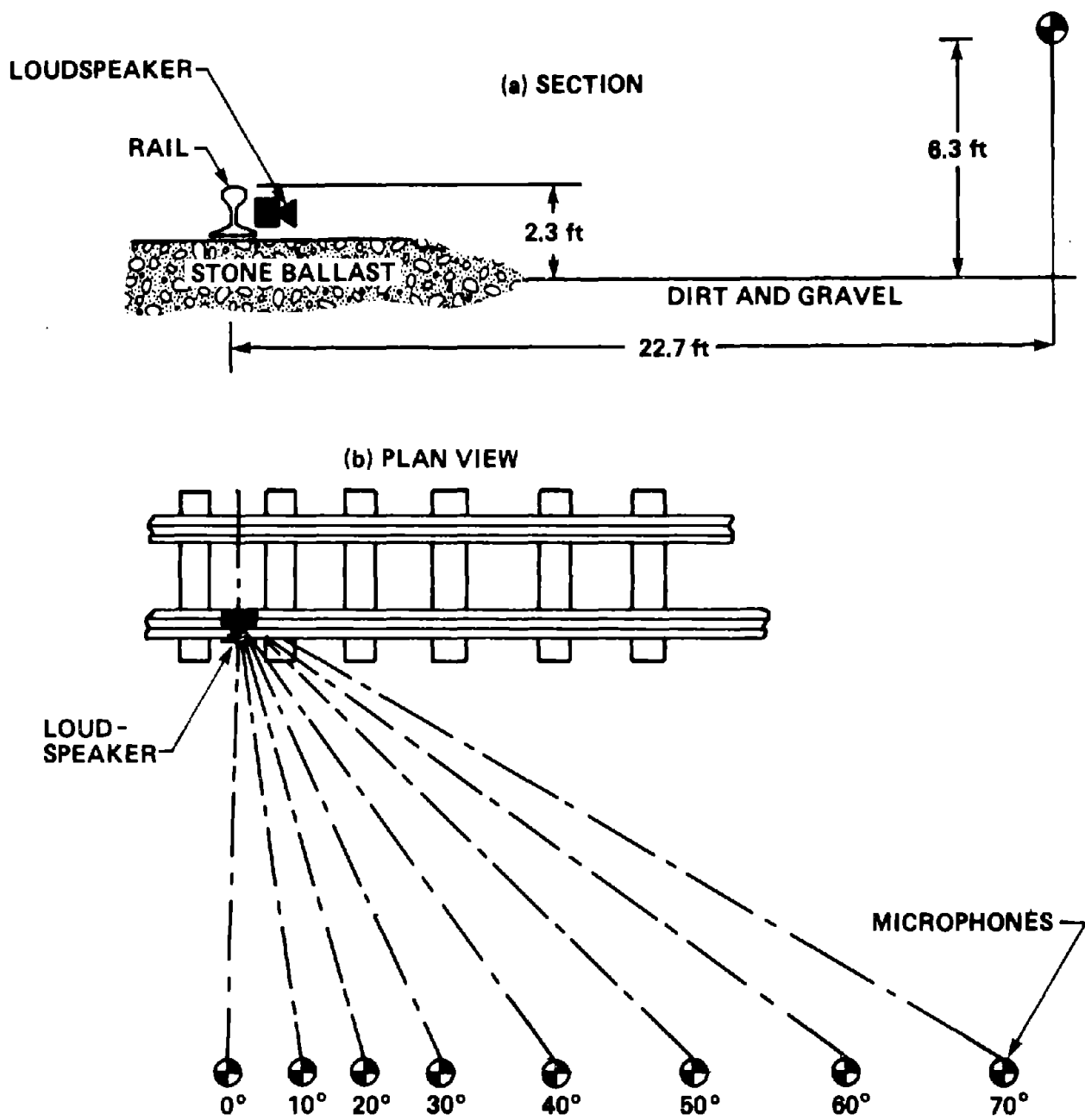


FIG. 32. TEST SITE GEOMETRY.

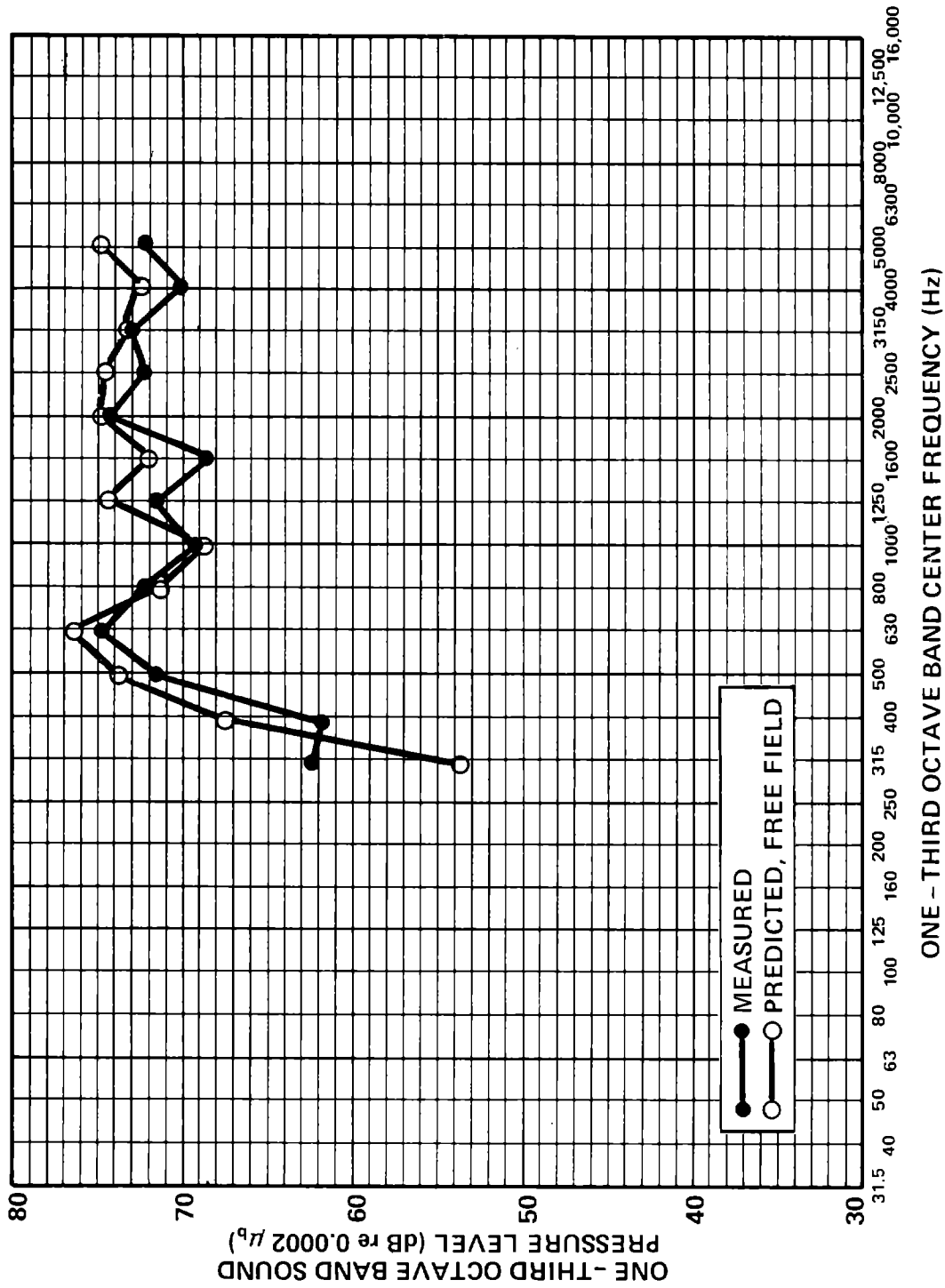


FIG. 33. MICROPHONE AT ZERO DEGREE POSITION; SOURCE AT WHEEL HEIGHT.

Figure 34 shows three curves representing measured and predicted loudspeaker response with the speaker at the rail height. The two predicted curves show the expected sound levels at the microphone, with and without the effect of the ground. The "without ground" curve was derived assuming simple freefield propagation. Note that this freefield curve agrees much better with the measured data than does the prediction that includes the image source and ground and surface wave contributions. We suspect that this is due to the presence of the clean, sound-absorptive ballast [7] directly under the speaker. The ballast effectively absorbs the sound from the rail that would be reflected off the ground. Figure 35 shows the ray path geometry for the test site, confirming the fact that the sound from the rail is reflected off the ballast, whereas that from the wheel is reflected off the hard ground. Therefore, we suspect that the ballast is highly absorptive and effectively absorbs the image source, so that only the direct wave reaches the microphone with significant intensity. The rail therefore appears to be in a freefield environment.

To examine the ability of our analytical model to deal with a line source, we averaged the measurements and predictions made at four separate angles. The angles chosen were the zero-, 20-, 40-, and 60-degree positions (see Fig. 32).

Figure 36 presents the measured and predicted curves with the loudspeaker at the wheel height. The agreement between the measured and theoretical curves is better for this averaged condition than for the single zero-degree position shown in Fig. 33.

Figure 37 presents the measured and predicted four-angle average curves for the loudspeaker at the rail height. Both the freefield and the ground-corrected curves are shown, as before. Again, it is clear that freefield propagation is a more accurate

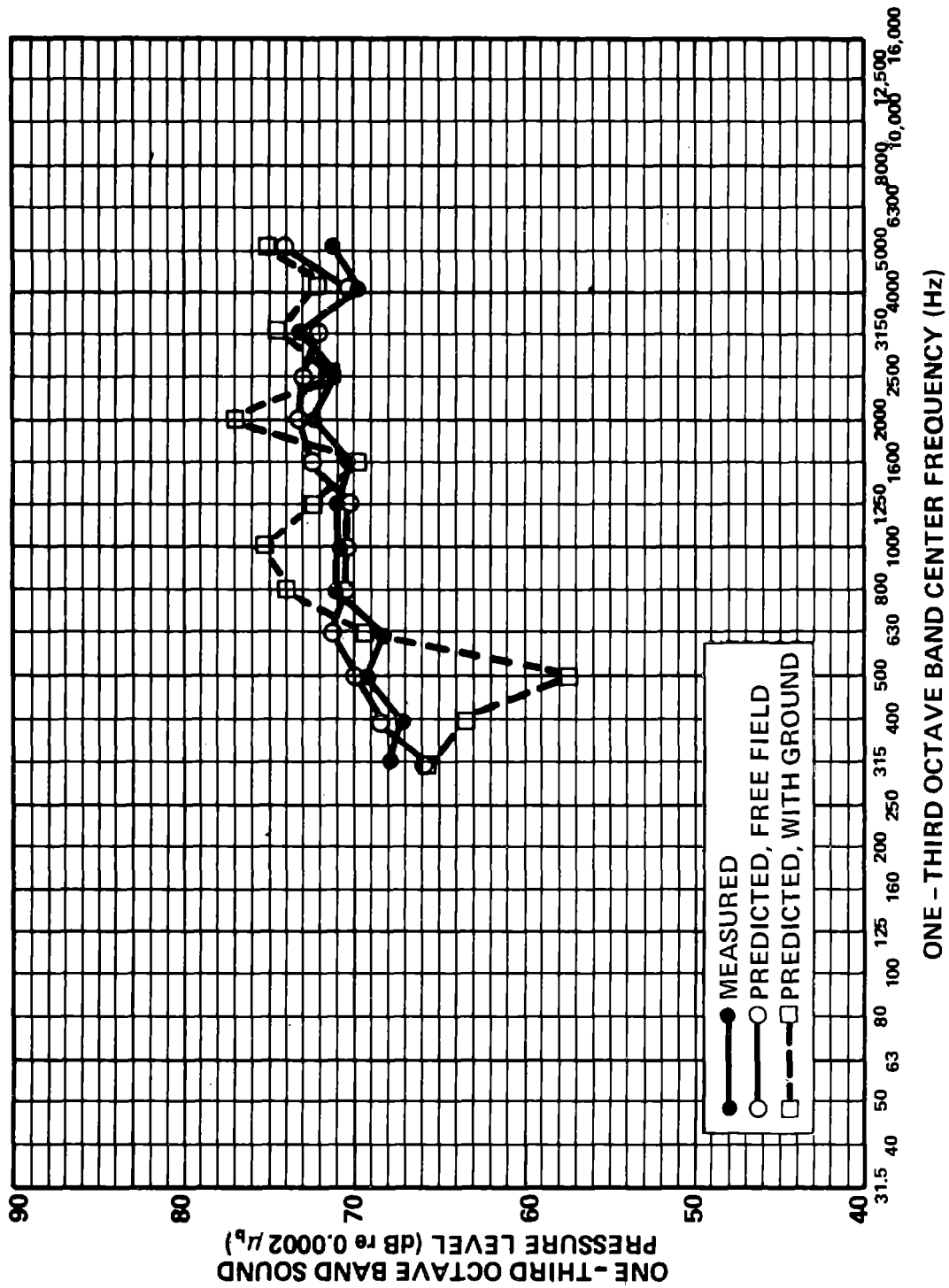


FIG. 34. MICROPHONE AT ZERO DEGREE POSITION; SOURCE AT RAIL HEIGHT.

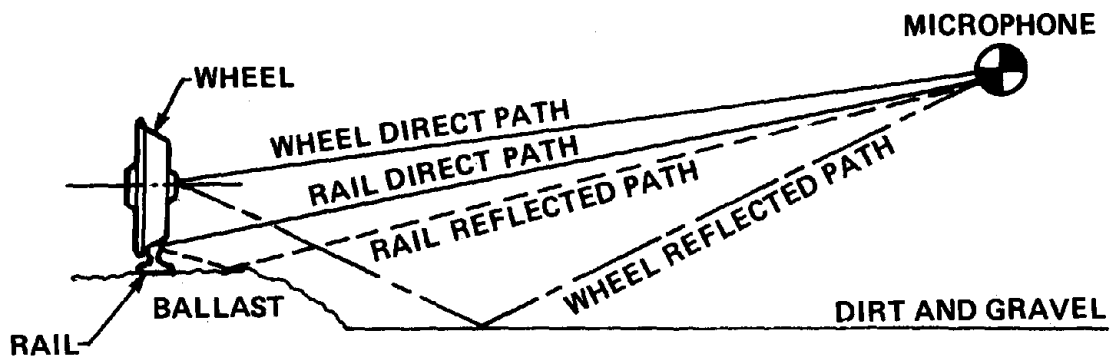


FIG. 35. DIRECT AND REFLECTED RAY PATHS FROM THE WHEEL AND RAIL.

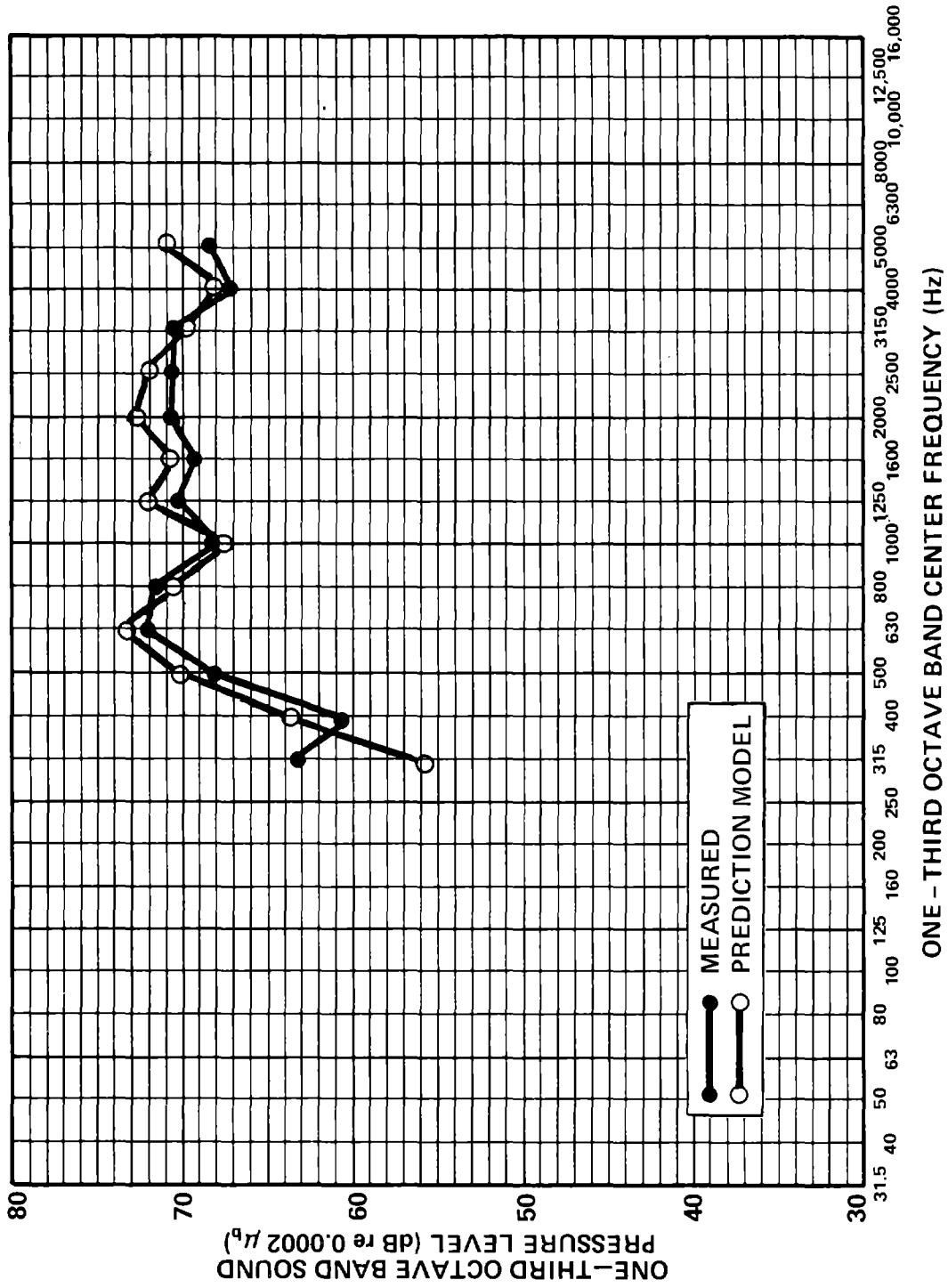


FIG. 36. FOUR-ANGLE AVERAGE LOUDSPEAKER RESPONSE; SOURCE AT WHEEL HEIGHT.

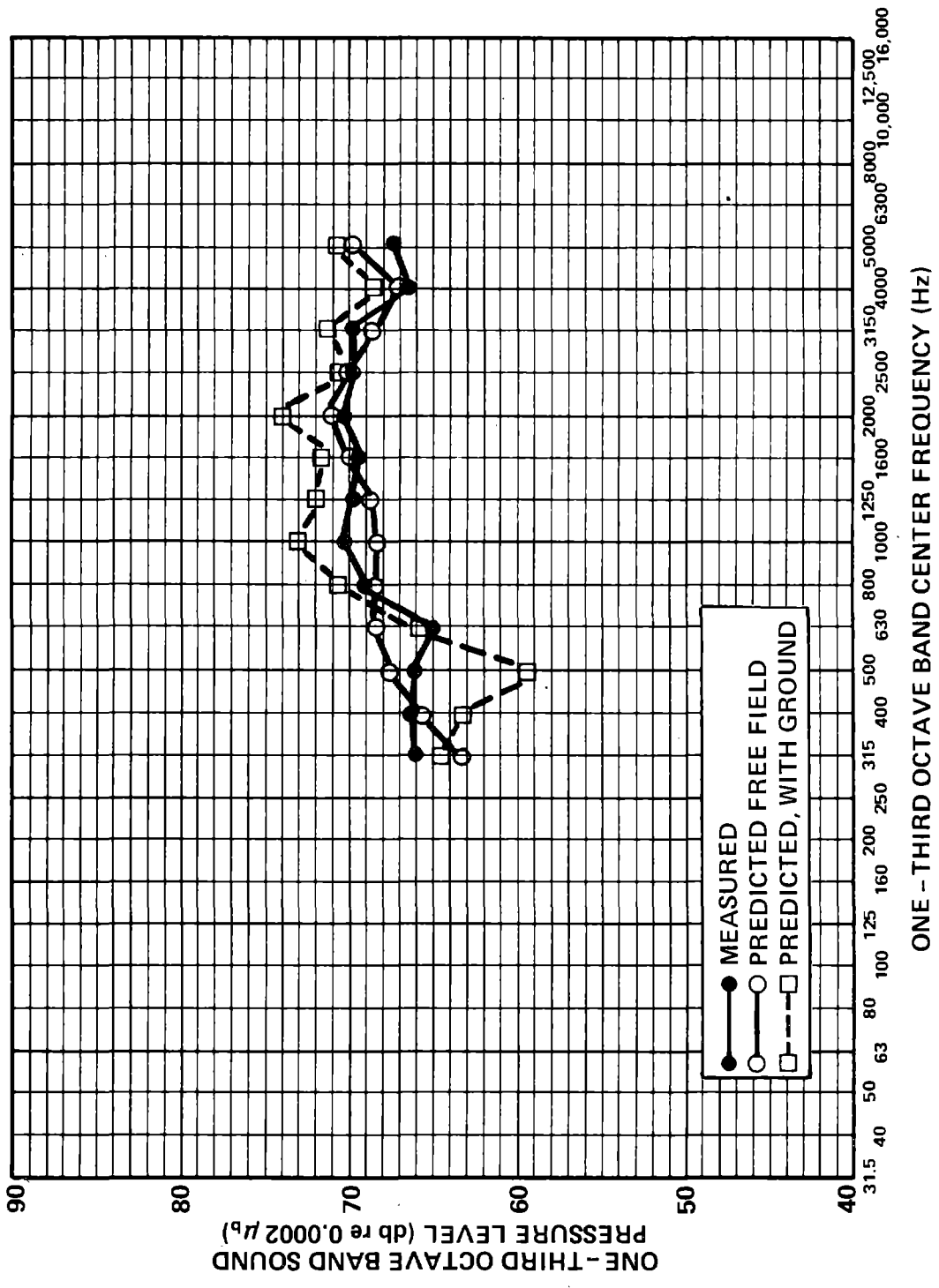


FIG. 37. FOUR-ANGLE AVERAGE LOUDSPEAKER RESPONSE; SOURCE AT RAIL HEIGHT.

representation for rail radiation than is ground-corrected propagation.

For purposes of comparison, Fig. 38 shows the propagation model's effect on wheel-radiated noise for a complete passby. The curve was generated by using Simpson's Rule integration in nine steps over an 85-degree angle, and is effectively a plot of $D(\omega, d)$, Eq. (61), where $d = 22.7$ ft. The curve shows the correction to the freefield spectrum. For rail-radiated noise, the correction is zero dB for all frequencies, as the loudspeaker measurements show that freefield radiation provides the best agreement. Note that the ground effect tends to enhance the wheel radiation over the rail radiation for this geometry by 1 to 2 dB at the higher frequencies.

Radiation Efficiency

The radiation efficiencies of wheels and rails have been examined in a number of earlier studies [3,5,18] and simplified expressions have been developed for the dependence on frequency. The expressions that we use here are

$$\sigma_{RV} = \sigma_{RH} = \frac{2}{1 + \left(\frac{630}{f}\right)^3} \quad (71)$$

$$\sigma_{WR} = \sigma_{WA} = 2 \quad (72)$$

Equation (71) is the result of fitting a curve to reverberation room measurements of rail radiation efficiency. It works well for rails of standard size for frequencies from about 250 to 8000 Hz. A more detailed analytical expression, based on a theoretical derivation that takes into account the details of the rail geometry, is available in Ref. 3. The wheel is an efficient

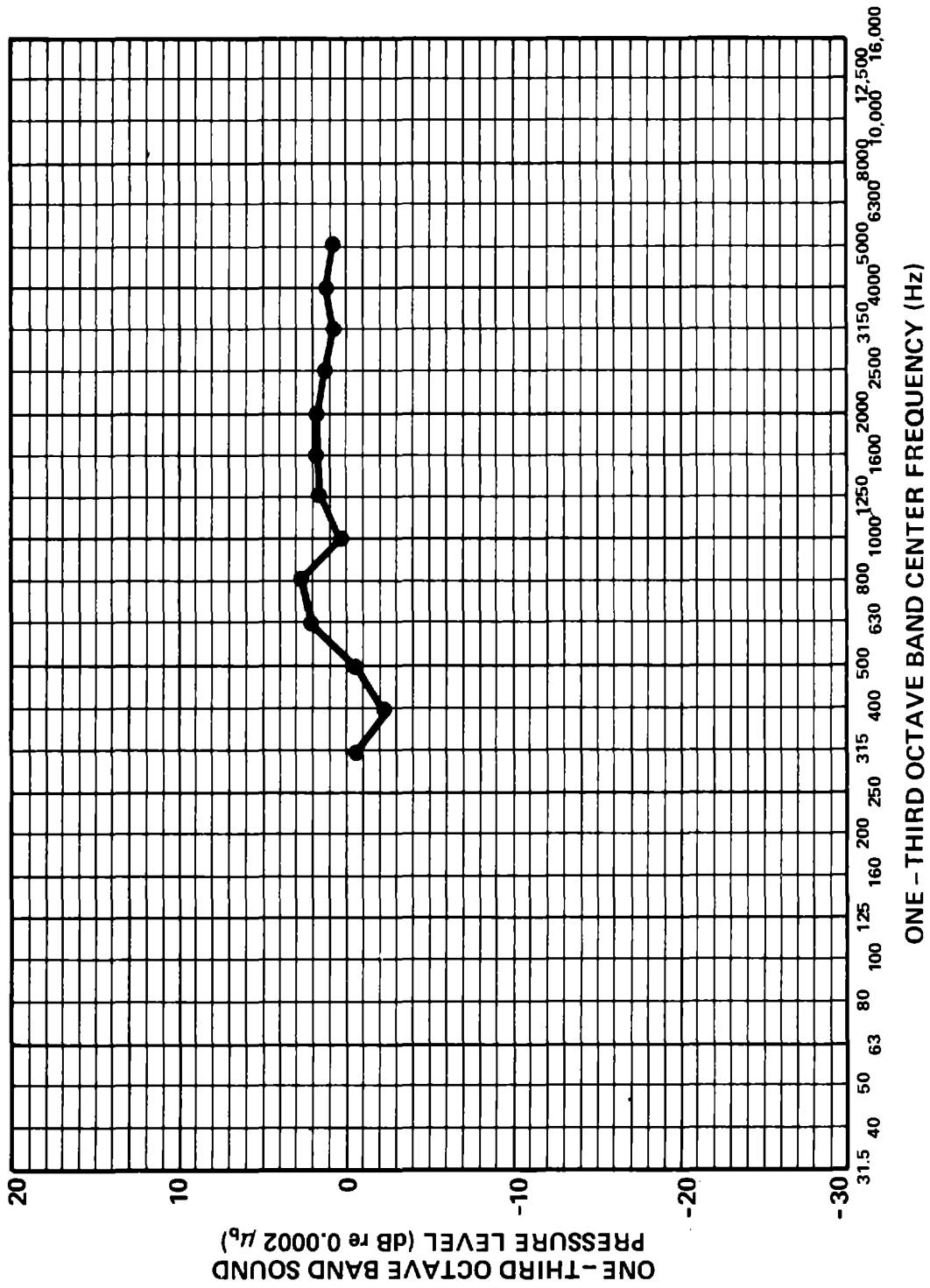


FIG. 38. PROPAGATION MODEL EFFECT ON WHEEL PASSBY, USING THE TTC TEST SITE GEOMETRY.

sound radiator, and Eq. (72) agrees reasonably well with laboratory measurements from 250-6300 Hz.

Summary

It is useful at this point to rewrite the final expressions in this section in terms of the one-third octave band sound pressure level spectrum $S_p(\omega)$ averaged over the train passby. For the rail we obtain

$$S_{p_R}(\omega) = \frac{N}{2d} \left(\frac{\rho c}{p_0}\right)^2 \left\{ \sigma_{RV}(r_F+r_H) S_{\dot{Y}_{RV}}^{(AVG)}(\omega) + \sigma_{RH} h_R S_{\dot{Y}_{RH}}^{(AVG)}(\omega) \right\} D(\omega, d) , \quad (73)$$

and for the wheel,

$$S_{p_W}(\omega) = \frac{N}{2d\sqrt{T}} \left(\frac{\rho c}{p_0}\right)^2 \left\{ \sigma_{WR} A_{WR} S_{\dot{Y}_{WR}}^{(AVG)}(\omega) + \sigma_{WA} A_{WA} S_{\dot{Y}_{WA}}^{(AVG)}(\omega) \right\} D(\omega, d) , \quad (74)$$

where p_0 is the standard reference pressure.

Table 4 summarizes the input information required to use Eqs. (73) and (74).

2.2 Impact Noise

Impact noise is generated by discontinuities on the running surfaces of the wheels and rails. Flat spots on wheels, rail joints, "burn-outs" on rails, and frogs are all responsible for impact noise. The excitation of impact noise is, in principle, identical to rolling noise, and all of the theoretical development in the preceding sections for rolling noise is applicable to the analysis of impact noise. A means is required for expressing

TABLE 4. ROLLING NOISE MODEL SUMMARY.

Variable	Description	Where to Find
$\dot{Y}_{RV}^{(AVG)}(\omega)$	one-third octave band vertical rail velocity spectrum averaged over the train passby	Eqs. (14) and (12)
η_{RV}	rail damping loss factor for vertical vibration	input data
k_{RV}	rail wavenumber for bending	Eq. (15)
r_{RV}	rail radius of gyration	input parameter
c_{ℓ}	longitudinal wave speed in rail	input parameter
$S_{RW}(k)$	wheel roughness wavenumber spectrum	input data
$S_{RR}(k)$	rail roughness wavenumber	input data
$H(k)$	wheel/rail contact area filter	Eq. (26)
k	roughness wavenumber	
b	contact area radius	Eq. (25)
V	train velocity	input parameter
K_C	contact stiffness	Eq. (10)
R_W, R_R	wheel and rail radius	input parameter
T	train passby averaging time	input parameter
N	number of axles on the train	input parameter
$\dot{Y}_{RH}^{(AVG)}(\omega)$	one-third octave band horizontal rail velocity spectrum averaged over the train passby	Eqs. (37), (34), and (12)
η_{RH}	rail damping loss factor for horizontal vibration	input data
k_{RH}	rail wavenumber for bending in the horizontal plane	Eq. (38)
r_{RH}	rail radius of gyration for horizontal bending	input parameter
Z_{RVH}	vertical to horizontal rail cross impedance	input data

TABLE 4. (Cont.) ROLLING NOISE MODEL SUMMARY.

Variable	Description	Where to Find
(AVG) $S(\omega)$ \dot{Y}_{WR}	one-third octave band spectrum of radial velocity at the wheel tread averaged over the circumference	Eqs. (21) and (12)
A_n	amplitude of the radial admittance of the nth wheel mode	Eq. (45a) and Table 2
(AVG) $S(\omega)$ \dot{Y}_{WA}	one-third octave band spectrum of axial velocity at the wheel tread averaged over the circumference	Eqs. (35), (34), and (12)
B_n	amplitude of the axial admittance of the nth wheel mode	Eq. (48) and Table 2
Z_{RV} ρ_R A_R	vertical rail impedance rail density rail cross-sectional area	Eq. (51) input parameter input parameter
Z_{RH}	horizontal rail impedance	Eq. (51)
Z_{WR}	radial wheel impedance	Eq. (45) and Table 2
Z_{WA}	axial wheel impedance	Eq. (49) and Table 2

the geometry of the discontinuities in terms of an "equivalent roughness." The wavenumber spectrum of that roughness will be such that the time-averaged noise generated by the roughness during a train passby will be the same as the time-averaged noise generated by the discontinuities. Thus, we uniformly distribute the discontinuity along the length of the rail or around the circumference of the wheel. By so doing, we greatly simplify the mathematics but lose our ability to predict some of the details of the noise. For example, we can predict the impact noise averaged over a time longer than the passby time of the train, but we cannot estimate the time history of the sound pressure or the effect of position along the rail in relation to the observer of a rail joint or other discontinuity.

In this section, we calculate the equivalent roughness spectrum for a wheel flat and a rail joint in terms of the geometry of each.

2.2.1 Rail joints

Ver, Ventres, and Myles [19] have examined in some detail the noise resulting from wheels impacting rail joints. They found that the elevation change at a rail joint was mostly responsible for impact noise. By contrast, gaps in the rail with no elevation change produce very little noise. Ver, Ventres, and Myles have also shown that stepup joints - where the wheel travels from the lower rail to the higher rail - are more important than stepdown joints for speeds above the critical speed. Below the critical speed, the two are equivalent. The critical speed, as defined by Ver, Ventres, and Myles, is the speed above which at a stepdown joint the rail and wheel came out of contact. In this derivation, we will focus on step-up rail joints. Our goal is to derive an expression for an equivalent roughness in terms of rail

joint parameters that can be used in the rail response equations of Sec. 2.1.

Figure 39 shows the geometry of a wheel impacting a stepup joint. In a manner analogous to the derivation of Eq. (6) for roar noise in Sec. 2.1, the Fourier transform of the radial wheel response at the point of contact can be written

$$\tilde{y}_{WR} = \frac{z_{WR}}{z_{WR} + z_{RV} - j\omega \frac{z_{WR} z_{RV}}{K_c}} \tilde{v}_0(\omega) , \quad (75)$$

where $\tilde{v}_0(\omega)$ is the Fourier transform of wheel velocity at the point of contact that would result if the rail were rigid, i.e., $z_{RV} \gg z_{WR}$ and z_{WR} and z_{RV} are the radial wheel and vertical rail impedance, respectively. The vertical wheel velocity at the rail joint $v_0(t)$, if the rail were rigid, can be derived from the geometry of Fig. 39 as

$$v_0(t) = v \left(\frac{1}{2} \left(\frac{2h_j}{R_W} \right)^{1/2} - \frac{vt}{R_W} \right); \quad - \left(\frac{2h_j R_W}{V} \right)^{1/2} < t < \left(\frac{2h_j R_W}{V} \right)^{1/2} \quad jh \ll R_W , \quad (76)$$

where V is the train velocity, h the joint height, and R_W the wheel radius. The Fourier transform of Eq. (76) defined as

$$\tilde{v}_0(\omega) = \frac{1}{2\pi} \int_{-\infty}^{\infty} v_0(t) \cdot e^{-j\omega t} dt$$

is given after some manipulations by

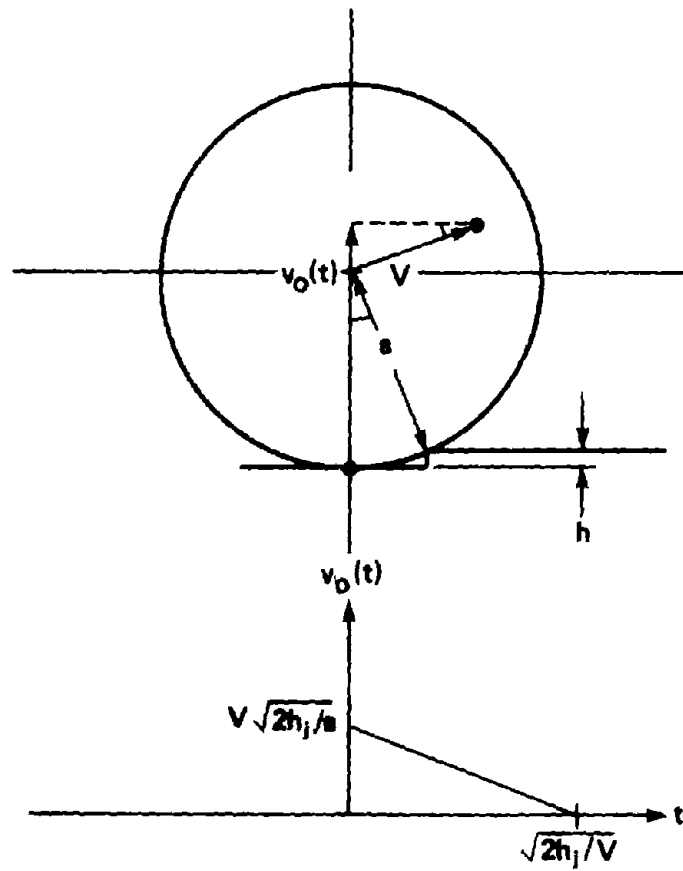


FIG. 39. RAIL JOINT GEOMETRY.

$$\tilde{v}_0(\omega) = \frac{h_j}{2\pi} \left[\frac{\sin \Omega_j}{\Omega_j} - j \left(\frac{\cos \Omega_j}{\Omega_j} - \frac{\sin \Omega_j}{\Omega_j} \right) \right]$$

$$\Omega_j = \sqrt{\frac{2h_j a}{2V}} \omega \quad . \quad (77)$$

As the wheel rolls along the rail, it will encounter many joints periodically, at time intervals T . If n is the number of the rail joint after the first, the Fourier transform of $v_0(t)$ at any point can be written

$$\tilde{v}_{0n}(\omega) = \tilde{v}_0(\omega) e^{+j\omega nT} \quad ,$$

and for a string of these impacts over interval $2NT$, one obtains

$$\tilde{v}_\tau(\omega) = \sum_{n=-N}^N \tilde{v}_0(\omega) e^{j\omega nT} \quad . \quad (78)$$

Equation (78) is the Fourier transform of the rail velocity at the point of contact with the wheel, assuming that $Z_W \gg Z_R$. This is completely analogous to the roughness velocity defined for random small-scale roughness. Consequently, in the limit as N approaches infinity, Eq. (78) would represent the Fourier transform of the equivalent rail joint roughness velocity.

It is convenient to express this equivalent roughness in terms of a power spectrum. To do so, note that

$$\tilde{v}_\tau(\omega) = \frac{1}{2\pi} \int_{-\tau}^{\tau} v_r(t) e^{-j\omega t} dt, \quad \tau = NT \quad ,$$

where $v_r(t)$ is the time history for all the joint impacts strung together over interval $2NT$. The power spectrum is defined as [20]

$$\phi_v(\omega) = E \left\{ \lim_{\tau \rightarrow \infty} \frac{|v_\tau(\omega)|^2}{\tau} \right\}, \quad (79)$$

where $E\{ \}$ means expected value. Substituting Eq. (76) into Eq. (78) and the result into Eq. (79), we obtain

$$\phi_v(\omega) = \frac{h^2}{4\pi^2} \left\{ \frac{\sin^2 \Omega_j}{\Omega_j^2} + \left(\frac{\cos \Omega_j}{\Omega_j} - \frac{\sin \Omega_j}{\Omega_j^2} \right)^2 \right\} \lim_{N \rightarrow \infty} \frac{1}{NT} \left| \sum_{n=-N}^{n=N} e^{j\omega nT} \right|^2. \quad (80)$$

It is straightforward to show that

$$\lim_{N \rightarrow \infty} \sum_{n=-N}^N e^{j\omega nT} = \text{Fourier transform of } \sum_{n=-\infty}^{\infty} \delta(t-nT),$$

where $\delta(\)$ is the Dirac delta function. Blackman and Tukey [21] have shown that the Fourier transform on the right-hand side of this equation can be expressed as

$$\frac{2\pi}{T} \sum_{n=-\infty}^{\infty} \delta\left(\omega - \frac{2\pi n}{T}\right),$$

and that

$$\text{Fourier transform of } \sum_{n=-N}^N \delta(t-nT) = \frac{\sin(2N+1)\omega T/2}{\sin \omega T/2} = \sum_{n=-N}^N e^{j\omega nT}.$$

Consequently, the limit in Eq. (80) can be rewritten as

$$\lim_{N \rightarrow \infty} \frac{1}{NT} \sum_{n=-N}^N e^{j\omega nT} = \lim_{N \rightarrow \infty} \frac{1}{NT} \frac{\sin(2n+1)\omega T/2}{\sin \omega T/2} \frac{2\pi}{T} \sum_{-\infty}^{\infty} \delta(\omega - \frac{2\pi n}{T}) \quad (81)$$

The right-hand side of Eq. (81) is zero unless $\omega = (2\pi n/T)$, where n is an integer. With $\frac{\omega T}{2}$ equal to $n\pi + \epsilon$, where ϵ is small, the above limit becomes for n odd or even

$$\lim_{N \rightarrow \infty} \frac{(2N+1)}{NT} \frac{2\pi}{T} \sum_{-\infty}^{\infty} \delta(\omega - \frac{2\pi n}{T}) = \frac{4\pi}{T^2} \sum_{-\infty}^{\infty} \delta(\omega - \frac{2\pi n}{T}) \quad .$$

Substituting this result into Eq. (80) we obtain

$$\Phi_V(\omega) = \frac{h_j^2}{\pi T^2} \left\{ \frac{\sin^2 \Omega_j}{\Omega_j^2} + \left(\frac{\cos \Omega_j}{\Omega_j} - \frac{\sin \Omega_j}{\Omega_j^2} \right)^2 \right\} \sum_{n=-\infty}^{\infty} \delta(\omega - \frac{2\pi n}{T})$$

$$\Omega_j = \frac{\sqrt{2hR_W}}{2V} \omega \quad . \quad (82)$$

The function of Ω in Eq. (82) is plotted in Fig. 40. We are interested in the function for values of $\Omega/2\pi$ from 0.3 (60 mph and 250 Hz) to 10 (20 mph and 3000 Hz). In that region, the function is well approximated by $1/\Omega^2$, as shown in Fig. 40. Consequently, Eq. (82) simplifies to

$$\Phi_V(\omega) = \frac{h_j^2}{\pi \Omega_j^2 T^2} \sum_{n=-\infty}^{\infty} \delta(\omega - \frac{2\pi n}{T}) \quad (83)$$

We are generally interested in one-third octave band roughness displacement spectra. In a one-third octave band, there are $2 \times [0.23\omega/(2\pi/T)]^*$ delta function spikes. Multiplying this factor times Eq. (83) is equivalent to integrating $\Phi_V(\omega)$ in frequency. To be certain that the integral converges to the mean

*The power spectrum is double-sided; hence the factor of 2.

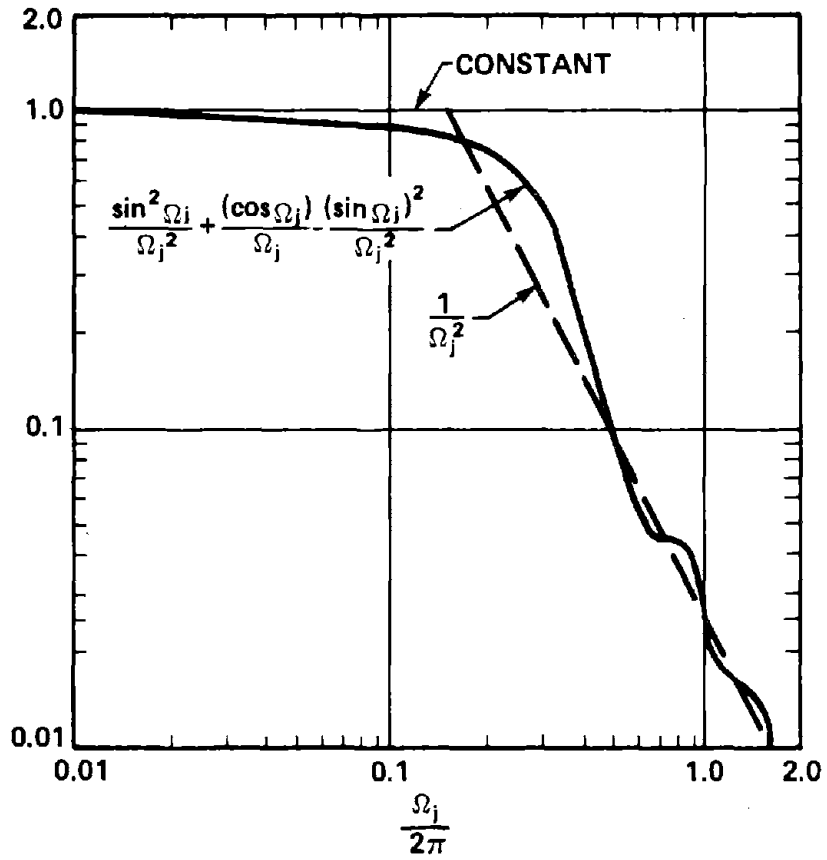


FIG. 40. APPROXIMATION TO THE RAIL JOINT EQUIVALENT ROUGHNESS SPECTRUM.

square velocity in any one-third octave band, we integrate both sides of Eq. (79) in frequency from $-\infty$ to ∞ and obtain

$$\int_{-\infty}^{\infty} \phi_v(\omega) d\omega = E \lim_{\tau \rightarrow \infty} \frac{1}{\tau} \left(\frac{1}{2\pi} \right)^2 \int_{-\tau}^{\tau} dt_1 v_0(t_1) \int_{-\tau}^{\tau} dt_2 v_0(t_2) \int_{-\infty}^{\infty} e^{-j\omega(t_1-t_2)} d\omega.$$

Noting that $\int_{-\infty}^{\infty} e^{-j\omega(t_1-t_2)} d\omega = 2\pi \delta(t_1-t_2)$, where $\delta(\)$ is the Dirac delta function, we simplify the above equation to

$$\pi \int_{-\infty}^{\infty} \phi_v(\omega) d\omega = E \left\{ \lim_{\tau \rightarrow \infty} \frac{1}{2\tau} \int_{-\tau}^{\tau} v_0^2(t) dt \right\}.$$

The right-hand side of the equation is the time-average mean square velocity. If $v_0(t)$ were filtered in a one-third octave band, $\phi_v(\omega)$ would represent the spectrum of that filtered signal. In order that $\int \phi_v(\omega) d\omega$ be the mean square velocity in that one-third octave band, we must multiply that integral by π . Finally, to transform the spectrum from a velocity to a displacement spectrum, we must divide $\phi_v(\omega)$ by ω^2 . Accordingly, the one-third octave band displacement spectrum $S_j(\omega)$ is given by

$$S_j(\omega) = \left[2 \left(\frac{0.23\omega T}{2\pi} \right) \right] (\pi) \frac{1}{\omega^2} \left(\frac{h_j^2}{\pi \Omega_j^2 T} \right) = \frac{0.46h_j V^2}{\pi R_W \omega^3 T}.$$

Recognizing that $T = L_j/V$, where L_j is the joint spacing, and that $k = \omega/V$, where k is the roughness wavenumber, we obtain for the "equivalent roughness" spectrum for rail joint impacts

$$S_j(k) = \frac{0.46h_j}{\pi R_W k^3 L_j}. \quad (84)$$

2.2.2 Wheel flats

Just as there is a critical speed for stepdown rail joints, there is also a critical speed for wheel flats. Above that speed, which is given by

$$V_{\text{critical}} = \left[ag \left(1 + \frac{F}{gM_W} \right)^{1/2} \right],$$

where g is the acceleration of gravity, M_W is the wheel mass, and F is the wheel load with the wheel and rail separate. We will not deal here with speeds above the critical; rather, we will concern ourselves with the condition where the wheel and rail remain in contact. Consequently, we will expect this model to be valid only below approximately 25 mph [19]. However, according to Ver, Ventres, and Myles [19] the excitation from wheel flats should level off above the critical speed. Therefore, our model should still be useful.

Figure 41 shows the geometry for the wheel flat impact. The quantity $v_0(t)$ in the figure is analogous to $v_0(t)$ in Sec. 2.2.1 for the rail joint, i.e., it represents the vertical velocity of the rail at the point of contact, if the wheel is rigid and the rail is allowed to move.

The Fourier transform of $v_0(t)$ is given by

$$\tilde{v}_0(\omega) = \frac{l^2}{4\pi R_W} j \frac{1}{\Omega_F} \frac{\sin \Omega_F}{\Omega_F} - 1, \quad (85)$$

where $\Omega_F = \omega l / 2V$. Repetitive impacts occur as the wheel goes around and the flat impacts the rail again and again. For $2N$ impacts of period $T = 2\pi R_W / V$ the Fourier transform becomes

$$\tilde{v}_T(\omega) = \sum_{n=-N}^N \tilde{v}_0(\omega) e^{+j\omega nT} = \frac{1}{2\pi} \int_{-\tau}^{\tau} v_T(t) e^{-j\omega t} dt, \quad (86)$$

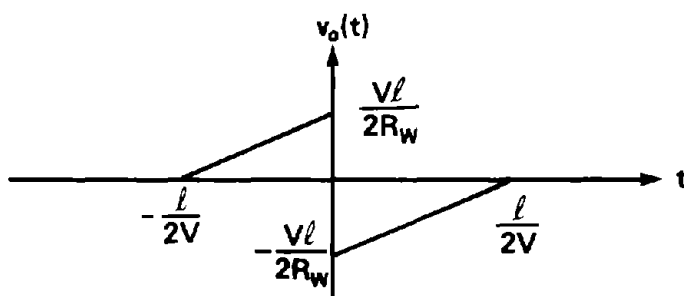
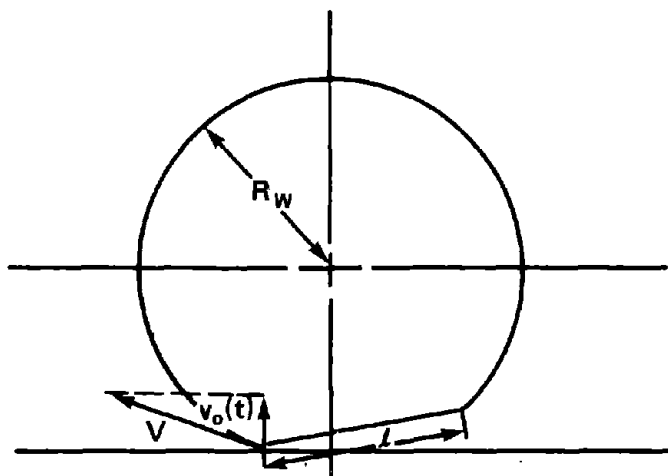


FIG. 41. WHEEL FLAT IMPACT GEOMETRY.

where $\tau = NT$. The power spectrum is defined as [15]

$$\Phi_V(\omega) = E \left\{ \lim_{\tau \rightarrow \infty} \frac{|\tilde{v}_\tau(\omega)|^2}{\tau} \right\}. \quad (87)$$

Substituting Eq. (84) into Eq. (85) and the result into Eq. (86), we obtain

$$\Phi_V(\omega) = \left\{ \left(\frac{\ell^2}{4\pi R_W} \right)^2 \frac{\sin \Omega_F}{\Omega_F^2} - \frac{1}{\Omega_F} \right\}^2 \lim_{N \rightarrow \infty} \frac{1}{NT} \left| \sum_{n=-N}^{n=N} e^{j\omega n T} \right|^2. \quad (88)$$

Taking the indicated limit as in Sec. 2.2.1, we obtain

$$\Phi_V(\omega) = \left(\frac{\ell^2}{4\pi R_W} \right)^2 \frac{4\pi}{T^2} \left\{ \frac{\sin \Omega_F}{\Omega_F^2} - \frac{1}{\Omega_F} \right\}^2 \sum_{n=-\infty}^{\infty} \delta\left(\omega - \frac{2\pi n}{T}\right). \quad (89)$$

The function of Ω_F in the brackets is plotted in Fig. 42. We will be using this result only for speeds up to about 25 mph; consequently, we are interested in Ω_F from about 0.3 to 10. In that region, we will approximate the bracketed function of in Eq. (89) by $\frac{1}{\Omega_F^2}$. That value was arrived at by squaring the function as indicated and integrating all the harmonic terms over one wavelength. The approximation is compared to the actual function in Fig. 42 and is seen to be a reasonable estimate over the range of Ω_F that is of interest here. Equation (89) now simplifies to

$$\Phi_V(\omega) = \left(\frac{\ell^2}{4\pi a} \right)^2 \left(\frac{4\pi}{T^2} \right) \left(\frac{1}{\Omega_F^2} \right) \sum_{n=-\infty}^{\infty} \delta\left(\omega - \frac{2\pi n}{T}\right).$$

Noting that $T = 2\pi R_W/V$; that $\Omega_F = \ell\omega/2V$; that $k = \omega/V$; and that the one-third octave displacement systems $S_f(\omega)$ is related to the power spectrum by

$$S_f(\omega) = 2\pi \left(\frac{1}{\omega^2} \right) \left(\frac{0.23}{2\pi/T} \right) \Phi_V(\omega),$$

we can express the equivalent roughness spectrum for a single wheel flat by

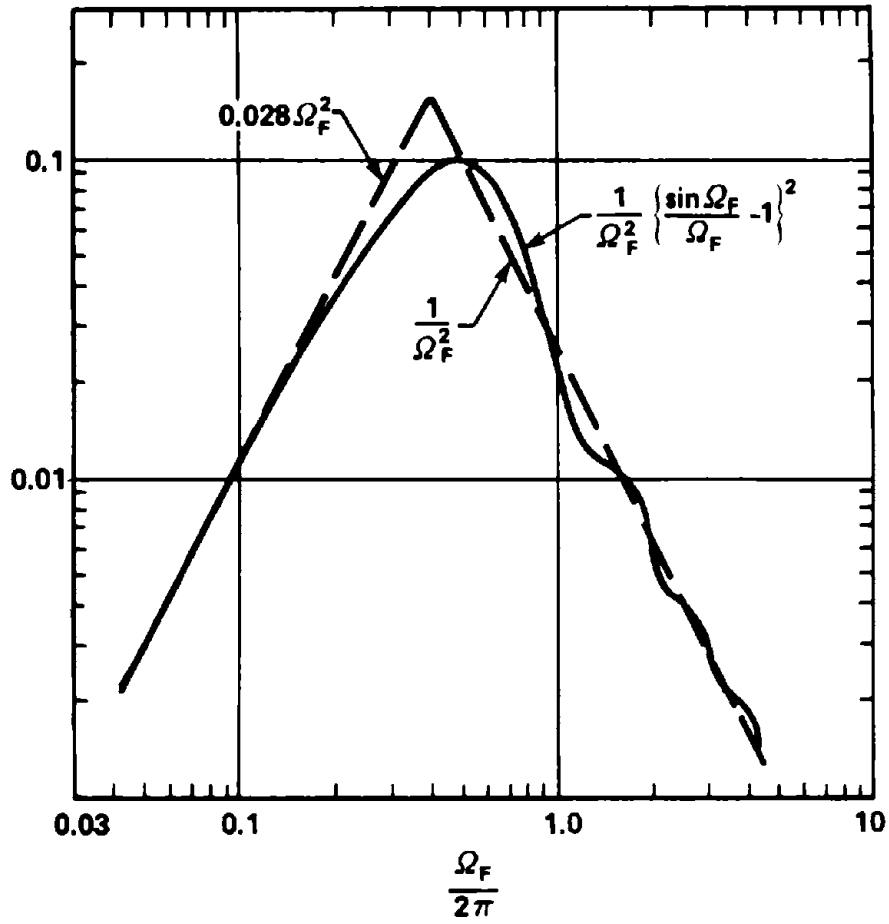


FIG. 42. WHEEL FLAT EQUIVALENT ROUGHNESS SPECTRUM APPROXIMATION.

$$S_f(k) = \frac{0.11\ell^2}{\pi^2 a^3 k^3} \quad (90)$$

In Fig. 43, we have plotted the equivalent roughness predicted by Eqs. (84) and (90). Also shown are roughness data measured on MBTA revenue service wheels and rails [3]. Three lengths of flat spots are shown along with the depth d , which is estimated by

$$d = \frac{\ell^2}{8R_W} \quad (91)$$

All of the estimates look a little low. This apparent small influence of wheel flats occurs, we believe, because these roughness estimates are good only for predicting the average noise during a passby. Consequently, the impacts from the wheel flats tend to be averaged out in comparison with the steady noise from the wheel and rail roughness.

To give ourselves some confidence in the equivalent roughness expressions, we note from the results of Sec. 2.2.1 that

$$\pi \int_{-\infty}^{\infty} \Phi_v(\omega) d\omega = \lim_{\tau \rightarrow \infty} \frac{1}{2\tau} \int_{-\tau}^{\tau} v_0^2(t) dt \quad (92)$$

The right-hand side of the equation can be readily integrated for the rail joint and wheel flat cases by substituting the expressions for $v_0(t)$ in Figs. 39 and 41, respectively, into Eq. (92). Carrying out that integration, we obtain

$$\lim_{\tau \rightarrow \infty} \frac{1}{2\tau} \int_{-\tau}^{\tau} v_0^2(t) dt = \begin{cases} 0.93 \frac{v^2 h}{L} \left(\frac{h}{R_W}\right)^{1/2} & \text{rail joint} & (93a) \\ 3.29 \frac{v^2 \ell^3}{8\pi^3 R_W^3} & \text{wheel flat} & (93b) \end{cases}$$

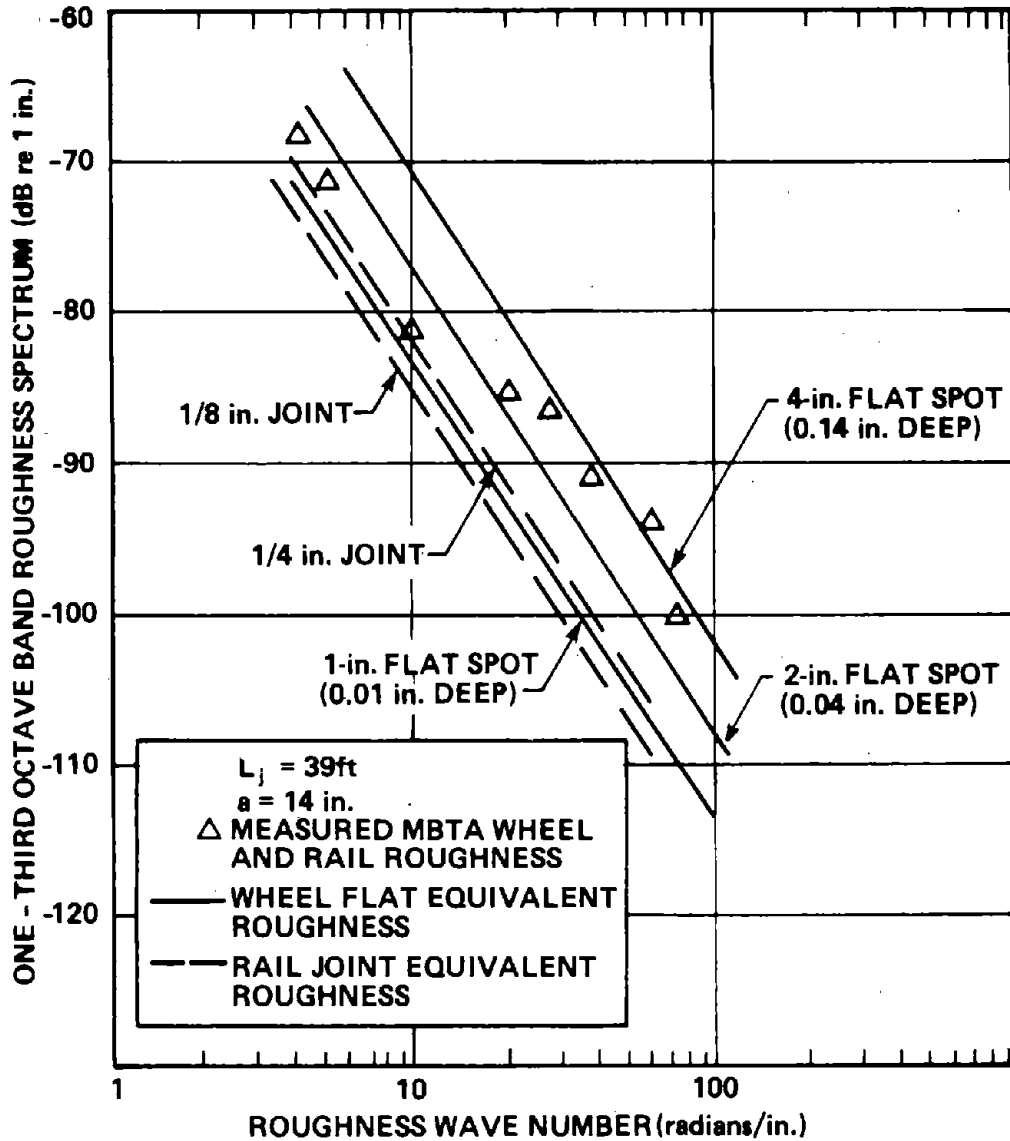


FIG. 43. COMPARISON OF EQUIVALENT ROUGHNESS AND MEASURED DATA.

To carry out the integration in frequency, we approximate $\phi_V(\omega)$ as follows:

$$\phi_V(\omega) = \left\{ \begin{array}{ll} \frac{h^2}{2\pi^2 T} & -0.15 < \frac{\Omega_j}{2\pi} < 0.15 \\ \frac{h}{2\pi^2 T} \frac{1}{\Omega_j^2} & \left| \frac{\Omega_j}{2\pi} \right| > 0.15 \end{array} \right\} \text{rail joint,} \quad (94)$$

where $T = L_j/V$, and

$$\phi_V(\omega) = \left\{ \begin{array}{ll} \left(\frac{\ell^2}{4\pi R_W} \right)^2 \frac{2}{T_F} & 0.028\Omega_F^2 > 0.4 < \frac{\Omega_F}{2\pi} < 0.4 \\ \left(\frac{\ell^2}{4\pi R_W} \right)^2 \frac{2}{T_F} \frac{1}{\Omega_F^2} & \left| \frac{\Omega_F}{2\pi} \right| > 0.4 \end{array} \right\} \text{wheel flat,} \quad (95)$$

where $T_F = 2\pi R_W/V$.

Both equations are simply the result of fitting curves to the functions in Figs. 40 and 42, respectively. The curves are shown as a dashed line in the figures.

Carrying out the integration, we obtain

$$\pi \int_{-\infty}^{\infty} \phi_V(\omega) d\omega = \left\{ \begin{array}{ll} 0.91 \frac{V^2 h}{L} \left(\frac{h}{R_W} \right)^{1/2} & \text{rail joint} \quad (96a) \\ 3.46 \frac{V^2 \ell^3}{8\pi^3 R_W^3} & \text{wheel flat} \quad (96b) \end{array} \right.$$

Equations (96a) and (93a) and Eqs. (96b) and (93b) agree quite closely, confirming our simplified models.

To further check the models, we note that if the rail joint height is related to the wheel flat length by

$$h = \frac{\ell}{8R_W} , \quad (97)$$

and the time interval between rail joints is the same as between wheel flats,

$$2R_W = L . \quad (98)$$

There is exactly twice the mean square velocity in the wheel flat history as in the rail joint time history. This can be seen by substituting for h in the rail joint velocity equation, using Eq. (97) and noting that the duration in time history of the sawtooth is identical to that for the wheel flat, except that the wheel flat velocity has two sawteeth and the rail joint just one.

Substituting Eqs. (98) and (97) into (96a), we obtain

$$\phi_v(\omega) = 1.60 \frac{V^2 \ell^3}{8\pi^3 R_W^3} ,$$

which is very close to 1/2 of Eq. (96b), as expected.

2.2.3 Summary

Equations (84) and (90) express the equivalent roughness displacement spectrum for step-up rail joints and wheel flats (at speeds below about 25 mph).

Rail Joint Equivalent Roughness

$$S_j(k) = \frac{0.46 h_j}{\pi R_W k^3 L_j} \quad (99)$$

Wheel Flat Equivalent Roughness

$$S_f(k) = \frac{0.11 \ell^2 n_w}{\pi^2 R_W^2 k^3} , \quad (100)$$

where we have multiplied the wheel flat equivalent roughness by n_w , the average number of flats per wheel. Equations (99) and (100) can then be substituted into Eq. (12), where they are added to $S_{WR}(k)$ and $S_{RR}(k)$, the wheel and rail roughness spectra. Equations (73) and (74) and the information in Table 4 can then be used to calculate the average noise from the wheel and rail discontinuities.

2.3 Squeal Noise

2.3.1 Theoretical background

It is now generally accepted that squeal noise is caused by the lateral sliding of the wheels of the transit car truck across the rail head as the car rounds a curve of short radius. The severity of the lateral sliding is usually described by a parameter called the lateral creep, ξ , which is defined as the ratio of the lateral velocity of the wheel at the wheel/rail interface, v , divided by the rolling velocity V , i.e.,

$$\xi = \frac{v}{V} \quad . \quad (101)$$

Figure 1 shows the geometry of the truck and curve that causes this lateral creep. To first order, the lateral creep will lie in the following range:

$$\bar{\xi} \approx \frac{W}{2R} \longrightarrow \frac{W}{R} \quad , \quad (102)$$

where W is the truck wheel base and R is the curve radius. In practice, however, the curve entry dynamics of the truck, the amount of gauge relief in the curve, and the axial vibration of the wheels all contribute to determining the actual lateral creep that occurs. Rudd [22], using measurements of adhesion in the presence of longitudinal creep in locomotive wheels, assumed that

the lateral friction coefficient μ could be approximated by an equation of the following form:

$$\mu = \mu_0 \frac{\xi}{\xi_0} e^{(1-\xi/\xi_0)} \quad (103)$$

For large values of lateral creep, i.e., $\xi > \xi_0$, the friction coefficient decreases, as illustrated in Fig. 44. Rudd showed that this decrease of friction coefficient with increasing lateral creep, $d\mu/d\xi < 0$, is responsible for generating squeal noise. The friction forces at the wheel/rail interface feed energy into the wheel and act like negative damping, in which the loss factor is given by

$$\eta_s = \frac{P}{M_i \omega_i V} \frac{d\mu}{d\xi} \quad (104)$$

where P is the wheel load, M_i is the modal mass of the wheel, ω_i is the modal resonant frequency, and V is the train velocity.

Consequently, the lateral vibration of the wheel will continue to grow at its resonant frequencies until nonlinear effects begin to reduce η_s with increasing wheel vibration amplitude. Rudd [22] has calculated the stable wheel vibration amplitude for squeal to be given by

$$v_s = V \xi_0 \left[\left(\frac{8}{3} \right) \frac{\bar{\xi} - \xi_0}{3\xi_0 - \bar{\xi}} \right]^{1/2} \quad (105)$$

where v_s is the axial wheel velocity at the wheel/rail point of contact, $\bar{\xi}$ is the steady-state lateral creep defined by Eq. (102), and the total creep is then given by

$$\xi = \bar{\xi} + (v_s/V) \sin \omega_i t \quad ,$$

as illustrated in Fig. 44.

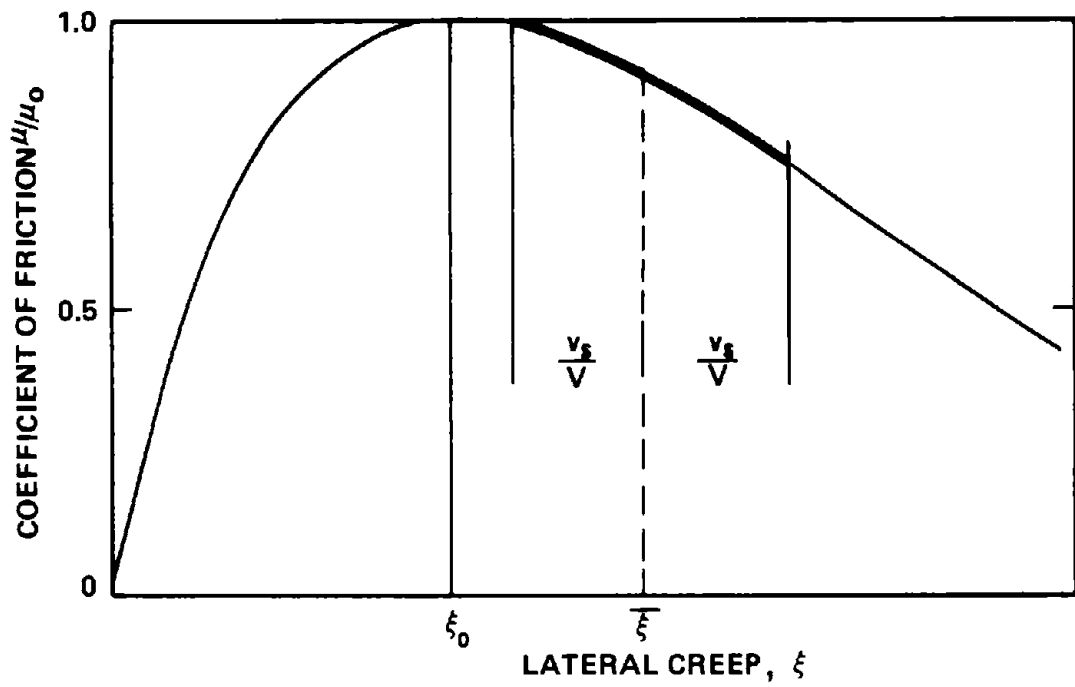


FIG. 44. FRICTION COEFFICIENT VS LATERAL CREEP.

Rudd's theoretical work has led to two major conclusions. First, sufficient internal damping in the wheel will prevent squeal. It is simply necessary that the wheel internal damping exceed the maximum negative damping generated by the friction forces at the wheel/rail interface, i.e.,

$$\eta_{INT} > \frac{P}{M_i \omega_i V} \left| \frac{d\mu}{d\xi} \right| . \quad (106)$$

Rudd's second conclusion concerns the maximum curve radius at which squeal will occur. Squeal occurs only when $d\mu/d\xi$ is negative, and $d\mu/d\xi$ will be positive until $\bar{\xi} > \xi_0$ in Eq. (103). The quantity ξ_0 depends on the dependence of μ on the lateral creep and is a property of the wheel and rail material and interface conditions. The steady-state creep $\bar{\xi}$ depends on truck and curve geometry and the detailed yaw response of the truck during curve entry. Rudd has estimated $\bar{\xi}$ as

$$\bar{\xi} \approx 0.7 \frac{W}{R} , \quad (107)$$

which is approximately the midpoint of the range in Eq. (102). Consequently, the maximum curve radius for squeal becomes

$$R_{MAX} = \frac{\xi_0}{0.7W} . \quad (108)$$

However, when Rudd carried out his theoretical work, no data were available to determine how correct Eq. (103) was in modeling the friction coefficient dependence on creep or what the proper values of μ_0 and ξ_0 should be. Consequently, one of the first tasks in this program was the measurement of the lateral friction vs creep.

2.3.2 Lateral friction vs creep

To measure the lateral friction force vs lateral creep, we made arrangements with Raychem Corp. of Menlo Park, California to use a roller rig built by that corporation for its nitinol wheel development program. The nitinol wheel was also examined under this program and will be described later. A photograph of the roller rig is shown in Fig. 45, and the rig is shown schematically in Fig. 46. It consists of a small, 7 1/2-in.-diameter test wheel that is run against a larger, 30-in.-diameter railroad wheel that simulates the rail. The rail wheel has had its flange machined to simulate the head of a rail. The radius of curvature is 5.83 in.

Figure 46 shows the test wheel mounted in bearings on a table that, through an arrangement of Thompson ball bushings, is free to move in three orthogonal directions. The table is constrained from motion by three force balances that measure the forces on the test wheel in those directions. Loading between the test wheel and rail wheel is accomplished by means of an air piston that forces the table in the direction of the rail wheel.

In order to introduce lateral creep, we placed shims under one of the two bearings supporting the test wheel, to rotate the plane of the test wheel relative to the rail wheel. By so doing, we introduced a relative velocity between the two wheels in the axial direction. That velocity divided by the rolling velocity is the lateral creep, as defined in Eq. (101).

Since the lateral velocity is given by the rolling velocity times the tangent of the angle, θ , between the planes of the two wheels, the creep is also given approximately by that angle in radians, i.e.,

$$\xi \approx \theta \quad . \quad (109)$$

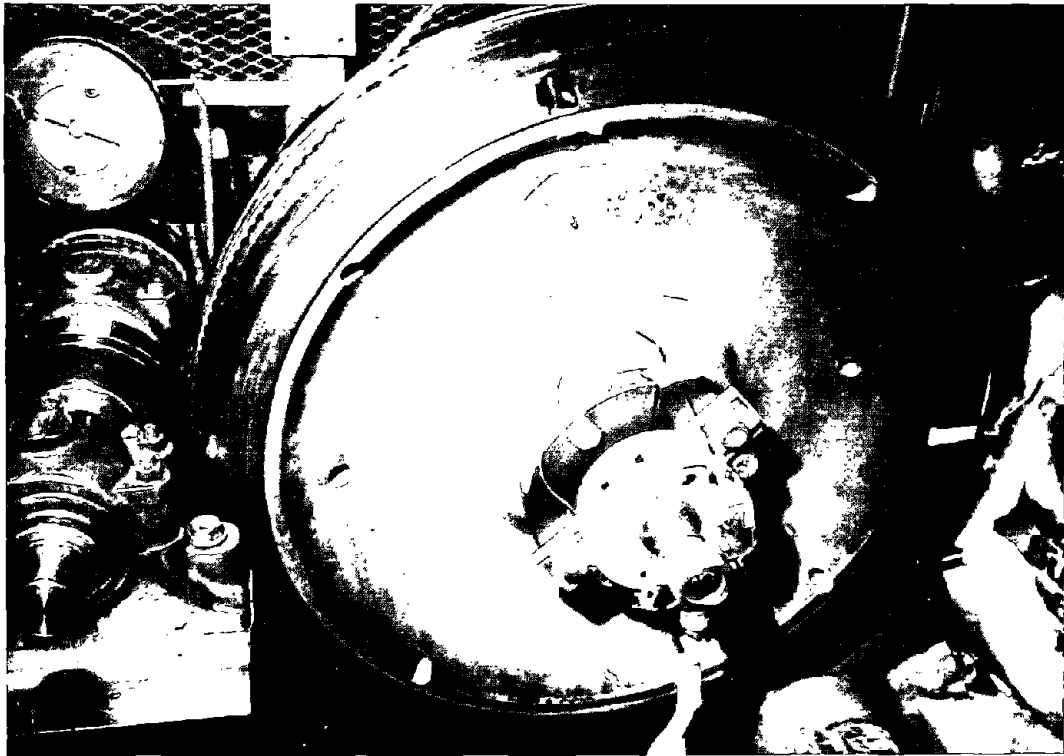


FIG. 45. THE RAYCHEM ROLLER RIG.

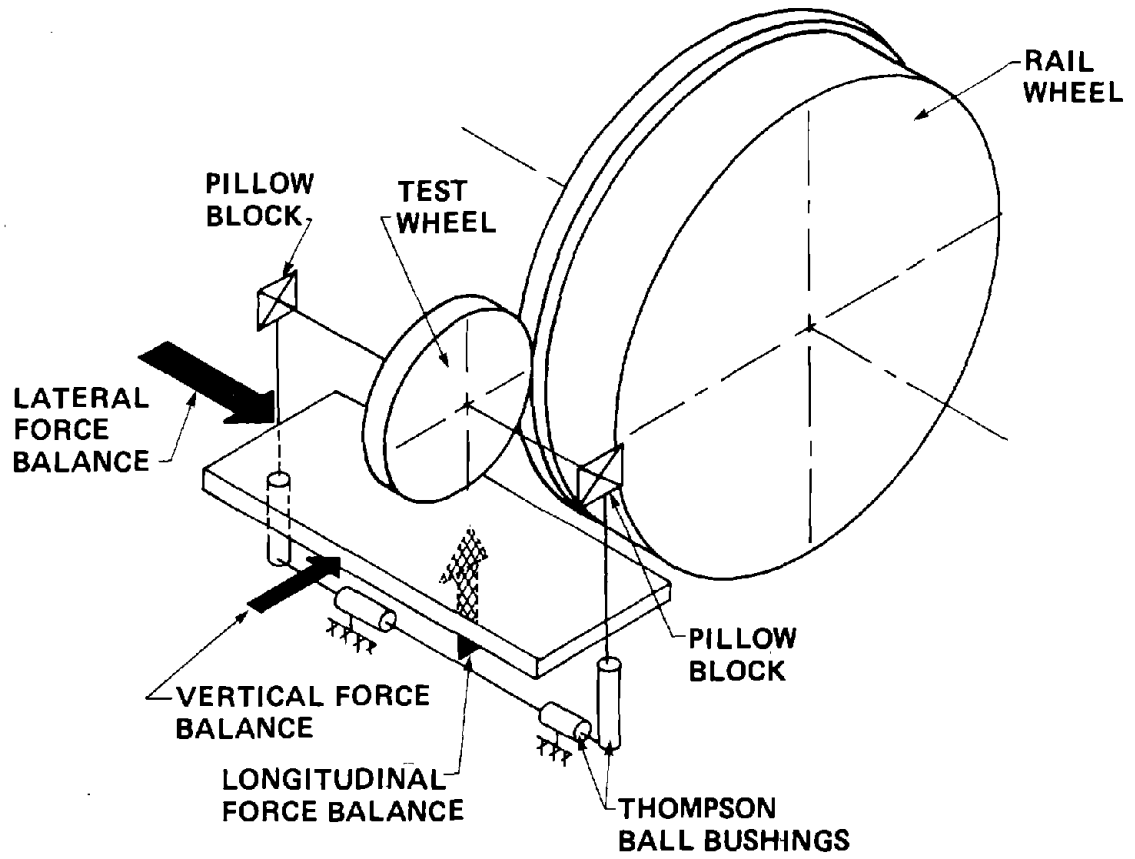


FIG. 46. SCHEMATIC OF THE RAYCHEM ROLLER RIG.

In order to scale the tests, we operated under the principle that the stresses in the contact area should be the same in model and full scale, that the ratio of any dimension of the contact area in the model to the comparable dimension in full scale should be the same as the ratio of all other comparable dimensions, and that the frequencies should scale. In mathematical terms, if α is the scale factor, we can write

$$\begin{aligned}\sigma_{\text{model}} &= \sigma_{\text{full scale}} \\ b_{\text{model}} &= b_{\text{full scale}} \\ \omega_{\text{model}} &= \frac{1}{\alpha} \omega_{\text{full scale}}\end{aligned}\tag{110}$$

where σ is stress, b is a dimension of the contact area, and ω is frequency.

The implications of Eq. (110) are that

$$\begin{aligned}V_{\text{model}} &= V_{\text{full scale}} \\ P_{\text{model}} &= \alpha^2 P_{\text{full scale}}\end{aligned}\tag{111}$$

where V is the rolling velocity and P the wheel load. Taking 30 in. as the diameter of a full-scale wheel, we find that the 7 1/2-in. model wheel implies a scale factor of $\frac{1}{4}$ one-fourth. Consequently, to scale a 10,000-lb wheel load, we used 625 lb. However, the radius of curvature of the simulated rail head at 5.83 in. corresponds in the full scale to 23.3 in., which is larger than the 10-in. or 14-in. radius typical of most rail heads.

Figure 47 shows the measured data for three runs at two speeds and compares them with Rudd's original model, Eq. (103). In the figure, the coefficient of friction is defined as the

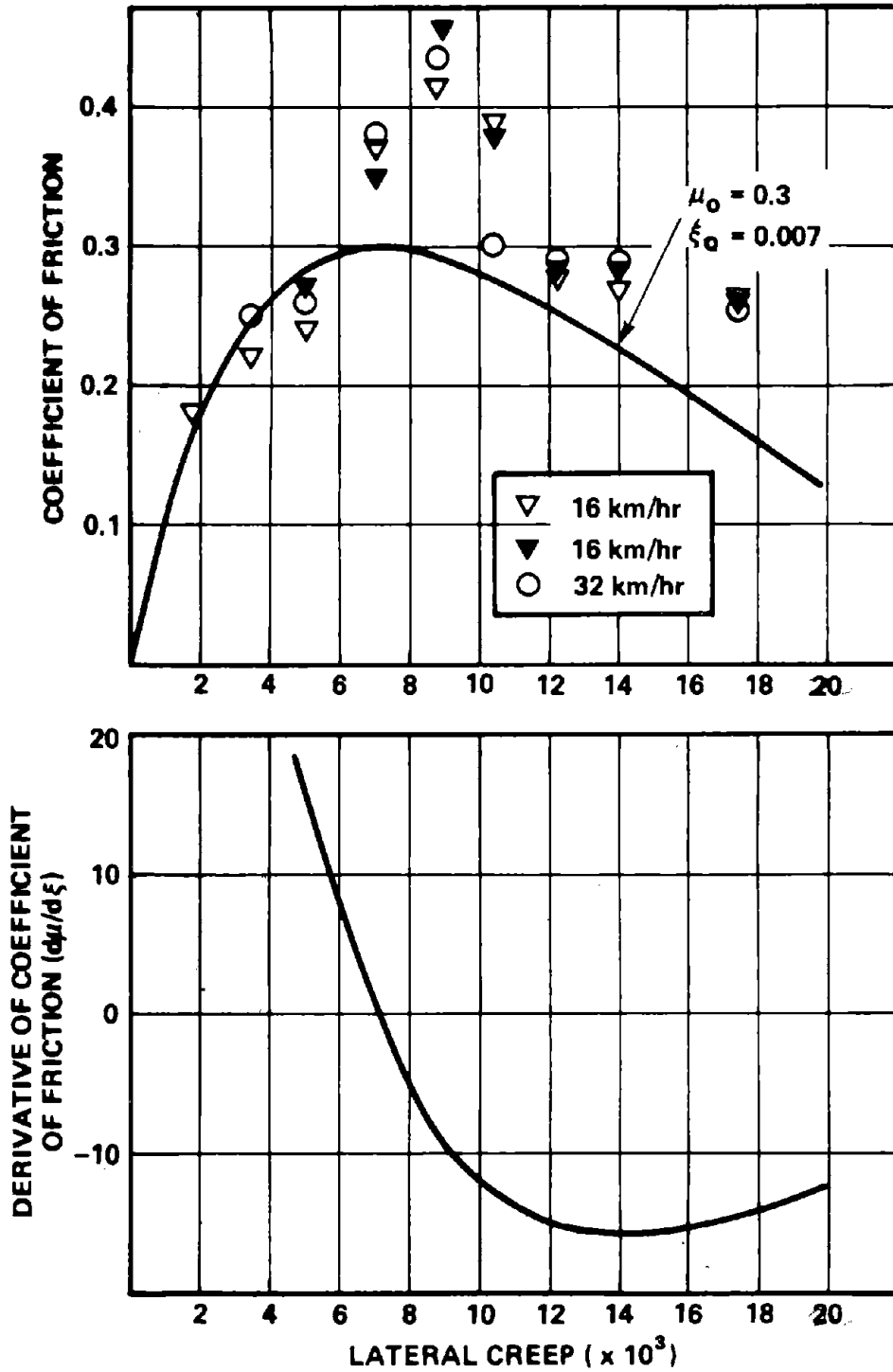


FIG. 47. LATERAL CREEP DATA COMPARED TO RUDD'S ORIGINAL MODEL.

force measured by the lateral force balance in Fig. 46 divided by the wheel load (625 lb). Considering the paucity of data when Rudd made his original estimate, one has to be impressed with how closely the data agree with his axis model. A somewhat improved agreement is obtained if the parameters μ_0 and ξ_0 are shifted slightly, as shown in Fig. 48.

During the tests, the lateral force would slowly increase and then slightly decrease before a steady value was reached. Consequently, the roller rig was run at each angle for approximately four minutes before a steady-state measurement of the lateral force was recorded. In addition, we had to wipe lightly (with a rag) on both wheels to remove excess material that was ground off at the wheel/rail contact area. We noticed that if we did not remove the ground-off particles, the coefficient of friction would increase to very high values as the particle went through the wheel/rail interface.

2.3.3 Maximum curve radius for squeal

One of the important findings of Rudd's original work was that squeal should not occur for curves with radii greater than approximately 100 times the truck wheelbase. This value comes from substituting Rudd's original estimate for $\xi_0 = 0.007$ into Eq. (108). This conclusion is based on an estimate of the value of lateral creep above which friction forces begin to decrease, as well as on a guess at what the truck attitude is during curving. Neither value is known with any certainty. Consequently, Rudd's conclusion can at best be viewed as a rough estimate.

To examine the influence of the ratio of curve radius to truck wheelbase on the occurrence of squeal, we carried out a detailed field survey on the MBTA in Boston, Massachusetts. We rode MBTA's Blue, Orange, and Red Lines from beginning to end and noted the occurrence of squeal and the presence or absence of a

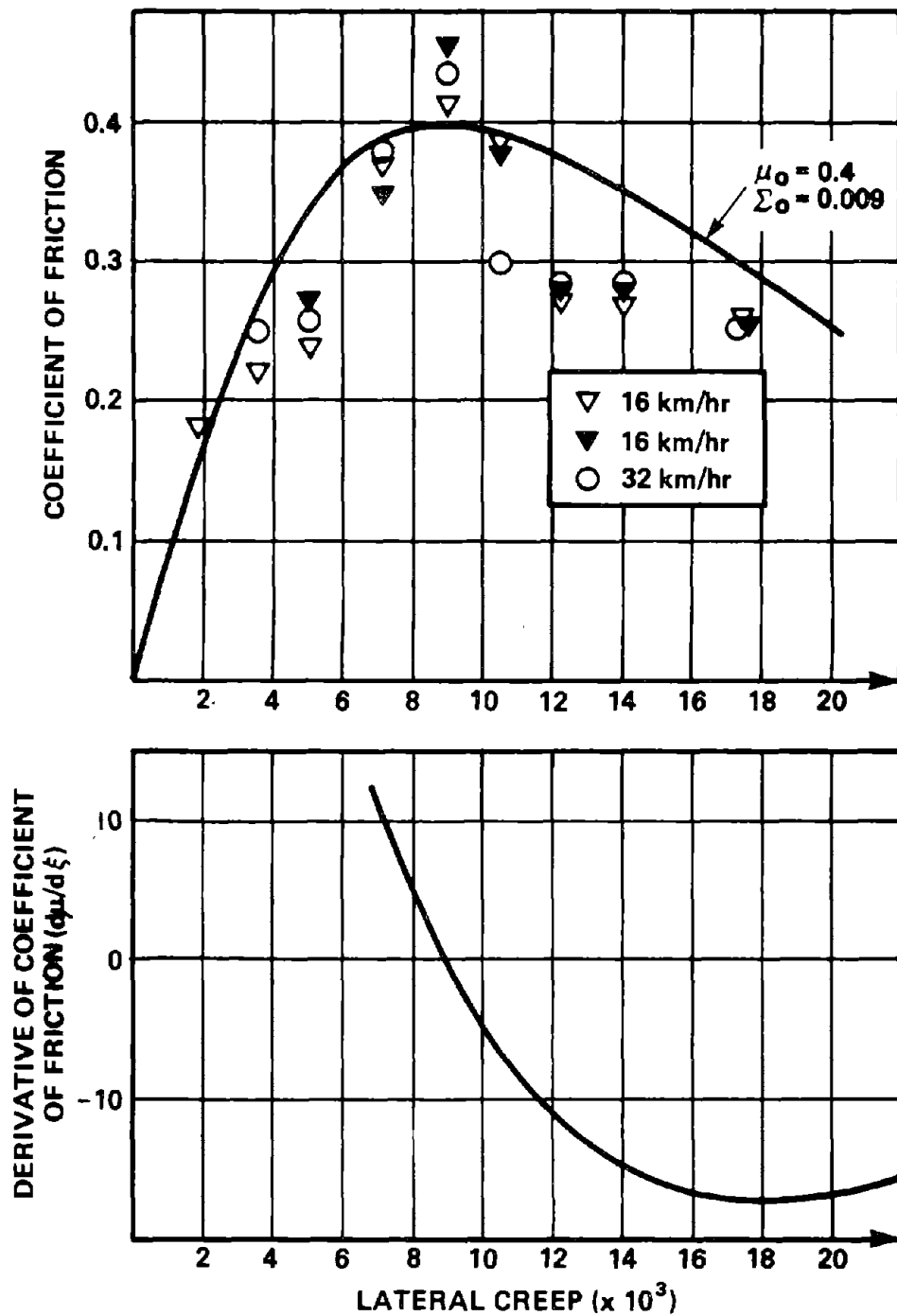


FIG. 48. REVISED CREEP MODEL.

restraining rail in each curve that we encountered. To aid in identifying curves, we made a map of the three rapid transit lines that included the radius, direction, and length of each curve. With this map, it was easy to identify each curve, even when passing through at high speed. MBTA alignment maps were the source of the radii data used. When transition curves were present, we took the tightest occurring radius.

The cars were ridden during off-peak hours, July 25, 1980, from 9:30 a.m. to 2:30 p.m. All trains had two cars with no resilient or damped wheels. The truck wheelbase was 6 ft, 10 in. for all vehicles.

High relative humidity may also influence the occurrence of squeal. Consequently, we looked for a day with low humidity. The weather data for July 25, 1980 were:

8:30 a.m. Temperature 72°F, 23°C
Relative humidity 51%

3:00 p.m. Temperature 84°F, 29°C
Relative humidity 40%

These low values of relative humidity should have had little influence on the occurrence of squeal noise.

There are two types of track on the three lines of the MBTA. The old rails are bolted, and the new rails, two sections of the Orange and Red Lines - are welded; on these newly constructed lines, we found no restraining rails, and the radii of all curves exceeded 1400 ft.

<u>Old Lines:</u>	(Bolted rail, tight curves, restraining rail)
Blue Line:	Wonderland - Bowdoin
Orange Line:	Haymarket - Forest Hills
Red Line:	Harvard/Brattle - Ashmont

New Lines: (Welded rail, large curves, no restraining rail)
Orange Line: Oak Grove - Haymarket
Red Line: Andrew - Quincy Center

On the old alignments, we found 133 curves equipped with restraining rail with radii less than 2500 ft. Ten curves with radii under 2500 ft had no restraining rail. Most of them were very short.

At the two newly constructed sections, 17 curves could be found with radii under 2500 ft. The tightest curve was 1432 ft.

Because of the limited number of curves without restraining rail, we restricted our analysis to only those curves with restraining rails.

In order to display the data, we grouped the curves by the ratio of curve radius to truck wheelbase. Figure 49 shows the curves classified into four groups with 28 to 36 curves per group and presents the percentage of curves that squealed in each. To show somewhat more detail, we have separated the group with the lowest ratio of curve radius to truck wheelbase into two parts. We have also distinguished between those curves where the squeal was virtually continuous as the car passed through the curve and those where the squeal was intermittent.

The data show that for curves with a ratio of radius to truck wheelbase of 50 or less, squeal is virtually guaranteed, whereas if the ratio exceeds about 200, squeal is very unlikely. Table 5 presents the data for curves with the ratio less than or greater than 100. The table shows that Rudd's original conclusion was fairly sound, and the ratio of 100 is a reasonable dividing line, at least for a simple rule of thumb.

SQUEAL OCCURENCE ON THE MBTA

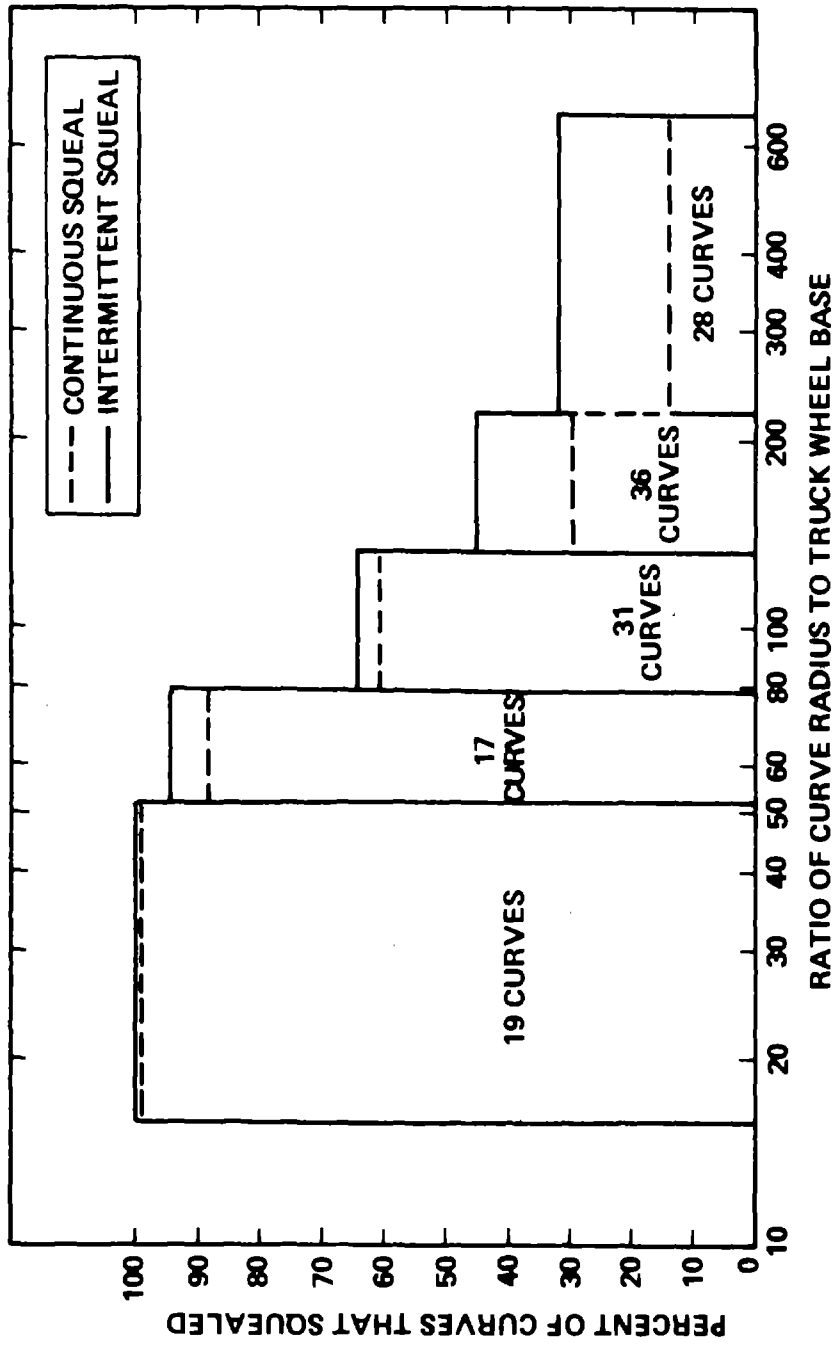


FIG. 49. FIELD SURVEY OF CURVES ON THE MBTA WHERE SQUEAL NOISE OCCURS.

TABLE 5. THE LIKELIHOOD OF SQUEAL FOR CURVES ON THE MBTA WITH A RATIO OF CURVE RADIUS TO TRUCK WHEELBASE GREATER OR LESS THAN 100.

Ratio R/W	No. of Curves	No. that Squealed	Percentage
15.5 - 50	49	43	88%
50 - 666	82	25	30%

2.3.4 Wheel damping to suppress squeal

If one uses Rudd's estimate of the damping required to eliminate squeal, the predicted wheel loss factors become impossibly large. Figure 50 presents predictions of the required loss factor based on Eq. (106). The calculation was made assuming that the velocity through the curve was great enough to produce a lateral acceleration of 0.1 g; the modal mass of the wheel was taken as 1/2 of the tread mass; the truck wheelbase was taken as 6 ft 10 in.; and three frequencies were chosen that are typical of the first three natural frequencies of axial vibration of a railroad wheel. Recent data on the loss factors of specialized railroad wheels that are known to suppress squeal indicate that much less wheel damping will eliminate squeal [23]. Table 6 presents data from Saurenman [23] on the loss factor of four wheels that substantially suppress or eliminate squeal. The Bochum wheel and Acoustaflex virtually eliminate squeal [23]. The SAB and ring-damped wheels, while reducing squeal noise, do not eliminate it. The data in Table 6 suggest that a wheel loss factor of approximately 0.01 would be sufficient to eliminate squeal. That factor is at least an order of magnitude less than predicted by Rudd's theory.

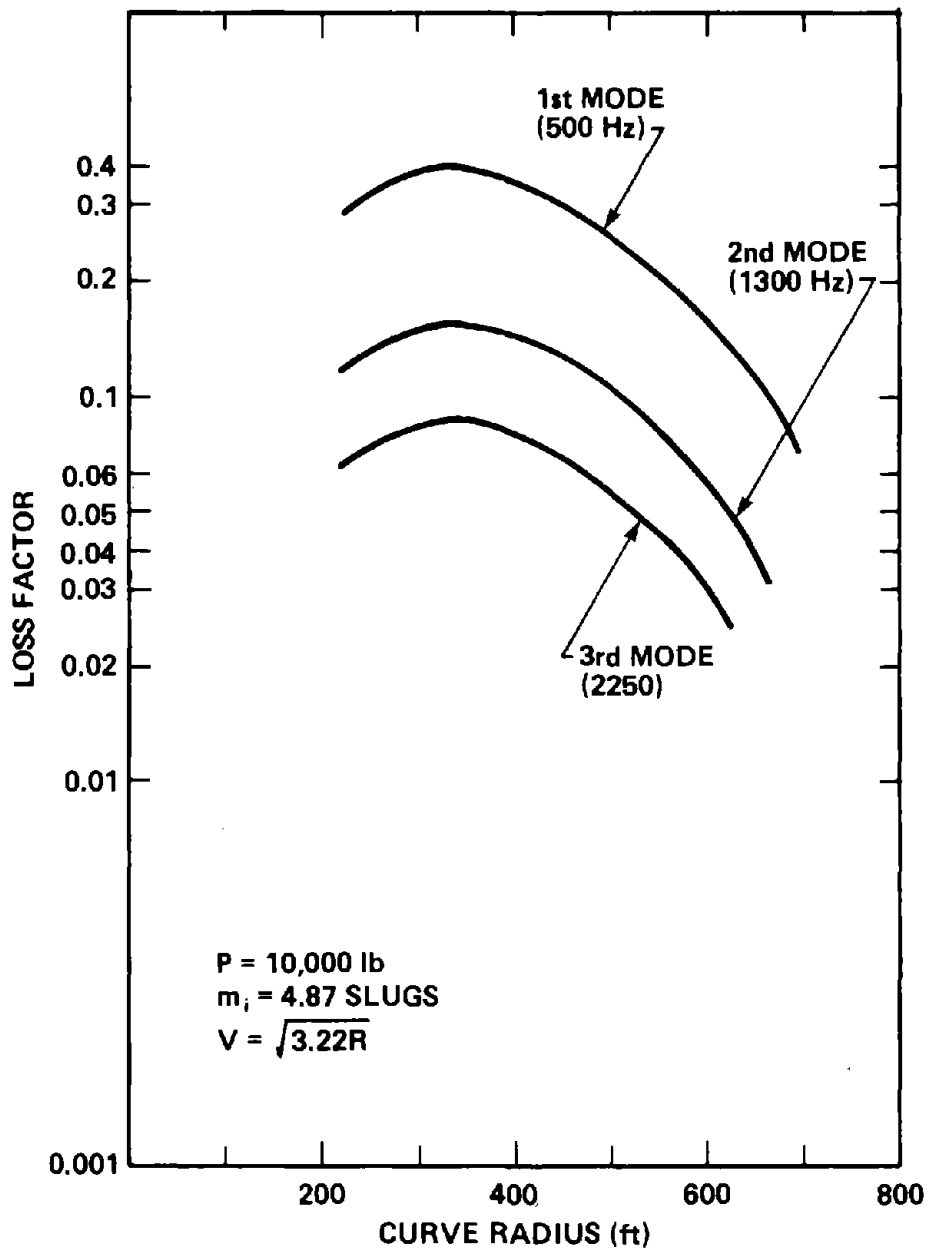


FIG. 50. THEORETICAL LOSS FACTOR REQUIRED TO SUPPRESS SQUEAL.

TABLE 6. TYPICAL LOSS FACTORS OF DAMPED WHEELS [23].

Wheel Type	Frequency		
	500	1000	2000
Bochum	0.012	0.014	0.0072
SAB	0.0026	0.0016	0.00087
Acoustaflex	0.012	0.0051	0.0034
Ring-Damped Wheel	0.00085	0.00042	0.0019

It is not clear why the theory does so well in predicting the maximum curve radius at which squeal will occur but misses by so much in predicting the damping. The problem may be due in part to Rudd's very simple model of the wheel as a spring mass system. In principle, such a model is reasonable for a single mode, but the identification of the appropriate parameter values - such as the effective modal mass - is not simple. It would be possible in principle to use Rudd's model of the lateral creep forces in conjunction with the more complicated model of the axial wheel dynamics developed here in Sec. 2.1.1. Although the resources of this project do not permit us to do so, such an effort would probably improve the predictions of the required damping. In the meantime, existing data on the loss factor of wheels that eliminate squeal will suffice to define the required damping.

3. FIELD VALIDATION OF THE ANALYSIS

3.1 Test Site

To ensure that the analytical model described in the previous section would be a useful tool for the design and evaluation of wheel/rail noise control treatments, we validated the model predictions with measurements in the field. The site selected for the field measurements was the Transit Test Track (TTT) at the Transportation Test Center (TTC) in Pueblo, Colorado. Figure 51 shows the track, which is a 9.1-mile oval consisting of six sections, each composed of different combinations of rail weight, tie type, and tie spacing.

Three test sections on the track were selected. Test Section No. 1 contained tangent track composed of 119-lb/yd continuously welded rail on concrete ties spaced 30 in. apart in ballast. The ties were Gerwick (Santa Fe-Pomeroy) RT-7 M-38 ties that had been modified to support the 150-lb/yd power rail. A cross section of the track and a photograph of the site are shown in Fig. 52. The microphones were located near station 38, where the grade was 0.68%.

Test Section No. 2 contained tangent track composed of 100-lb/yd bolted rail on 7-in. x 9-in. x 8-ft 6-in. hardwood ties spaced 24 in. apart in ballast. A cross section of the track and a photograph of the site are shown in Fig. 53. The microphones were located near station 33, where the track was level. The rail here and at Test Section No. 1 exceeds FRA class 6 and IRT class 4 standards.

The third test section was the screech loop, a 150-ft radius curve on which a number of noise tests were run. When acquiring rail vibration data at this site, we encountered what appeared to be severe electromagnetic interference. In addition, many of the

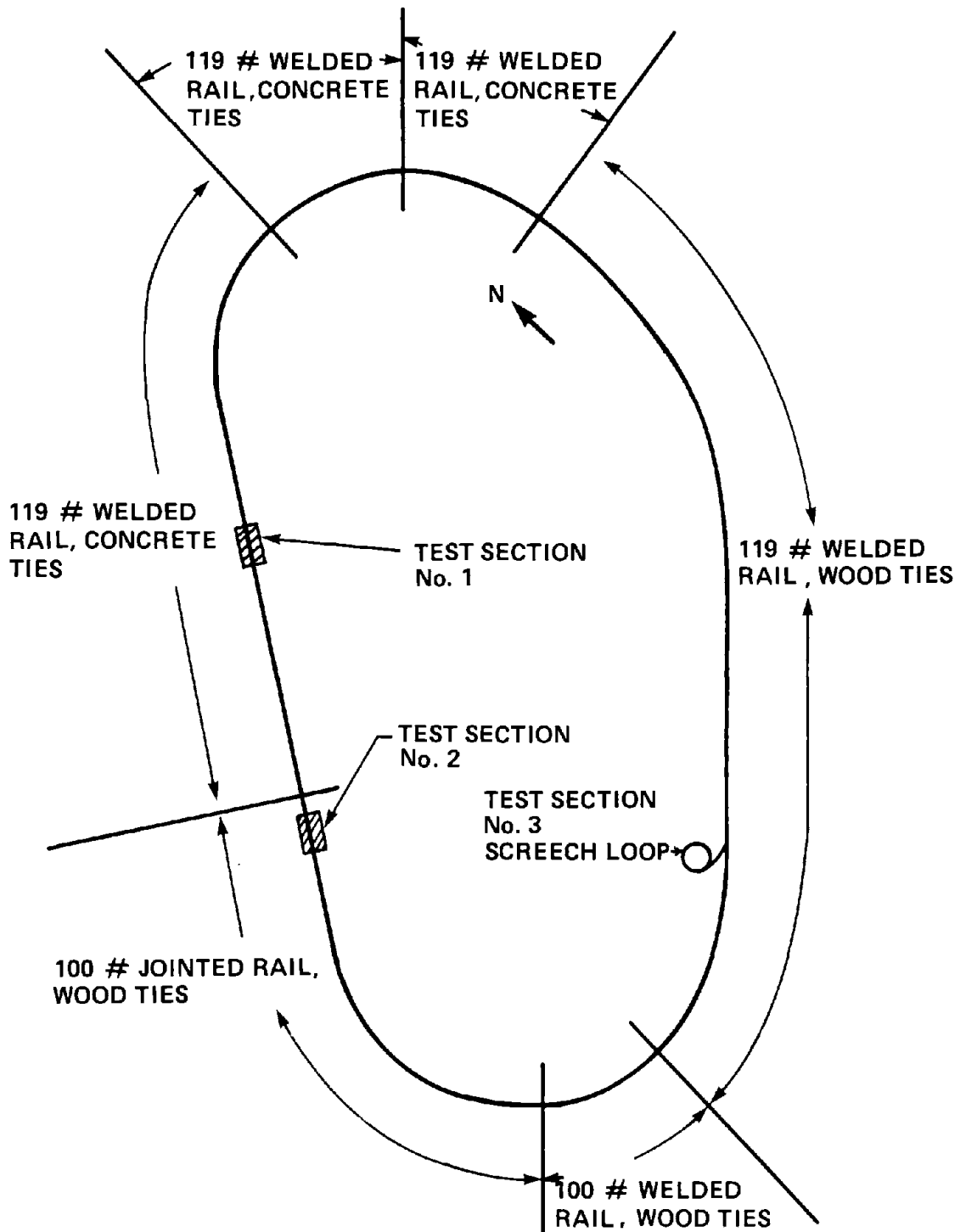


FIG. 51. THE TRANSIT TEST TRACK AT THE TRANSPORTATION TEST CENTER.

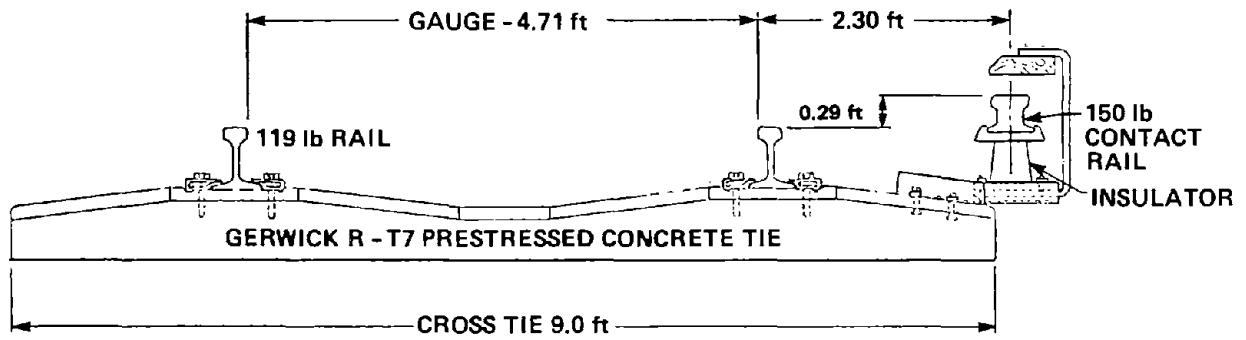


FIG. 52. TEST SITE NO. 1 - WELDED RAIL ON CONCRETE TIES.

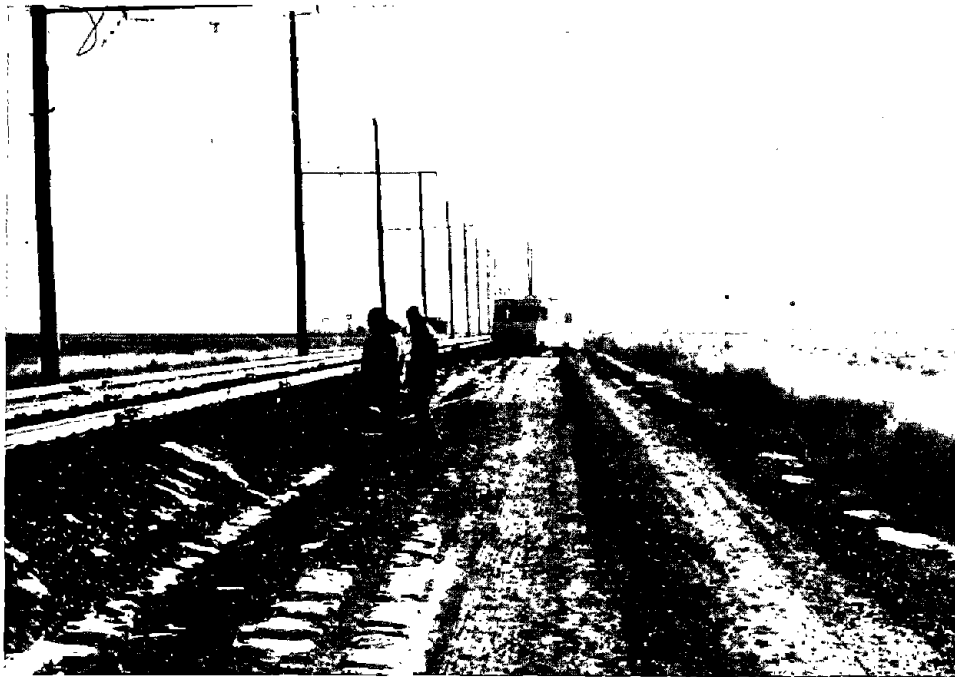
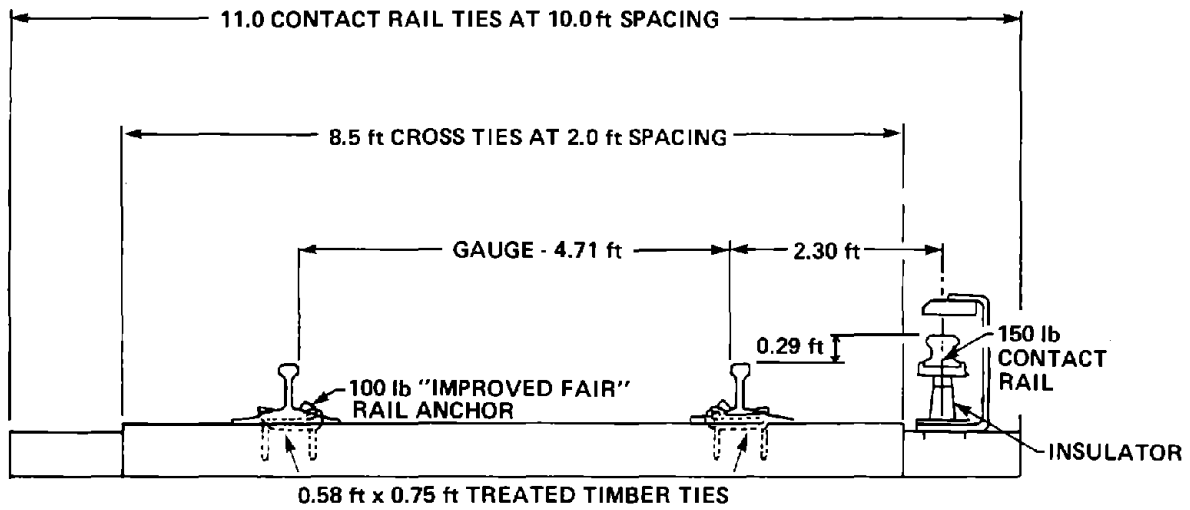


FIG. 53. TEST SITE NO. 2 - BOLTED RAIL ON WOODEN TIES.

wheel vibration data were so high that the accelerometers appeared to be overloaded. Consequently, we have not analyzed these data to any extent and will discuss them no further here.

The transit car used for all of the tests was the State of the Art Car (SOAC) shown in Fig. 54. The SOAC program was initiated by the U.S. Department of Transportation to demonstrate the current state of the art in rail rapid transit vehicle technology. The Boeing Vertol Co. was the prime contractor. St. Louis Car was responsible for the stainless steel body, General Steel Industries built the trucks, and Garrett AiResearch developed the propulsion and braking systems.

Two cars were built and first tested at the Transportation Test Center (then the High Speed Ground Transportation Test Center) in September of 1972. Each car weighed approximately 90,000 lb. The principal dimensions are shown in Fig. 55. The trucks were inboard bearing four-wheel trucks, using 30-in.-diameter solid steel wheels,* and weighing approximately 14,500 lb. The suspension consisted of a rubber chevron primary and air spring secondary. The propulsion system consisted of four 175-hp (continuous) DC electric motors with separately excited fields, each coupled to an axle through a double reduction helical gear set with a ratio of 4.83 to 1. The traction motors and chopper control units were forced-air-cooled by two 6.3-kW vane axial fans. These fans were quite noisy and had to be shut down during all noise tests as the vehicle coasted through the test sections, so that they would not contaminate the wheel/rail noise. Another source of contaminating noise was a 125-kW motor alternator used to power auxiliary equipment and to excite the traction motor field windings. This unit had an integral fan for cooling that

*The original configuration used Acoustaflex resilient wheels. For our tests, the trucks were equipped with ring-damped solid steel wheels from which the rings were removed.

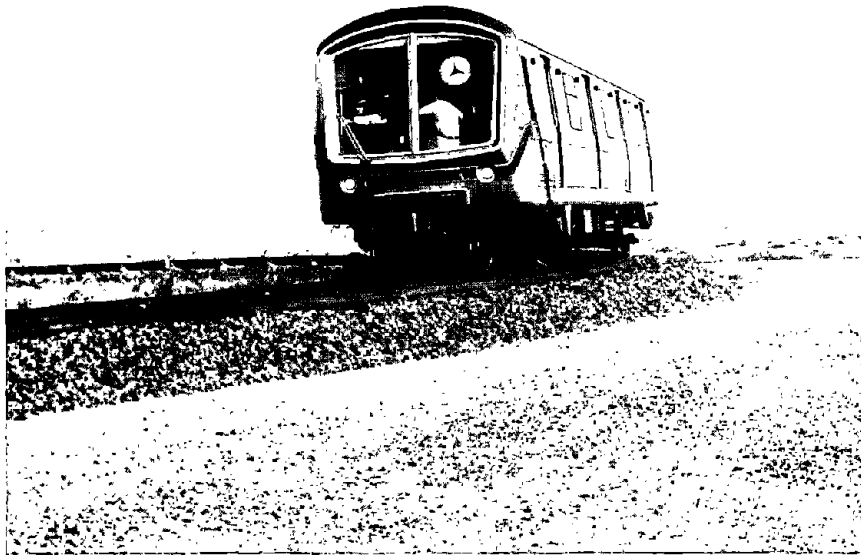


FIG. 54. THE SOAC ON THE SCREECH LOOP AT TTC (PUEBLO) (TTC Photos).

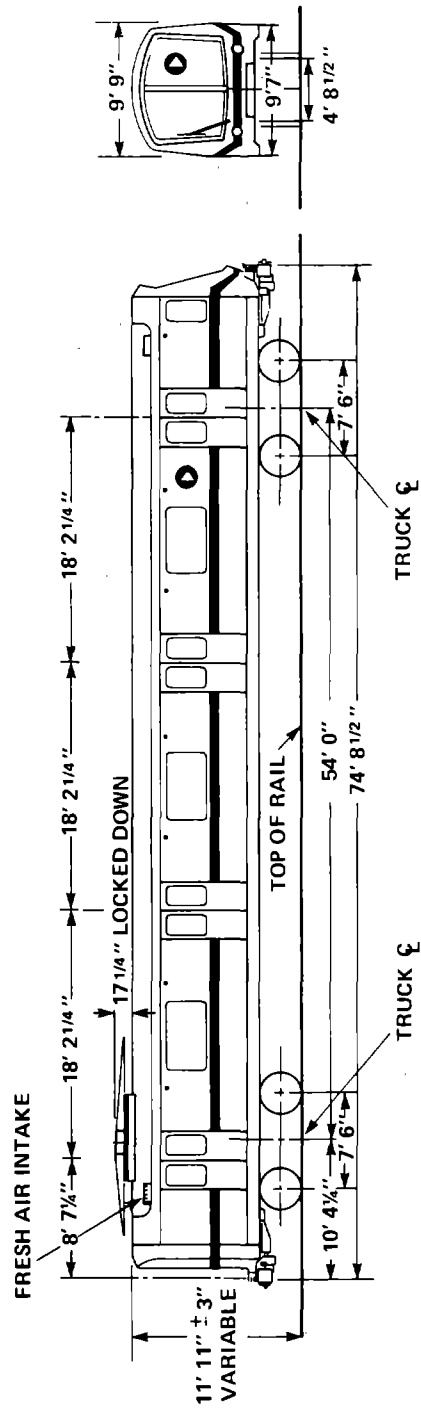


FIG. 55. PRINCIPAL DIMENSIONS OF THE SOAC.

proved to be quite noisy. It, too, had to be shut down during all test runs. All wheels on the SOAC were trued on the Hegen-scheidt wheel truing machine at the Test Center just before testing began. This provided uniform and reproducible roughness on the running surfaces of all four wheels.

3.2 Instrumentation

3.2.1 On-board instruments

On board the SOAC, instrumentation was installed to record

- Wheel acceleration
- Exterior noise
- Speed
- Time.

A speaker system was also installed outside the vehicle at wheel height. The system was designed to provide a broadband calibrated source of sound, so that changes in the propagation of sound from the vehicle to the wayside microphones caused by atmospheric or weather changes could be monitored and corrected when the data were compared to analytical predictions. However, during the course of the wayside noise field measurements, the weather and ground conditions were so uniform that no propagation corrections were necessary.

Figure 56 presents a block diagram of the on-board instrumentation. Three accelerometers were mounted on one wheel of the car, as shown in Fig. 57, to measure axial tread and web vibration and radial tread vibration. The signals from the accelerometers were fed from the rotating wheel to the on-board

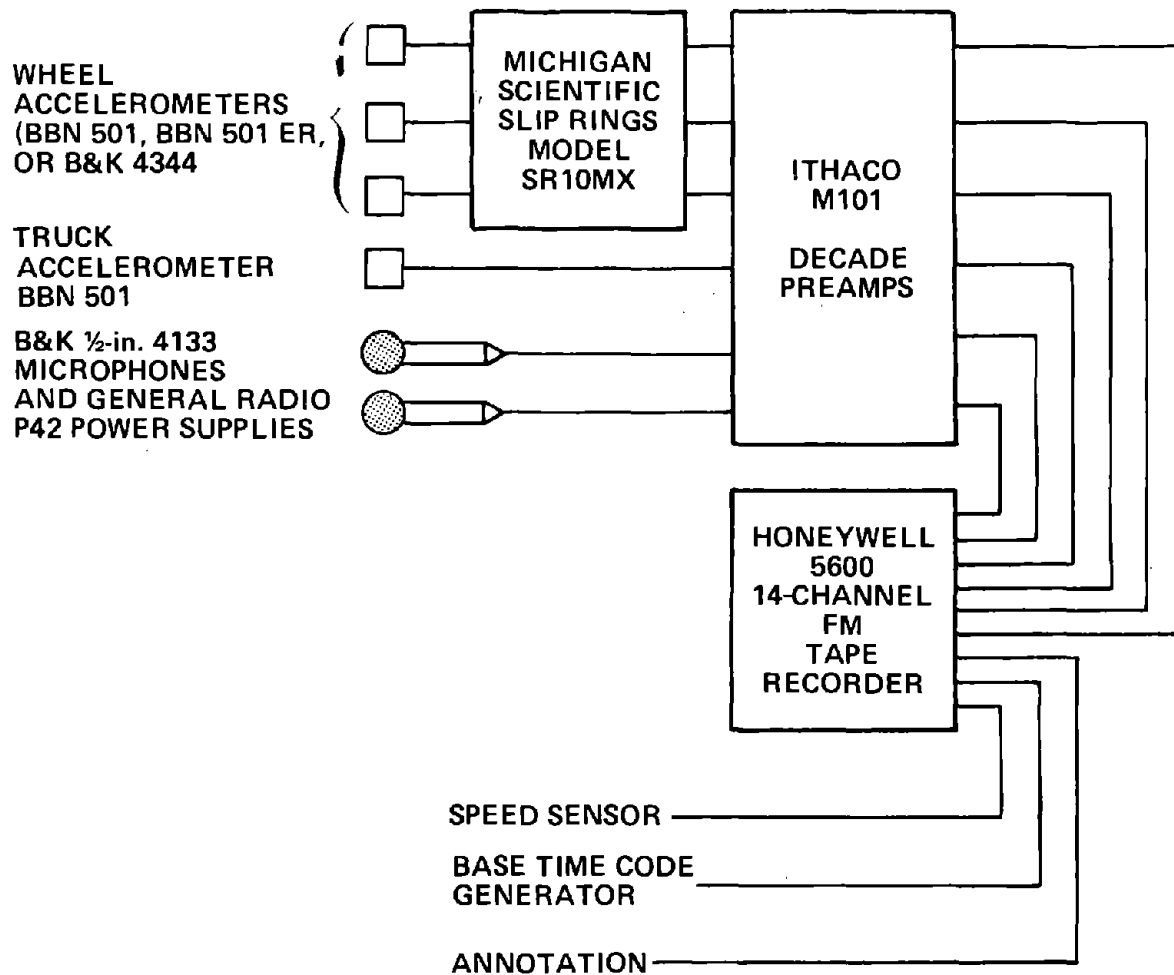


FIG. 56. ON-BOARD INSTRUMENTATION SYSTEM.

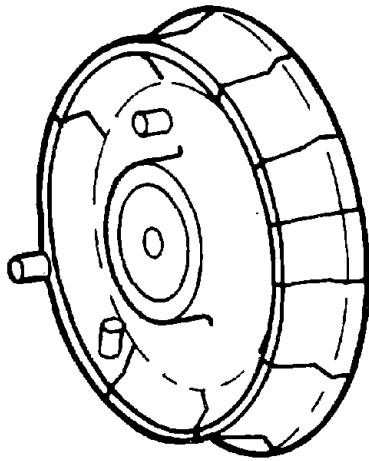


FIG. 57. WHEEL ACCELEROMETER LOCATIONS.

preamplifying and recording systems by means of a slip ring assembly shown mounted on the wheel, in Fig. 58.* The right rear wheel of the rear truck was instrumented for most tests, although a limited amount of data were taken with the right rear wheel of the forward truck instrumented.

Three different accelerometers were used on the wheel at each location. The BBN 501 and 501ER are piezoelectric accelerometers with an internal FET preamplifier. They are identical except that the 501ER has very low sensitivity for dealing with very high-vibration environments. Because accelerometers with internal preamplifiers tend to saturate and provide erroneous data when exposed to high-level transient vibration, we also used a piezoelectric accelerometer with no internal preamplifier, the B & K 4344.

A fourth accelerometer, mounted on the truck frame, was used to determine whether sound radiation from that source could be significant. Truck frame vibration levels were generally 30 to 40 dB below wheel tread vibration levels, and consequently are not discussed further.

For a few runs, microphones were mounted on the car body opposite the truck center at a height equal to the center of the wheel, as shown in Fig. 59. Two microphones were installed, one opposite each truck on the right-hand side. A number of runs were made with this arrangement, during which we recorded both sound and wheel vibration.

Train speed was obtained from two sources: an on-board speedometer with a digital readout in the motorman's cab and a pulse generator provided by the Test Center. The latter is shown in Fig. 60. The wheel is spring-loaded against the rail to

*The speaker system described above can be seen at the left in the top photograph.

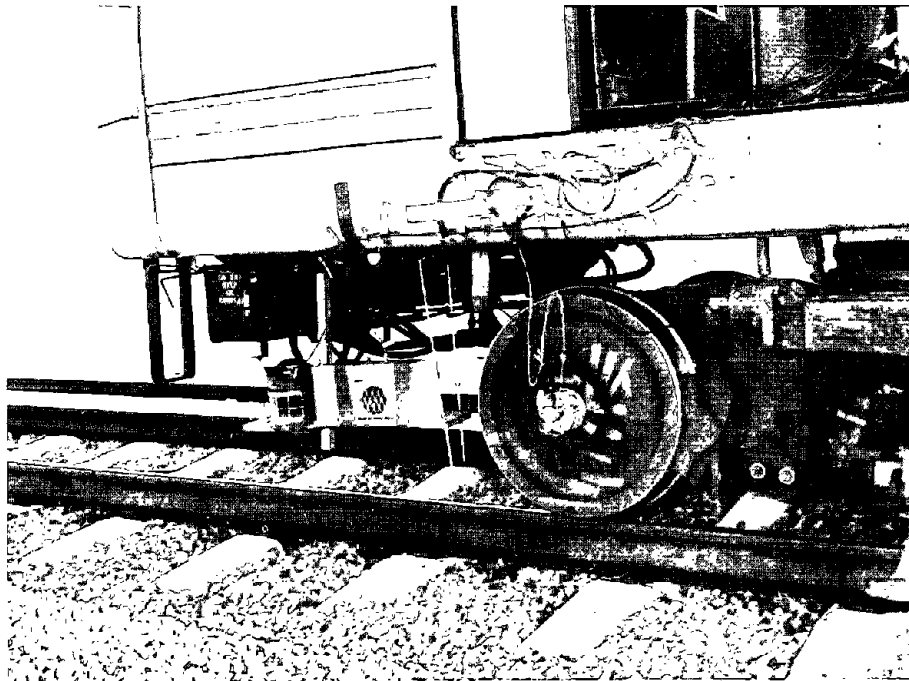


FIG. 58. SLIP RING ASSEMBLY USED IN THE WHEEL VIBRATION MEASUREMENTS (TTC PHOTOS).



FIG. 59. CAR-MOUNTED MICROPHONE.

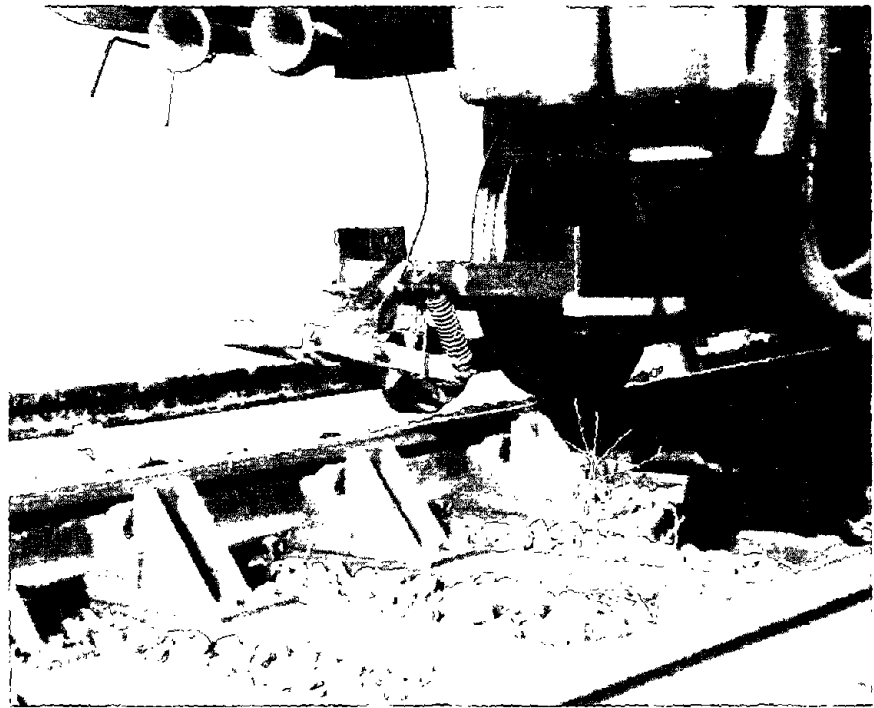


FIG. 60. THE SPEED AND POSITION SENSOR PROVIDED BY THE TEST CENTER (TTC PHOTO).

ensure nonslip operation; it generates 2048 pulses per revolution. The pulses can then be recorded on a tape recorder and later used to determine both position and speed of the train.

In case we later needed to synchronize on-board and wayside tape recorders, the Test Center provided us with two radio receivers for receiving a time code broadcast by the Center. The output of these receivers (an IRIG time code, the same as produced by standard time code generators commonly used in instrumentation work) was recorded on one channel of each tape recorder. The on-board tape recorder, a 14-channel FM recorder (Honeywell Model 5600) set for intermediate band recording at 30 ips (DC-10kHz), was provided by the Test Center.

3.2.2 Wayside instrumentation

The wayside instrumentation at the two tangent track test sites was installed to record

- Rail and tie acceleration
- Wayside noise.

A photocell was also set up to detect the passage of the car wheels past the line of microphones. A low-powered laser beam was directed across the rails at the photocell, so that the passage of each wheel would break the beam and cause a pulse from the photocell that could be recorded. This system proved to be unreliable. Vibration generated during the passage of the SOAC tended to move the laser so that it was no longer properly aimed at the photocell and had to be constantly readjusted.

A block diagram of the wayside instrumentation system is shown in Fig. 61. The tape recorder and preamplifiers were mounted in an instrumentation van, shown in Fig. 62, that was provided by the Test Center.

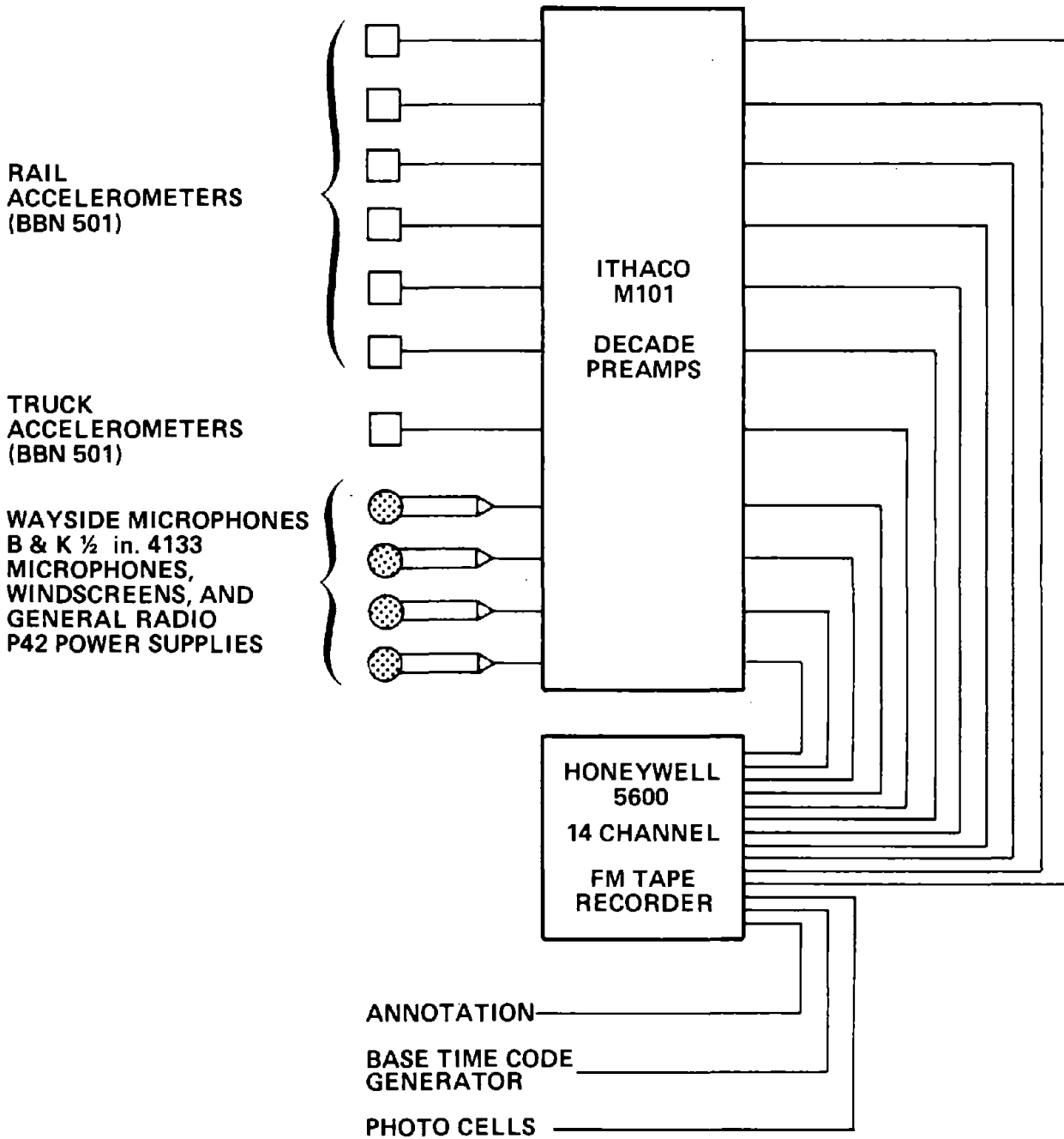


FIG. 61. WAYSIDE INSTRUMENTATION.



FIG. 62. THE WAYSIDE INSTRUMENTATION VAN.

Rail acceleration was measured using six accelerometers, as shown in Fig. 63. A seventh accelerometer was placed in the center of an adjacent tie to measure vertical vibration. Wayside noise in the welded rail test site was measured using four microphones, placed as shown in Fig. 64. The placement was the same at the jointed rail test site.

As with the on-board data acquisition systems, the tape recorder was provided by the Test Center and set for intermediate band recording at 30 ips.

In the course of recording the passby data, a problem was encountered with the rail vibration measurements. Bursts of noise were recorded in all rail accelerometer channels. These bursts overloaded the accelerometers and occasionally destroyed any usable data. Figure 65 illustrates the random occurrence of these bursts. The vertical acceleration at the rail foot during the passby of the SOAC on jointed rail at 60 mph is shown in Fig. 65a. There, two noise bursts occurred just as the train passed over the accelerometers, destroying any usable data. In Fig. 65b, we see two distinct noise bursts occurring well after the SOAC passed over the accelerometers. For this run, we were able easily to extract usable data. It is interesting to note that in the next run (Fig. 65c), under identical conditions, no noise bursts occurred. The problem was most severe on the screech loop where no usable rail vibration data were obtained and on the jointed rail test section, where only limited rail vibration data were usable.

The source of the problem remains a mystery. The noise bursts occurred whether the car was under power or totally dead (third rail deenergized and all car electronics shut down) and no matter what combination of accelerometer instrumentation was used. It also made little difference whether the accelerometers

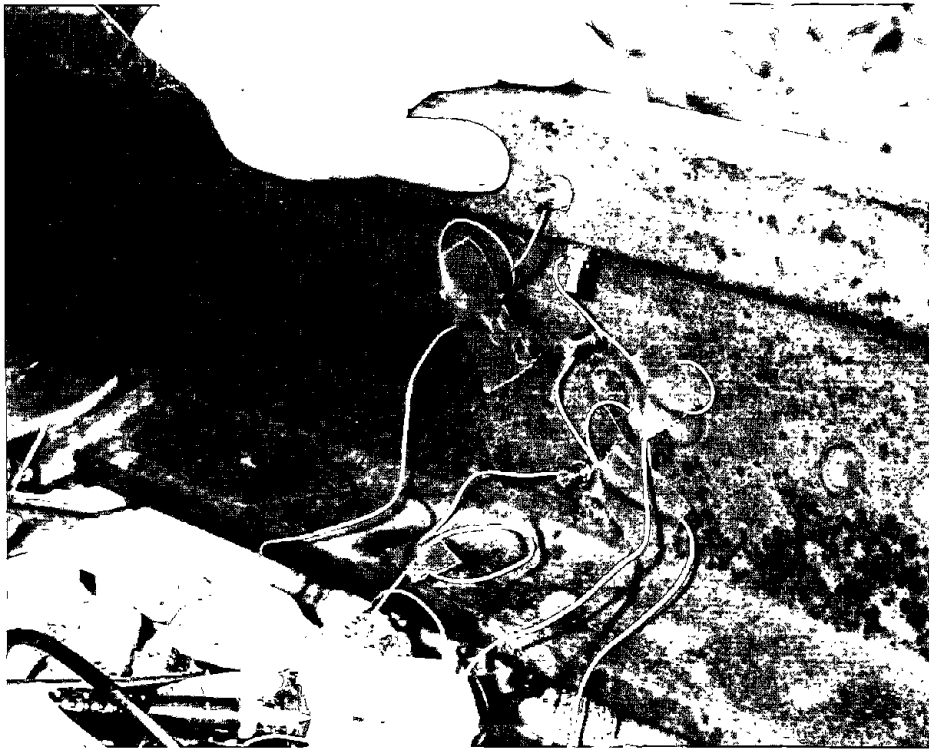
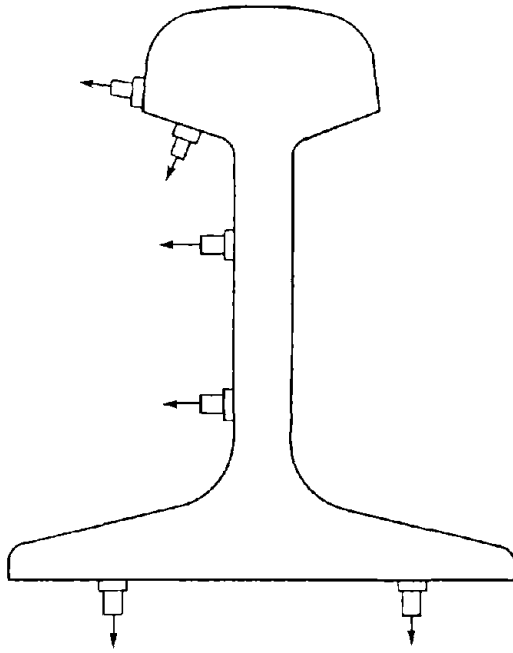


FIG. 63. RAIL ACCELEROMETER LOCATIONS (TTC PHOTO).

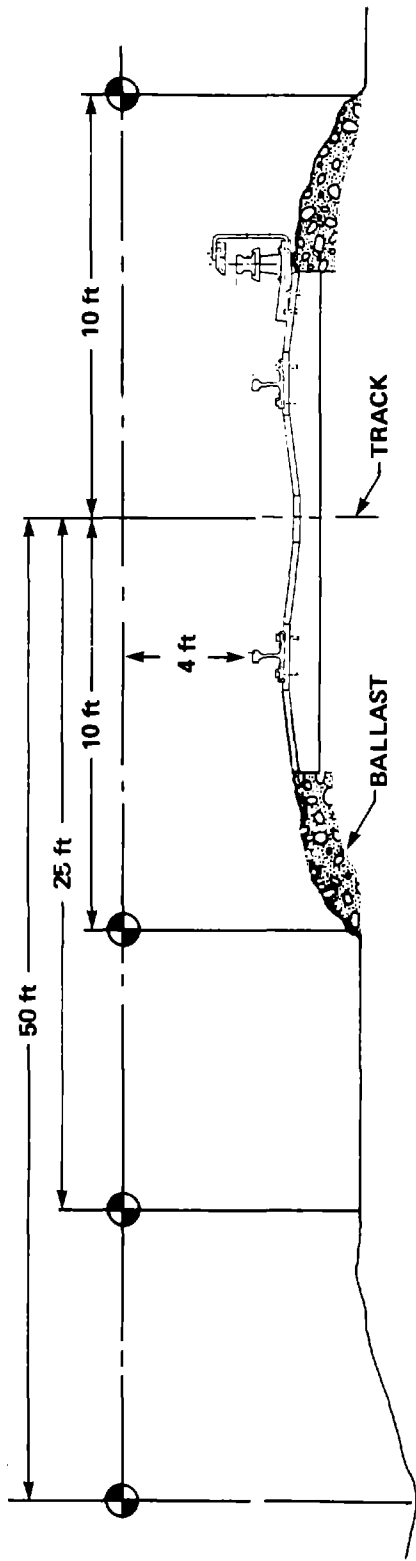


FIG. 64. WAYSIDE MICROPHONE LOCATIONS AT TEST SITE NO. 1.

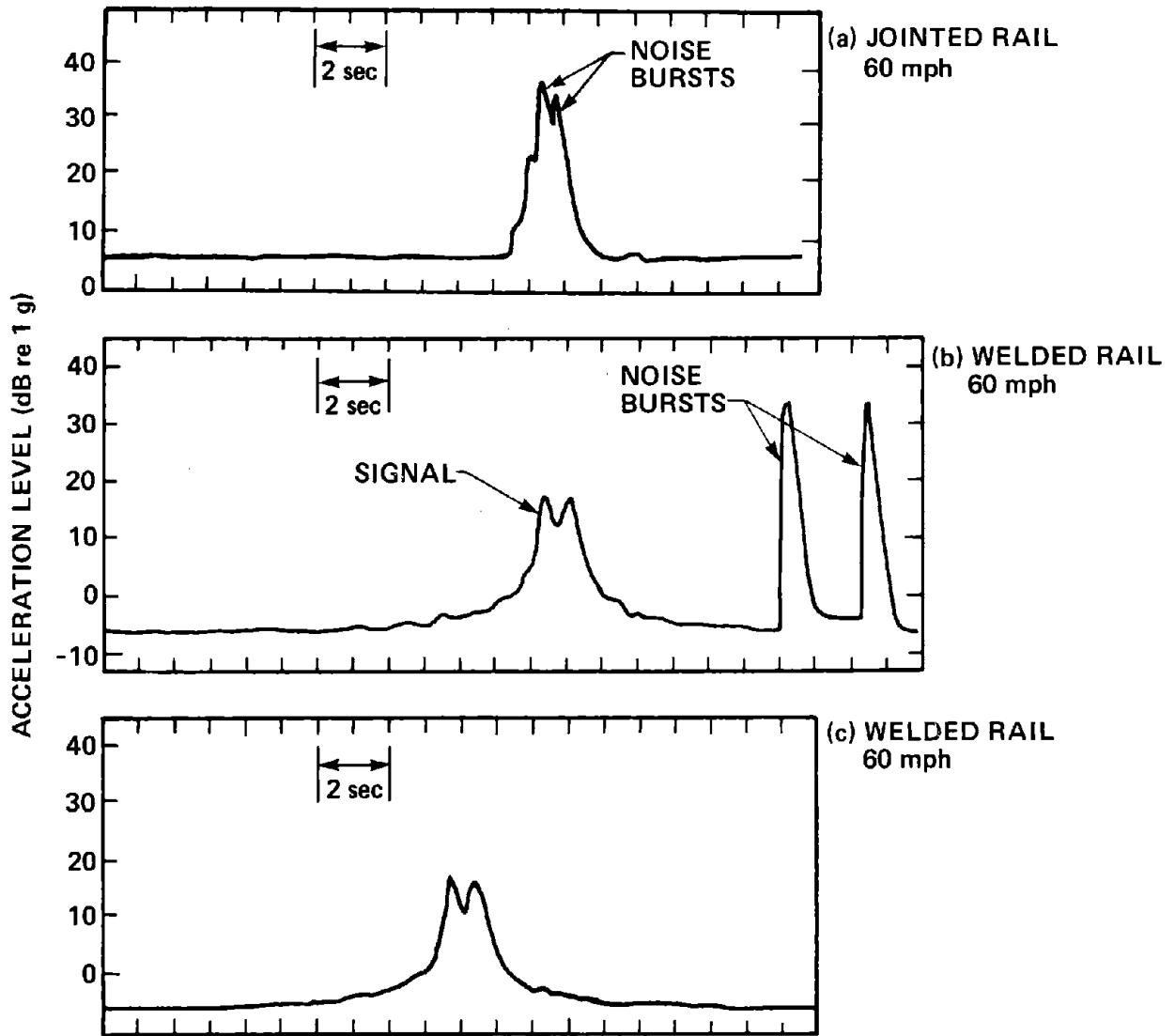


FIG. 65. SPURIOUS NOISE IN THE RAIL VIBRATION RECORDINGS, VERTICAL ACCELERATION AT THE RAIL FOOT.

were attached to the rail, electrically isolated from the rail, or disconnected from the rail. In any event, this noise problem prevented our acquiring many of the data that we wanted and made the task of extracting good data from the tapes much more difficult.

3.2.3 Special instrumentation

Wheel and Rail Roughness

An improved device for measuring wheel and rail roughness was developed as part of this program. Using the same principle as in earlier devices [3], the roughness sensor has a probe with improved capabilities for measuring roughness and is more portable. Figure 66 is a drawing of the device showing its principal features. The roughness is measured by an accelerometer attached to a spherical (1-in.-diameter) hardened-steel probe. The probe is pressed against the surface to be measured using a spring steel arm and pulled along that surface at a known speed. The frequency spectrum of the resulting time-varying acceleration can be easily related to the wavenumber spectrum of roughness.

For measuring rail roughness, the probe and arm are mounted in the cart shown in Figs. 66 and 67. The cart is then drawn along the rail at a known speed, using a variable-speed motor. (If the cart were to vibrate excessively as it rolled along the rail, that vibration - if transmitted down the probe arm - could contaminate the roughness measurements. Consequently, we monitored the cart vibration during all tests.) The roughness on both tangent and curved track can be readily measured with this device, as shown in Fig. 68, and the probe can be adjusted to measure the roughness along any line on the rail head. The speed of the cart is measured using a photocell device that gives four pulses per rotation of the lead wheel. This measurement is usually supplemented by stopwatch measurements of the time for

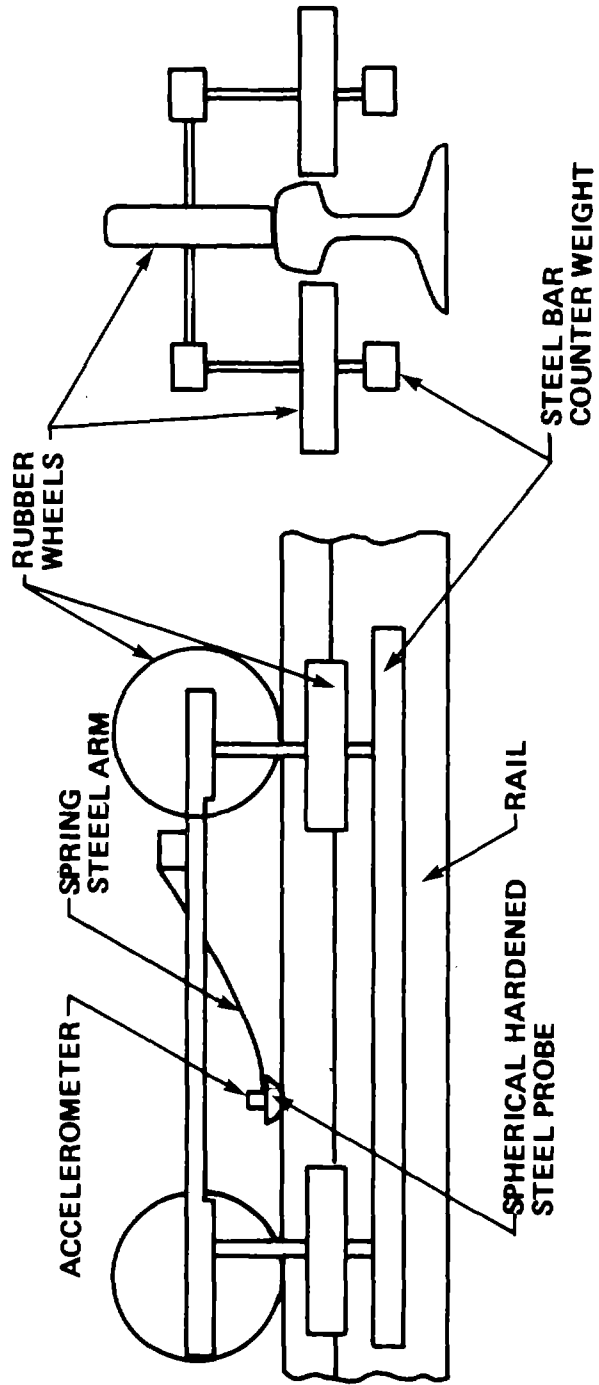


FIG. 66. SCHEMATIC OF ROUGHNESS MEASURING DEVICE.

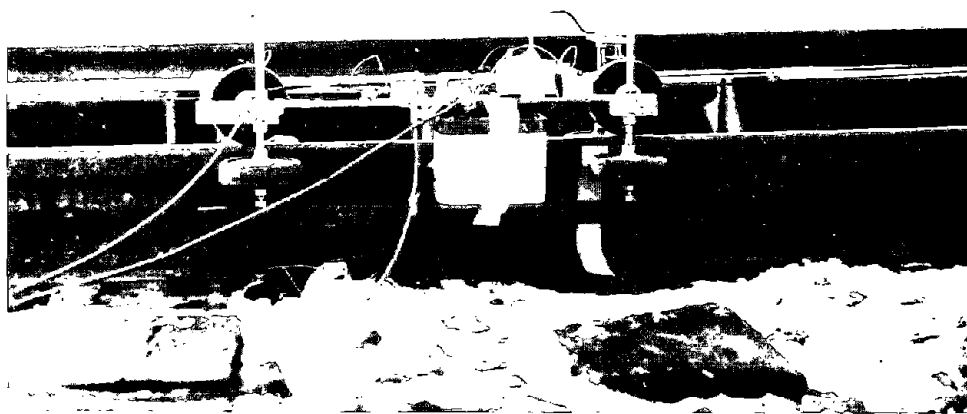
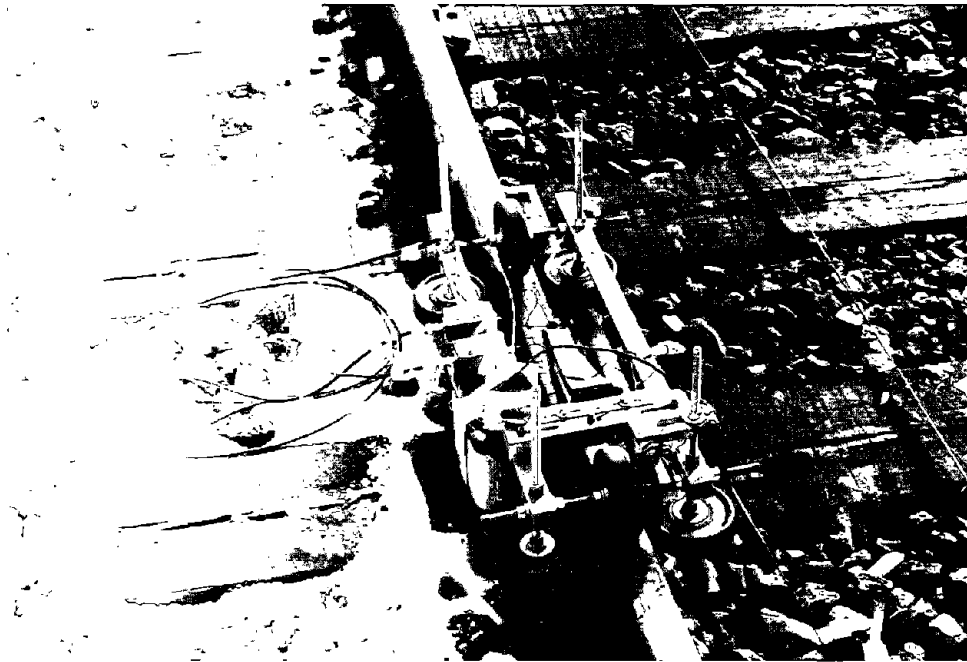


FIG. 67. THE TEST CART FOR MEASURING RAIL ROUGHNESS.

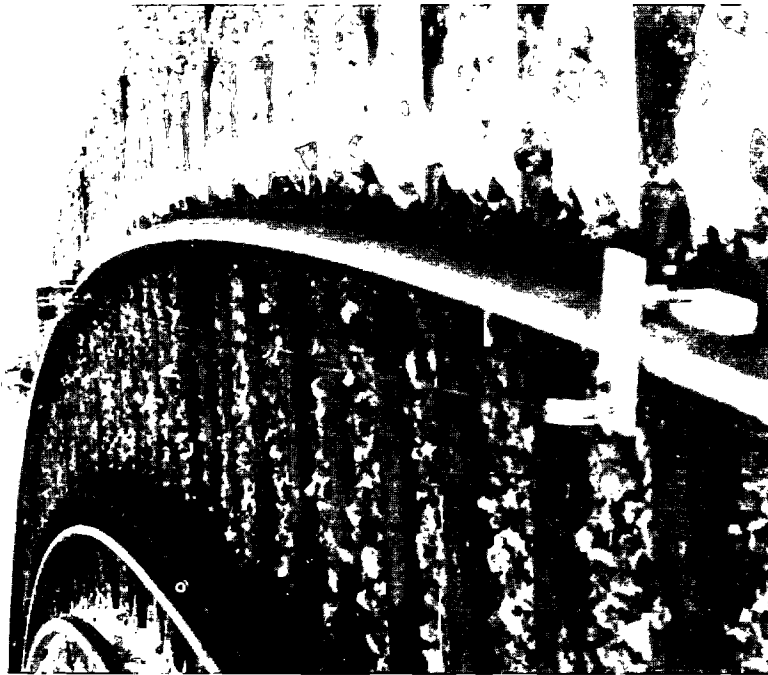


FIG. 68. THE MEASUREMENT OF ROUGHNESS ON BOTH TANGENT AND CURVED TRACK
(TTC PHOTO).

the cart to pass between two fixed points. All these signals are brought to a wayside tape recorder using BNC cables. This task usually requires that someone walk beside the cart holding the cables, as shown in Fig. 69, to keep them from interfering with the motion of the cart along the rail.

To measure wheel roughness on the SOAC, one needs only the probe, the spring steel arm, and some means for turning the wheel at a steady speed. We used the Hegenscheidt wheel-truing machine, as shown in Fig. 70, to turn the wheel at a steady speed. The lower photograph shows the probe and spring steel arm held back from the surface of the wheel. The truing machine turns the wheel by means of two rollers that support the wheel at the flange. If these rollers were to generate excessive vibration, it could contaminate the roughness measurements. To ensure that the vibration was not excessive, we mounted an accelerometer on the wheel tread and brought the signal through slip rings to the tape recorder.

Typical acceleration spectra from the rail and wheel roughness tests at TTC are given in Figs. 71 and 72. The acceleration spectrum for the welded rail in Fig. 71 exhibits a smooth function with frequency, except for two one-third octave bands, 50 and 63 Hz. The influence of the cart acceleration is partly responsible for this.

As described above, acceleration levels from the cart that pulls the roughness device along the rail were monitored during the tests. When the transfer function relating vibration on the cart to that on the probe is subtracted from these measurements, one obtains curve 2 in Fig. 71. At 50 Hz, the probe acceleration is 1 dB higher, because of the influence of the cart vibration. However, at 63 Hz, logarithmic subtraction of the two levels does not account for the slight increase in level of the probe



FIG. 69. TECHNICIAN GUIDING THE CABLES FROM THE ROUGHNESS CART (TTC PHOTO).

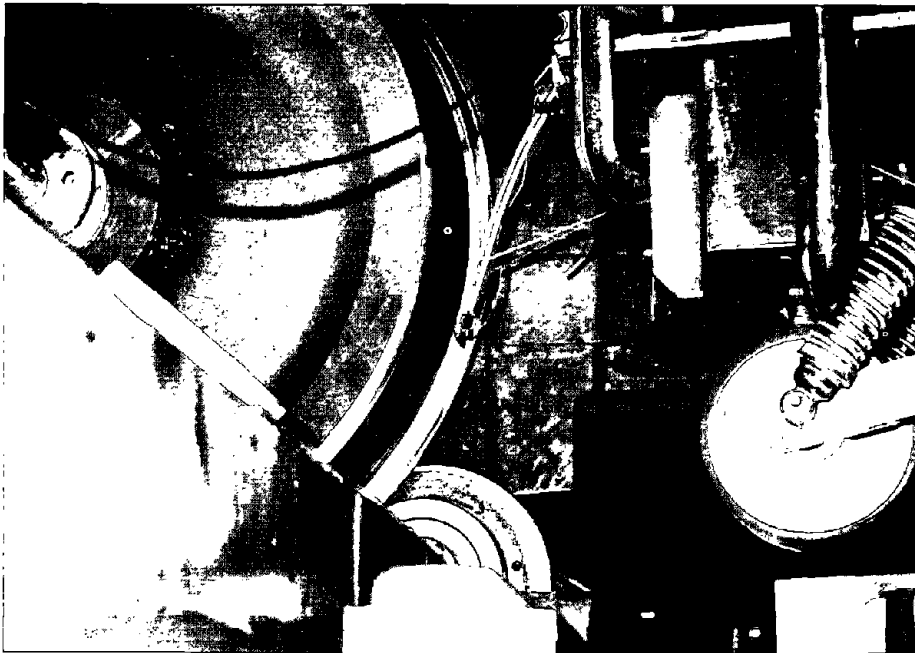
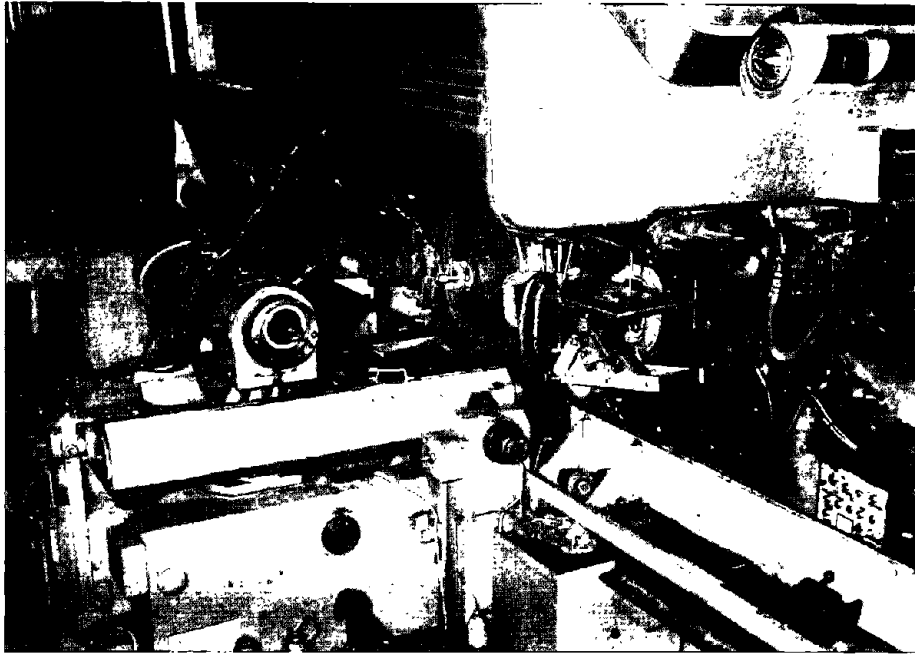


FIG. 70. THE HEGENSCHIEDT WHEEL-TRUING MACHINE SET UP FOR MEASURING WHEEL ROUGHNESS (TTC PHOTOS).

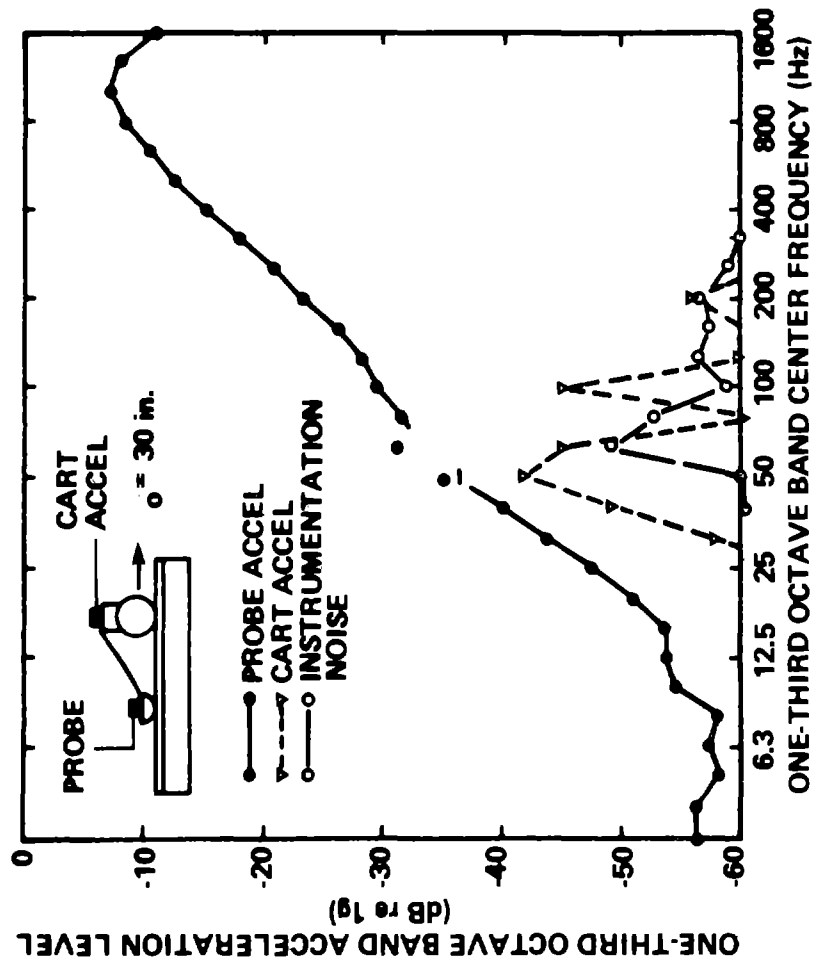


FIG. 71. TYPICAL RAIL ROUGHNESS ACCELERATION SPECTRUM - WELDED RAIL.

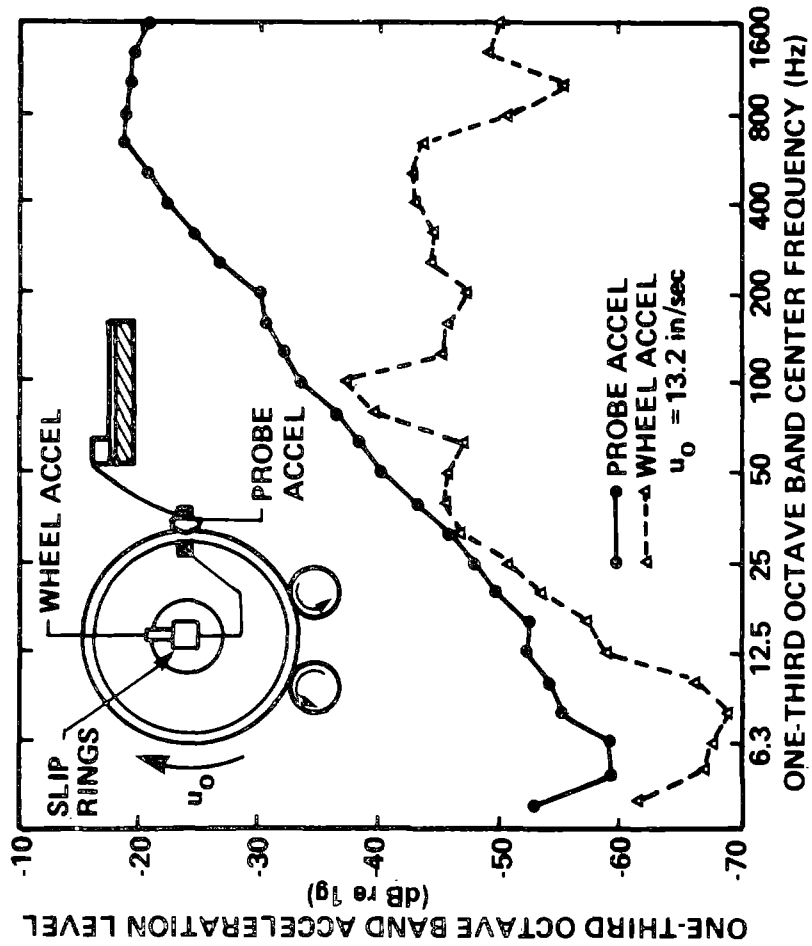


FIG. 72. TYPICAL WHEEL ACCELERATION SPECTRUM.

acceleration. These roughness tests were made in very cold conditions, and it is probable that the vibration isolation between the cart and probe (at some frequencies) was not as good as that measured in the lab. However, this influence was seen only on these two frequencies, i.e., the isolation being very adequate (>13 dB) for the rest of the spectrum.

The wheel roughness data were measured with the SOAC mounted on the Hegenscheidt wheel-truing machine, with the wheel driven at a perimeter speed of 13.2 in./sec. Acceleration measurements made on the rim of the wheel are compared to probe acceleration in Fig. 72. In only a few bands is there the possibility of significant contamination of the probe signal by truing machine-induced wheel vibration.

The acceleration data were reduced using previously developed relationships [3], i.e.,

$$\phi_{RR}(k) \Delta k = \frac{1}{\omega^4} \phi_{aa}(\omega) \Delta \omega,$$

where ϕ_{RR} is the roughness spectra, ϕ_{aa} is the acceleration spectra, $\omega = ku_0 = 2\pi f$, and u_0 is velocity of probe.

Assuming that the spectra are constant over one-third octave band width, one can show that:

$$L_{RR}(k) = L_{aa}(f) + 19.75 - 40 \log(f) - 20 \log |H_{RP}(f)| ,$$

where $L_{RR}(k)$ is one-third octave roughness spectra (re 1 in.), and $L_{aa}(f)$ is one-third octave acceleration spectra (re 1 g). The term H_{RP} accounts for the rail-to-probe transfer function, which is given in Fig. 73.

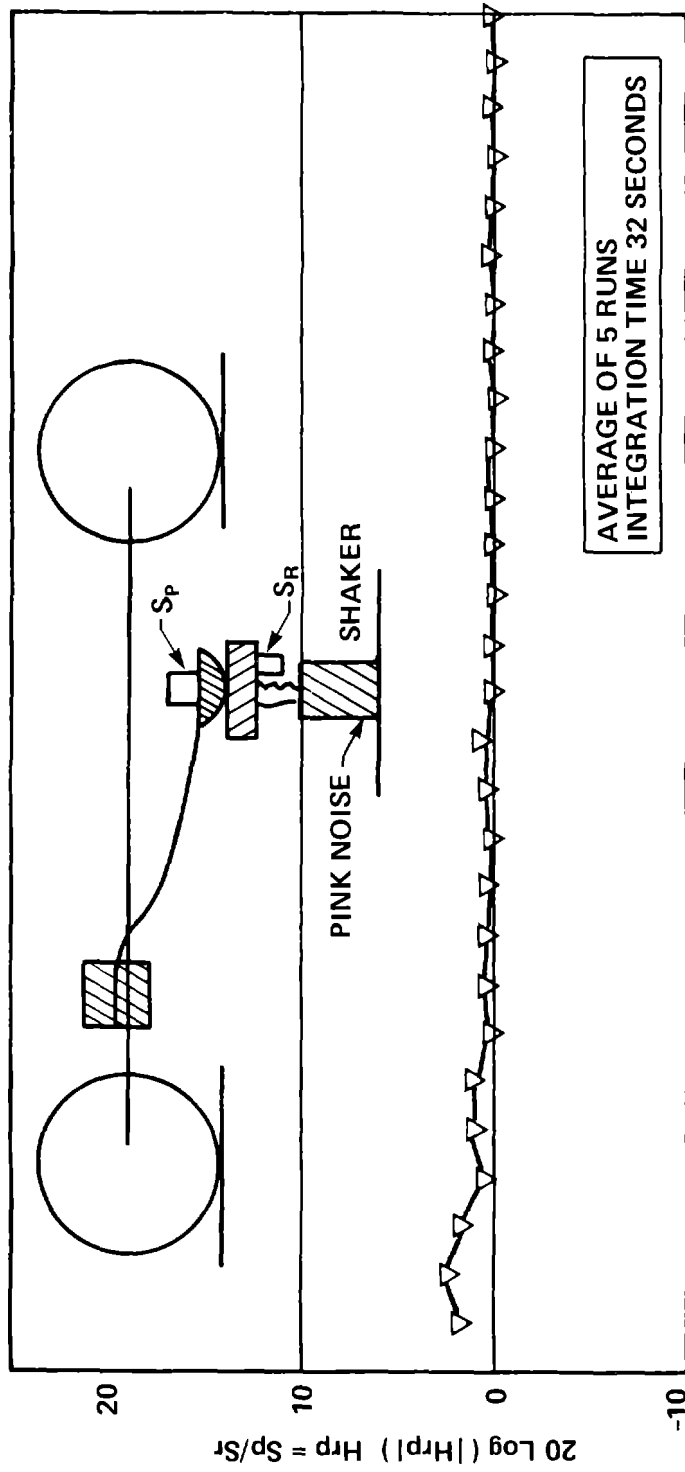


FIG. 73. PROBE TRANSFER FUNCTION.

The rail roughness spectra for the welded rail test section at the Transit Test Track are given in Fig. 74. Four separate parallel runs were made along that portion of the rail head (approximately 3/4-in. wide) that is worn from contact with the wheel. The probe speed, U_0 , is given for each run. The largest spread in the data points is around $k = 16$ radians/in., which corresponds to the 63-Hz, one-third octave band. As we mentioned previously, there may be some influence from the cart vibration at this frequency.

The points in Fig. 74 are plotted as a line in Fig. 75 and compared with the previous measurements made on rails at the MBTA and at the Pullman Standard Test Track [3].* The rail at TTC is considerably smoother than the other two rails, reflecting the extremely high quality of the rail at the Transit Test Track.

Roughness spectra obtained from the welded test section, the jointed test section, and the screech loop are given in Fig. 76. All these measurements were made in the center of the region on the rail head where the wheel contacts the rail. The screech loop is much rougher than the jointed or welded test sections. The greater roughness is a consequence of the severe wear that occurs between wheel and rail on this short radius curve.

Additional screech loop rail roughness is given in Fig. 77. The roughness spectra from two parallel runs in the wheel track can vary considerably at high wave numbers, as is apparent in curves 1 and 2.

Finally, roughness data measured from the wheels of the SOAC are presented in Figs. 78 and 79. In Fig. 78, the roughness

*Note that for the previous MBTA and Pullman Standard roughness measurements, we have smoothed the data in the 10-80 radian/in. special frequency range where it appears that earlier roughness measuring devices may have introduced some of their own dynamics.

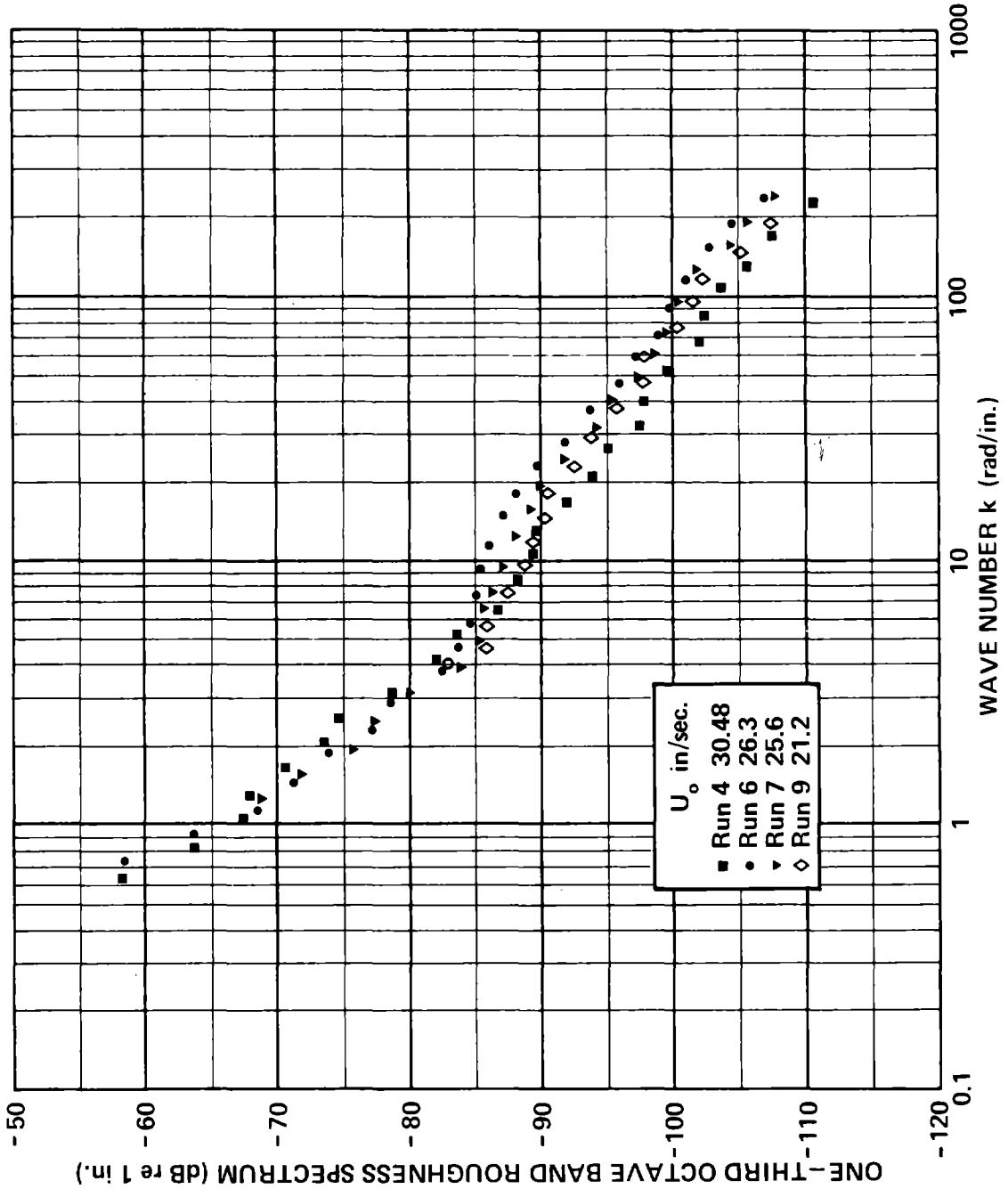


FIG. 74. RAIL ROUGHNESS ON THE WELDED RAIL TEST SECTION.

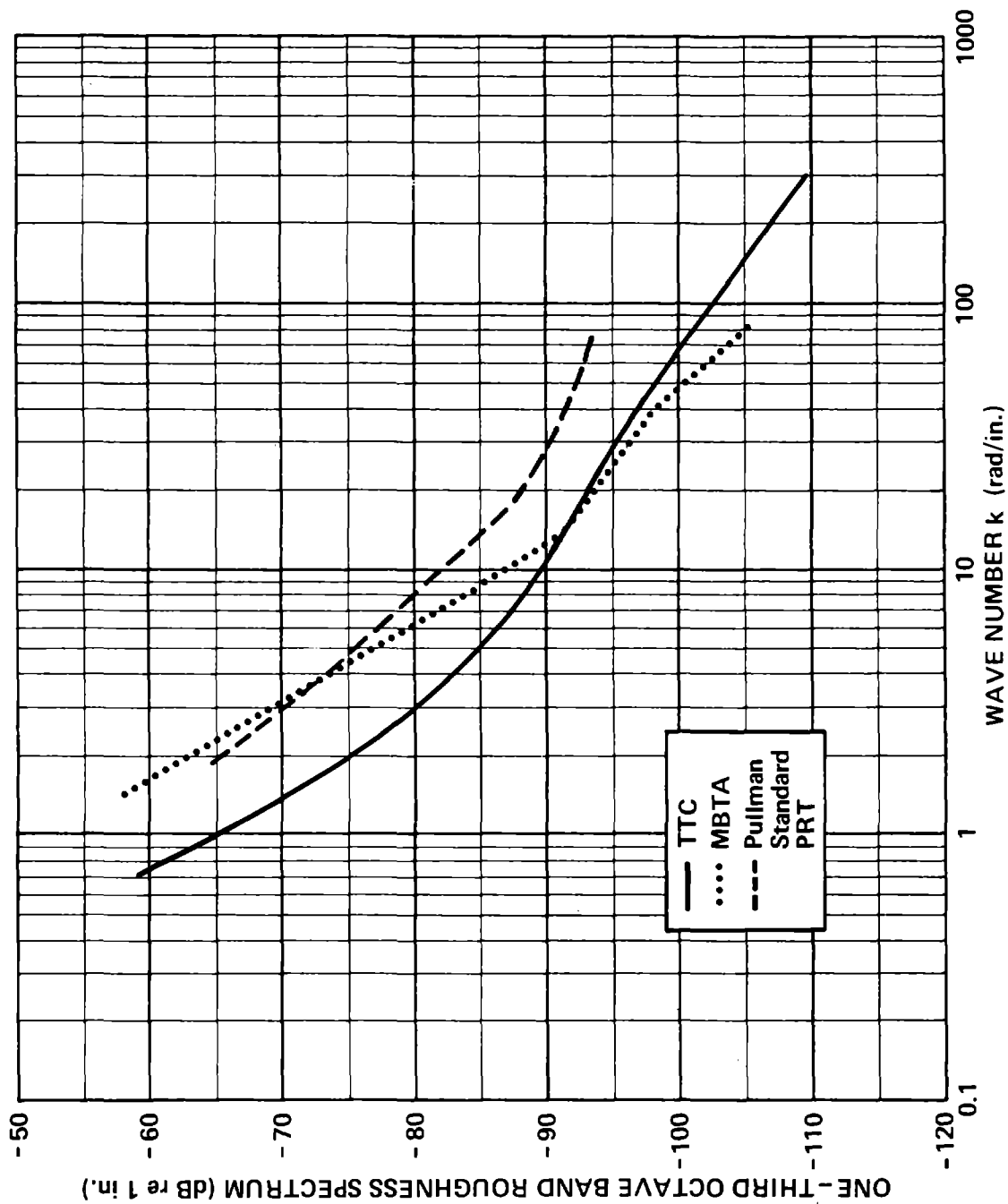


FIG. 75. RAIL ROUGHNESS SPECTRA AT THREE PROPERTIES.

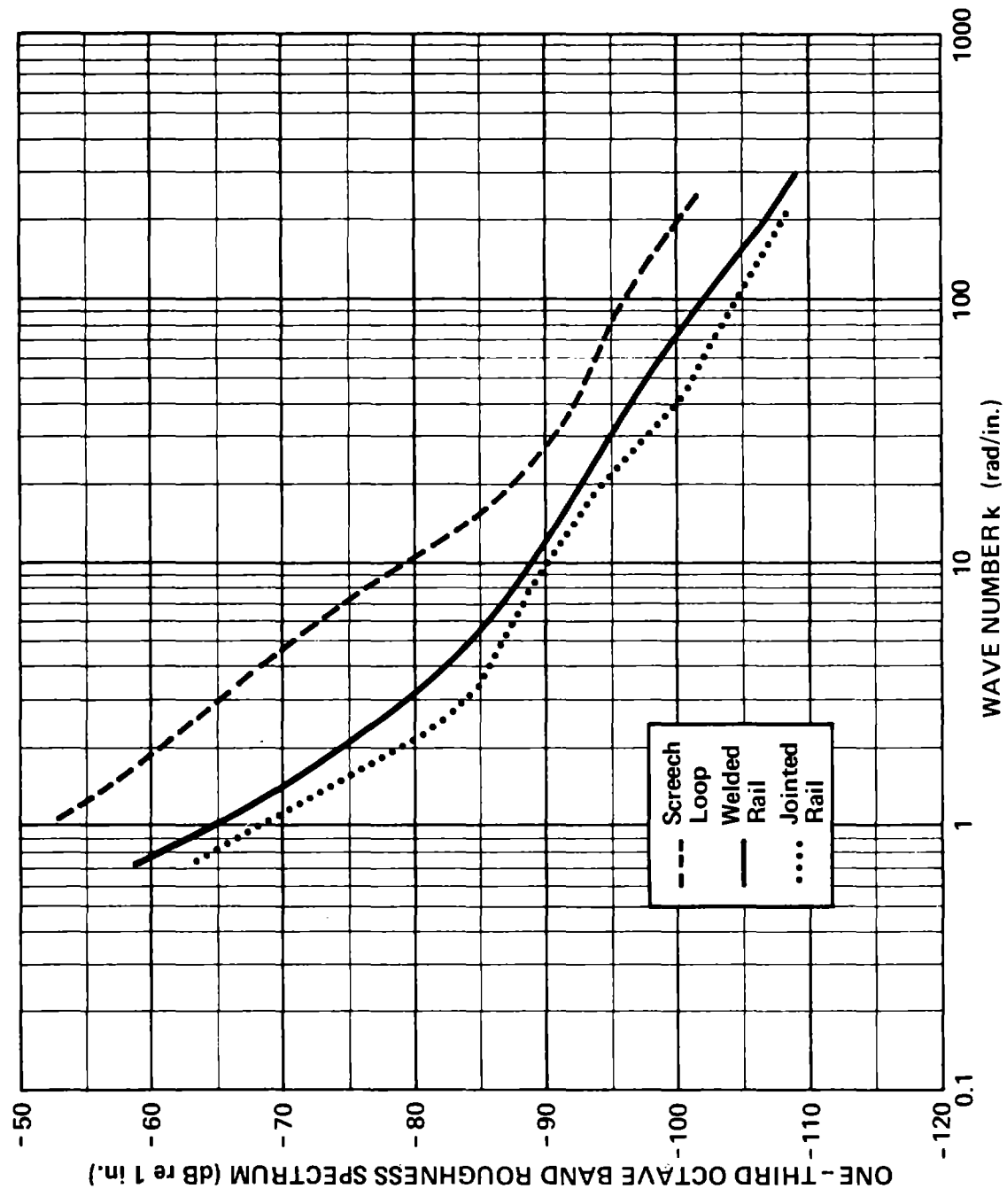


FIG. 76. RAIL ROUGHNESS SPECTRA FOR THREE DIFFERENT TRACK SECTIONS AT TTC, PUEBLO.

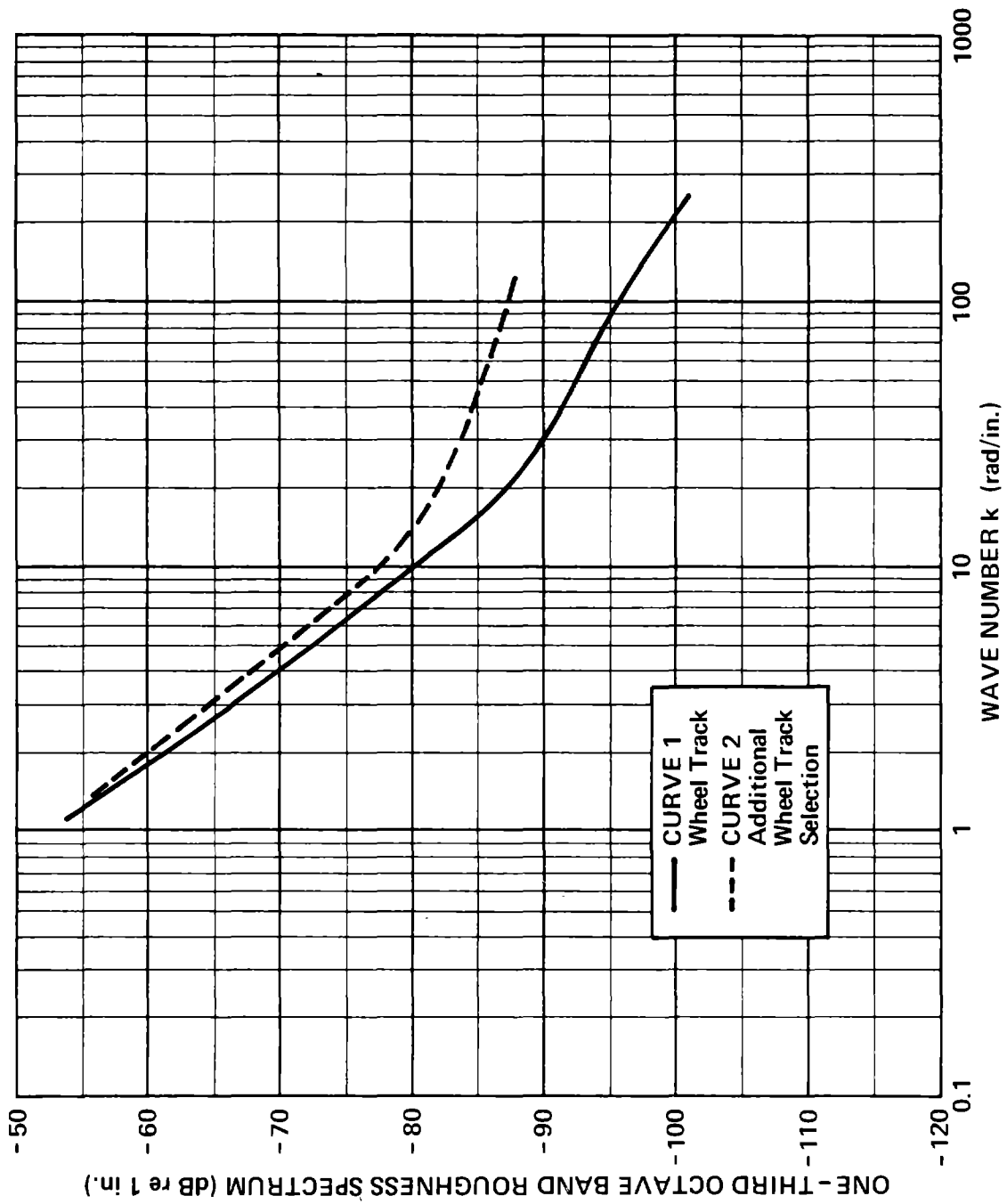


FIG. 77. RAIL ROUGHNESS SPECTRA ON THE SCREECH LOOP.

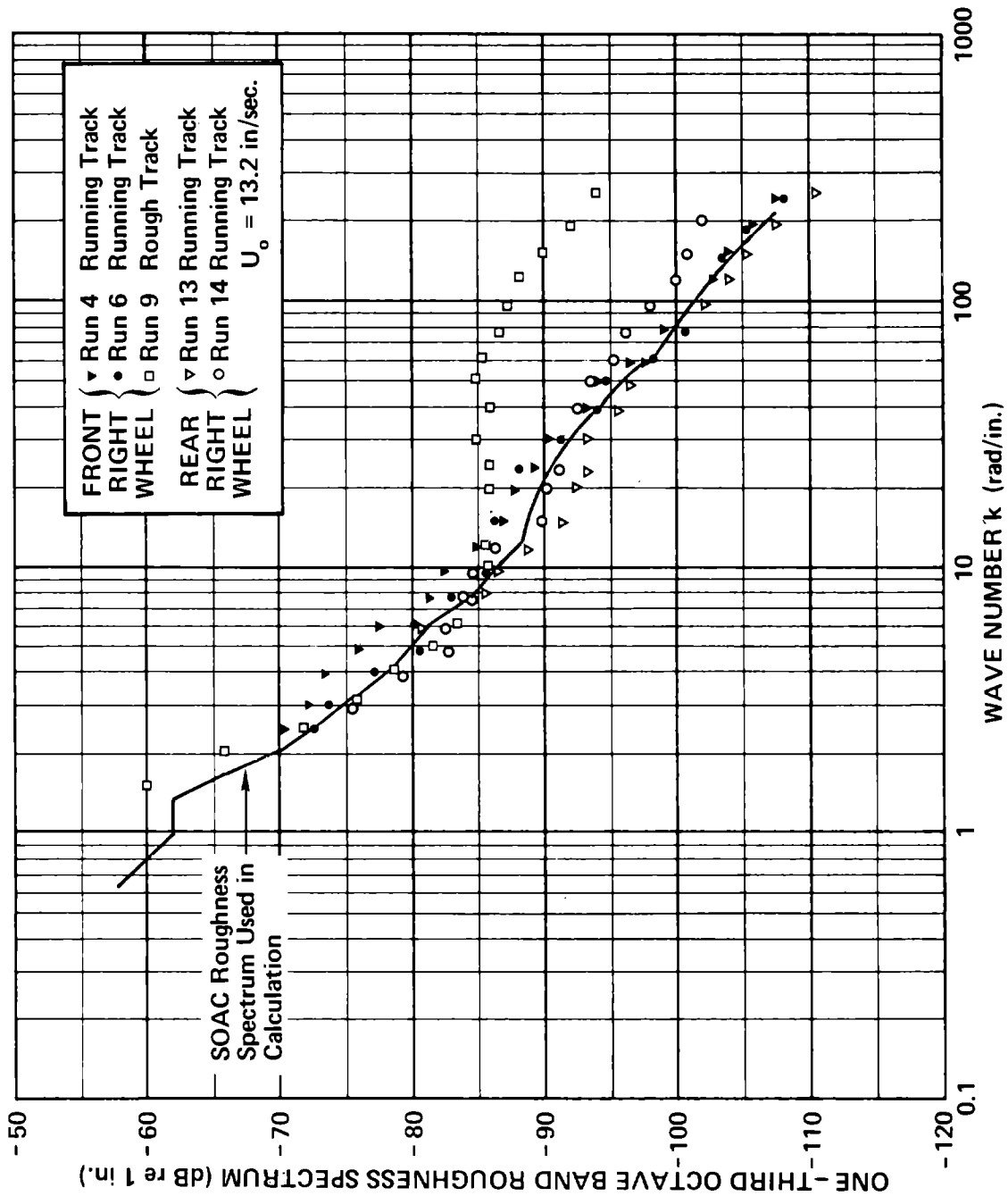


FIG. 78. WHEEL ROUGHNESS SPECTRA ON SOAC.

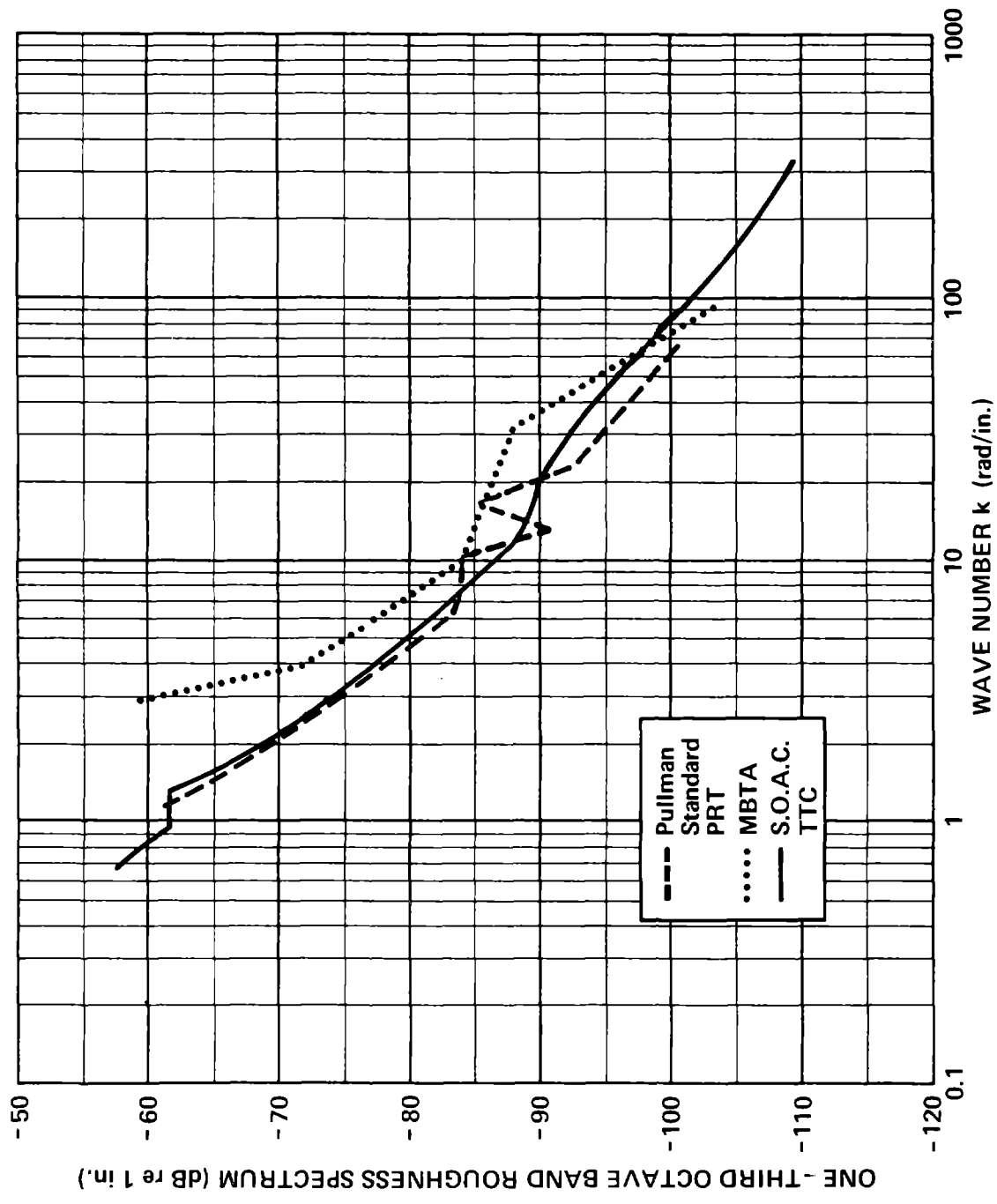


FIG. 79.. WHEEL ROUGHNESS SPECTRA FROM THREE CARS.

spectra for two different car wheels fall very closely on a single curve. When compared with the data in Fig. 76, the wheels are rougher than either the jointed or welded rail section.

The square points in Fig. 78 (Run 9) show the extremely rough section of the wheel that was torn up going around the screen loop. At high wave numbers the spectra are 5 to 8 dB higher than the screech loop roughness given in Fig. 76.

Figure 79 compares the present SOAC wheel roughness with measurements made at the MBTA on a revenue service wheel [3] and at Pullman Standard on wheels of their small personalized rapid transit (PRT) test vehicle [3]. Very similar spectra are seen for all three car wheels, although the MBTA wheel roughness is a little higher. This result is somewhat surprising, since we had the SOAC wheels trued on the Hegenscheidt machine just before carrying out the noise measurements that will be described later in this section. Although the noise measurements were all made within three days of truing the wheels, the roughness on the wheels was not measured until almost a week after truing. The delay occurred because the Test Center had difficulty finding a means for rotating the SOAC wheels at the very slow, steady speed needed to measure the roughness. When it was finally decided to use the Hegenscheidt machine for this purpose, the SOAC had been heavily used in the intervening period in another, unrelated test program. As we explain later in this section, we believe the wheels roughened considerably in that period, and that the wheel roughness in Fig. 79 is considerably higher than was present on the wheels during the noise measurements.

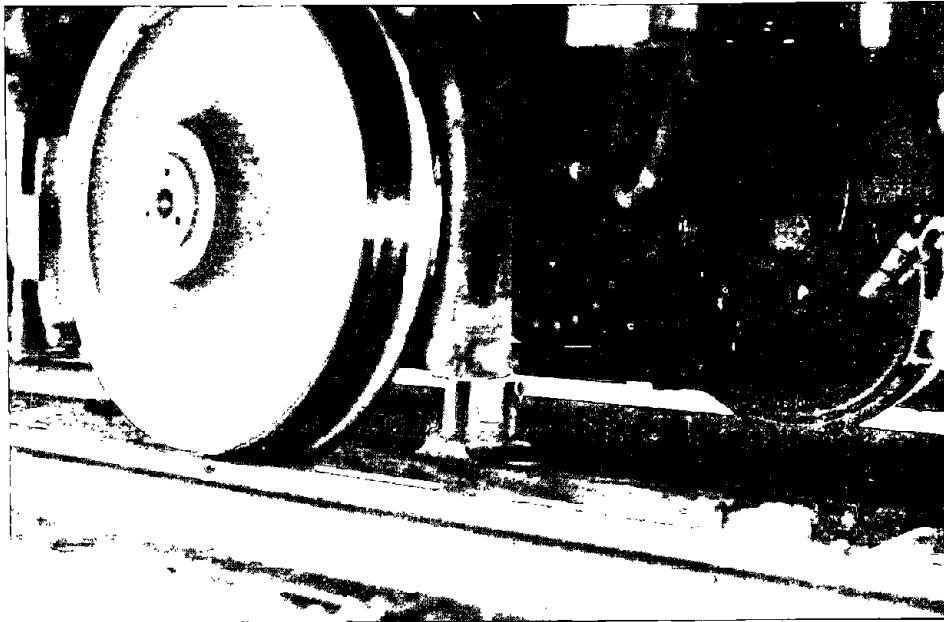
Contact Area

The contact area between wheel and rail is an important parameter in the generation of wheel/rail noise, and we measured that area during our tests with SOAC at the Test Center.

To obtain measurements of the contact patch, we used a technique pioneered by Dr. Sudhir Kumar of the Illinois Institute of Technology. The technique requires that a strip of Scanning Electron Microscope (SEM) replicating tape be inserted between wheel and rail, as shown in Fig. 80. A small hydraulic jack was used to lift the wheel, as shown in Fig. 80a, and the wheel and rail surfaces were cleaned with solvent. Two thicknesses of 5-mil tape were then inserted between wheel and rail, and the valve in the jack was slowly opened so that the wheel would gently settle on the rail. The wheel was left there for three minutes, then raised and the tape removed. The impression left on the tape is similar in shape to (but larger in size than) the actual region of contact between the wheel and rail.

Kumar [24] has made laboratory measurements of the contact area between wheels and rails with well-defined new profiles, using his replicating tape technique. By comparing the measured areas with theoretically predicted areas, he has developed correction factors relating measured area to actual area. For the temperature at which these data were taken and for the ellipticity of the contact area (ratio of major to minor axes), Kumar has estimated that the ratio of actual to measured contact areas is 0.76.

A total of nine wheel/rail contact imprints were made. These were analyzed by Kumar [25] and are shown in Fig. 81. The test number and the number of the wheel for which the test was conducted are shown in the figure. The areas are plotted as seen by an observer looking down on the rail. Certain parts of the imprint show a high stress character, which is marked with shaded lines. Some of the imprints (Test Nos. 2, 3, and 5) were not completely on the tape. These imprints were completed by extrapolation and are shown as dotted lines.

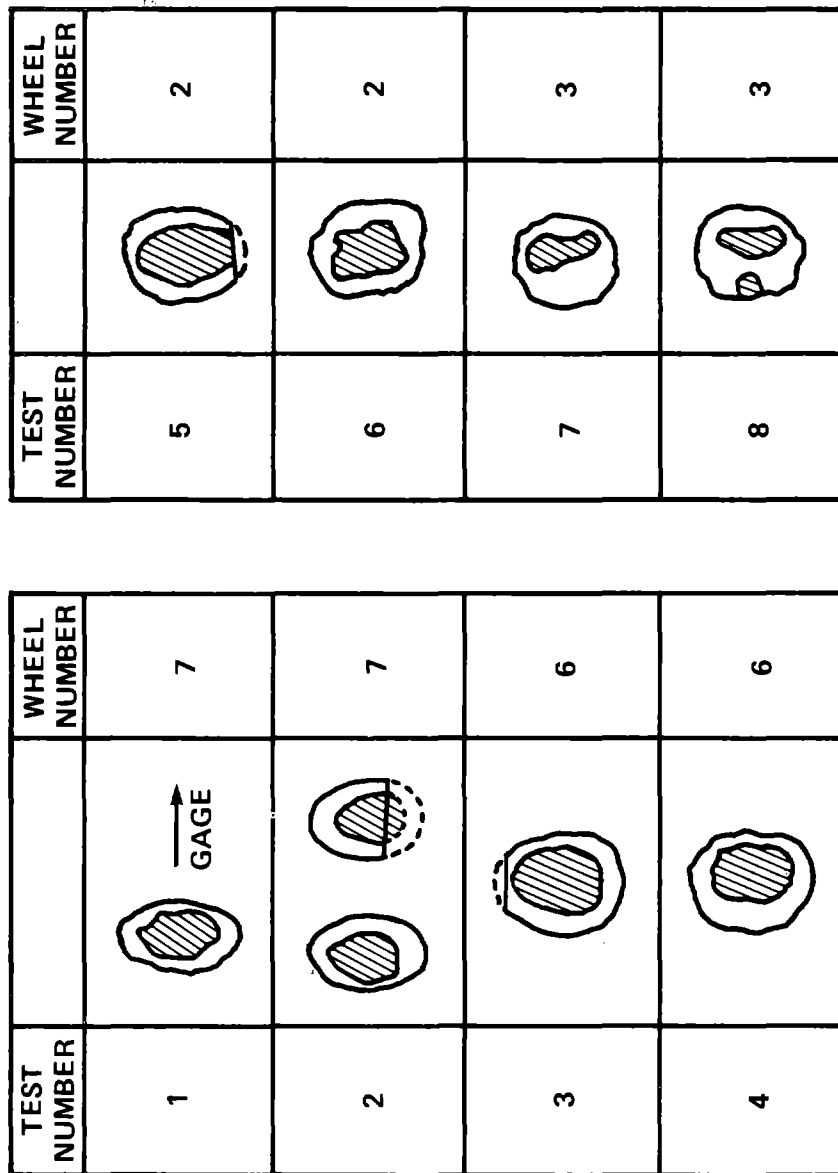


(a) Jacking up one wheel.



(b) The replicating tape inserted.

FIG. 80. MEASURING THE WHEEL/RAIL CONTACT AREA.



WHEEL NUMBER DESIGNATION

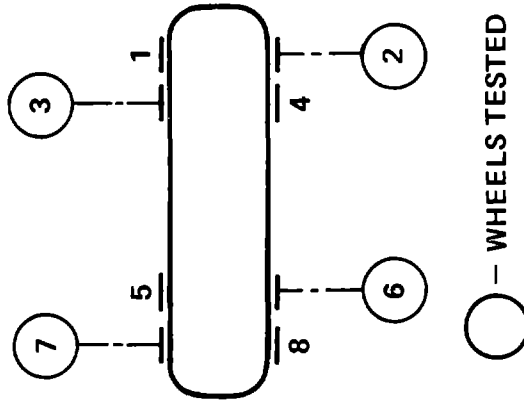


FIG. 81. SOAC WHEEL/RAIL CONTACT IMPRINTS.

Detailed measurements of the contact impressions are presented in Table 7. The major axis of the ellipse, $2a$, the minor axis, $2b$, and the area of contact (determined with the help of a planometer) were measured by Kumar. The area measurements are the average of three readings with an error estimated at ± 0.003 in.². Calculation of ellipticity (a/b) for the area of contact was made and is shown as a/b experimental in the table. There is significant variation, with wheel No. 7 having the highest ellipticity and wheel No. 3 the lowest. The theoretical ratio of a/b and the theoretical area of contact based on unworn wheel and rail profiles are 1.045 and 0.134 in.², respectively. Using the correction factor of 0.76 described above, Kumar has estimated the true area of contact in the table. The measured contact areas and ellipticities are generally more than the theoretical values, probably because the wheels of the car have a slightly worn, hollow profile.

3.3 Comparison of Measured and Predicted Rolling Noise

Using one SOAC operating at speeds from 20 to 80 mph on the welded rail test section of the Transit Test Track, we measured the noise and wheel and rail vibration and compared the measurements with the predictions of the analytical model of Sec. 2. Before carrying out that comparison, however, we used only that portion of the analytical model that predicts wayside noise, given the vibration of the components of the wheel/rail system (see Sec. 2.1.2), in order to estimate the sound radiated by each component.

Figure 82 shows the acceleration levels on the three components of interest (wheels, rails, and ties), measured as the SOAC passed by on welded rail at 30 mph. The rail vertical acceleration in the figure is the output of one accelerometer on the rail foot (see Fig. 63) and the horizontal rail acceleration

TABLE 7. SOAC WHEEL/RAIL CONTACT AREAS.

Test No.	Wheel No.	Measured		Meas. Area [in. ²]	Measured $\frac{a}{b}$	Corrected Area [in. ²]
		2a [in.]	2b [in.]			
1	7	0.63	0.36	0.167	1.67	0.127
2A	7	0.59	0.39	0.197	1.52	0.150
2B	7	0.58	0.41	0.180	1.42	0.137
3	6	0.66	0.53	0.293	1.23	0.223
4	6	0.66	0.52	0.247	1.27	0.188
5	2	0.63	0.48	0.260	1.29	0.198
6	2	0.59	0.48	0.230	1.22	0.175
7	3	0.53	0.48	0.177	1.09	0.135
8	3	0.56	0.47	0.183	1.20	0.139
Avg.		0.60	0.46	0.215	1.32	0.164
Theoretical		0.42	0.40	-	1.05	0.134

Wheel Diameter = 30 in.

Rail = 119 lb/yd RE

Wheel Profile = 1/20 conicity

Max. Hertzian stress = 150,000 psi

Nominal Wheel Load = 107,000/8 = 13,375 lb

Temperature = 46°F

Estimated correction factor = 0.76.

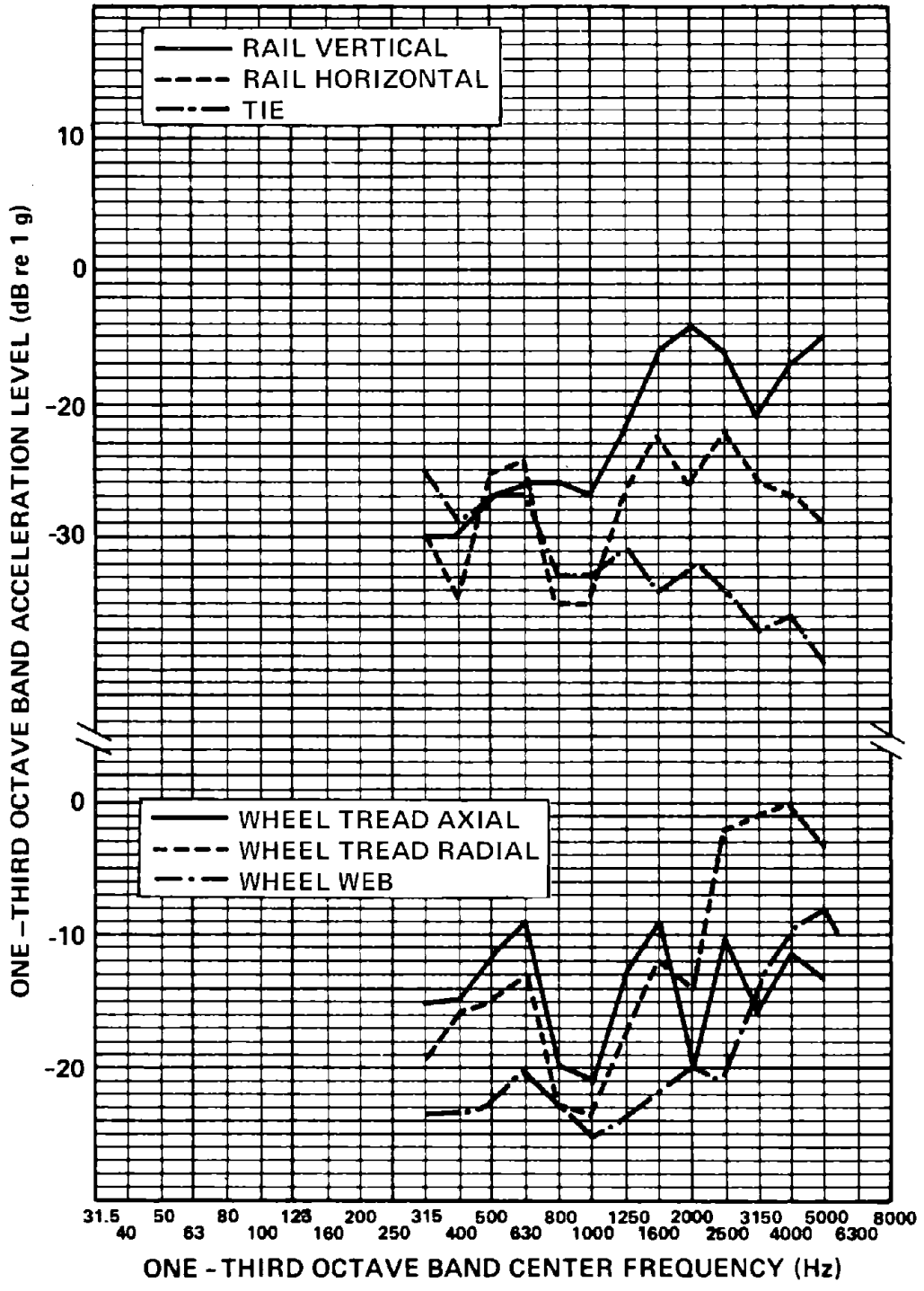


FIG. 82. WHEEL/RAIL SYSTEM COMPONENT VIBRATION FOR THE SOAC PASSING BY AT 30 MPH ON WELDED RAIL; 4-SEC AVERAGING TIME.

is the output of the accelerometer on the rail web closest to the foot (see Fig. 63). The wheel accelerations in the figure are the outputs of the three wheel accelerometers (see Fig. 57). The estimated sound radiated by the wheel, the vertical and horizontal rail vibration, and the ties,* is shown in Fig. 83 and is compared with the measured overall noise.

Although there is clearly some overestimation of the sound radiated by the rail, a number of conclusions are possible, based on the results in the two figures:

- The wheel web vibration is very low compared to the tread vibration. Since the surface areas of tread and web are comparable, we conclude that sound is radiated primarily by the tread of the wheel.
- The ties are not a significant source of wheel/rail noise, except possibly at low frequency.
- Vertical rail vibration accounts for most of the sound radiated by the rail, except possibly at low frequency.

In order to simplify the comparisons in the remainder of this section, we will use the above conclusions and focus only on: (1) wheel tread vibration and sound radiation, and (2) vertical rail vibration and sound radiation. These simplifications may lead to some underestimation of sound radiation in the low-frequency

*To estimate the tie radiation, we simply used the same relationship as derived for the rail in Sec. 2.1.2 but corrected to account for the difference in radiating area. The correction factor is given by

$$\frac{A_T/L_T}{4(r_F+r_H)}$$

where A_T is the area of the top surface of a tie, L_T is the tie spacing, and r_F and r_H are the rail foot and head width, respectively.

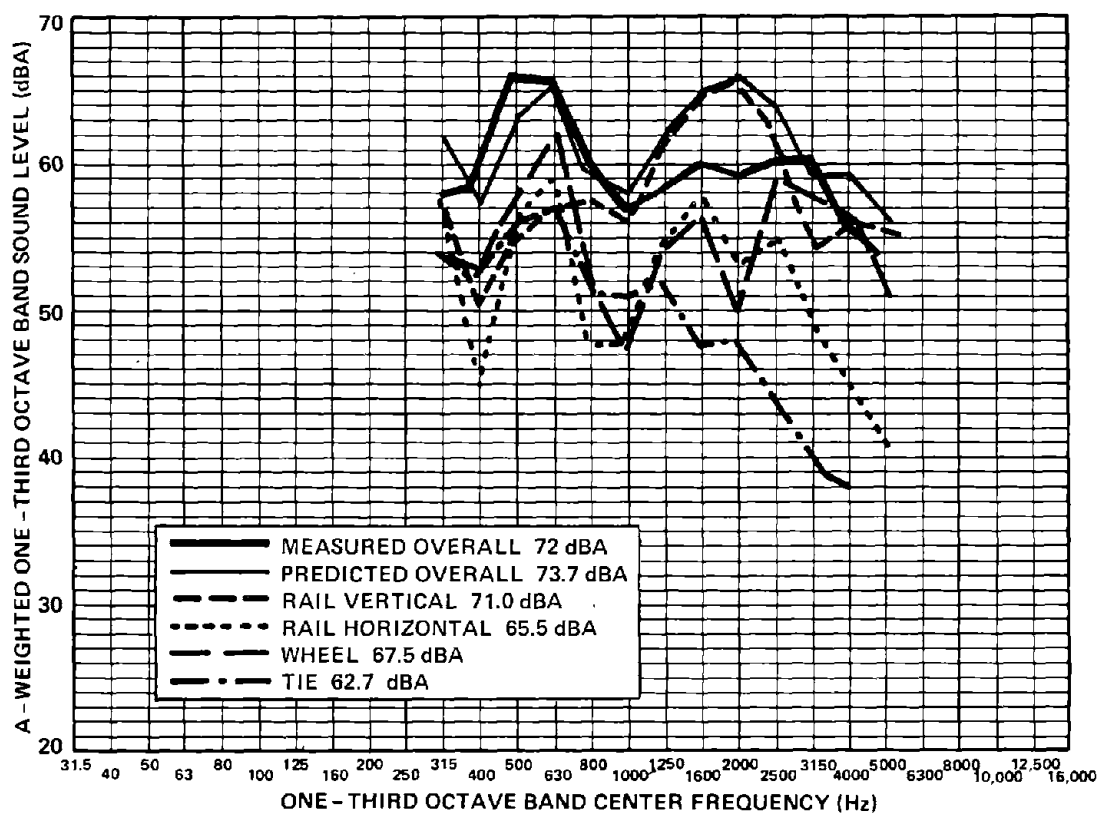


FIG. 83. ESTIMATES OF THE CONTRIBUTION OF EACH OF THE COMPONENTS OF THE WHEEL/RAIL SYSTEM FOR THE SOAC PASSING BY AT 30 MPH ON WELDED RAIL; 4-SEC AVERAGING TIME.

bands, but they should provide adequate estimates of overall sound radiation.

Figure 84 compares measurements and predictions for wheel/rail noise from one SOAC operated at 30 mph on welded rail at the TTC. The measured data were obtained as described earlier in this section, and the predictions were obtained using the analytical model of Sec. 2 with the measured TTC rail roughness spectrum for welded rail in Fig. 76 and the measured SOAC wheel roughness spectrum in Fig. 79. The range of the measured data is shown as the cross-hatched areas in the figure. In general, the data were reasonably repeatable except for the wheel radial vibration, which shows a considerable spread. In fact, there were three additional runs - one anomalously high and two anomalously low - that we have not shown in the figure because we doubt their validity.

Two theoretical prediction curves are shown in each figure. The solid curve is calculated, using measured wheel and rail roughness spectra as described above. Those predictions are generally higher than the measured data, especially for rail vibration; radial wheel vibration above 1000 Hz; axial wheel vibration between 1000 and 3000 Hz; and wayside noise between 630 and 3000 Hz. The discrepancy is probably caused by the use of a wheel roughness spectrum that is too high. As described earlier, there was nearly a week's delay between the noise and vibration measurements and the wheel roughness measurements. During that week, the test car was used heavily as a locomotive to pull the other SOAC around the test track as part of another unrelated program. We believe that, during that intervening week, the wheels roughened considerably.

The solid curves in Fig. 84 represent an upper bound on the predictions. As a lower bound, we have calculated the noise and

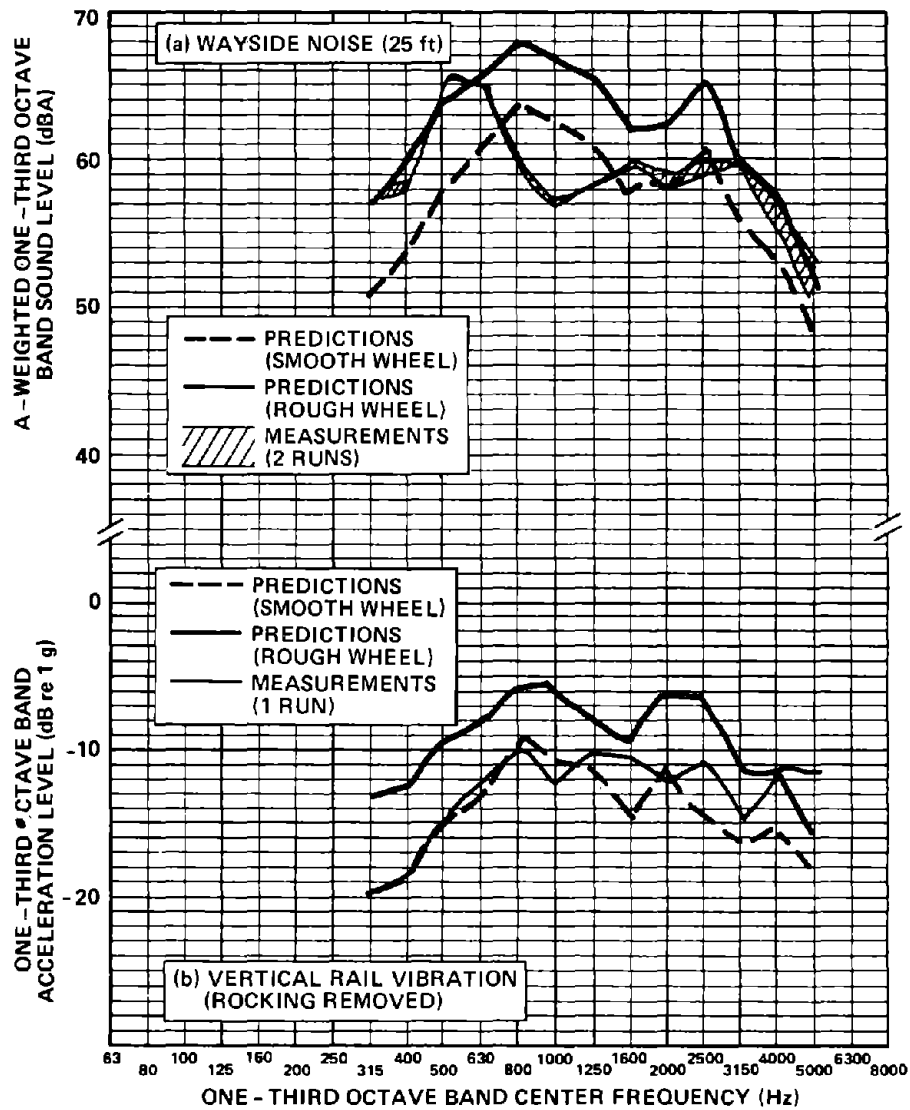


FIG. 84. COMPARISON OF PREDICTIONS AND MEASUREMENTS USING MEASURED WHEEL AND RAIL ROUGHNESS AT 30 MPH; 4-SEC AVERAGING TIME.

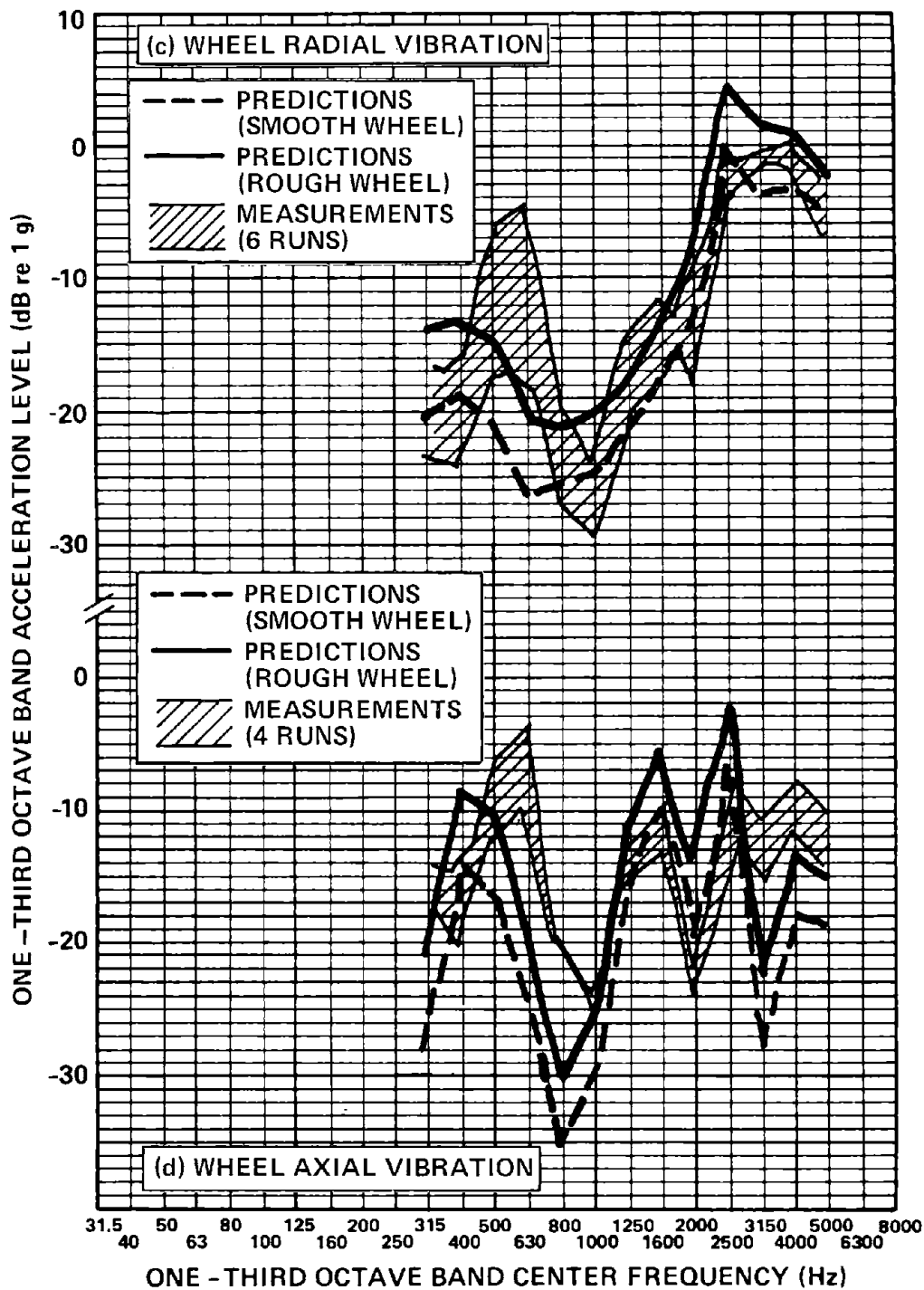


FIG. 84. (Cont.) COMPARISON OF PREDICTIONS AND MEASUREMENTS USING MEASURED WHEEL AND RAIL ROUGHNESS AT 30 MPH; 4-SEC AVERAGING TIME.

vibration, assuming the wheels to be perfectly smooth. The dashed curve in the figure shows the results of those calculations. Although they are strictly a lower bound, the calculations (assuming smooth wheels) provide excellent agreement with the rail vibration measurements across the frequency range. The rail vibration in the figure was obtained by adding together the signals from the two accelerometers on the rail foot (see Fig. 63) and dividing the result by two before taking the spectrum. Figure 84b thus represents the true vertical acceleration of the rail, with all rocking of the rail about its axis removed.

The measured and predicted noise spectra also agree well, if one assumes that the wheels are smooth. Below 630 Hz, the predictions are low; this was expected because tie radiation and radiation from the horizontal vibration of the rail have been neglected. The error is somewhat worsened, however, by the underprediction of the wheel axial vibration at 500 and 630 Hz, as shown in Fig. 84d. That discrepancy is mainly due to the wheel impedance model's tendency to predict too low a natural frequency for the first axial wheel mode. At higher frequency, the smooth wheel predictions agree quite well with the measurements up to about 3000 Hz. The reason for the discrepancy between measurements and predictions above 3000 Hz is unknown.

Finally, above 1000 Hz the measured wheel radial acceleration agrees well with the smooth wheel predictions. At low frequency, however, the measured acceleration is much greater than the predictions. We now believe that this discrepancy between measurements and predictions at low frequencies is an error in the measured data and not necessarily in the predictions. At low frequency, the radial accelerometer, because of its location and orientation, is sensing axial acceleration and torsional acceleration of the tread rather than radial acceleration. Figure 85 illustrates why this error, or cross talk,

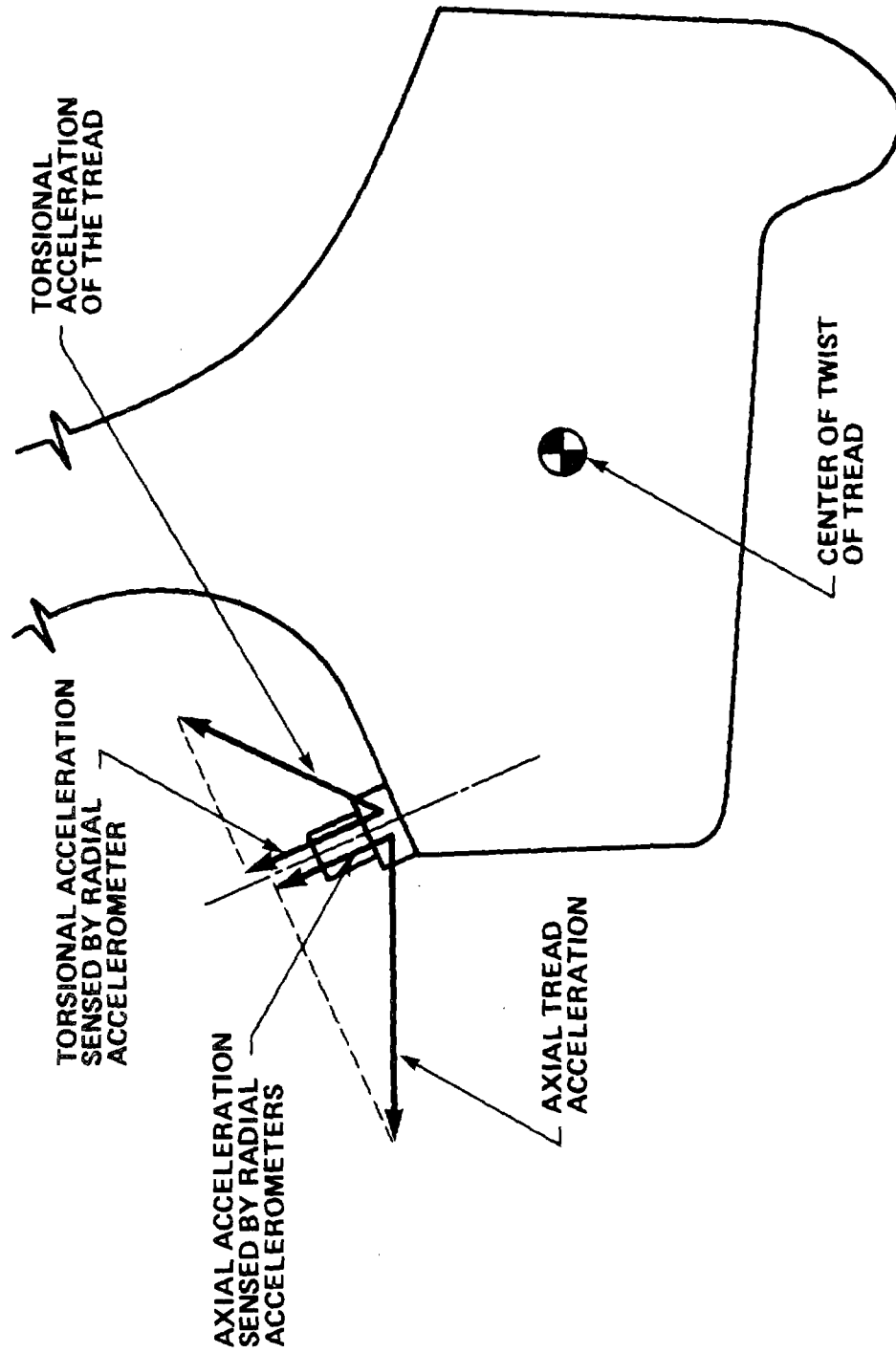


FIG. 85. WHEEL TREAD CROSS SECTION SHOWING POSSIBLE ERRORS IN THE MEASURED RADIAL ACCELERATION.

occurs. Because of the geometry of the wheel, the radial accelerometer was not mounted exactly perpendicular to the wheel axis. Consequently, some axial acceleration is sensed by the radial accelerometer. For example, if the angle between accelerometer axis and wheel axis is 75° rather than 90° , the axial acceleration sensed by the radial accelerometer will be only 12 dB below the true axial acceleration. If the radial acceleration is low and the axial acceleration is high, such as at the axial resonant frequencies of the wheel, significant errors in the measured radial acceleration could result. The peaks in the radial wheel acceleration at 500 to 630 Hz and 1250 to 1600 Hz could be partially due to this cross talk.

Another source of error that could be significant at the axial wheel resonant frequencies is the torsional acceleration of the tread, as illustrated in Fig. 85. Axial vibration of the tread is a combination of out-of-plane bending and torsion about the tread axis. Since the radial accelerometer is not located directly above the center of twist of the tread, some of the torsional acceleration will be sensed by the radial accelerometer. The degree to which the torsional motion of the tread will contaminate the radial acceleration measurements is not known, but one would expect the contamination to be most severe at the wheel axial resonant frequencies.

In the remainder of this section, we compare measurements and predictions, assuming that the wheel is much smoother than the rail. Although the predictions resulting from this assumption are - strictly speaking - a lower bound, the results in Fig. 84 suggest that the wheel was much smoother during the noise and vibration measurements than it was a week later, when its roughness was measured.

Figures 86 through 90 present a comparison of predictions and measurements for speeds of 20 to 80 mph. In the following cases, no data are available: rail vibration at 60 mph and rail and axial wheel vibration at 80 mph. In addition, at 45 and 60 mph, the measured axial wheel vibration appears to be anomalously low, e.g., at 45 and 60 mph it is nearly the same as at 30 mph.

In general, the predictions agree well with measured data, although there is a tendency for the predicted wayside noise to overestimate the measured noise, especially at the higher speeds. This tendency is illustrated in Fig. 91, where the predictions of overall noise level are seen to underestimate the measurements at low speed, but to overestimate those measurements at high speed.

3.4 Comparison of Measured and Predicted Impact Noise

3.4.1 Jointed rail

An elevation change usually exists across most rail joints on revenue service track on rapid transit systems. Typically, the rail on the side of the joint supporting the transit car is lower than the rail on the other side of the joint. Elevation changes of 1/8 in. are common [23]. The analysis in Sec. 2.2 was specifically developed to deal with this geometry.

However, as illustrated in Fig. 92, the jointed rail on the Transit Test Track at the Test Center is in such excellent condition that no measurable elevation changes across the rail joints exist, even with the transit car parked with one wheel right next to the joint. We considered creating an artificial elevation change across the rail joints of the test section by adding shims under one rail end at each joint. We abandoned this plan, however,

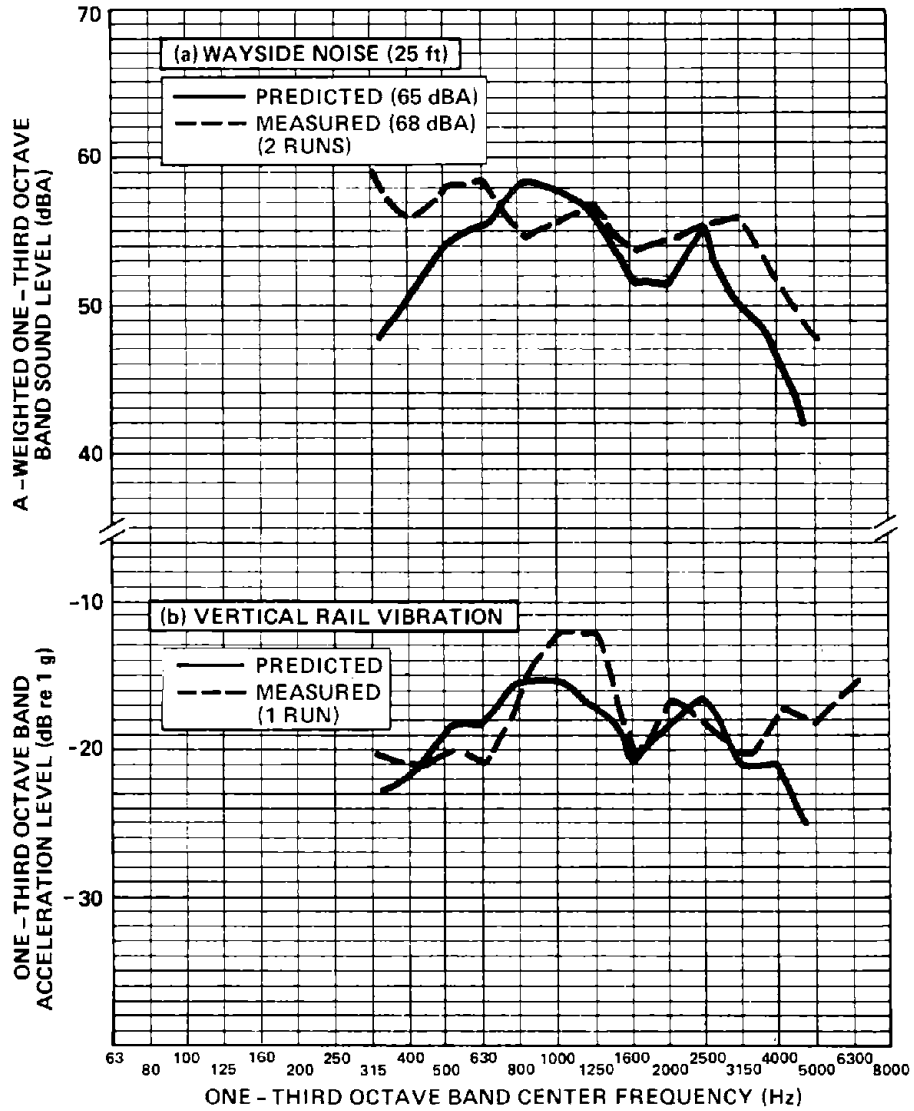


FIG. 86. COMPARISON OF MEASURED AND PREDICTED WHEEL/RAIL NOISE AND VIBRATION FOR THE SOAC AT 20 MPH ON WELDED RAIL; 4-SEC AVERAGING TIME.

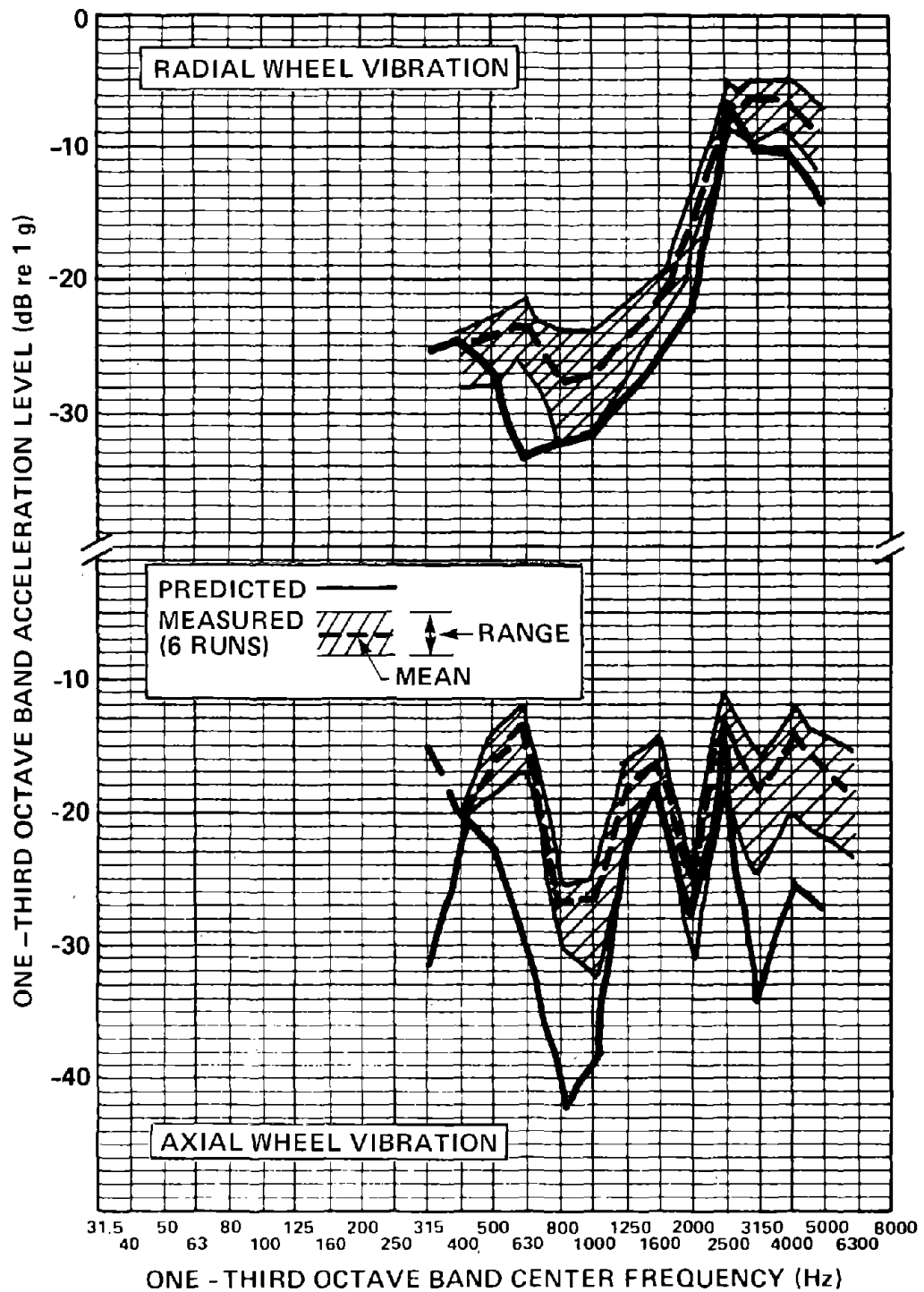


FIG. 86. (Cont.) COMPARISON OF MEASURED AND PREDICTED WHEEL/RAIL NOISE AND VIBRATION FOR THE SOAC AT 20 MPH ON WELDED RAIL; 4-SEC AVERAGING TIME.

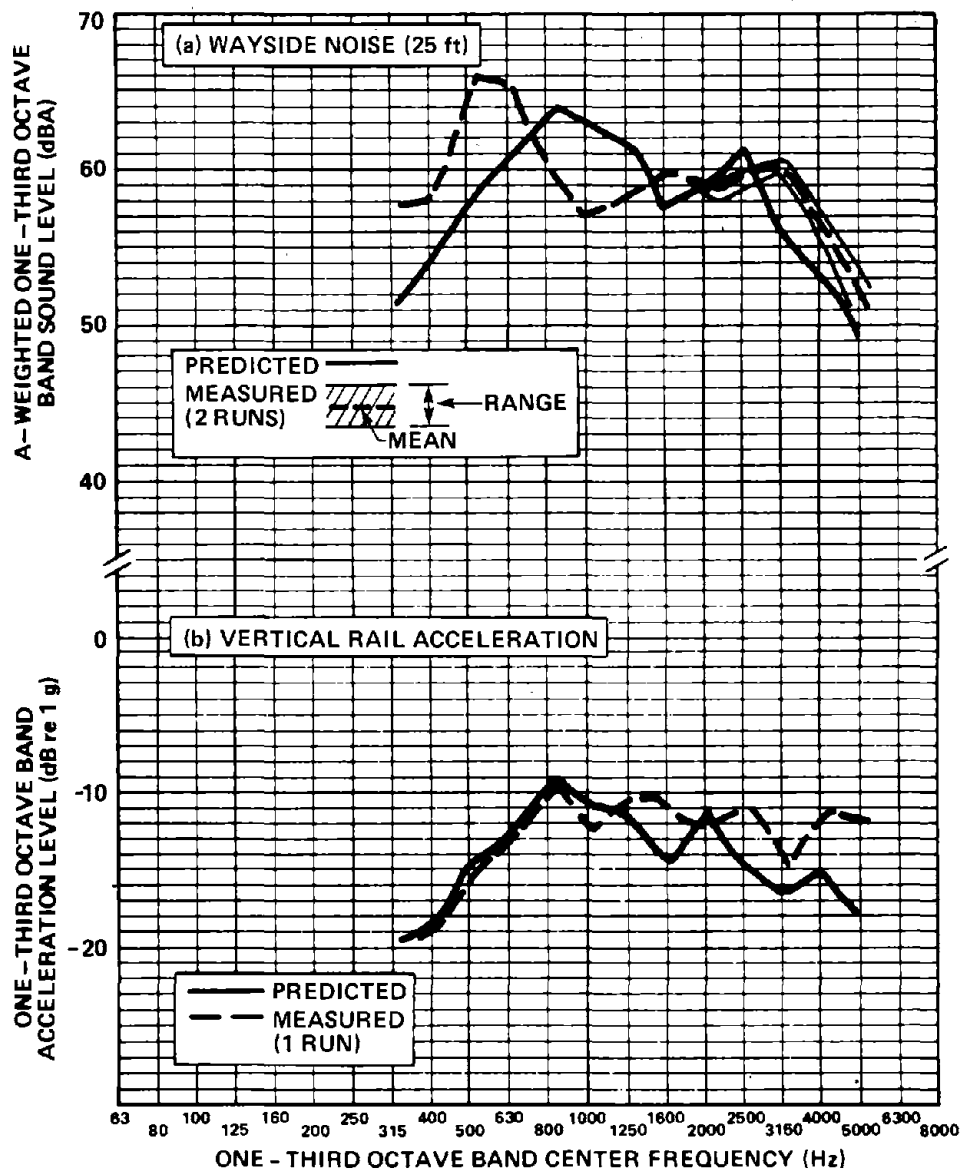


FIG. 87. COMPARISON OF MEASURED AND PREDICTED WHEEL/RAIL NOISE AND VIBRATION FOR THE SOAC AT 30 MPH; 4-SEC AVERAGING TIME.

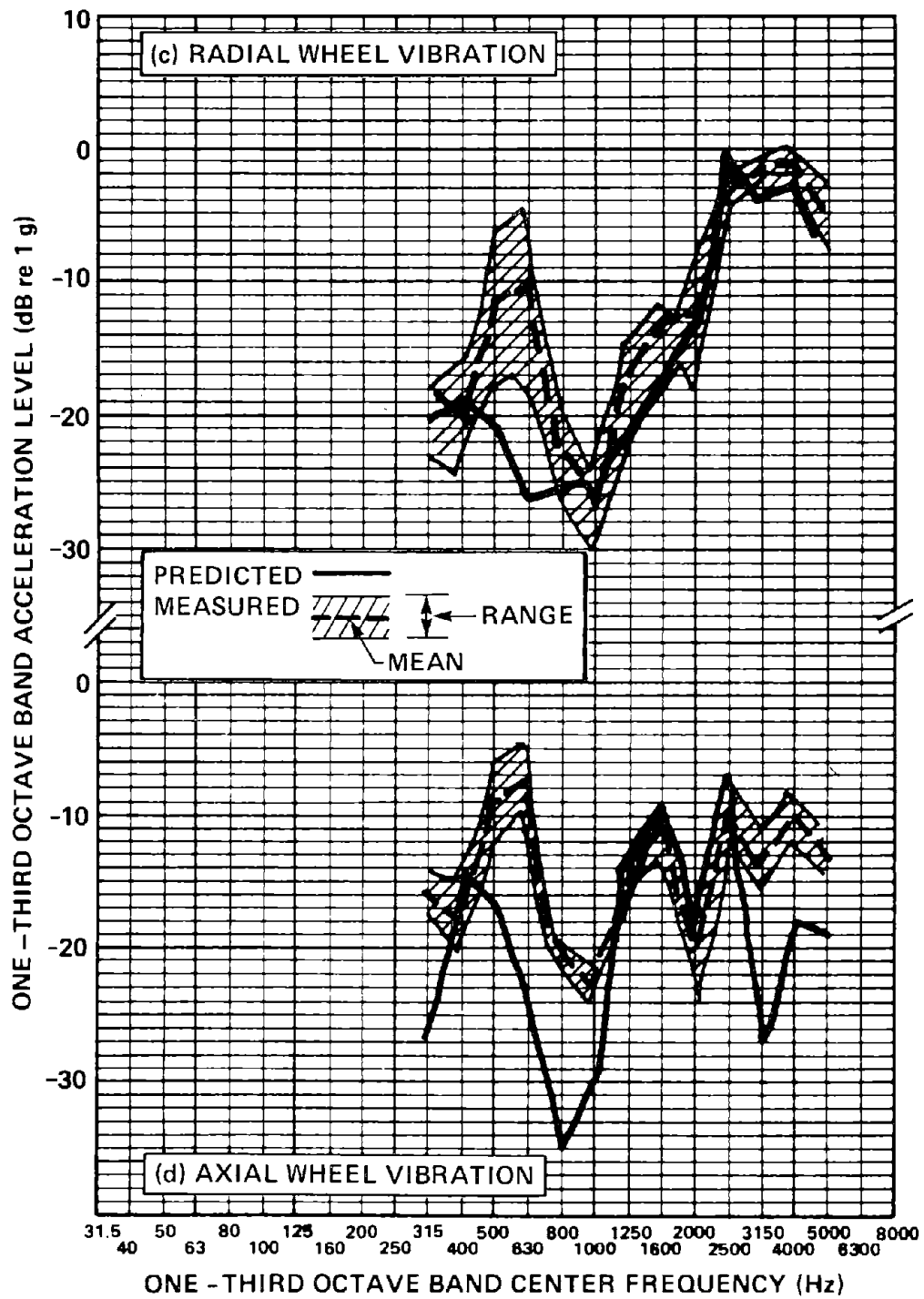


FIG. 87. (Cont.) COMPARISON OF MEASURED AND PREDICTED WHEEL/RAIL NOISE AND VIBRATION FOR THE SOAC AT 30 MPH; 4-SEC AVERAGING TIME.

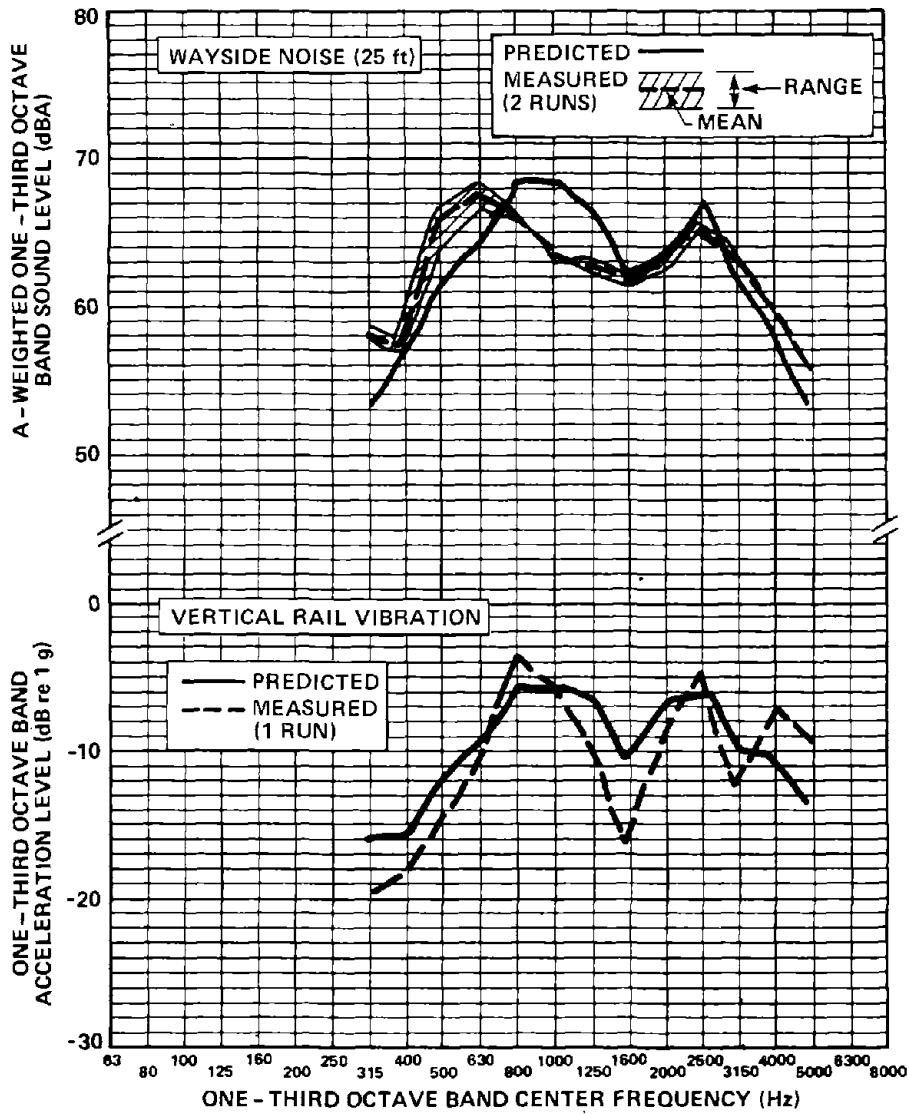


FIG. 88. COMPARISON OF MEASURED AND PREDICTED WHEEL/RAIL NOISE AND VIBRATION FOR THE SOAC AT 45 MPH; 4-SEC AVERAGING TIME.

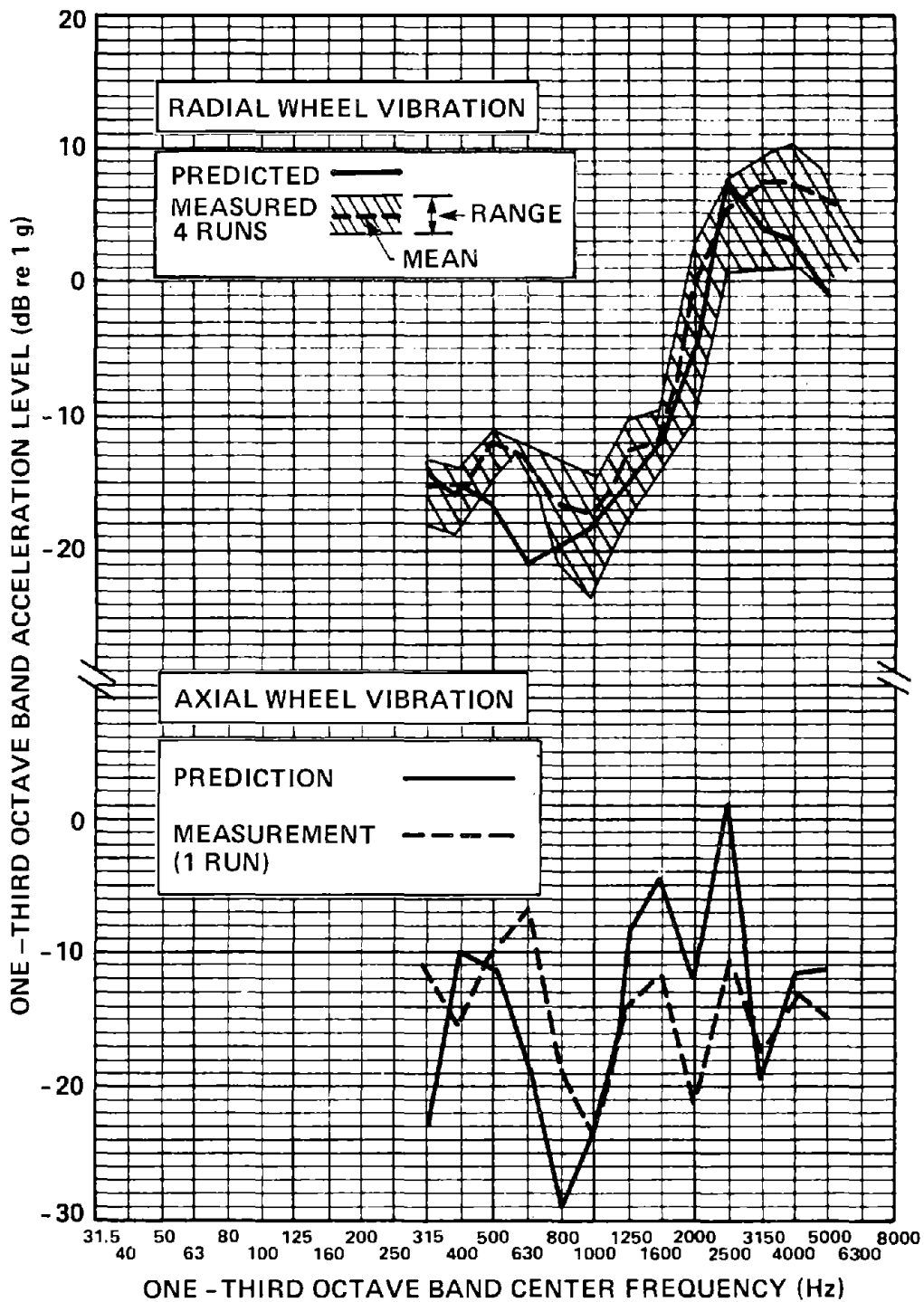


FIG. 88. (Cont.) COMPARISON OF MEASURED AND PREDICTED WHEEL/RAIL NOISE AND VIBRATION FOR THE SOAC AT 45 MPH; 4-SEC AVERAGING TIME.

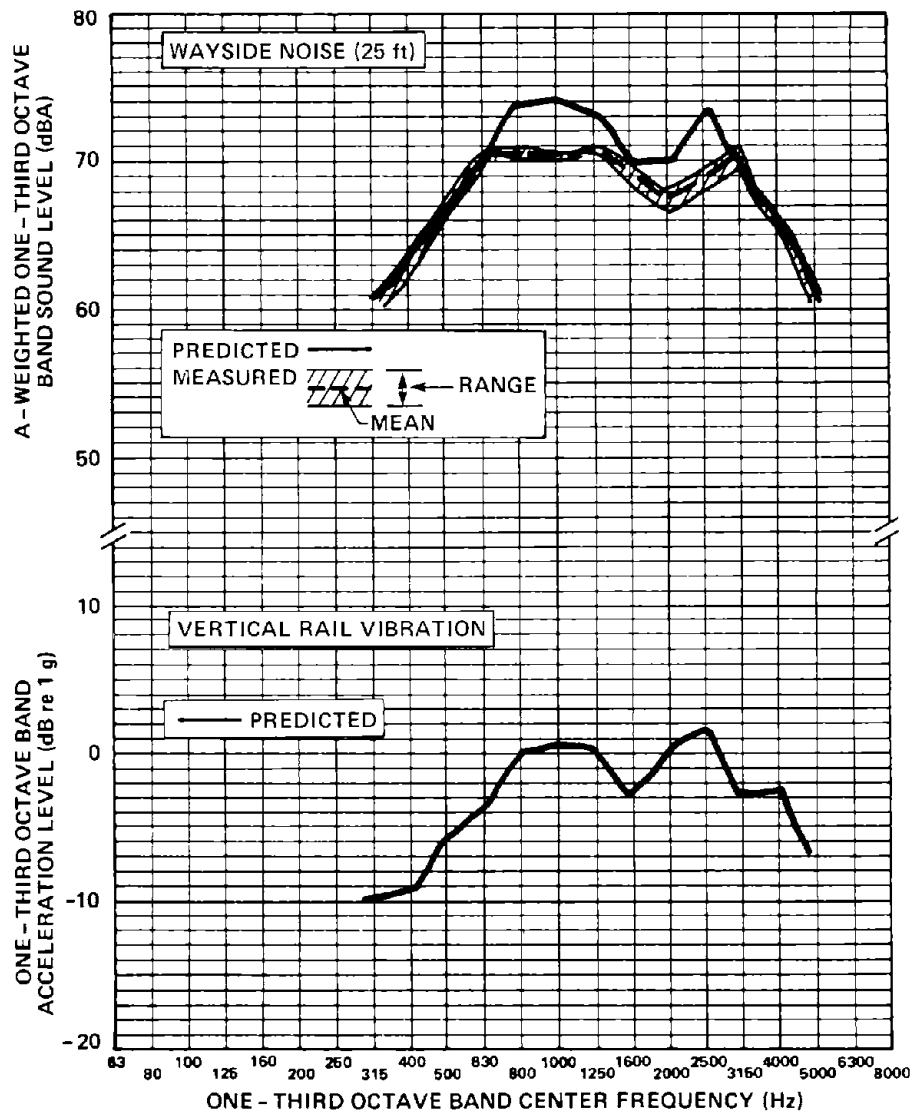


FIG. 89. COMPARISON OF MEASURED AND PREDICTED WHEEL/RAIL NOISE AND VIBRATION FOR THE SOAC AT 60 MPH; 2-SEC AVERAGING TIME.

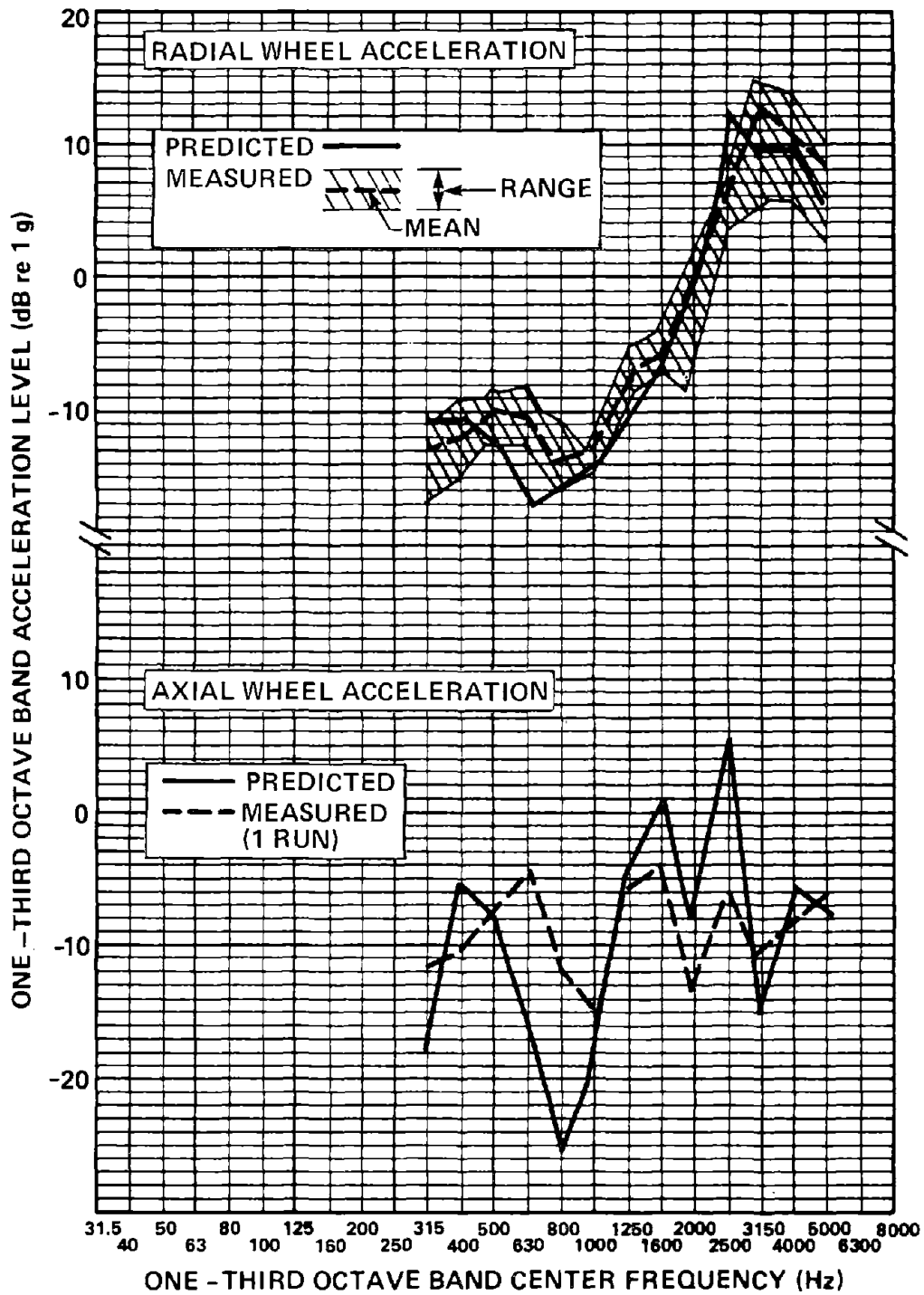


FIG. 89. (Cont.) COMPARISON OF MEASURED AND PREDICTED WHEEL/RAIL NOISE AND VIBRATION FOR THE SOAC AT 60 MPH; 2-SEC AVERAGING TIME.

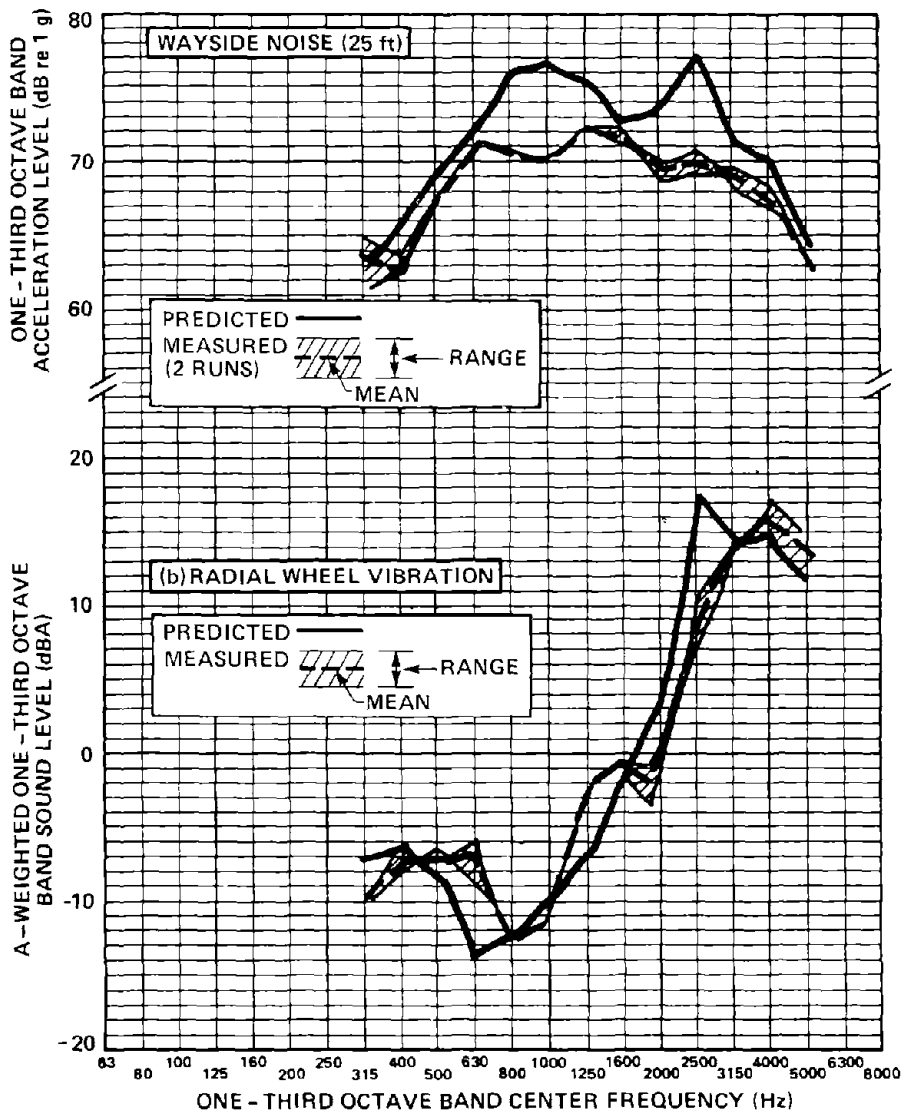


FIG. 90. COMPARISON OF MEASURED AND PREDICTED WHEEL/RAIL NOISE AND VIBRATION FOR THE SOAC AT 80 MPH; 2-SEC AVERAGING TIME.

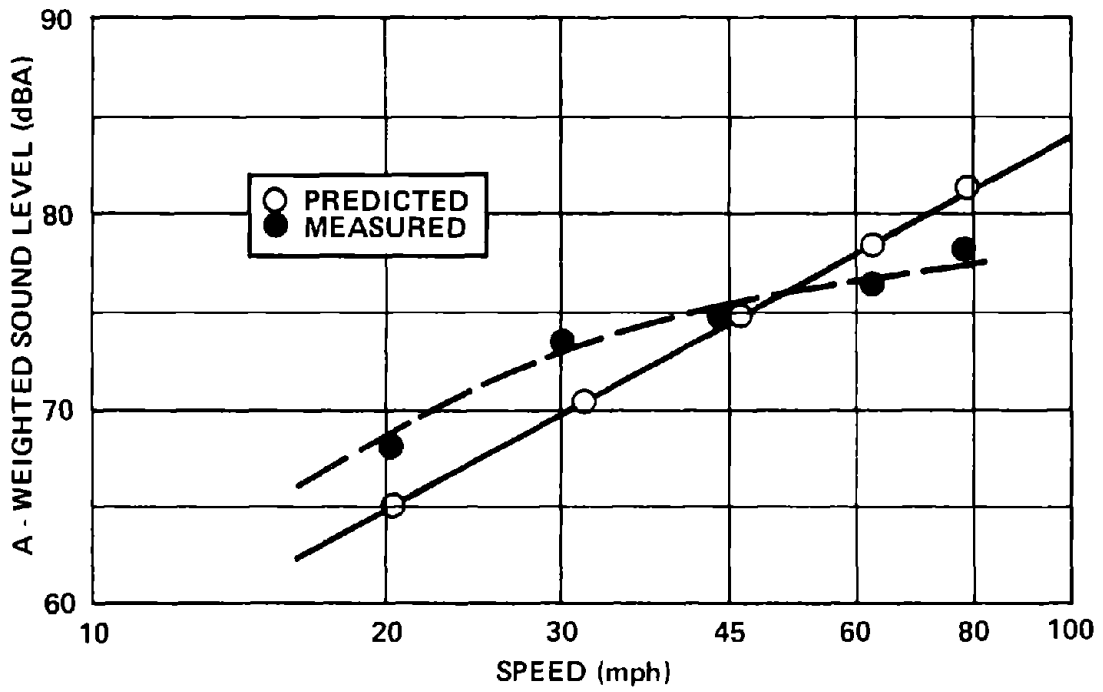


FIG. 91. COMPARISON OF MEASURED AND PREDICTED WAYSIDE NOISE AT 25 FT; 4-SEC AVERAGING TIME.

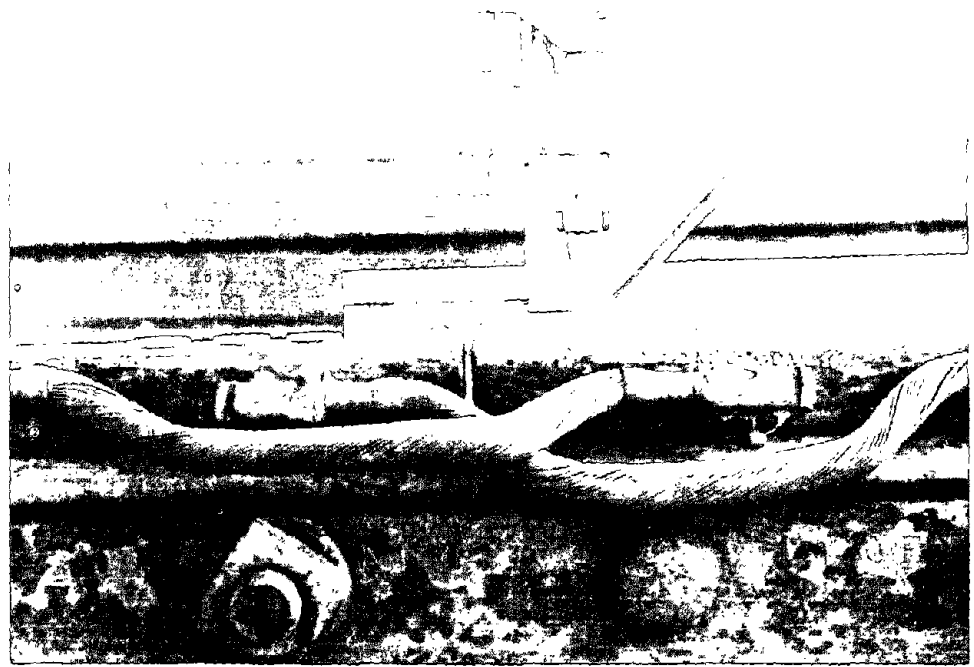


FIG. 92. TYPICAL RAIL JOINT ON THE TRANSIT TEST TRACK.

because of time and funding constraints and because we felt that such artificial changes might not be representative of the noise-generating properties of such joints in revenue service.

There is a gap and a slight dip at the joints (as illustrated in Fig. 93) but, according to the original theory [3], little increase in noise should be expected from those discontinuities. The wayside noise data in Fig. 94 are the same as on welded rail up to 45 mph. Above that speed, the jointed rail wayside noise data are 3 to 6 dBA higher. The reason for this change is unknown. Equally puzzling is the difference in the wayside noise spectra from welded and jointed rail, as illustrated in Fig. 95. The dashed curve from jointed rail and the solid curve from welded rail in the figure should be slightly different because the rail roughness is slightly different on the two test sections (see Fig. 76), i.e., the jointed rail is somewhat smoother. We have subtracted this difference in roughness between the two test sections from the wayside noise spectrum on welded rail to obtain the dotted curve in the figure. All other things being equal, the dotted and dashed curves in Fig. 95 should be the same. However, the wayside noise from the jointed rail is consistently higher in the mid frequencies. Whether this higher noise is due to the joints or some other source is presently unknown. For completeness, we also illustrate the difference in wayside noise spectra from jointed and welded rail at 60 and 80 mph in Fig. 96.

Figure 97 compares wheel vibration at 30 mph on welded and jointed rail. This is the only speed for which comparison data are available. Wheel vibration on the jointed rail test section is in the same range as on the welded test section.

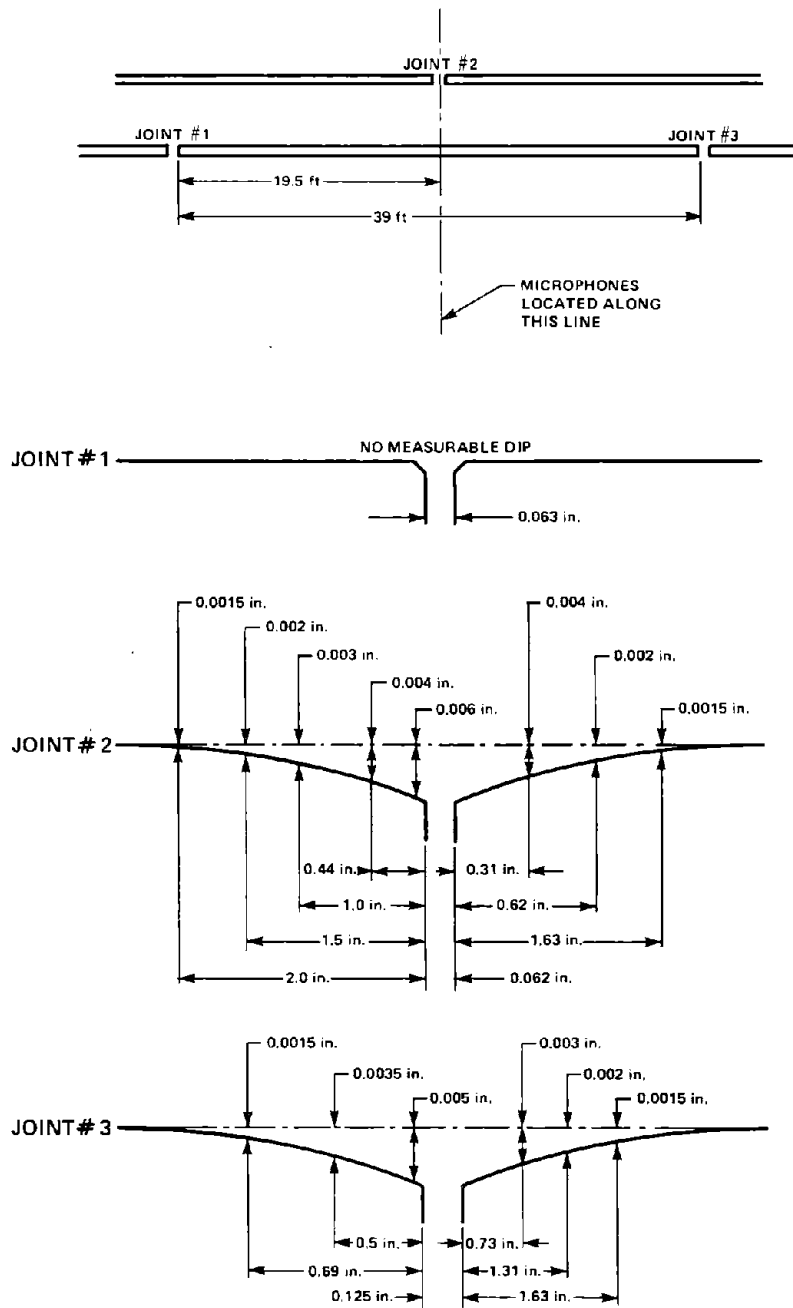


FIG. 93. RAIL JOINT GEOMETRY AT THE TEST SECTION.

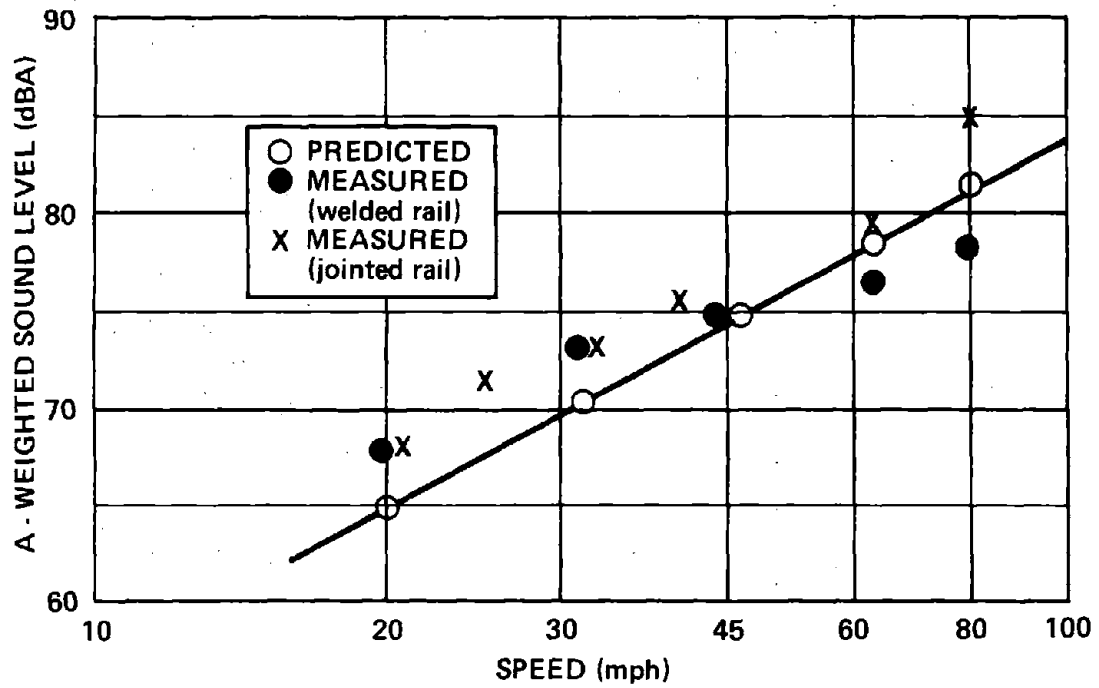


FIG. 94. COMPARISON OF MEASURED AND PREDICTED WAYSIDE NOISE AT 25 FT ON WELDED AND JOINTED RAIL; 4-SEC AVERAGING TIME.

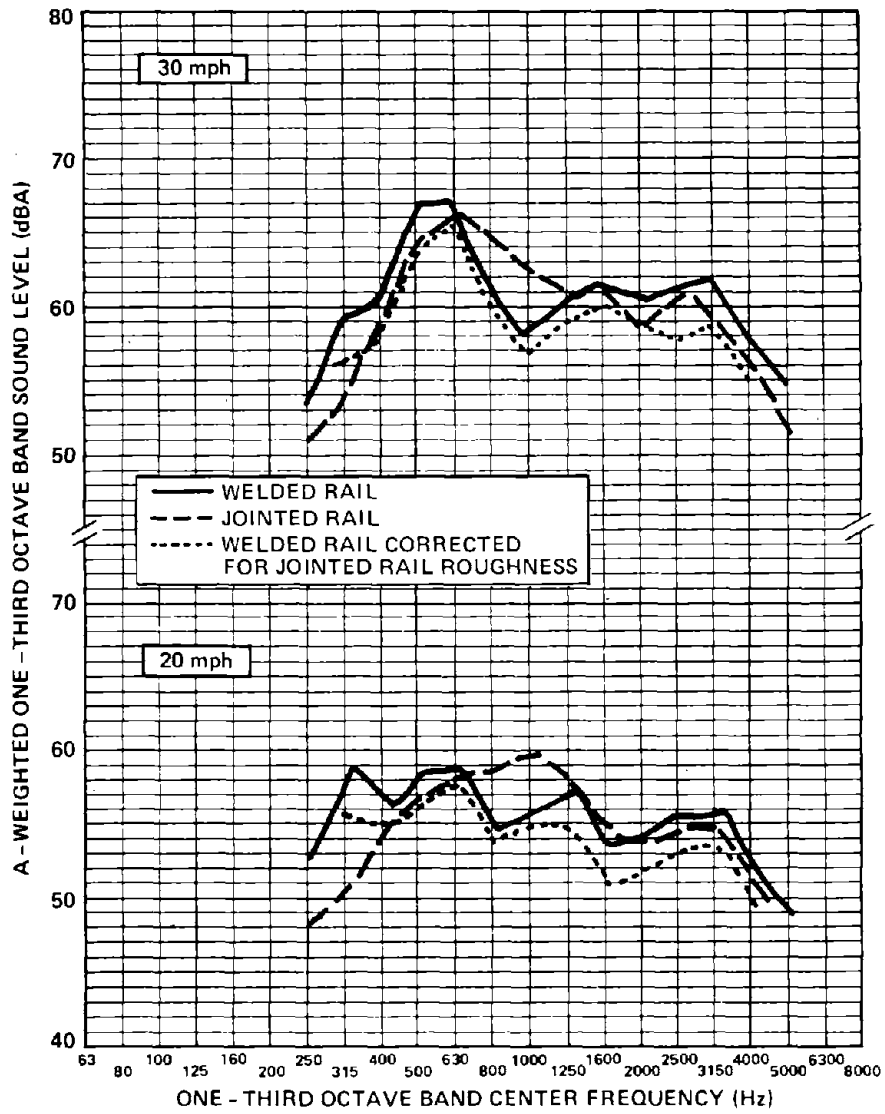


FIG. 95. WAYSIDE NOISE AT 25 FT ON WELDED AND JOINTED RAIL; 4-SEC AVERAGING TIME.

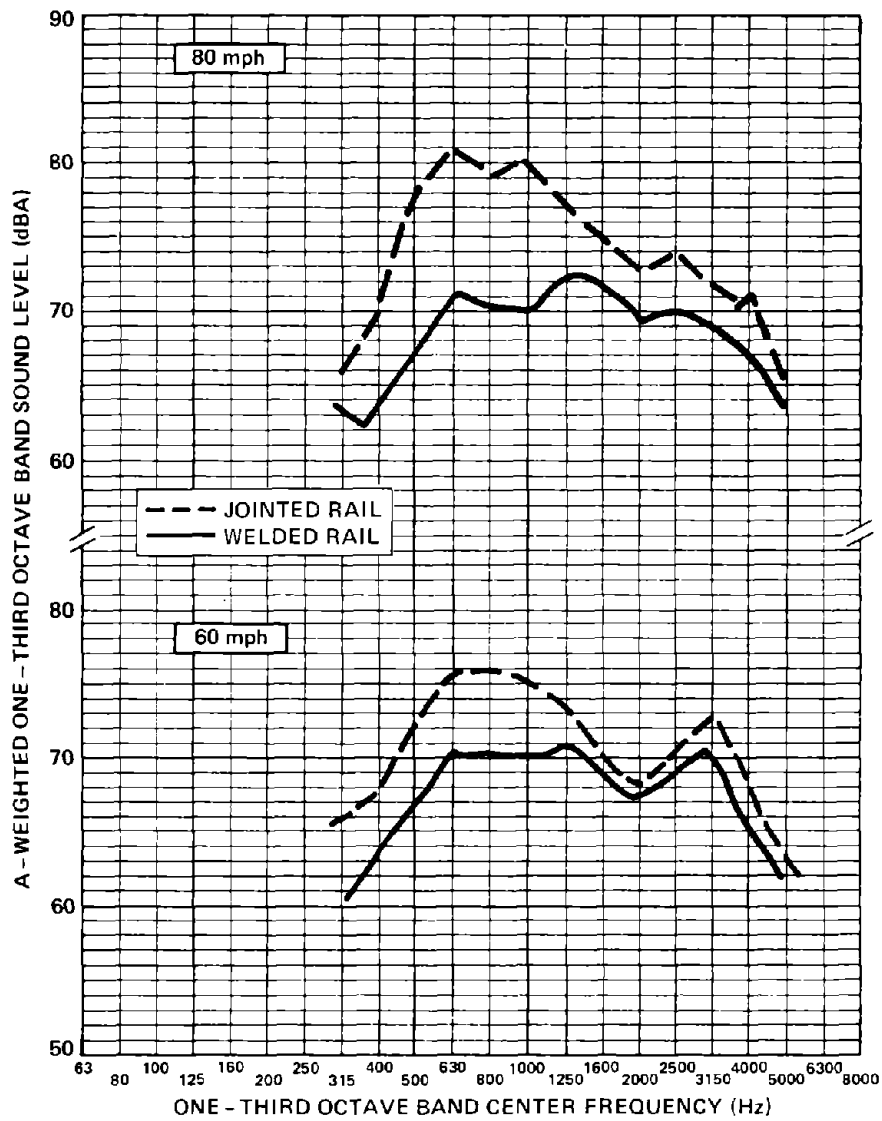


FIG. 96. WAYSIDE NOISE AT 25 FT ON WELDED AND JOINTED RAIL; 2-SEC AVERAGING TIME.

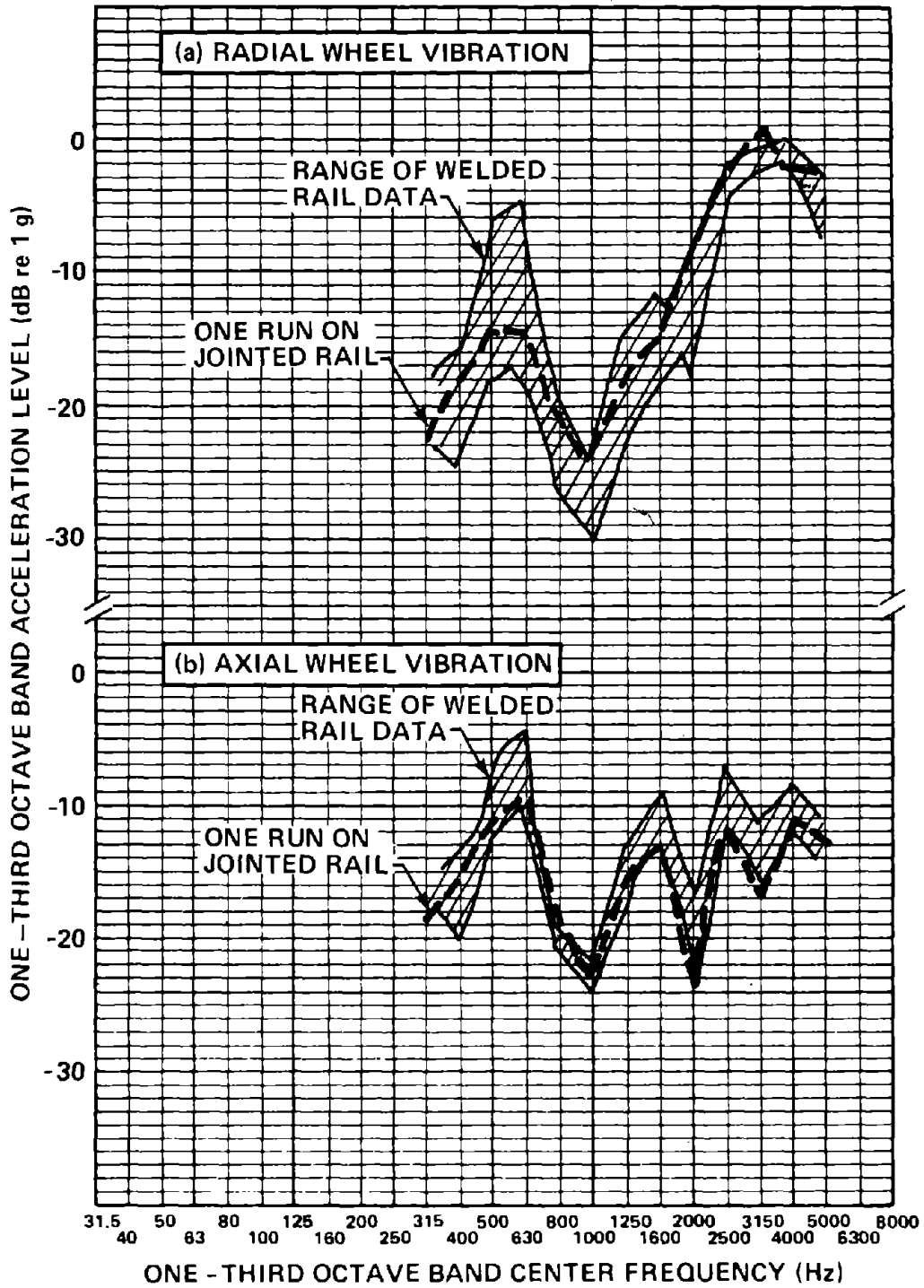


FIG. 97. COMPARISON OF WHEEL VIBRATION ON WELDED AND JOINTED RAIL AT 30 MPH.

It was not possible to extract any rail vibration data from the jointed rail test section because of the noise problem described in Sec. 3.1.2 and no welded/jointed comparisons of rail vibration are possible.

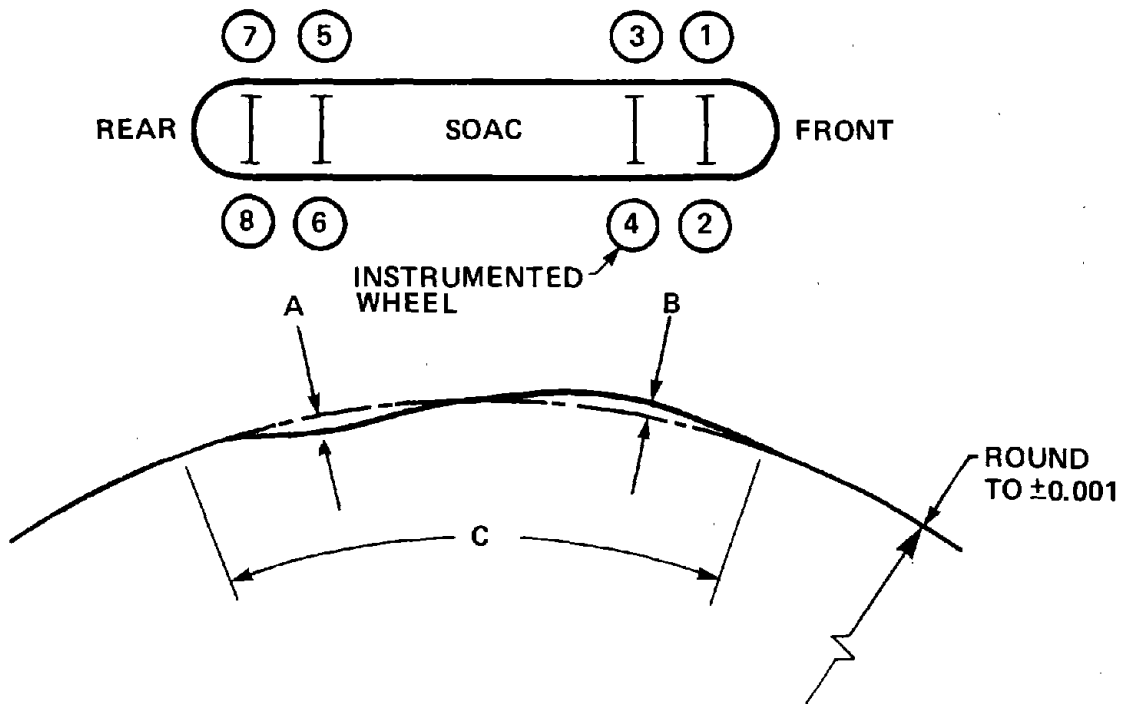
3.4.2 Wheel flats

One of the most common causes of excessive wheel/rail noise on operating rapid transit systems is wheel flats. These are usually generated during braking, when one wheel locks and slides along the rail. This sliding creates a worn spot on the wheel.

In order to validate our model of wheel flat equivalent roughness in Sec. 2.2.2, we attempted to generate flats on the wheels of the SOAC by locking the wheels of the car and pulling it with a locomotive. We initially thought that this would be a controlled way of generating flats, but it actually proved to be difficult. We were able to generate only the three flats shown in Fig. 98 on three wheels of the lead truck. The flats were generated from pulling the SOAC in reverse.

The geometry of the flats is somewhat different from that used to estimate equivalent roughness in Sec. 2.2.2. The raised area behind the flat was not accounted for. That area appears to consist of metal removed from the flatted area and redeposited on the running surface of the wheel. The geometry measurements shown in the figure were obtained with the car on a wheel-truing machine. The wheel was slowly turned to expose the flat spots. A dial gauge was used to obtain the height and depth, and a straight edge was used to obtain the width and length.

The SOAC with flatted wheels was operated on the same welded section of track that was used for the rolling noise tests. Figure 99 compares the wayside noise at 25 ft from the car with smooth and flatted wheels. The data, all for operation in the



DIRECTION OF ROTATION
FOR FORWARD MOTION

WHEEL NUMBER	A MAXIMUM FLAT DEPTH (in.)	B MAXIMUM FLAT HEIGHT (in.)	C FLAT LENGTH (in.)	FLAT WIDTH (in.)
2	0.001	0.002	$\frac{1}{2}$	$\frac{3}{8}$
3	0.004	0.006	$1\frac{1}{8}$	$\frac{3}{4}$
4	0.004	0.005	$\wedge\frac{1}{16}$	$\frac{5}{8}$

FIG. 98. WHEEL FLAT GEOMETRY.

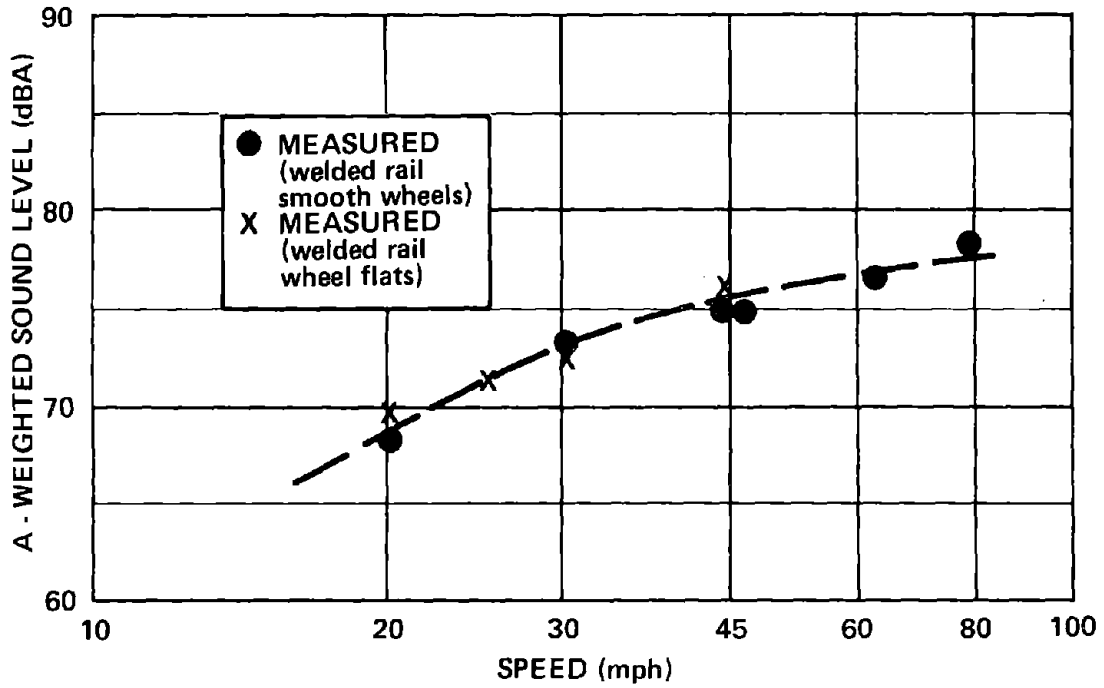


FIG. 99. COMPARISON OF MEASURED WAYSIDE NOISE AT 25 FT FOR SMOOTH AND FLATTED WHEELS (NORMALIZED TO A 4-SEC AVERAGING TIME).

forward direction, show little or no increase caused by the presence of the flats, even though the banging from the flats could be distinctly heard as the train passed. Since the 4-sec averaging time* used to analyze the data is longer than the time it takes the train to pass the microphone, the data in the figure are the average noise during the train passby. That average noise is not greatly affected by the impacts from the wheel flats, which have a duration of only a few milliseconds [3].

Figure 100 compares the rail roughness at the test site with the equivalent roughness due to the wheel flats. To estimate the equivalent roughness, we have assumed that there are four flats (0.5 flats per wheel) with a length of 1/2 in. The wheel flat equivalent roughness formula - Eq. (100) - was designed to model that portion of the flat where material has been removed from the wheel, region A in Fig. 98. Here, we are assuming that the geometry of region B is the same as, but opposite in sign to, region A. Although that assumption is not strictly correct, it does provide a reasonable first-order estimate of the wheel flat noise-generating capability. As Fig. 99 shows, these wheel flats increase the apparent roughness only at long wavelengths. Figure 100c shows that the resulting theoretical increase in noise and vibration is small and confined to low frequency. Figures 100a and 100b compare the measured wayside noise and rail vibration (one accelerometer on the rail foot) at 20 mph. The figures show at least qualitative agreement between the predicted increase in noise and vibration and the measured increase. Unfortunately, because the flats are so small and few in number, the increase in noise and vibration is small. Since the scatter in the measured

*The data at 45 mph were actually averaged for 2 sec. These have been reduced by 3 dB to normalize the data to a 4-sec averaging time.

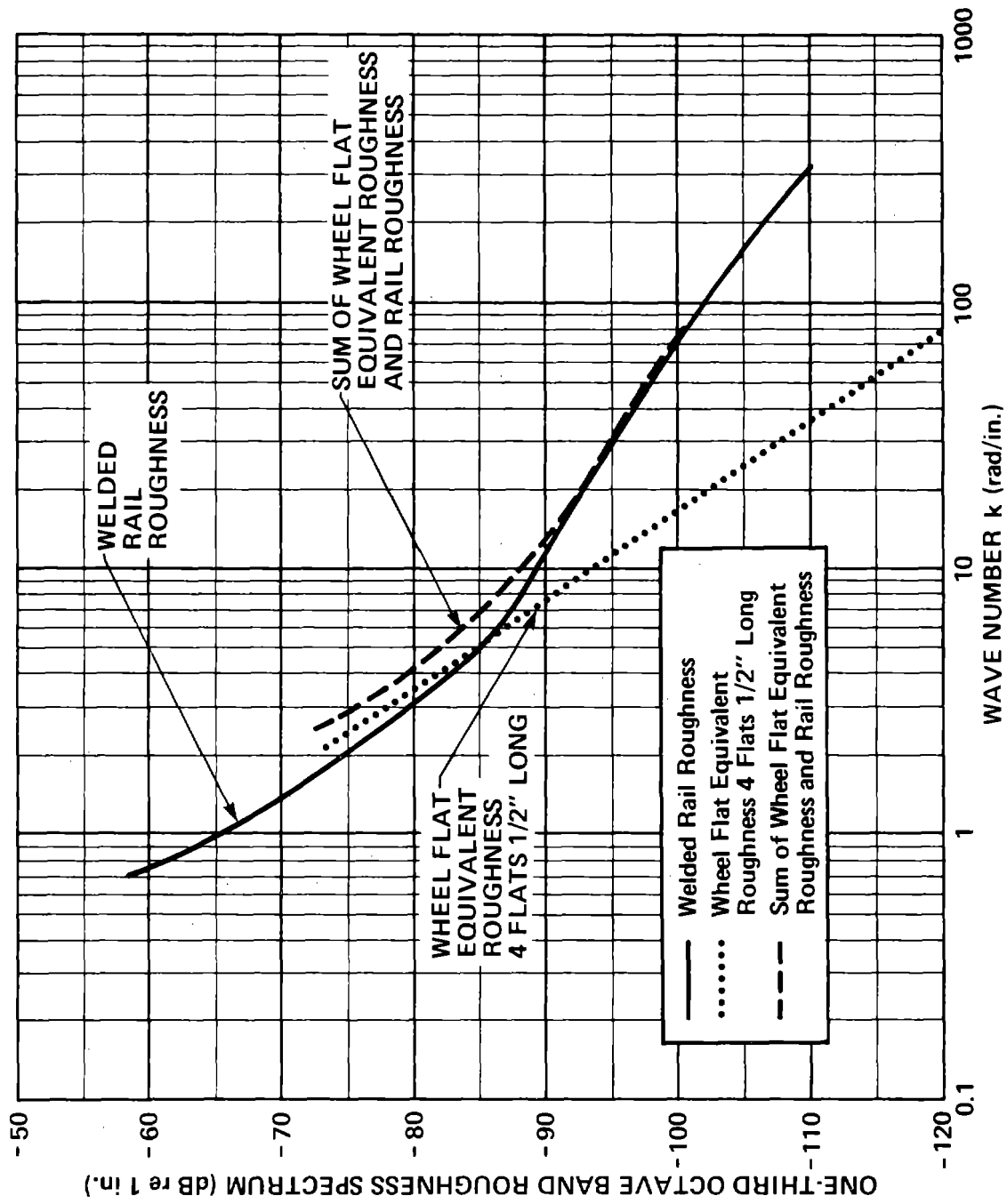


FIG. 100. RAIL ROUGHNESS SPECTRA AT WELDED RAIL TEST SITE COMPARED WITH EQUIVALENT ROUGHNESS DUE TO WHEEL FLATS.

data is almost as large as the change in noise and vibration caused by the flats, it is difficult to validate the predictions quantitatively with any certainty. However, Fig. 101 does indicate that the analytical model provides a reasonable estimate of the effects of wheel flats on noise and vibration.

3.5 Rail Response

The rail responds in a somewhat complex way to the passage of a train. Figure 102 illustrates that response for the SOAC passing by at 30 mph.

For the vertical direction (Fig. 102a), we have summed the signals from accelerometers 5 and 6, divided by two, and taken the spectrum as shown in the figure. That result corresponds to pure vertical translation of the rail. The spectrum of the difference of these two channels, also shown in the figure, corresponds to the rocking of the rail about its axis. Except for a peak at 630 Hz, the rail responds essentially in pure vertical translation with little rocking up to 1250 Hz. Above that frequency, rocking becomes as important as vertical translation. The spectrum of the signal from accelerometer 5 is also shown in Fig. 102a. It illustrates that a single accelerometer on the rail foot provides a good measure of the vertical translation of the rail up to 1250 Hz.

For lateral vibration (Fig. 102b), similar signal processing was carried out for accelerometers 1 and 4. The spectrum of the sum of the two signals divided by two (i.e., the average) corresponds to pure lateral translation, whereas the spectrum of the difference corresponds to rocking about the rail axis. For the most part, lateral translation dominates rocking up to about 2000 Hz, although at 630 Hz rocking does become important.

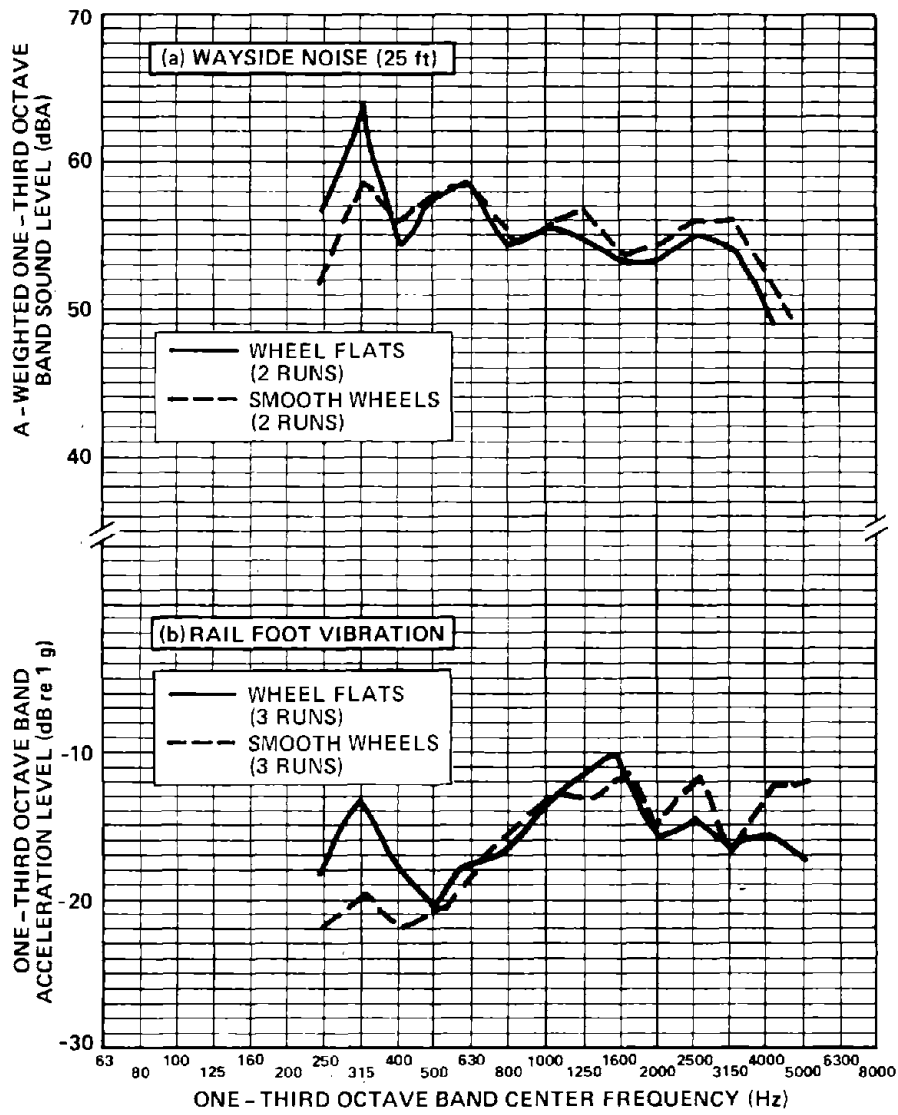


FIG. 101. COMPARISON OF NOISE AND VIBRATION WITH AND WITHOUT WHEEL FLATS.

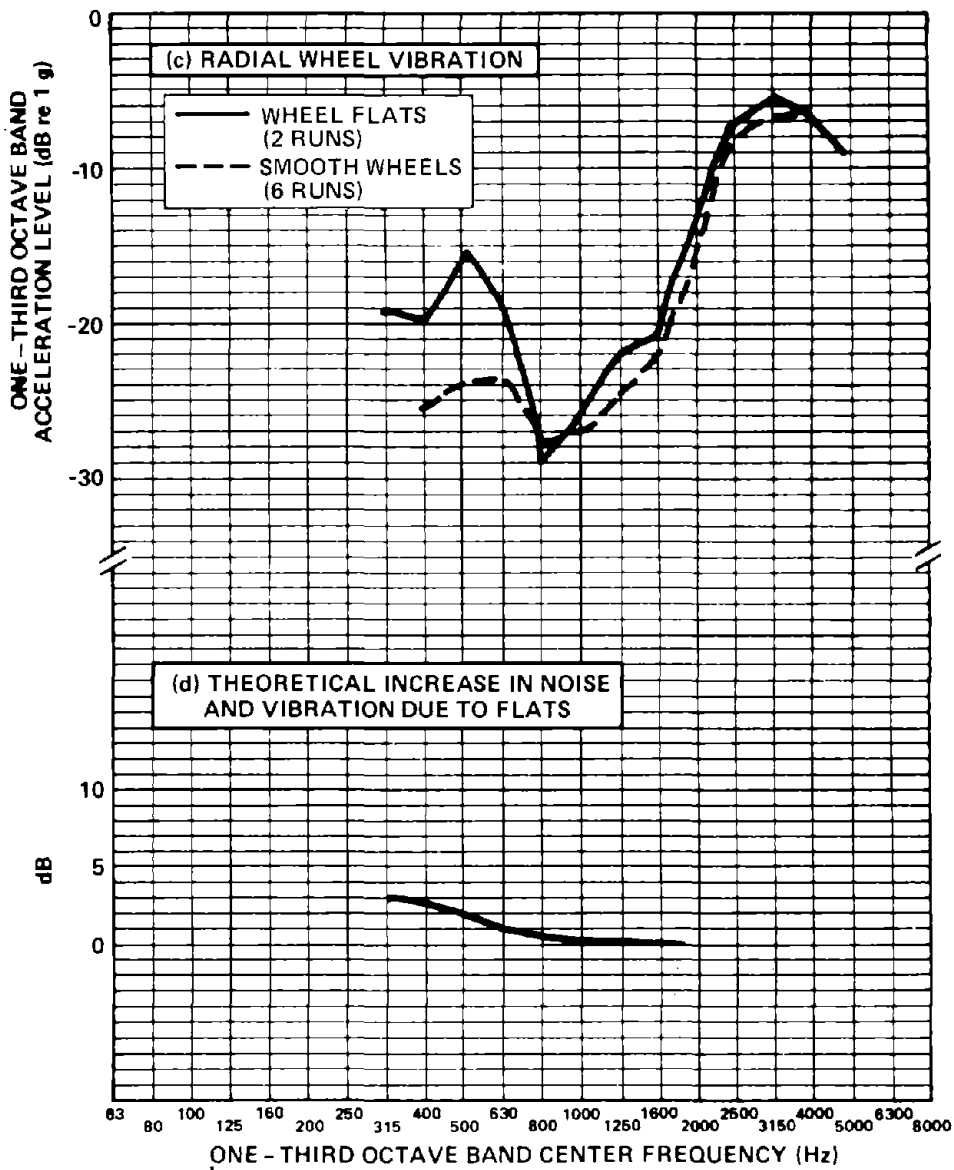


FIG. 101. (Cont.) COMPARISON OF NOISE AND VIBRATION WITH AND WITHOUT WHEEL FLATS.

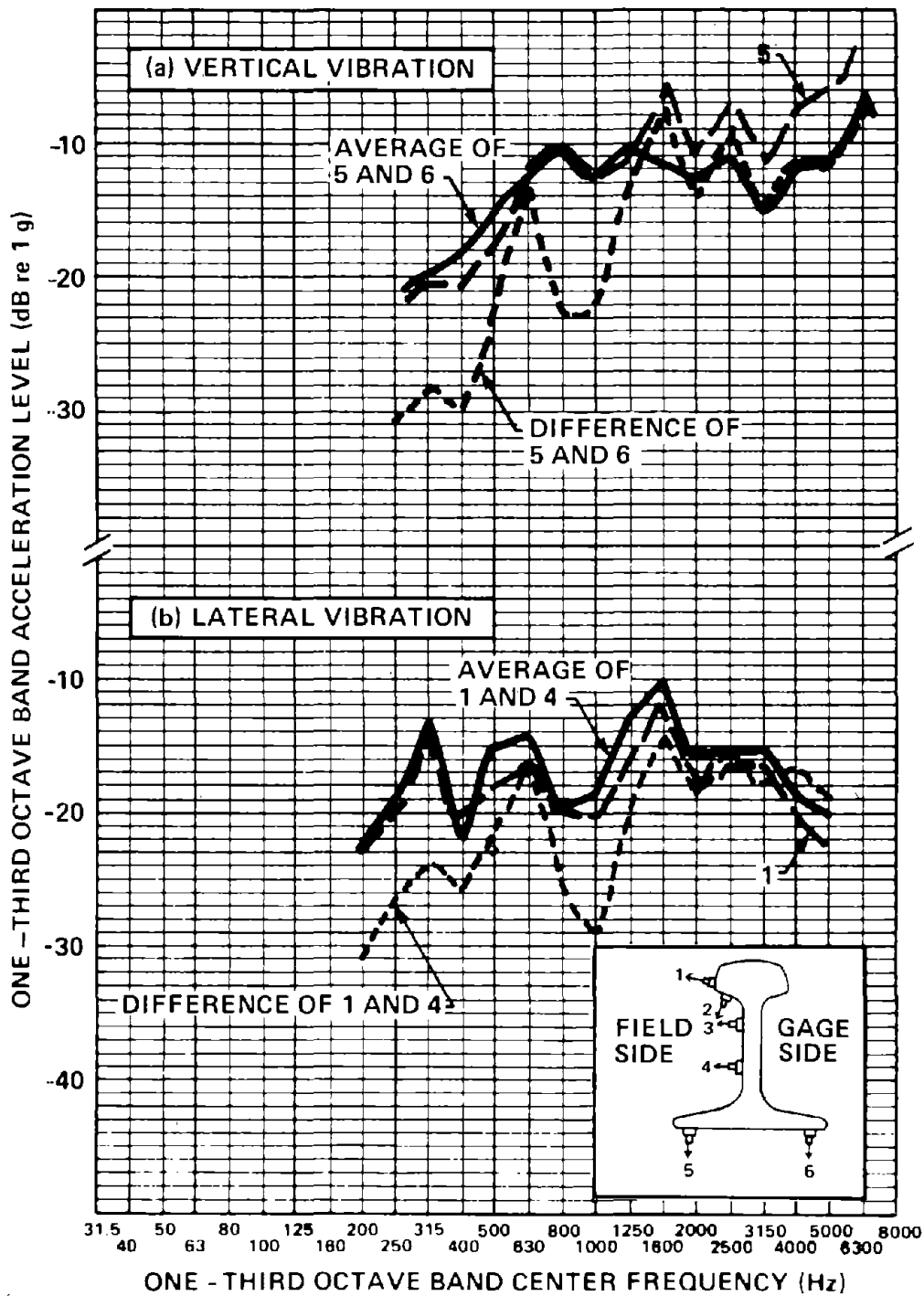


FIG. 102. RAIL VIBRATION DURING PASSAGE OF SOAC AT 30 MPH (NORMALIZED TO A 4-SEC AVERAGING TIME).

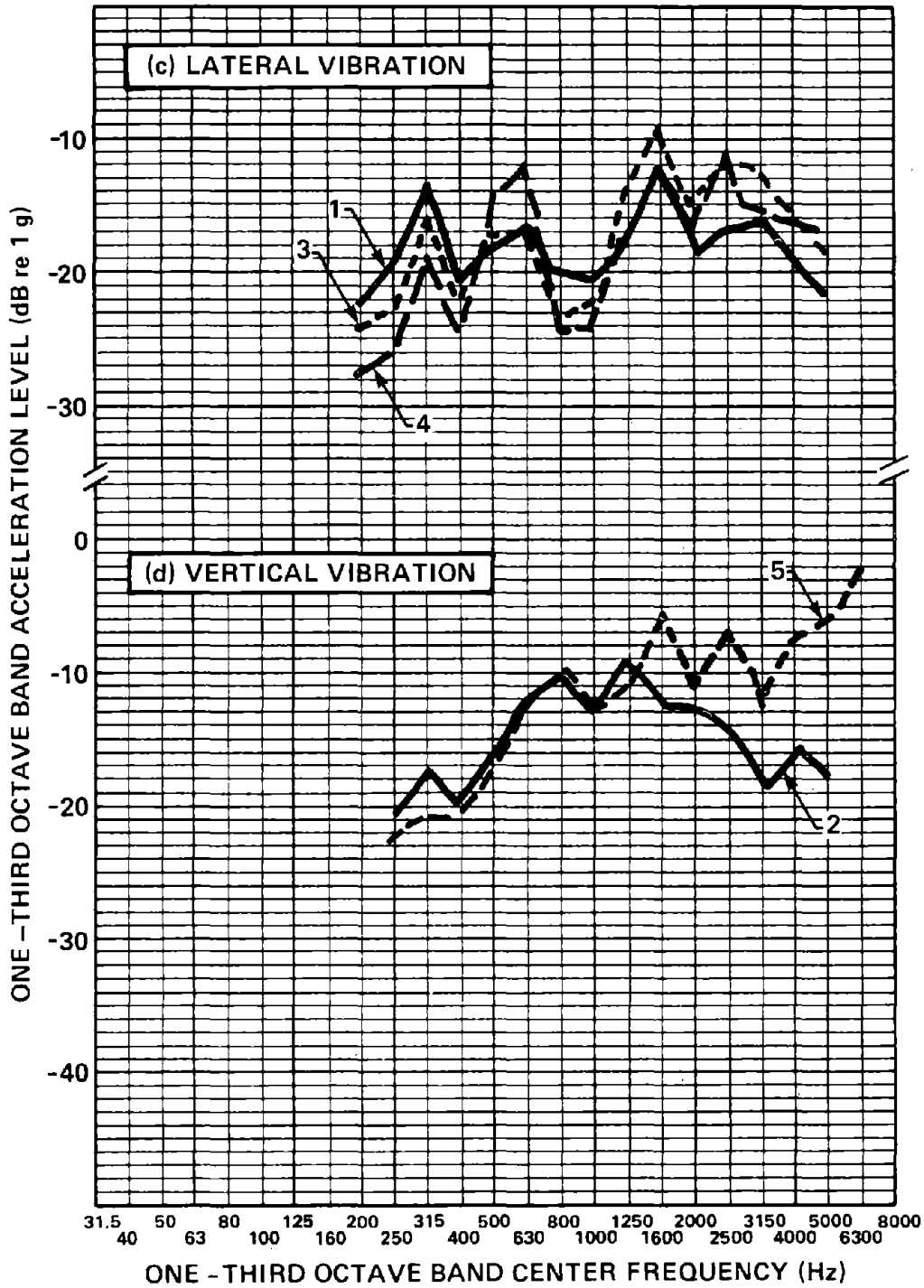


FIG. 102. (Cont.) RAIL VIBRATION DURING PASSAGE OF SOAC AT 30 MPH (NORMALIZED TO A 4-SEC AVERAGING TIME).

Figures 102c and 102d present additional acceleration data from the rail. Although these data are for only one speed, they are typical of data taken at both higher and lower speeds. It is particularly interesting to note that both lateral translation of the rail and rocking peak in those frequency bands where the axial wheel vibration peaks, are usually those frequency bands that contain the axial resonant frequencies of the wheel, e.g., 500/630 Hz, 1600 Hz, and 2500 Hz. This observation is consistent with the picture of wheel/rail lateral coupling presented in Sec. 2.

4. SENSITIVITY ANALYSIS

Having validated the analysis to the extent possible in the previous section, we now use the analytical model to determine the sensitivity of the noise radiated by the wheel/rail system to changes in the values of the parameters defining that system. We begin by selecting the parameter values of a baseline system. We then calculate the wayside noise radiated by that system and examine the estimated changes in the noise as we vary system parameter values within realistic limits.

4.1 Baseline System

The baseline system that we will use in this section is defined by:

- Wheel and rail roughness as measured on the MBTA (see Fig. 103)
- 30-in.-diameter SOAC wheel
- 10,000-lb wheel load
- 100-lb/yd welded rail on wood ties and ballast
- Rail loss factor as defined in Fig. 104
- Two-car train
- Speed of 30 mph
- Surrounding ground surface with a specific flow resistance 1000 cgs rays, e.g., dirt and loose stones.

To compare the effects of various parameter value combinations on the noise, we will use the overall A-weighted sound level at 25 ft from the track centerline, averaged for 8 sec as the train passes by.

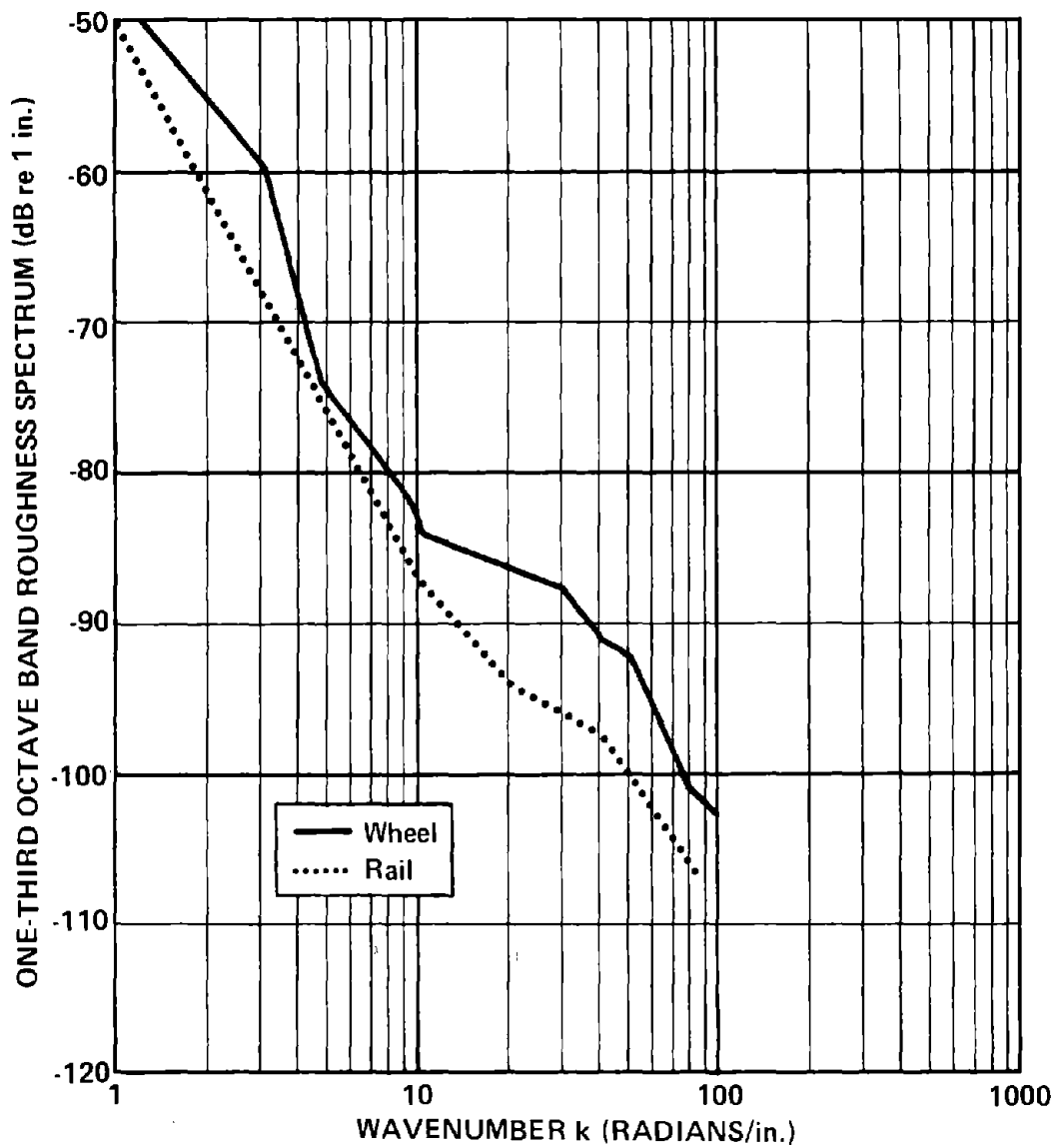


FIG. 103. BASELINE WHEEL AND RAIL ROUGHNESS.

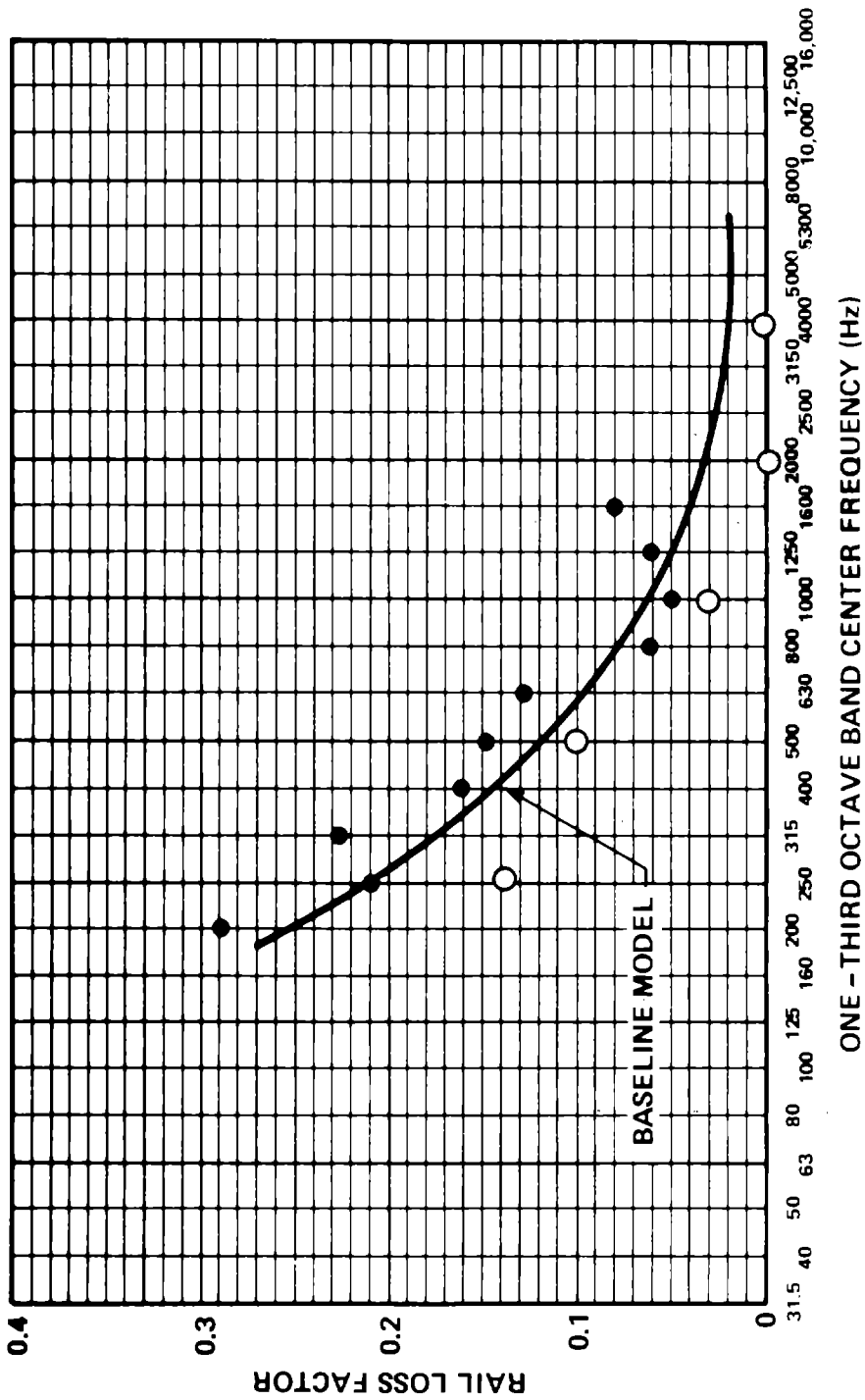


FIG. 104. BASELINE RAIL LOSS FACTOR. (• Naake [11]; o Remington, Rudd, and Ver [3].)

With the above system parameter values, we have calculated wheel/rail noise and vibration using the analytical model of Sec. 2. Figure 105 presents predictions of wheel and rail noise radiation and vibration. For these system parameter values, which are typical of operating transit systems in the United States, the rail dominates the sound radiation in the mid frequencies, whereas the wheel dominates at high and low frequencies. Note that at those frequencies where the wheel dominates the sound radiation, the radial vibration of the wheel is primarily responsible for that sound radiation.

4.2 Parameter Value Changes

The following parameters have been examined to determine their effect on wheel/rail noise:

- Wheel radius
- Wheel tread thickness
- Wheel web thickness
- Rail weight
- Wheel damping
- Wheel load
- Wheel/rail contact stiffness
- Wheel/rail contact area.

We also looked into the effects on noise caused by changes in roughness from

- Wheel truing
- Rail grinding

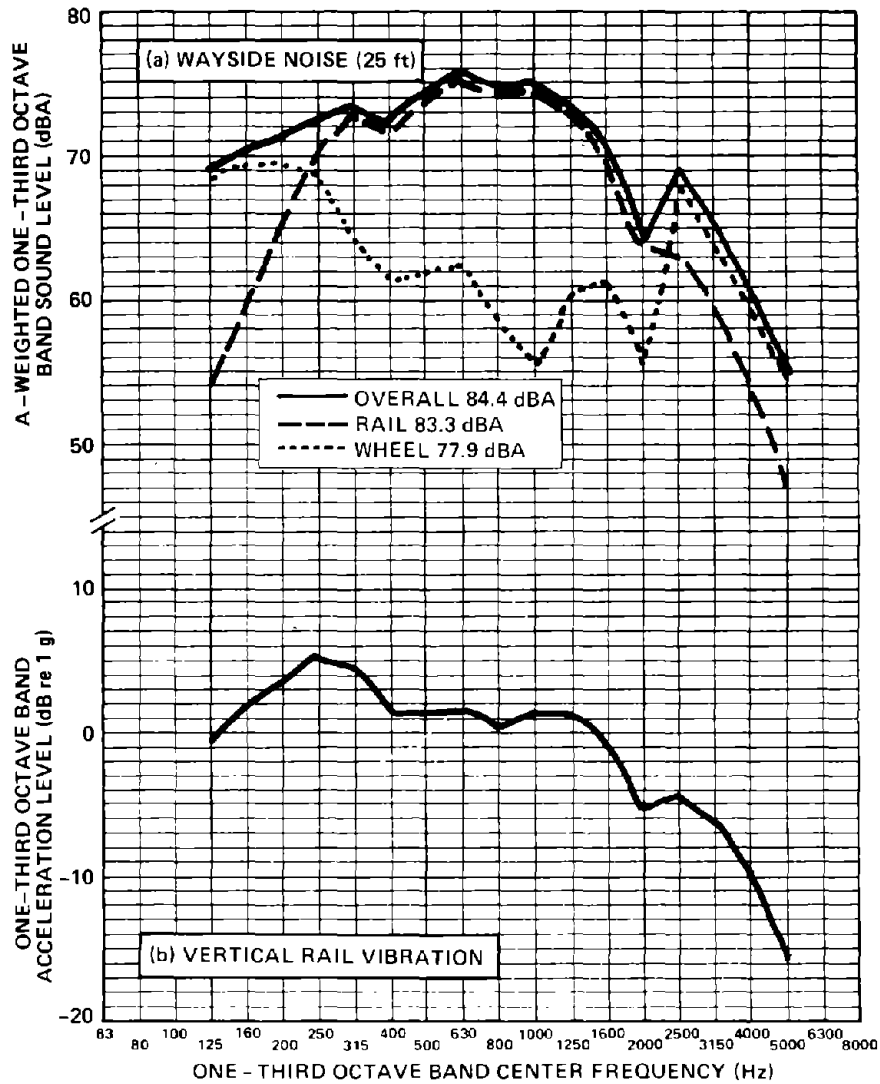


FIG. 105. BASELINE SYSTEM PREDICTIONS OF WHEEL/RAIL NOISE AND VIBRATION.

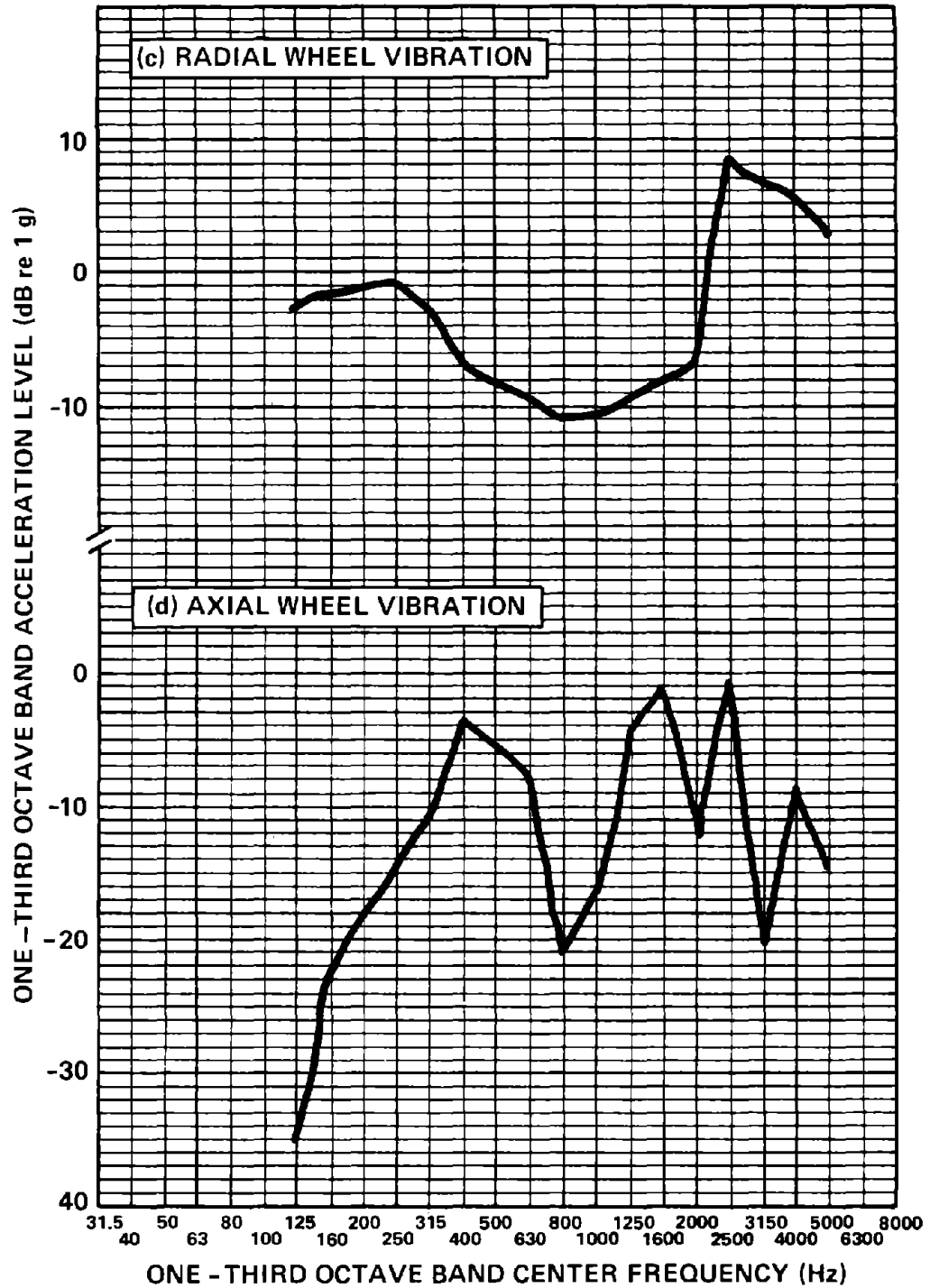


FIG. 105. (Cont.) BASELINE SYSTEM PREDICTIONS OF WHEEL/RAIL NOISE AND VIBRATION.

- The presence of rail joints
- The presence of wheel flats.

Wheel Radius

Figure 106 shows the changes in wayside noise at 25 ft from the track centerline caused by changes in wheel size. For 24- to 36-in.-diameter wheels there is little change in noise, assuming that other wheel dimensions such as tread thickness, tread width, and web thickness, remain unchanged.

Wheel Tread Thickness

Changing the thickness of the wheel tread, nominally 2 3/8 inch on the SOAC, over a range of 1 to 3 inches has little effect on noise, as shown in Fig. 107, although at very low tread thicknesses wheel radiation increases sufficiently so that overall noise is slightly increased.

Wheel Web Thickness

As Fig. 108 shows, increasing the web thickness decreases the sound radiated by the wheel. However, for this baseline case, wheel radiation is already well below rail radiation and this decrease in wheel radiation has little effect on total noise.

Rail Weight

Increasing rail weight results in a small increase in total noise, as illustrated in Fig. 109. Although the heavier rail has a higher impedance and responds less than lighter rail, its greater radiating area results in increased rail sound radiation. The higher impedance of the heavier rail also causes the wheel to respond more than on light rail, causing increased wheel sound radiation.

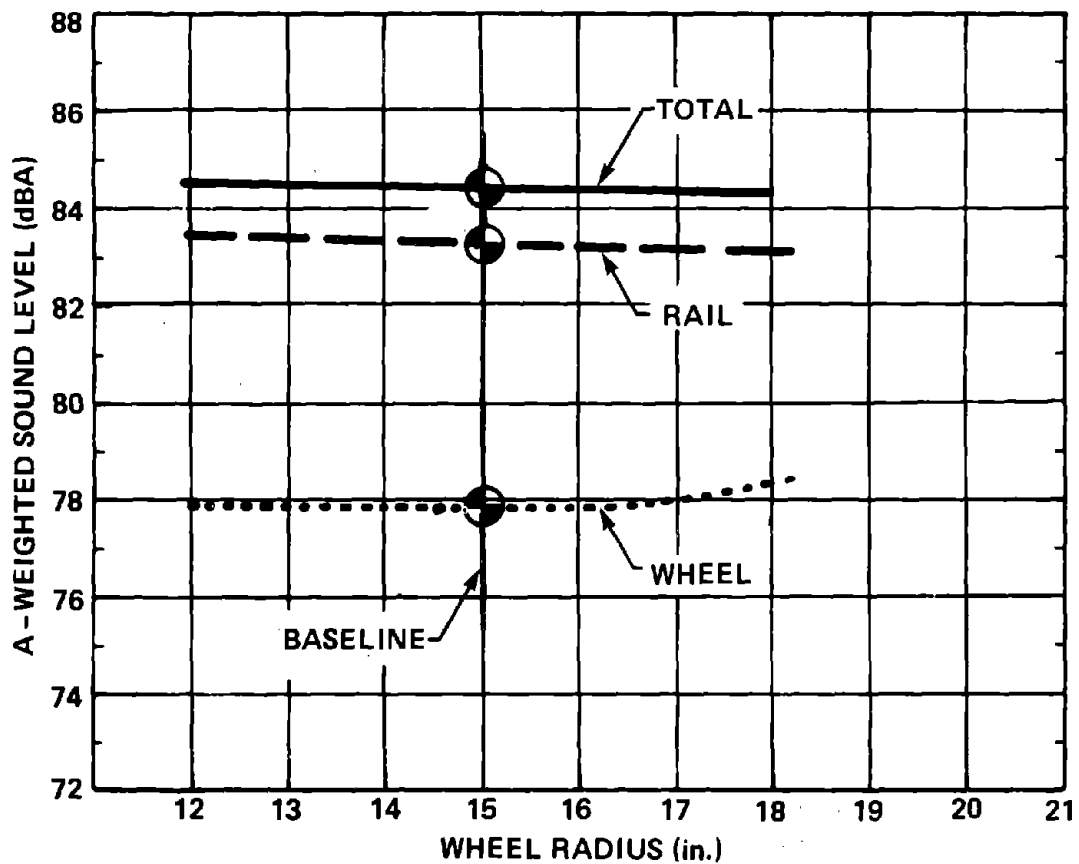


FIG. 106. ESTIMATED EFFECT OF CHANGES IN WHEEL RADIUS ON WAYSIDE NOISE AT 25 FT; TWO-CAR TRAIN AT 30 MPH.

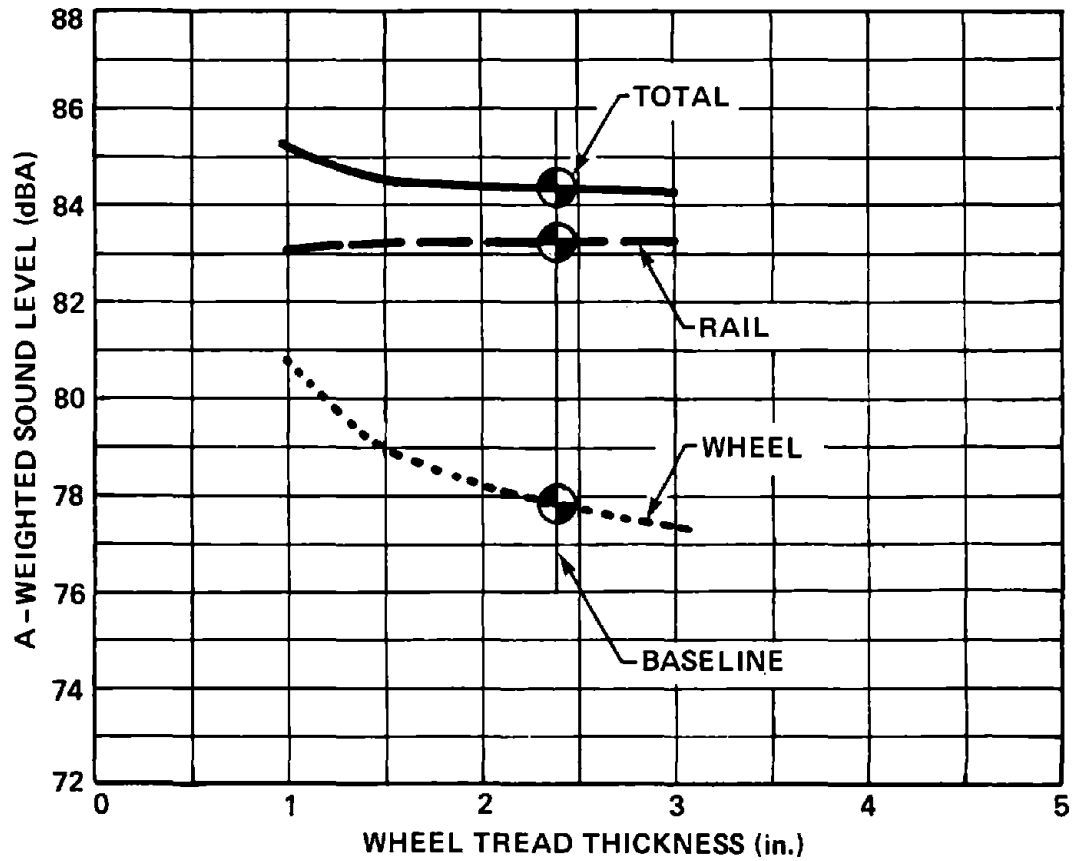


FIG. 107. ESTIMATED EFFECT OF WHEEL TREAD THICKNESS CHANGES ON WAYSIDE NOISE AT 25 FT; TWO-CAR TRAIN AT 30 MPH.

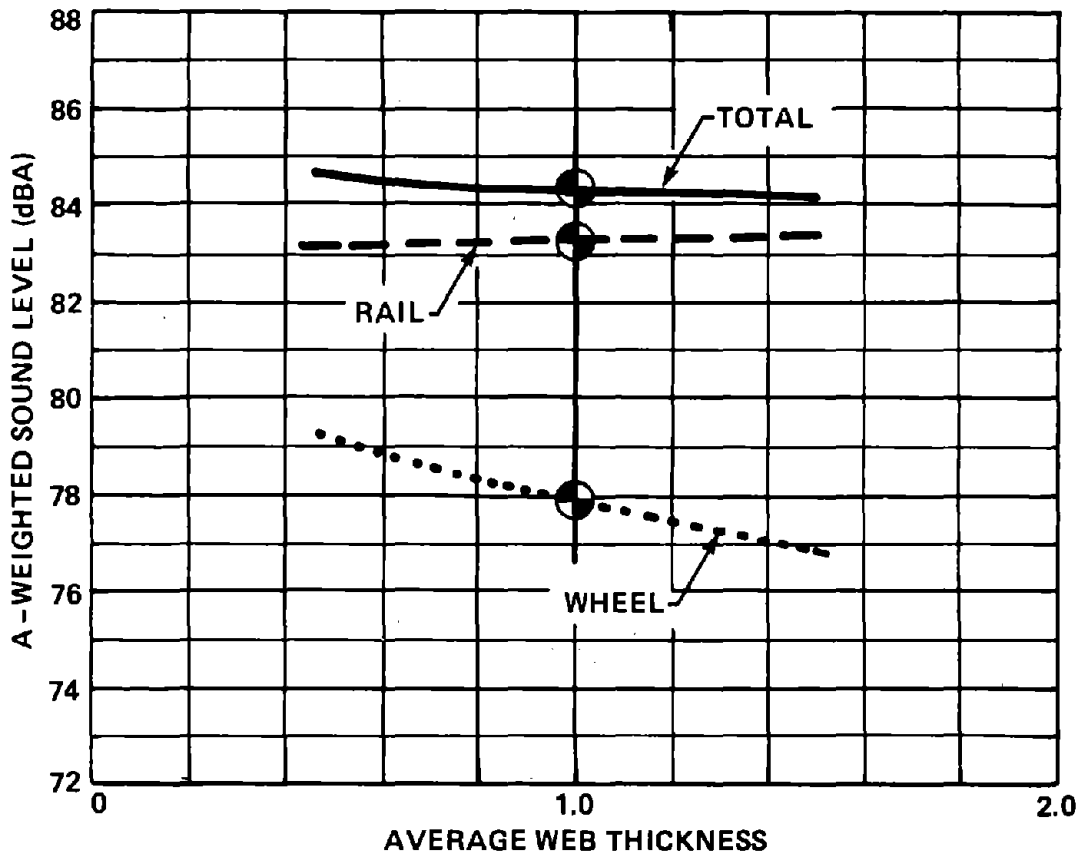


FIG. 108. ESTIMATED EFFECT OF WHEEL WEB THICKNESS ON WAYSIDE NOISE AT 25 FT; TWO-CAR TRAIN AT 30 MPH.

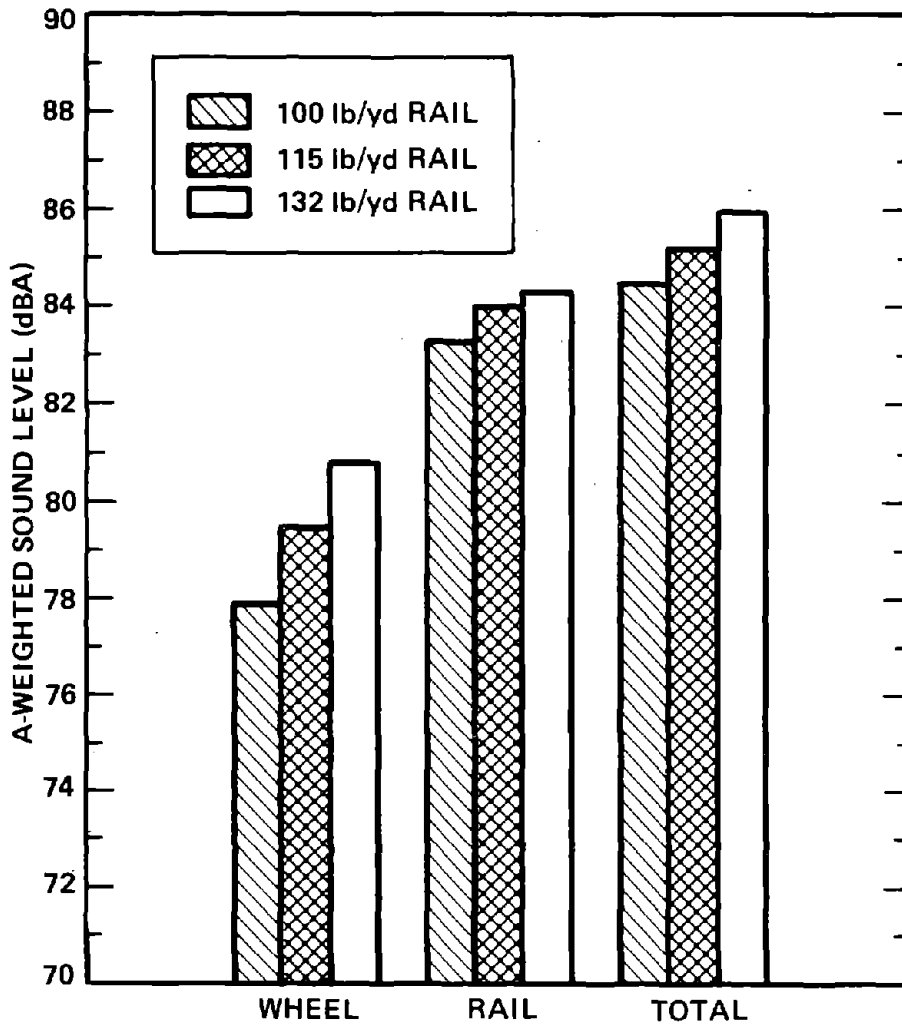


FIG. 109. ESTIMATED EFFECT OF RAIL WEIGHT ON WAYSIDE NOISE AT 25 FT; TWO-CAR TRAIN AT 30 MPH.

Wheel Damping

Figure 110 shows that increasing the damping of the wheel has little effect on the overall radiated sound. Although wheel damping is known to decrease squeal noise in the field, it has little impact on rolling noise. The impact of wheel damping is small because in rolling noise, the wheel and rail response amplitudes are limited to be no more than the amplitude of the roughness on wheel and rail running surfaces. Increasing the wheel damping simply increases its impedance at resonance and decreases its impedance at its antiresonant frequencies. The wheel response is greatest at its resonant frequencies, where the wheel impedance is typically much less than the rail impedance. Increasing the wheel impedance at resonance by damping will have little effect on the wheel response until the wheel impedance becomes comparable to the rail impedance. In general, damping the wheel cannot increase the wheel impedance at resonance enough to make that impedance comparable to the rail's. Consequently, little decrease in wheel sound radiation occurs with additional damping.

The rail response, on the other hand, tends to be greatest at the wheel antiresonant frequencies where the wheel impedance is much greater than the rail impedance. For reasons similar to those given for the wheel, the rail response decreases only slightly with increases in wheel damping.

Wheel Load

Increasing the wheel load (see Fig. 111) decreases the sound radiation, but not substantially. For example, if one increases the wheel load from 10,000 to 14,000 lb (a typical increase from an empty to a full transit car), the decrease in noise would be less than 1 dBA.

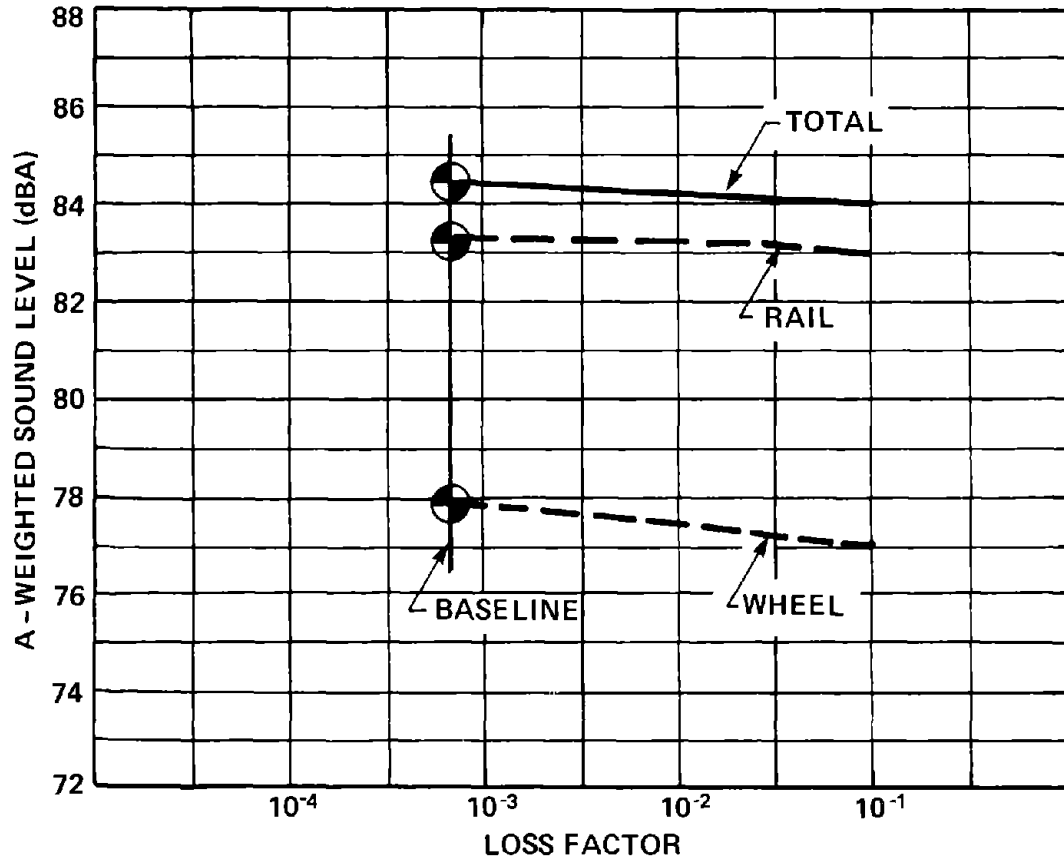


FIG. 110. ESTIMATED EFFECT OF WHEEL DAMPING ON WAYSIDE NOISE AT 25 FT; TWO-CAR TRAIN AT 30 MPH.

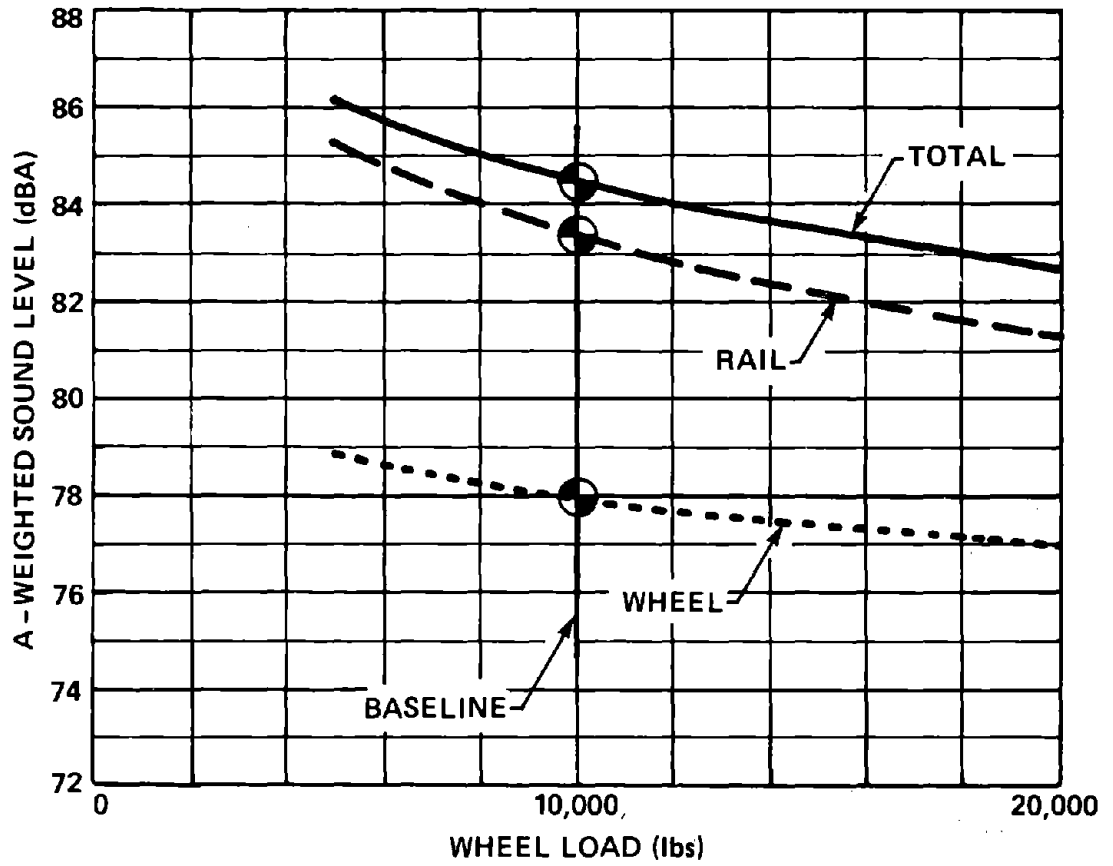


FIG. 111. ESTIMATED EFFECT OF WHEEL LOAD ON WAYSIDE NOISE AT 25 FT; TWO-CAR TRAIN AT 30 MPH.

The sensitivity of the wayside noise to wheel load is due to two competing factors: increasing contact area and increasing contact stiffness with increasing load. As we will see later in this section, increasing the contact area decreases the noise, whereas increasing the contact stiffness increases the noise. The former effect is stronger in the example in Fig. 111, and the noise decreases with increased load.

Contact Stiffness

When the wheel rests on the rail, there is local elastic deformation in both at the point of contact. This local deformation is different from the gross bending deformation of the rail and the bending and torsional deformation of the wheel that radiate sound. If the contact stiffness is low enough, irregularities on the running surfaces of the wheel and rail will produce mostly local deformation and thereby reduce the sound radiated by the wheel and rail. Figure 112 illustrates this effect.

However, substantial changes in contact stiffness are required to obtain significant noise reduction, and that noise reduction is confined chiefly to the rail. Wheel sound radiation actually increases slightly, mostly because of a well-damped* resonant interaction between the wheel mass and contact stiffness at low frequency that dominates the wheel response. As the contact stiffness decreases, the frequency at which this interaction occurs moves lower. For example, as shown in Fig. 113, wheel sound radiation is enhanced around 500 Hz, when the contact stiffness is reduced from $3 \cdot 10^7$ lb/in. to $3 \cdot 10^6$ lb/in. For still lower contact stiffness of 10^6 lb/in. and $3 \cdot 10^5$ lb/in., the enhancement occurs around 200 and 125 Hz, respectively. Because the wheel sound radiation is dominated by low frequencies, this

*The resonance is damped because bending waves in the rail tend to carry energy away from the point of contact.

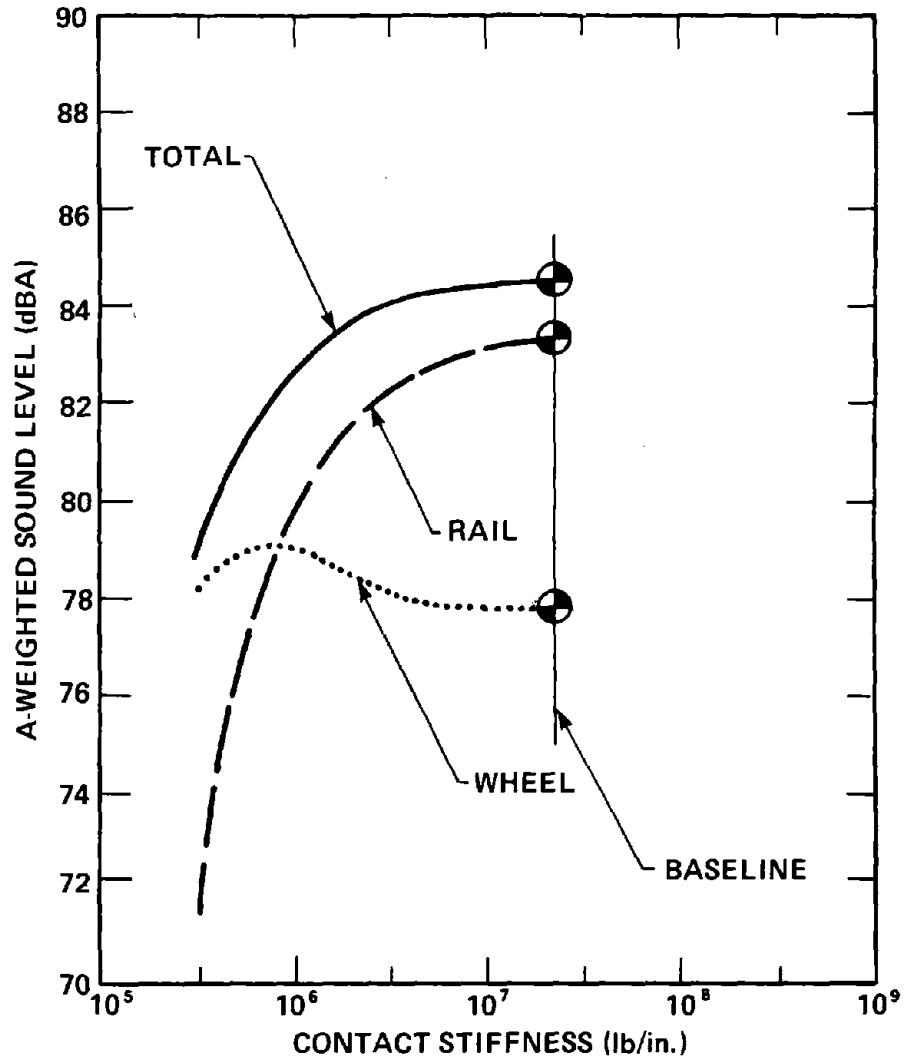


FIG. 112. ESTIMATED EFFECT OF CHANGING CONTACT STIFFNESS ON WAYSIDE NOISE AT 25 FT; TWO-CAR TRAIN AT 30 MPH.

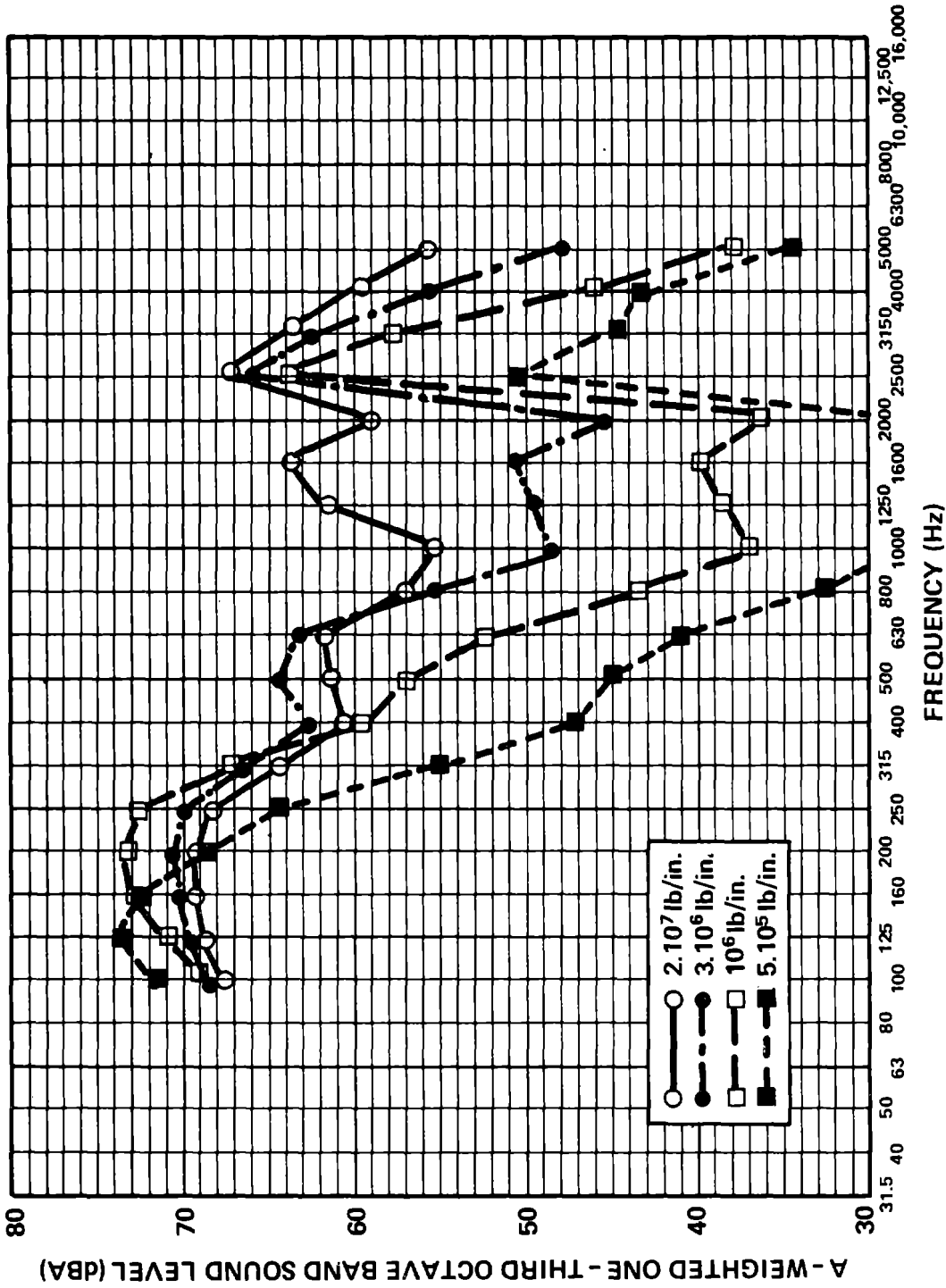


FIG. 1.13. ESTIMATED WHEEL SOUND RADIATION FOR VARIOUS CONTACT STIFFNESSES.

contact resonance begins to increase the sound radiation from the wheel as the contact stiffness is first reduced. Further reduction in the contact stiffness pushes the contact resonance to low enough frequencies that the A-weighting begins to reduce its influence and the sound radiation from the wheel begins to fall. The rail sound radiation, on the other hand, falls uniformly with decreasing contact stiffness. The contact resonance does not influence the rail sound radiation, because the sound radiation from the rail is not significant at the low frequencies where the contact resonance occurs.

Area of Contact

Increasing the area of contact has a significant effect on the noise from both wheel and rail, as illustrated in Fig. 114. Note that the noise from the rail is more affected than the noise from the wheel. We can see why this is so by referring to Fig. 105, which shows that the noise from the wheel is dominated by noise at low frequency and by only a few bands at high frequency. The noise from the rail, on the other hand, is dominated by noise in the mid frequencies. The area of contact between the wheel and rail acts effectively like a low-pass filter whose roll-off frequency decreases with increasing contact area. For the baseline case considered here, the roll-off frequency is about 400 Hz. Increasing the contact area affects the rail across the entire frequency region where rail radiation is important, but it initially affects the wheel only in the few bands at high frequency that are important contributors to wheel noise.

Although contact area probably affects wheel/rail noise more than other parameters, an increase in contact radius by a factor of two only decreases noise by 5.5 dBA.

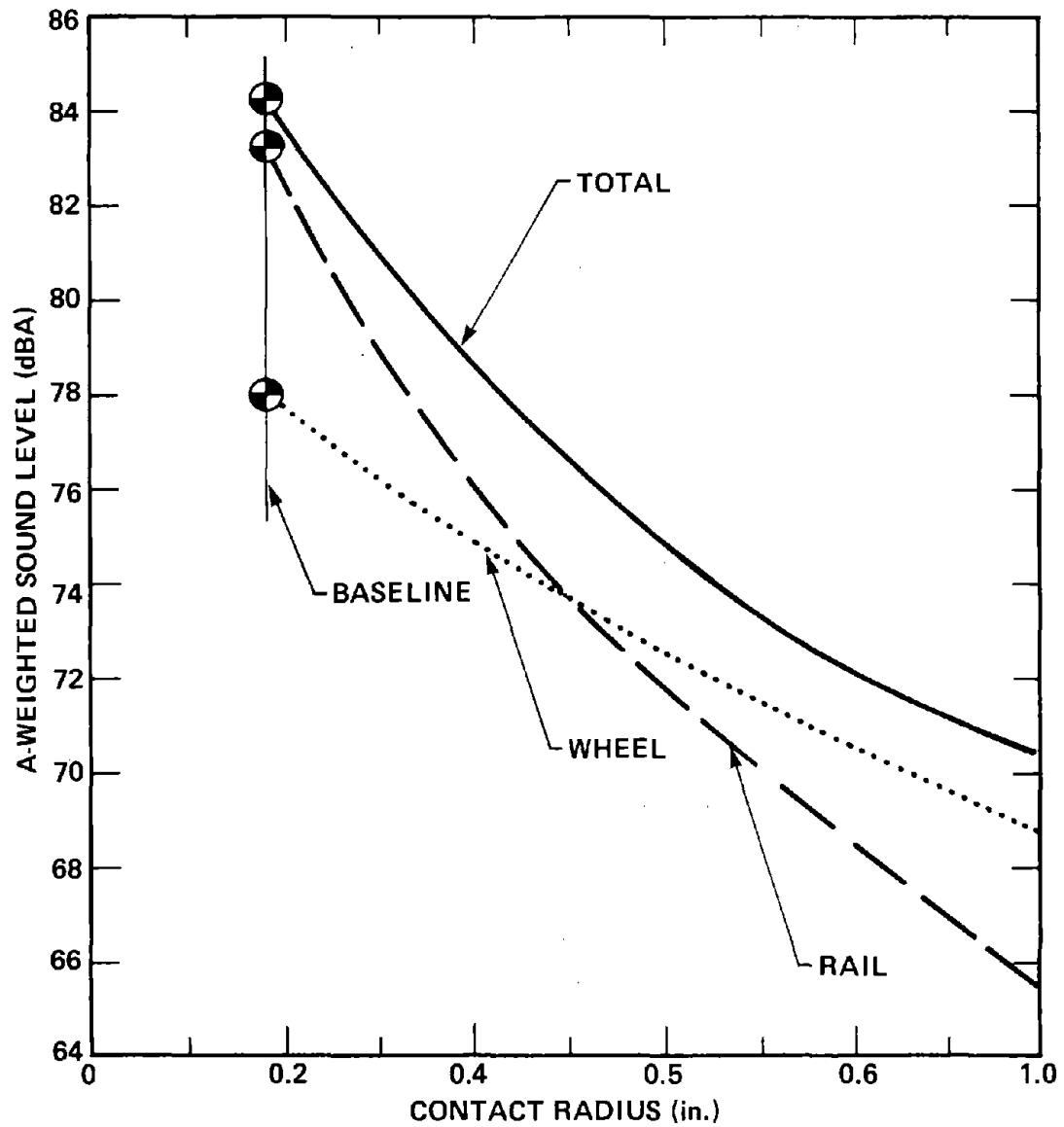


FIG. 114. ESTIMATED EFFECT OF INCREASING CONTACT AREA ON WAYSIDE NOISE AT 25 FT; TWO-CAR TRAIN AT 30 MPH.

Wheel Truing and Rail Grinding

The previous examples have illustrated the difficulty of reducing wheel/rail noise once the wheel and rail running surface conditions have deteriorated sufficiently to create a problem. Here, we examine just how much we can realistically expect to reduce wheel/rail noise by smoothing the running surfaces of the wheels and rails. Figure 115 shows a bar graph of the overall noise and wheel and rail sound radiation for the baseline system, as well as for three additional conditions:

- Smooth wheels and normally rough rails
- Smooth rails and normally rough wheels
- Smooth wheels and rails.

A smooth wheel or rail is one with the roughness spectrum shown in Fig. 116. The curve in the figure is a lower bound on roughness data from the open literature for ground-end lathe-turned discs [26], as well as roughness data on a small 14-in.-diameter railroad wheel that was turned smooth with great care on a lathe [3]. We feel that those data represent the smoothest surfaces that are practically achievable in the transit environment. In fact, as we shall see in Sec. 5, only one wheel or rail smoothing technique has achieved surface conditions as smooth as those shown in Fig. 116.

Figure 115 shows that if one could maintain smooth wheels and rails, a reduction in noise of almost 12 dBA is possible.

Rail Joints

Using the "equivalent roughness model" of stepup rail joints described in Sec. 2.2, we have estimated the change in the average sound level at the wayside during the passage of a two-car train on jointed rail (39-ft joint spacing). The noise increases

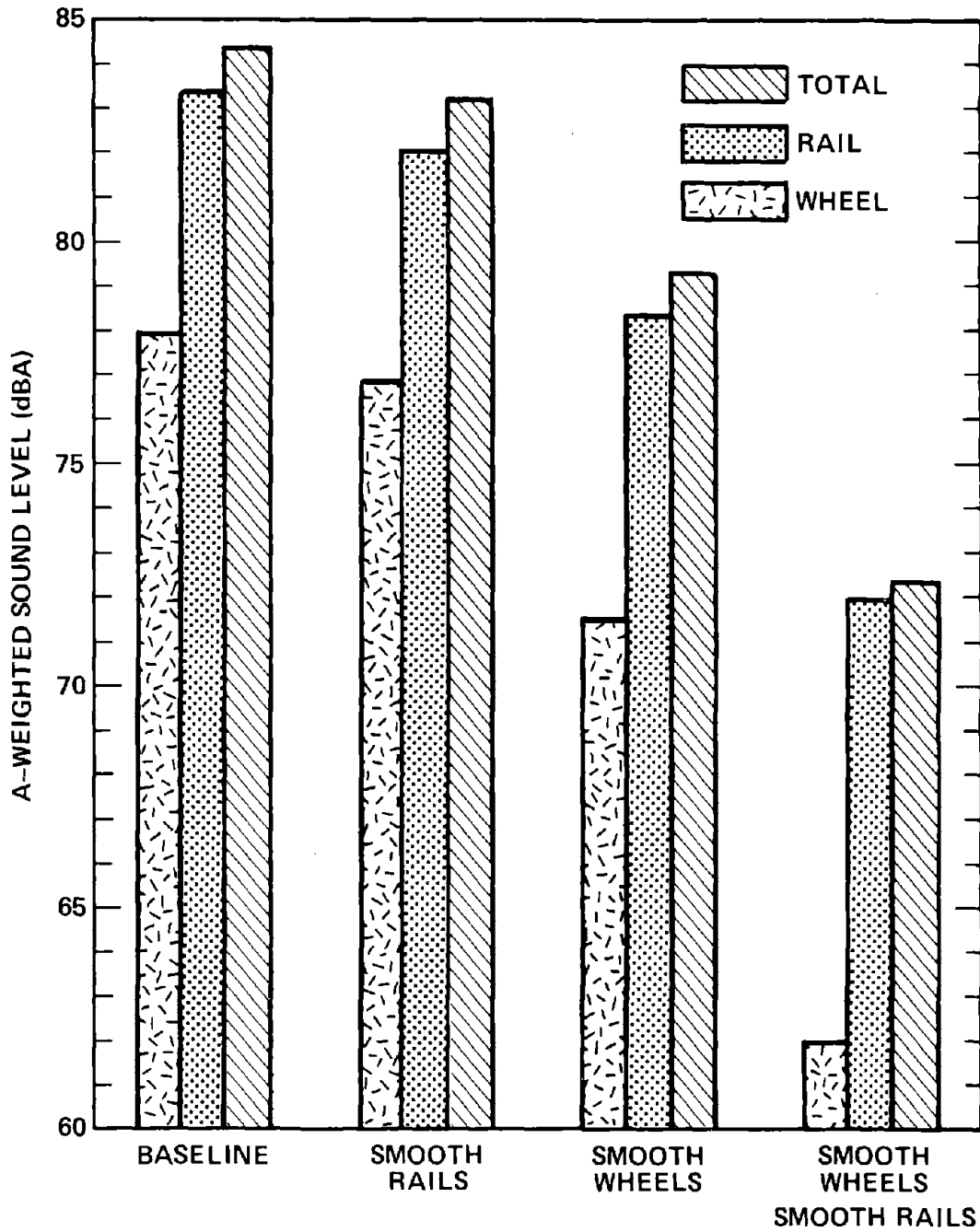


FIG. 115. ESTIMATED NOISE LEVELS AFTER WHEEL AND RAIL SMOOTHING.

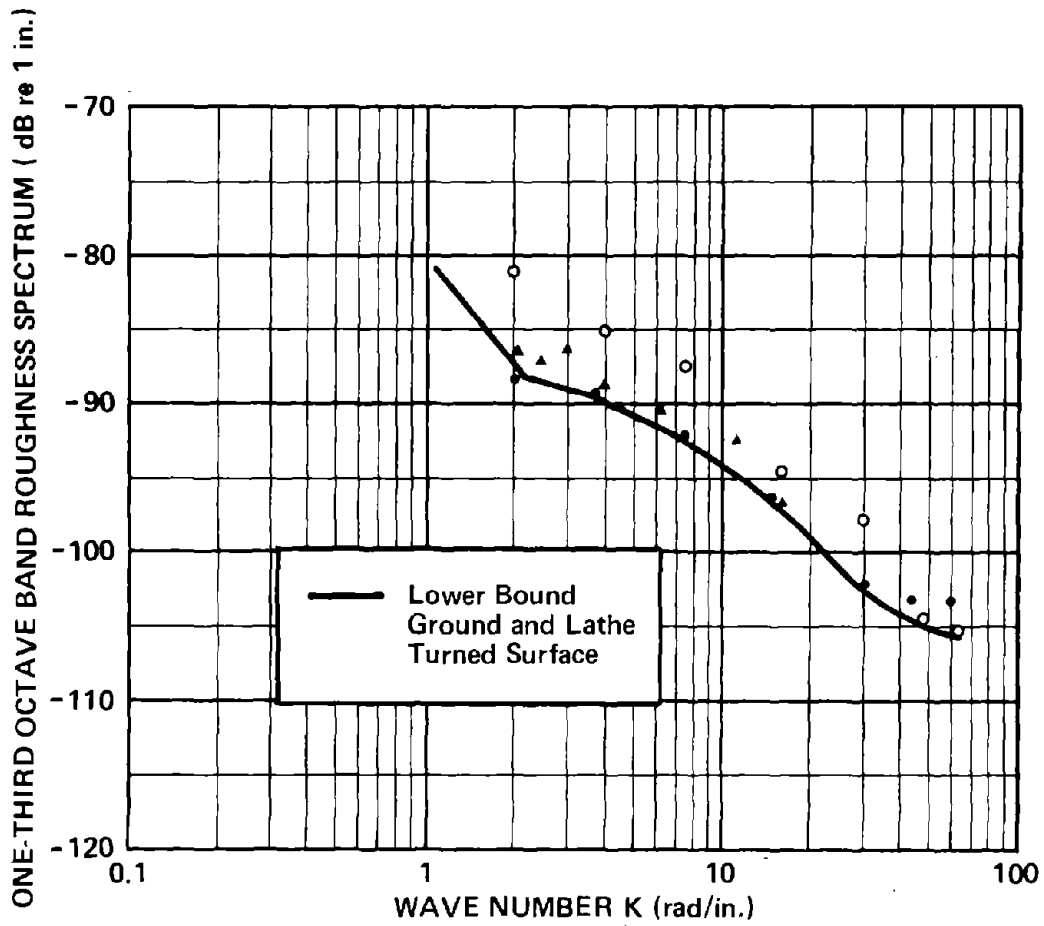


FIG. 116. LOWER-BOUND WHEEL AND RAIL ROUGHNESS. (\blacktriangle lathe-turned 14-in.-diameter railroad wheel [3]; \circ lathe-turned surface [26]; \bullet ground surface [26].)

only slightly, even for fairly large height discontinuities at the joints (Fig. 117). We suspect that even for very small joint height discontinuities, the joint impacts will be audible. The A-weighted sound level averaged over the time that the train is passing is not very sensitive to these impacts because they have a very short duration. Of course, the wheels and rails in this calculation are fairly rough. If we had used smoother wheels and rails in our baseline system, the rail joints would have had a more significant effect on wheel/rail noise.

Wheel Flats

Flat spots on wheels are typically generated when sliding occurs during braking. Figure 118 shows a wheel set with a large wheel flat just before truing on an undercar milling machine. Wheel flats result in significant increases in the noise from rapid transit cars.

Figure 119 shows the effect of wheel flats on the average sound level. Both the size of the flats and the number of flats per wheel affect the average sound level. Once again, because our measure of noise is the sound level averaged over the time that the train is passing, wheel flats appear to be less noisy than one would ordinarily expect. In fact, wheel flats much less than an inch in length can be clearly heard above the din of the average train. But because of the short duration of the impacts, the effect on the average sound level is not dramatic.

The results in Fig. 119 are for a train speed of 30 mph. We should caution the reader that at so high a speed the wheel flat "equivalent roughness" model of Sec. 2.2 may somewhat overestimate the noisiness of wheel flats. The "critical speed," i.e., the speed above which the wheel loses contact with the rail, is a little less than 30 mph, and the wheel flat model is only good for those speeds where wheel/rail contact is maintained.

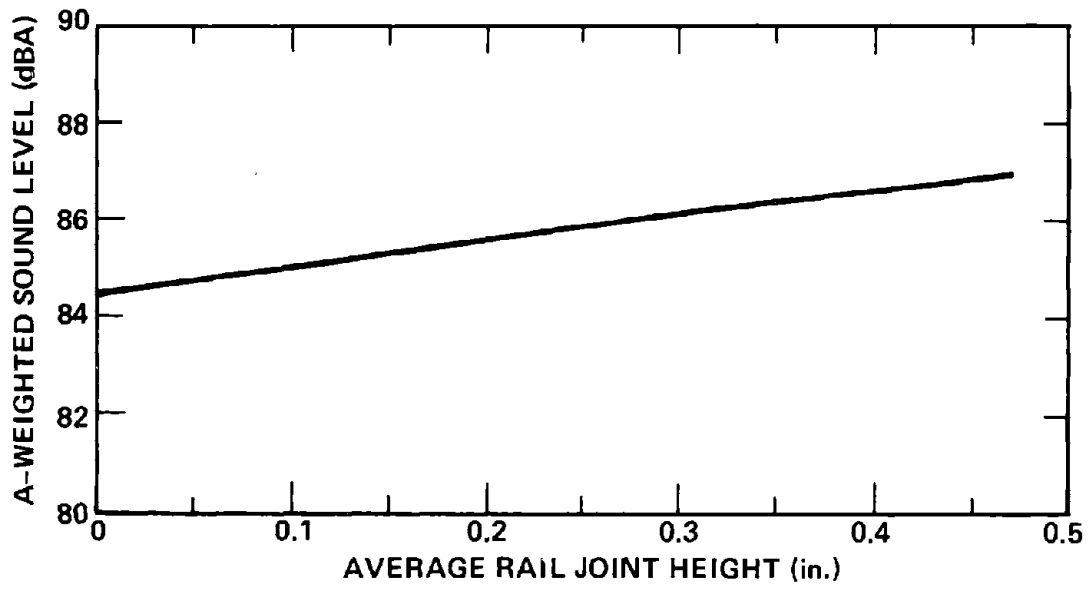


FIG. 117. EFFECT ON NOISE OF RAIL JOINTS.

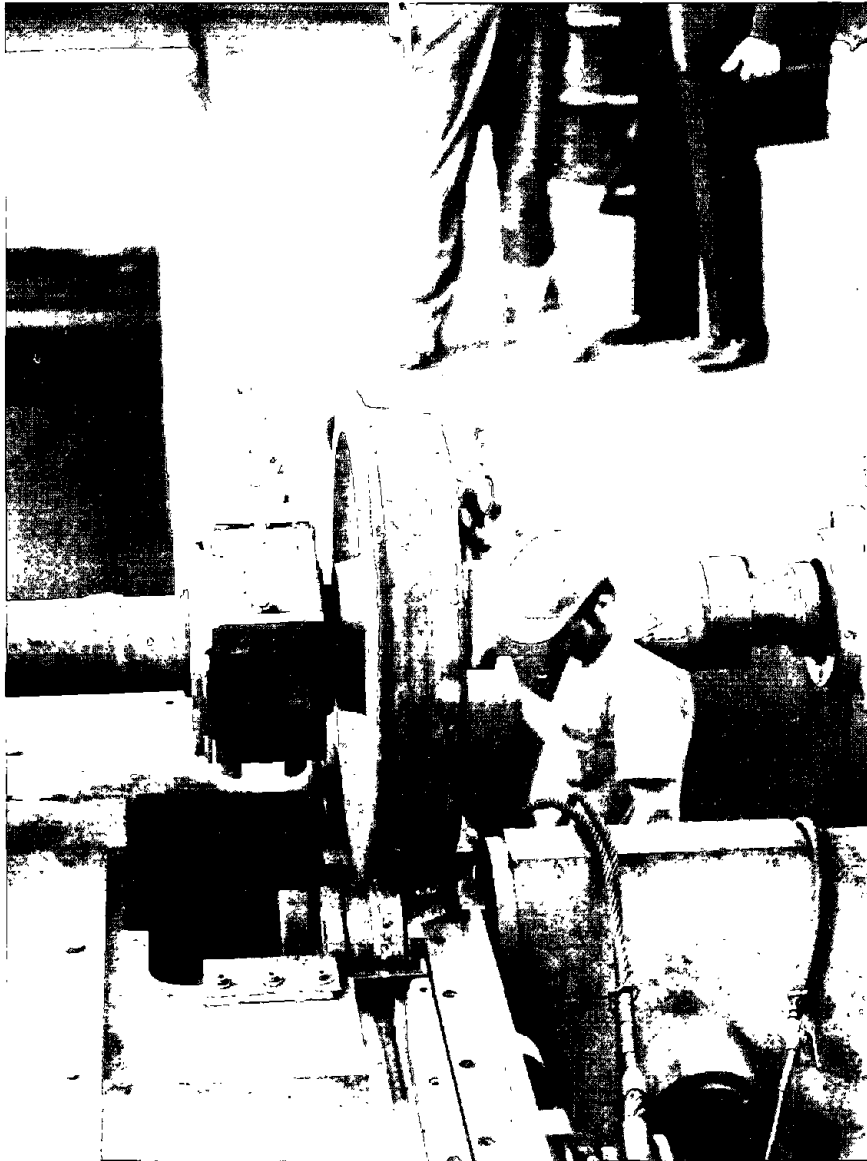


FIG. 118. TYPICAL WHEEL FLAT.

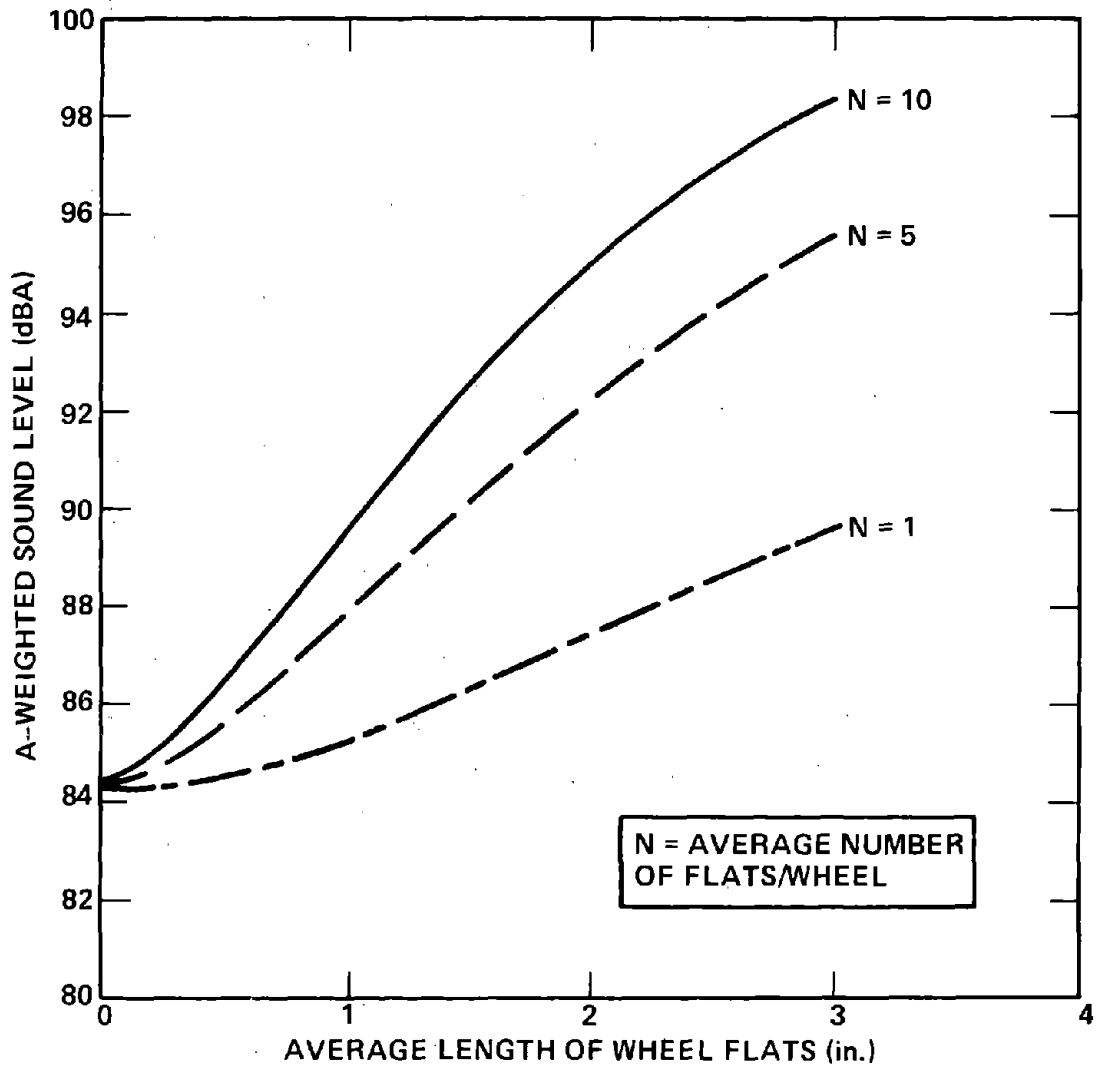


FIG. 119. EFFECT ON NOISE OF WHEEL FLATS.

5. TREATMENTS FOR THE CONTROL OF NOISE

In an earlier investigation under this program [1], all available information on wheel/rail noise control treatments was examined, and the most cost-effective treatments were identified. From these, a number were selected for further study under this program. For squeal noise suppression, a need was found for site-specific treatments. Most squeal noise suppression treatments are applied to the wheels. Even if only a few troublesome curves exist on a system, these wheel-specific treatments would have to be applied to the whole fleet of cars to be effective. It would certainly be convenient to have a treatment that could be applied only at the curves.

Rail lubrication and hard-faced rails are two site-specific treatments. The former, which was examined in a series of tests at TTC as part of another program, will not be reported on here. We have, however, examined the effect of curve radius on squeal noise for two transit systems. One, the MBTA, already discussed in Sec. 2, had no curve lubrication; the other, the CTA, had lubricators on most of its short-radius curves. In the sections that follow, we will compare the two sets of data to determine the effectiveness of curve lubrication in suppressing squeal on an operating transit system. Hard-faced rails have been used on an experimental basis in Europe with mixed results. We will discuss those results in the sections that follow.

For rolling noise and impact noise, we decided to examine wheel and rail smoothing techniques and a new concept of a resiliently treaded wheel. The results of Sec. 4 have confirmed this decision. Of the few parameter changes that had any effect on wheel/rail noise, one was wheel/rail contact area and the other, to a lesser extent, was wheel/rail contact stiffness. The values of both of these parameters can be varied by proper design of a resiliently treaded wheel. Accordingly, we have designed, built,

and tested a one-third-scale prototype resiliently treaded wheel, described later.

The fact that wheel/rail noise is so resistant to change implies the need to keep the running surfaces of wheels and rails as smooth as possible. Section 4 has shown that a 12-dBA reduction in wheel/rail noise is theoretically achievable if wheels and rails are kept as smooth as possible. In the following sections, we examine the smoothness achievable with various wheel-truing and rail-grinding techniques.

5.1 Control of Squeal Noise

5.1.1 Hard-faced rails

The hard-faced (Anti-Quietsch Schweissung) rail is a specially treated rail for squeal suppression manufactured by Elektro-Thermit GmbH, Essen, West Germany. A cross section of the rail is shown in Fig. 120. Two strips of weldment called ETECTA 5 Spezial, approximately 5 mm high by 12 mm wide, are laid on the full length of the rail. The wheel runs on these strips, and the claim is that no squeal noise is generated and rail wear is reduced.

Hard-faced rail has been installed on an experimental basis on curves on the inner rail on a number of transit systems throughout Europe (Hamburg, Hannover, Köln, Mainz, Mannheim, München, Stuttgart, Würzburg). We contacted a number of the systems and carried out measurements on the Hannover streetcar system.

The test site at Hannover is shown in Fig. 121. It was an ideal site, with two curved tracks approximately 3 m apart, one with hard-faced rail approximately 3 months old and one without. Unfortunately, on the day that noise measurements were

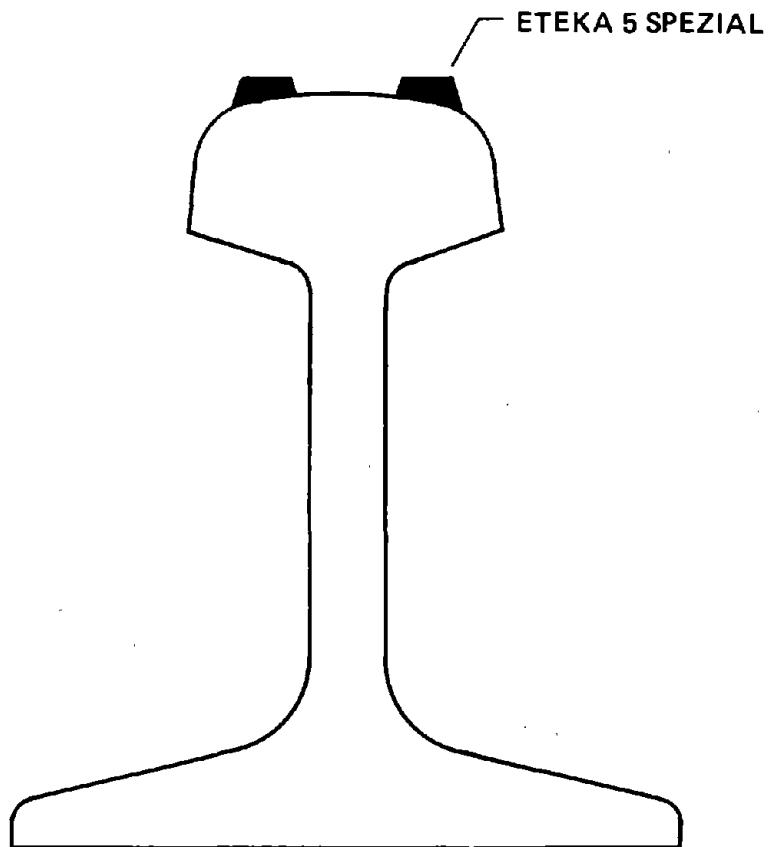


FIG. 120. HARD-FACED RAIL.

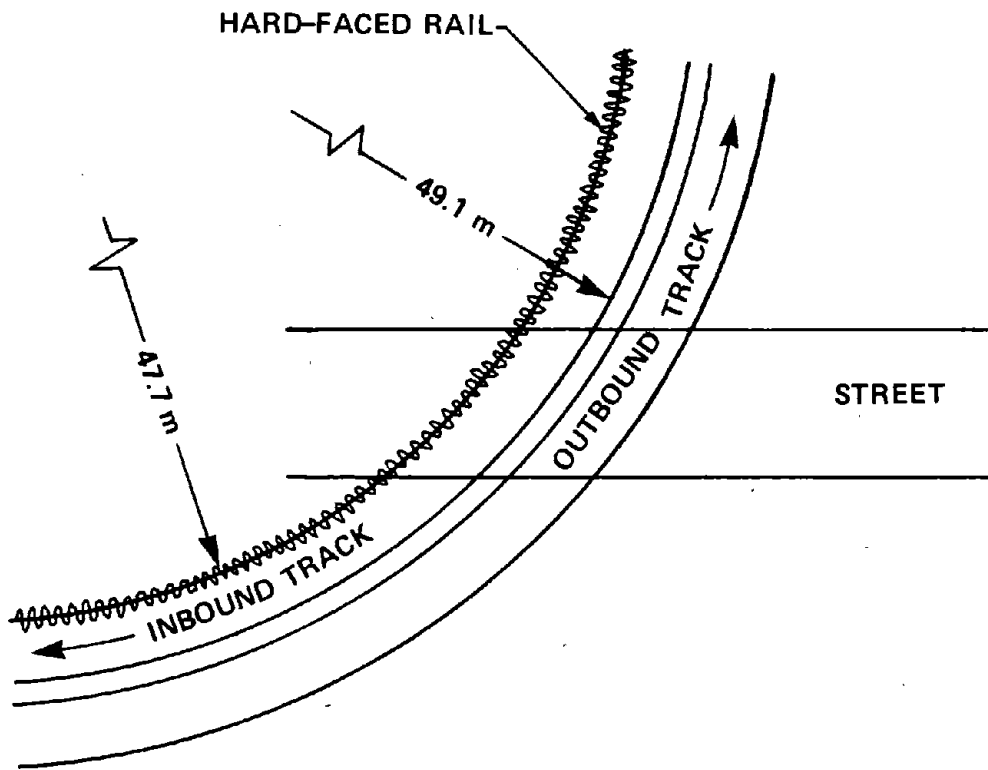


FIG. 121. TEST SITE IN HANNOVER.

made, trains did not squeal on either track. It had rained earlier in the day and, although the rails appeared to be dry, there may have been enough moisture on them to prevent squeal. The rail was installed on the curve in Hannover to deal with a squeal problem, and Hannover personnel reported that the rail did eliminate squeal.

To obtain further information, we contacted two additional systems in Germany. In 1976, the Stuttgart streetcar system experimented with hard-faced rail. The rail did eliminate squeal, but after 3 to 4 months the squealing came back. In addition, the rails did not wear as long as claimed. Stuttgart transit personnel therefore felt that the additional cost of hard-faced rail was not justified and the city is not using any on its system.

The Frankfurt streetcar and subway system personnel used hard-faced rail on a number of curves on both the streetcar and subway lines. They are presently content with the performance of the rail, but they still have several more years of testing to carry out. They did mention that the hard-faced rail had to be ground more often than normal rail to prevent corrugations.

In summary, it appears that hard-faced rail does prevent squeal, but it is uncertain how long the rail wears well and/or suppresses squeal. The next logical step would be to make a test installation in the United States, either at the TTC screech loop or on an operating transit system.

5.1.2 Comparison of MBTA and CTA squeal noise occurrence

In Sec. 2.3.2, we examined the effect of the ratio of curve radius to truck wheel base on the occurrence of squeal for the MBTA. To obtain those data, we rode the system, noted the occurrence of squeal, and correlated those observations with the

radius of the curves. For the Chicago Transit Authority (CTA), we used the squeal occurrence data compiled by Silver, Bachus and Priemer [27]. The radii of the curves and the presence of lubrication and restraining rail were determined with the help of the CTA. Approximately 108 curves on seven lines were analyzed, ranging in radius from 90 ft to 2,200 ft.

The results are shown in Fig. 122 and compared with the MBTA results. For the most part, there is substantially less squeal on the CTA for curves with a curve-radius-to-wheelbase ratio of 150 or less. Since over 45% of these curves are lubricated, whereas only one curve with that ratio above 150 is lubricated, one is tempted to attribute the reduction in squeal occurrence to the lubrication. However, Table 8 casts some doubt on that hypothesis. A large percentage of the short-radius curves that did not squeal were not lubricated. In fact, as shown in Table 9, for the short-radius curves where squeal would be expected to occur, the unlubricated curves appear less likely to squeal than the lubricated ones. Therefore, it is incorrect to attribute the decrease in the occurrence of squeal on the CTA solely to the use of lubrication on curves. Other factors, such as truck design, use of restraining rail, etc., may play a role.*

5.2 Impact and Rolling Noise

5.2.1 Wheel truing and rail grinding

The sensitivity analysis in Sec. 4 has clearly shown that once the wheels and rails become rough and - as a result - noisy, it is extremely difficult to control the noise. Changing most wheel/rail system parameter values has little effect; therefore,

*All but eight of the curves with radius-to-wheelbase ratios less than 150 had restraining rail. For curves with that ratio greater than 150, only six had restraining rails.

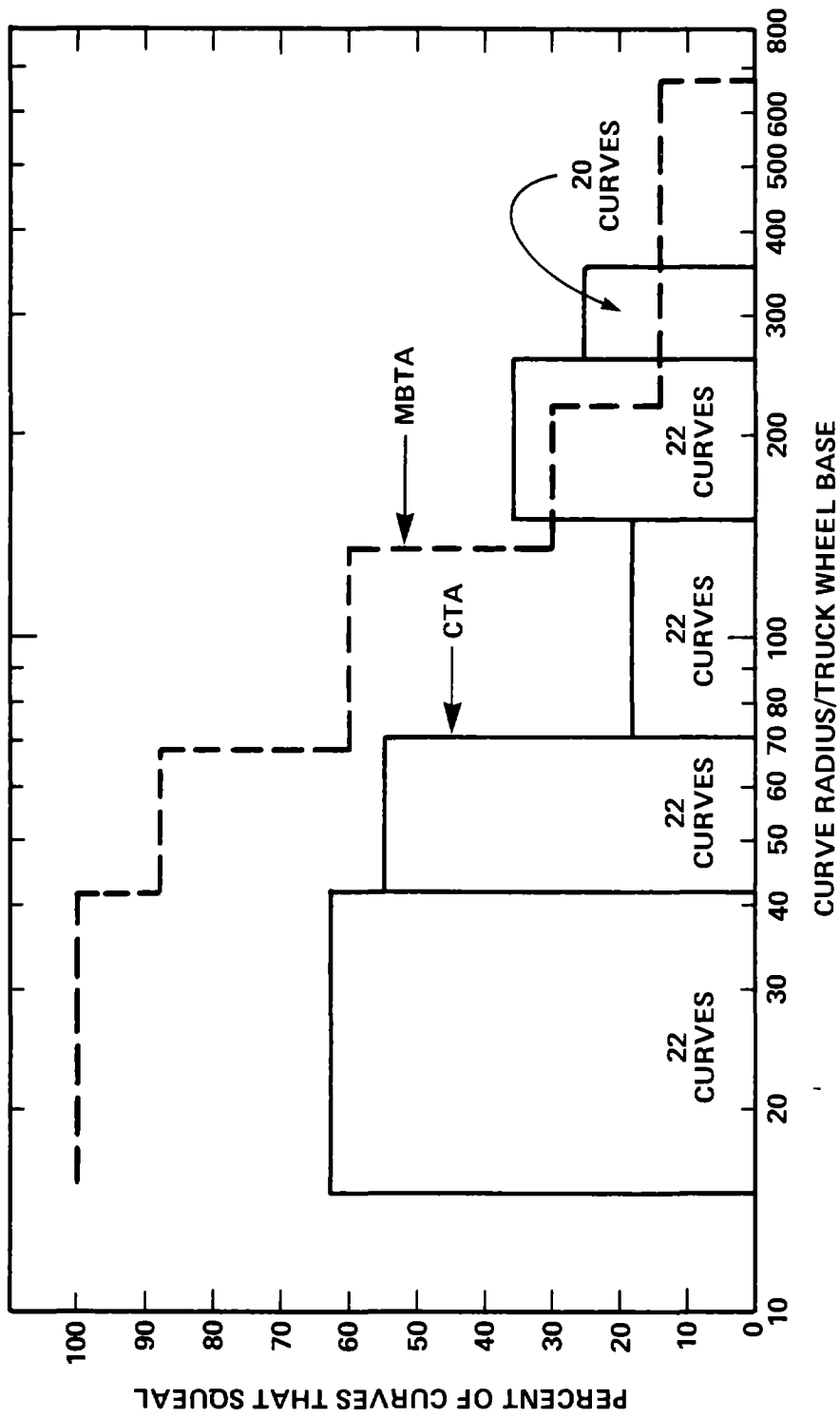


FIG. 122. COMPARISON OF SQUEAL OCCURRENCE ON THE MBTA AND CTA.

TABLE 8. INCIDENCE OF SQUEAL AND LUBRICATION ON CTA CURVES.

Range of (Curve Radius) (Wheelbase)	Lubricated Curves that Squeal	Unlubricated Curves that Squeal	Lubricated Curves that do <u>not</u> Squeal	Unlubricated Curves that do <u>not</u> Squeal
15-42	11	3	3	5
43-70	8	4	1	9
70-150	1	3	7	11
150-260	0	8	1	13
260-355	0	5	0	15

TABLE 9. PERCENTAGE OF LUBRICATED AND UNLUBRICATED CURVES THAT SQUEAL.

Range of (Curve Radius) (Wheelbase)	Percent of Lubricated Curves that Squeal	Percent of Unlubricated Curves that Squeal
15-42	79	38
42-70	89	31
70-150	19	21
150-260	0	38
260-355	-	25

it is crucial to find ways to smooth the running surfaces of wheels and rails and keep them as smooth as possible. Consequently, in the course of this program, we examined the following wheel-truing techniques:

- Undercar milling machine
- Undercar lathe
- Wheelset lathe
- Belt grinder

and two rail-grinding techniques:

- Vertical axis rail-grinding machine
- Grinding block machine.

We obtained data on the roughness after wheel truing and rail grinding with each of these techniques. For the undercar milling machine, data were available from Saurenman [23], measured on the Southeastern Pennsylvania Transportation Authority (SEPTA). For the wheelset lathe, data were measured in an earlier program by BBN on the Massachusetts Bay Transportation Authority (MBTA). For the remaining four smoothing techniques, measurements were carried out at an operating transit property or at TTC (Pueblo).

In the following sections, we will discuss the roughness data obtained using the device described in Sec. 3.2.3. Using the analytical model of wheel/rail noise, we will then estimate the change in wayside noise that would result from various combinations of these smoothing techniques.

Undercar Milling Machine

A Stanray undercar milling machine at SEPTA is shown in Fig. 123. Although in the photographs a wheelset removed from the

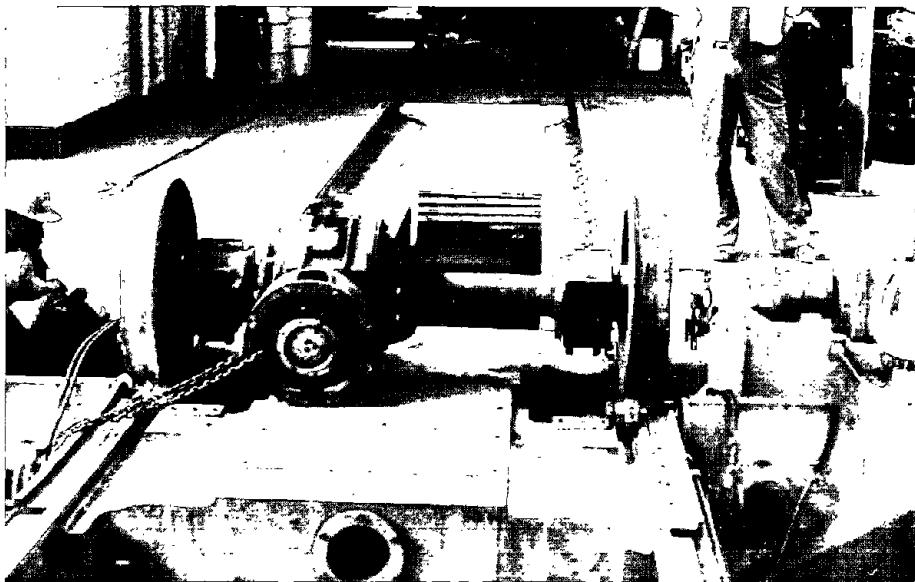
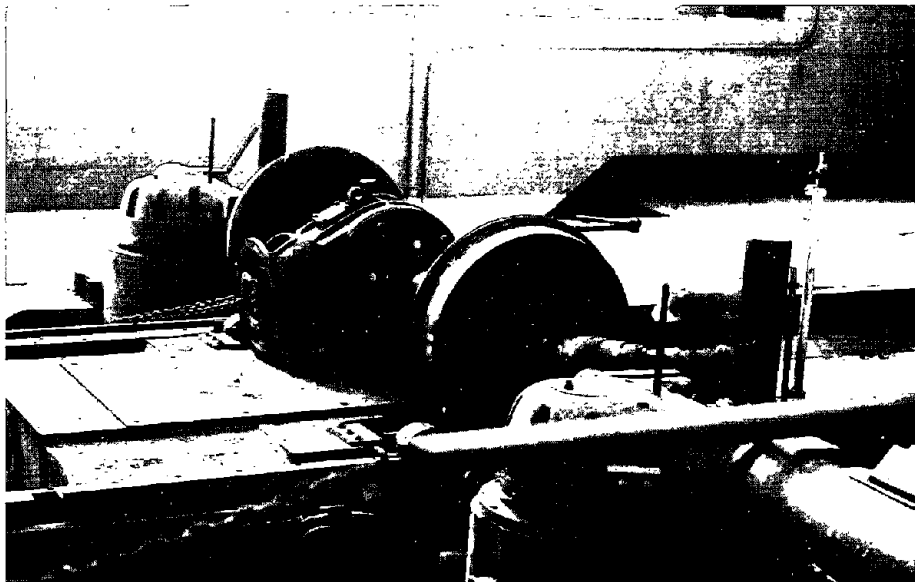


FIG. 123. STANRAY UNDERCAR MILLING MACHINE.

truck is being trued, removing the wheelset is not necessary. Usually the transit car is brought up to the machine and the particular wheelset to be trued is parked above the milling cutters. Each wheel of the wheelset is supported at the flange by two rollers, visible in Fig. 123. Two large mandrils fit into locating holes at each end of the axle to locate the axle center relative to the cutters. The mandrils can be seen in Fig. 123, pulled back out of contact with the axle. The milling cutters, one for each wheel, are located below the wheel and between the rollers. In order to change wheel tread contour, the milling cutter must be changed.

Figure 124 shows the measured roughness spectrum after truing, using the undercar milling machine at SEPTA and that same roughness spectrum after running the car for 100 miles. The roughness decreases after the short period of running in. This reduction in roughness is consistent with the observation that the machinery marks from the milling cutter gradually disappear after a short period of running the wheels on the rails.

As Fig. 124 shows, the degree of wheel running surface smoothness achieved by this machine falls short of what we estimate to be the practical limit of smoothness, especially at the longer wavelengths, i.e., spatial frequencies less than 10 radians/in.

Undercar Lathe

During the extensive field test program carried out at the TTC (Pueblo), we measured the wheel roughness on the SOAC after truing on the Hegenscheidt undercar lathe at the test center. Figure 70 in Sec. 3.2.3 shows the SOAC on the machine. In principle, this machine operates like the undercar milling machine. The major difference is that a lathe tool, rather than

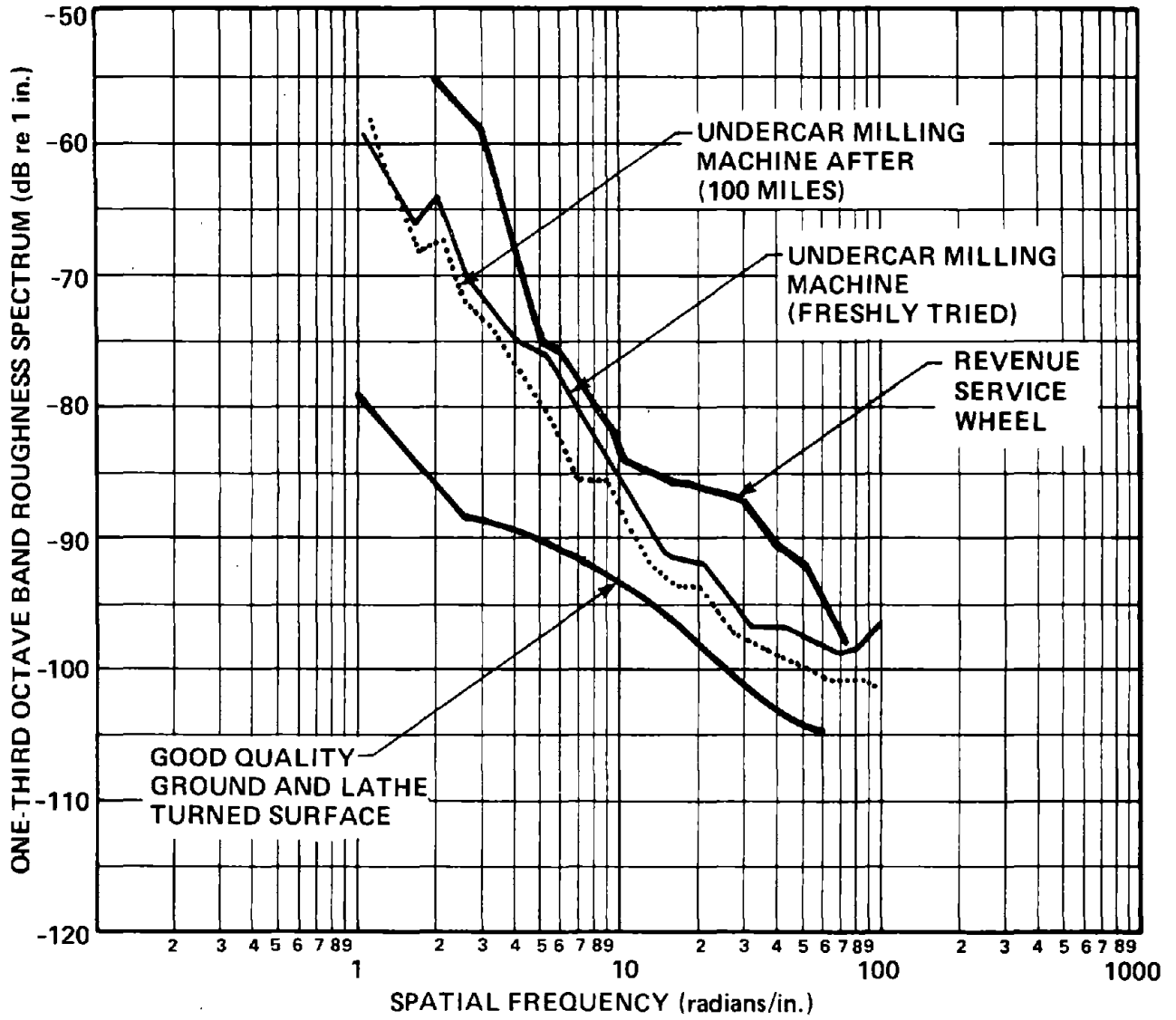


FIG. 124. WHEEL ROUGHNESS AFTER SMOOTHING WITH THE UNDERCAR MILLING MACHINE.

a milling cutter, cuts material from the running surface of the wheel and flange. By inserting templates into the machine, one can use the same tool to cut a variety of wheel contours.

Figure 125 shows the resulting roughness spectrum on the wheels of the SOAC measured as described in Sec. 3.2.3. The data were obtained after truing the wheels on the Hegenscheidt machine, but only after the SOAC had been run on the Transit Test Track for approximately 100 miles. Up to a spatial frequency of approximately 10 radians/in., the undercar lathe and the undercar milling machine produce identical degrees of smoothness. Above that spatial frequency, the milling machine produced a surface finish that, after 100 miles of service, was superior to the surface produced by the lathe after a similar wear-in period. Unfortunately, we do not have data on the wheel roughness immediately after truing with the lathe. The 100 miles of service that we mention here is an approximation based on several days of testing in which the SOAC was used as a locomotive to pull another test car around the Transit Test Track. As we described in Sec. 3.2.3, we believe this service roughened the wheels considerably. Consequently, Fig. 125 may overestimate the roughness from the undercar lathe.

Wheelset Lathe

The use of a wheelset lathe is a relatively old technique that involves the removal of the wheelset from the transit car truck. The wheelset is then mounted in a lathe and turned smooth. In an earlier DOT program [3], BBN measured the roughness on an MBTA wheel at the Everett shops after it was turned on a wheelset lathe. The resulting roughness is shown in Fig. 126. The roughness before lathe turning is indicated by the curve labeled "Revenue Service Wheel" in the figure. Interestingly, the roughness actually increased somewhat after lathe turning.

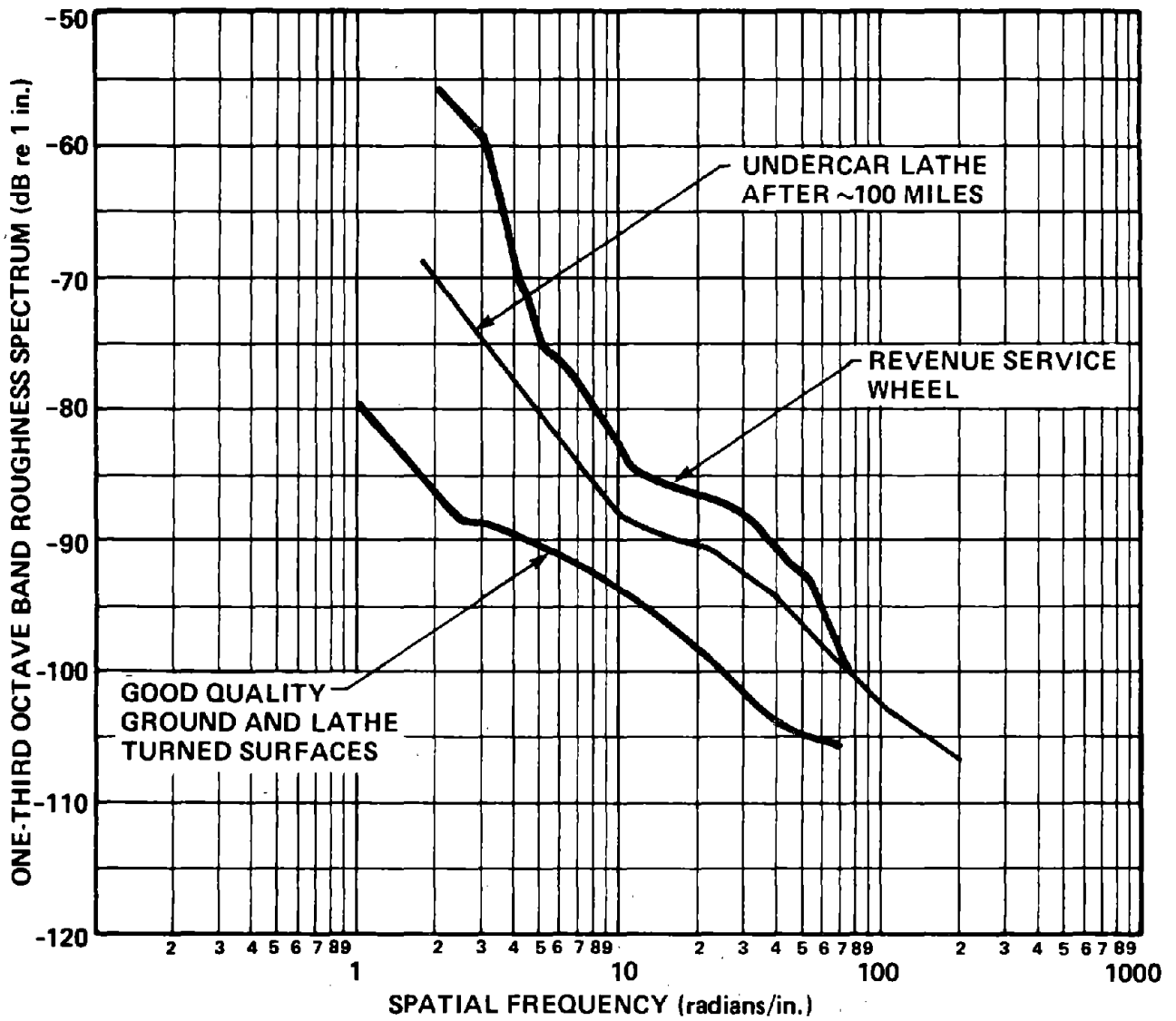


FIG. 125. WHEEL ROUGHNESS AFTER SMOOTHING WITH AN UNDERCAR LATHE.

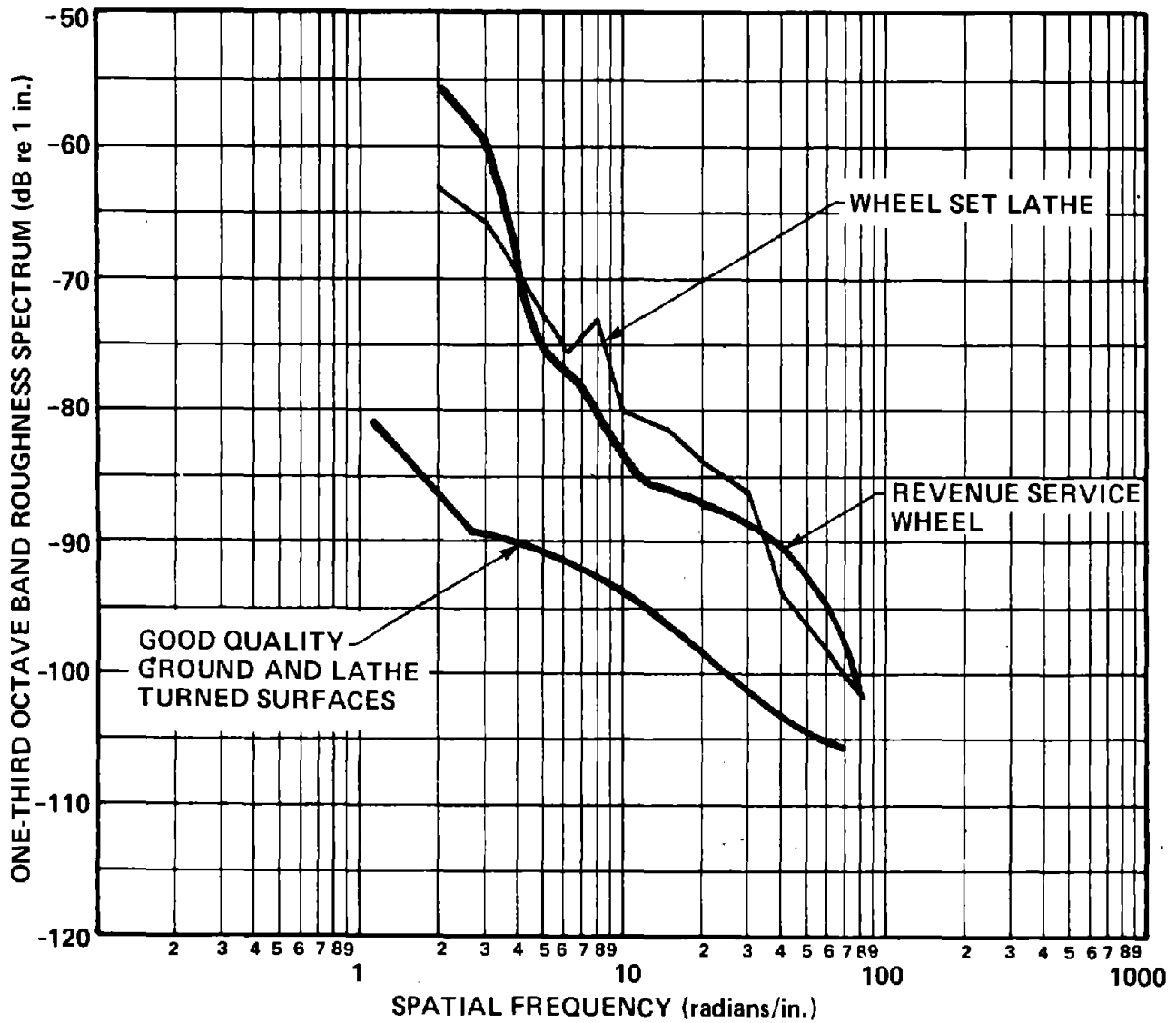


FIG. 126. WHEEL ROUGHNESS AFTER TURNING ON A WHEELSET LATHE.

There was some tool chatter in this machine, and the increased roughness may be a consequence of the machinery marks from that chatter. We were unable in this instance to measure the roughness again after the wheel had been run in service for 100 miles or so. We expect that as with the undercar milling machine, these machinery marks will gradually wear away in normal service, and the roughness will decrease.

Belt Grinder

For several years, the Toronto Transit Commission [TTC (Toronto)] has been using wheel grinding (belt grinder) as a means of truing subway car wheels that had only relatively small irregularities. The Commission still uses an undercar wheel lathe for the large flat spots and general repair work. With the cooperation of TTC (Toronto), we measured the running surface roughness on a subway car wheel immediately before and after belt grinding, to determine the effectiveness of this smoothing technique.

The belt grinder used at TTC (Toronto) is located at the Davisville shop; it consists of two 106-in. x 4-in.-wide abrasive belts that are pressed against each wheel of the rotating wheelset. Figure 127 shows a number of views of the machine. The sequence of operation starts with the car being pulled up over the belt grinder and hydraulic jacks raised to support the car, as shown in Fig. 128. The rails below the wheelset to be ground are then swung away, allowing the belt grinder access to the running surface of each wheel. The wheelset is then rotated and the belt grinder raised into contact with the wheels, as shown in Fig. 129. The wheelset is rotated at 60 rpm by connecting an external power supply to the traction motor.

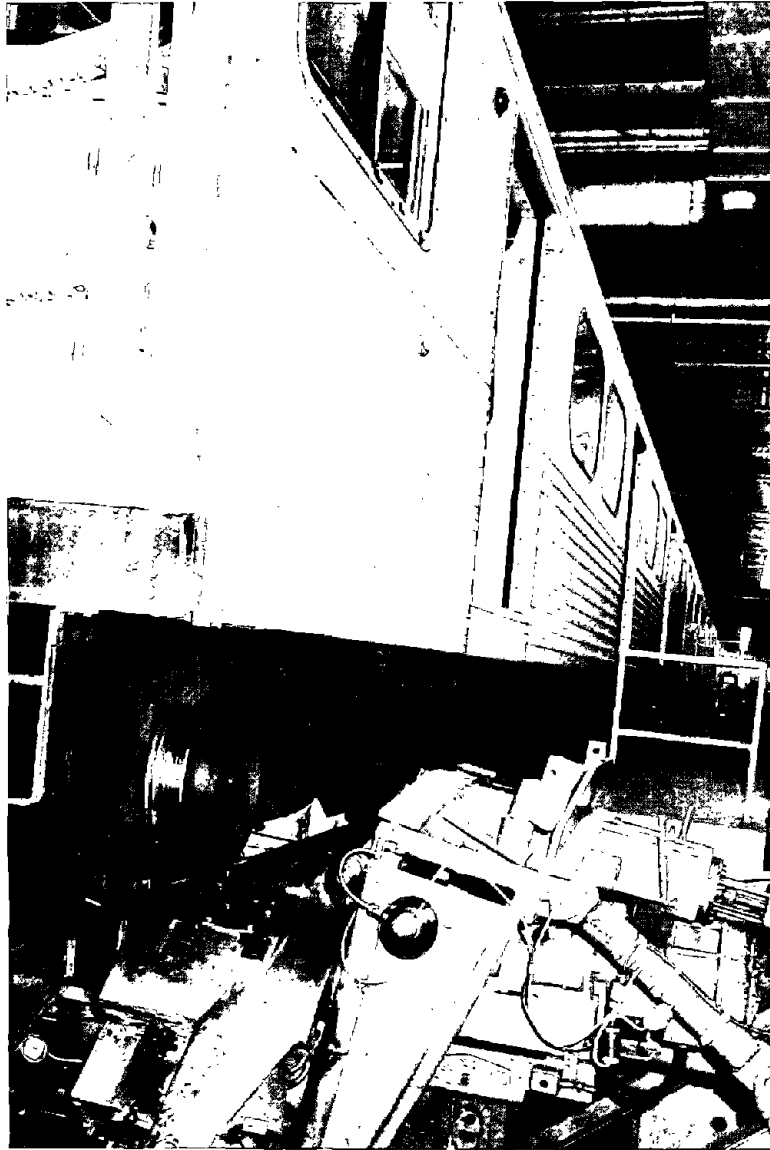


FIG. 127. THE BELT GRINDER AT TTC (TORONTO).

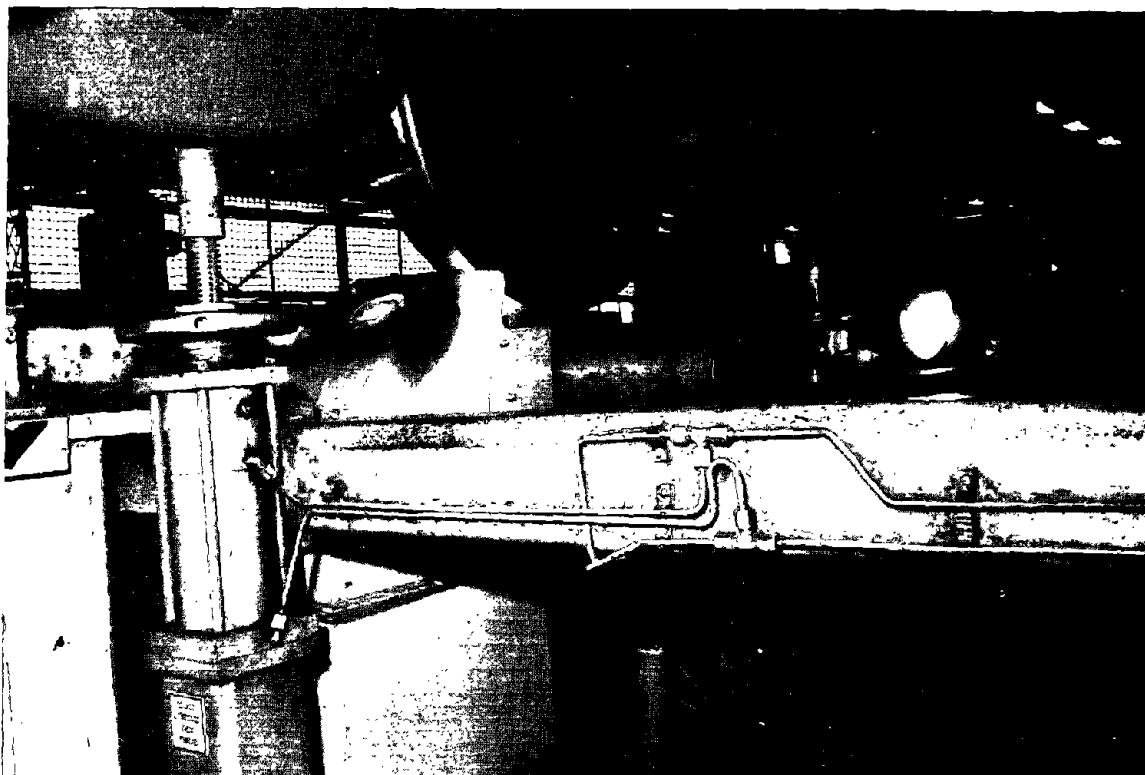


FIG. 128. THE HYDRAULIC JACKS USED TO SUPPORT THE TRANSIT CAR ON THE BELT GRINDER.

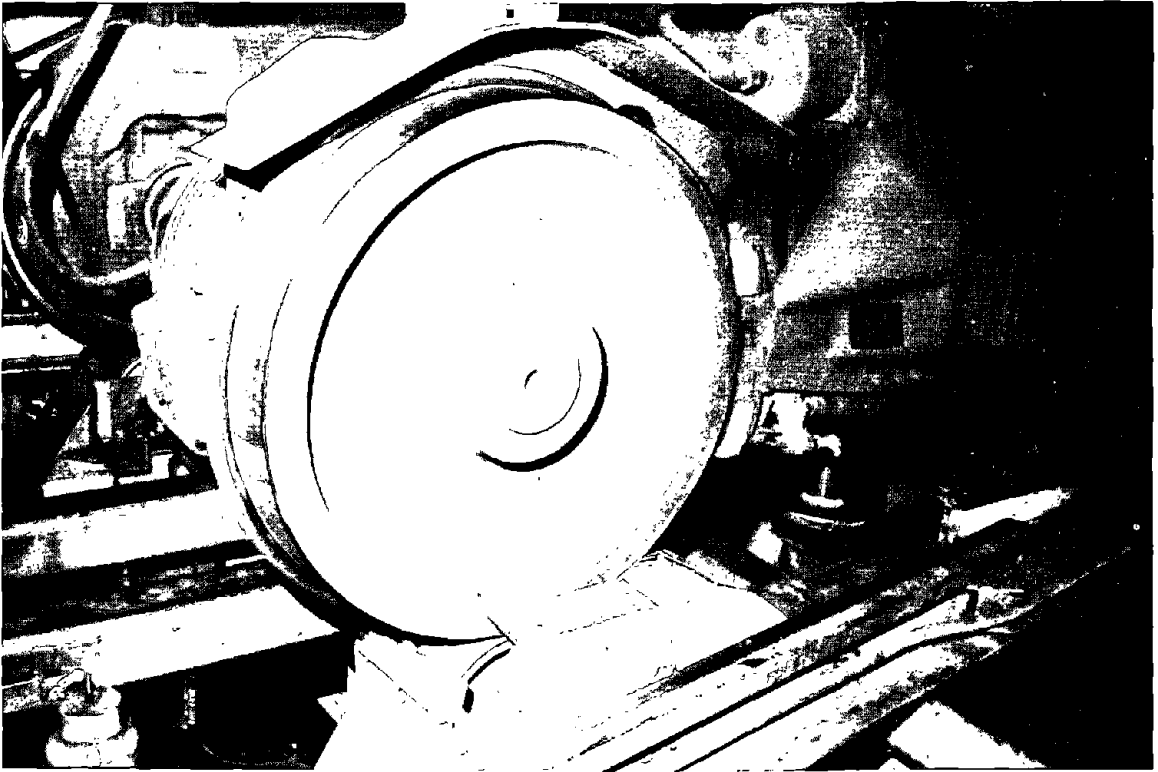
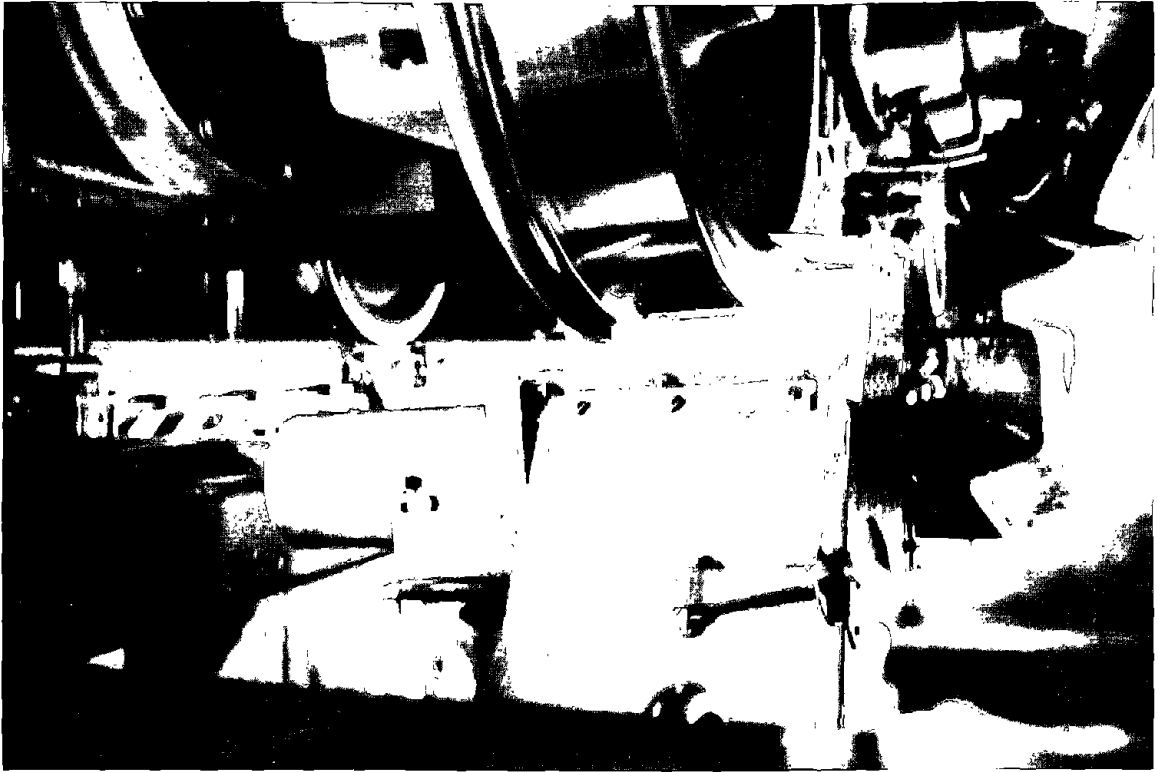


FIG. 129. THE GRINDING OPERATION.

A 90-durometer rubber pulley is used to support the grinding belt during contact with the car wheel, and 15-hp motor drives the belts at 5800 ft/min. A power lift moves the whole belt grinder up into the wheel running surface. Norton R827 belts (24 grit) are used.

Roughness measurements of the car wheels were made using the BBN roughness device described in Sec. 3.2.3. Since this device requires the wheels to rotate at a constant velocity, the measurements had to be made with the car mounted in the Hegenscheidt undercar wheel lathe at TTC (Toronto) in the Greenwood shop. A lathe speed of 15-1/2 rpm (22.7 in./sec) was chosen as a compromise between the fastest speed possible with the least amount of lathe vibration. Rubber mounting blocks were used to vibration isolate the measurement probe from the lathe. In addition, the vibration level on the lathe was monitored during all tests.

Roughness measurements were made before and after grinding and finally after the car had approximately 520 miles of in-service use. Since the belt grinder and wheel lathes were in two different shops, the roughness measurements could not be made immediately after belt grinding. However, we believed that the seven miles between the Davisville and Greenwood shops would not significantly change the surface roughness.

The instrumentation system used to obtain the roughness measurements was essentially the same as that used at TTC (Pueblo) (see Sec. 3.2.3), except that the data were recorded on an FM tape recorder and later analyzed in the laboratory. Two different wheelsets were measured and are identified as axle 1 and axle 3. Different tracks around the wheel perimeter on the running surfaces were measured for each wheel to obtain several samples of surface finish for each.

A visual inspection of each wheel was made to ensure that there were no flat spots on the test wheels. The surface condition of both wheels appeared to be very good, with only a slight spalling on wheel 3. Under normal conditions, neither of the wheels would have been called in for belt grinding. Figures 130 and 131 show typical one-third octave band acceleration spectra obtained from the roughness probe for the three test conditions; before and after belt grinding and after 520 miles in service.

Axle 3 (in Fig. 130) shows a 2- to 4-dB decrease in the probe acceleration level measured between the before and after belt grinding tests. After the 520 miles in service, there is an additional 1- to 3-dB drop in level at low frequencies up to 20 Hz. The slight drop in level after this 520 miles in service is to be expected, because a new running track forms after the belt grinding. In Fig. 131, the probe acceleration measured on axle 1, the three spectra do not show the same orderly reduction in level. The spectra have very similar levels, and no improvement in surface finish appears with the belt grinder. This is probably due to the excellent surface finish that this wheel had before any surface treatment was applied.

The vibration levels from the wheel lathe itself were monitored for each test and are shown by the dashed lines in Figs. 130 and 131. These background levels are low compared to the data (except for the 63-Hz band) and will be considerably attenuated by the vibration isolation and damping in the probe support mechanism.

The acceleration spectra have been converted to roughness spectra in Fig. 132; they are compared with wheel roughness on the MBTA and the practical lower limit of roughness that we estimated earlier. The belt grinder nearly achieves the lower

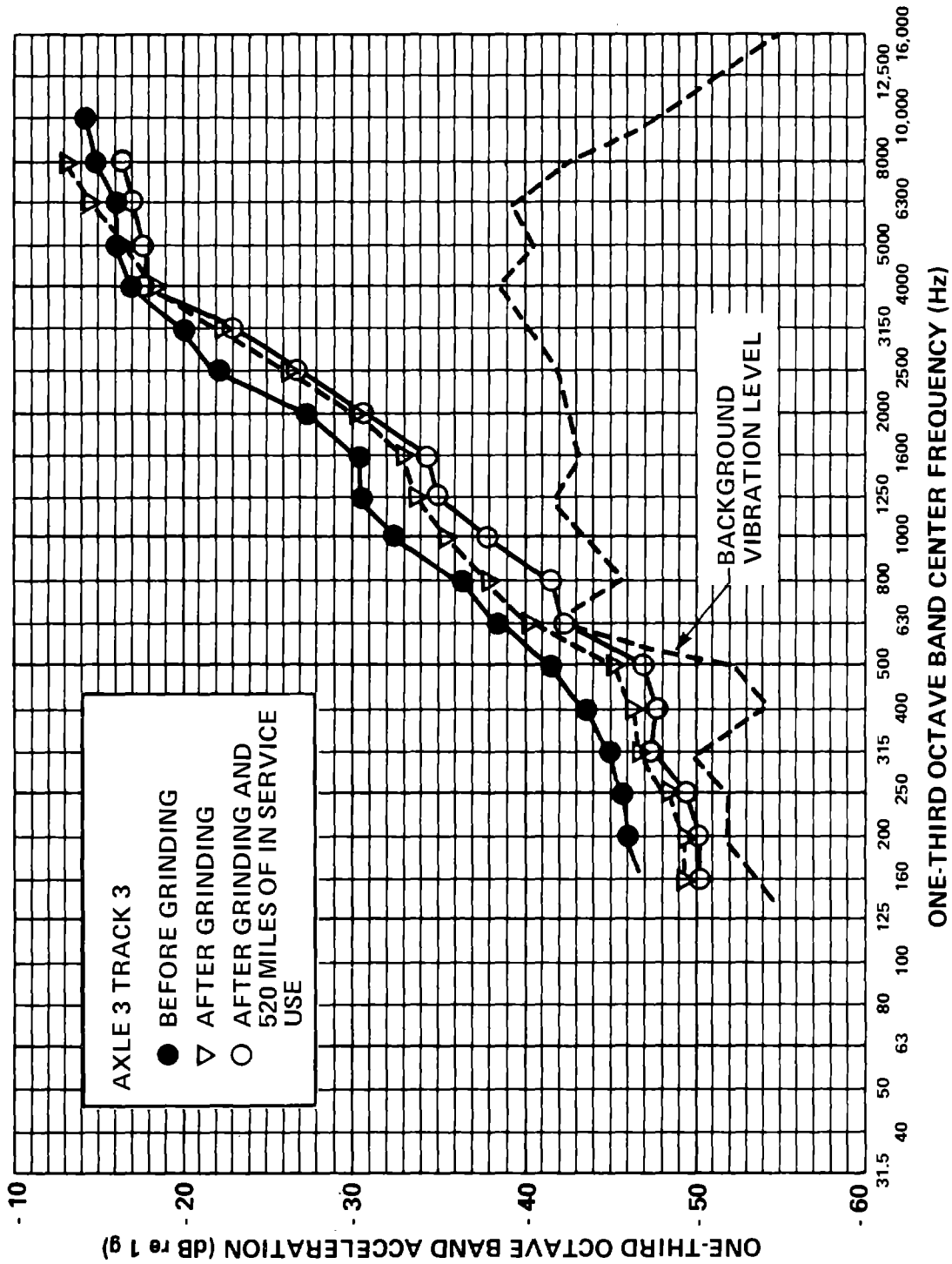


FIG. 130. ONE-THIRD OCTAVE BAND ACCELERATION LEVEL OBTAINED FROM SURFACE ROUGHNESS PROBE BEFORE AND AFTER BELT GRINDING. (WHEEL AXLE 3, TRACK 3; WHEEL SURFACE SPEED = 22.7 in./sec.)

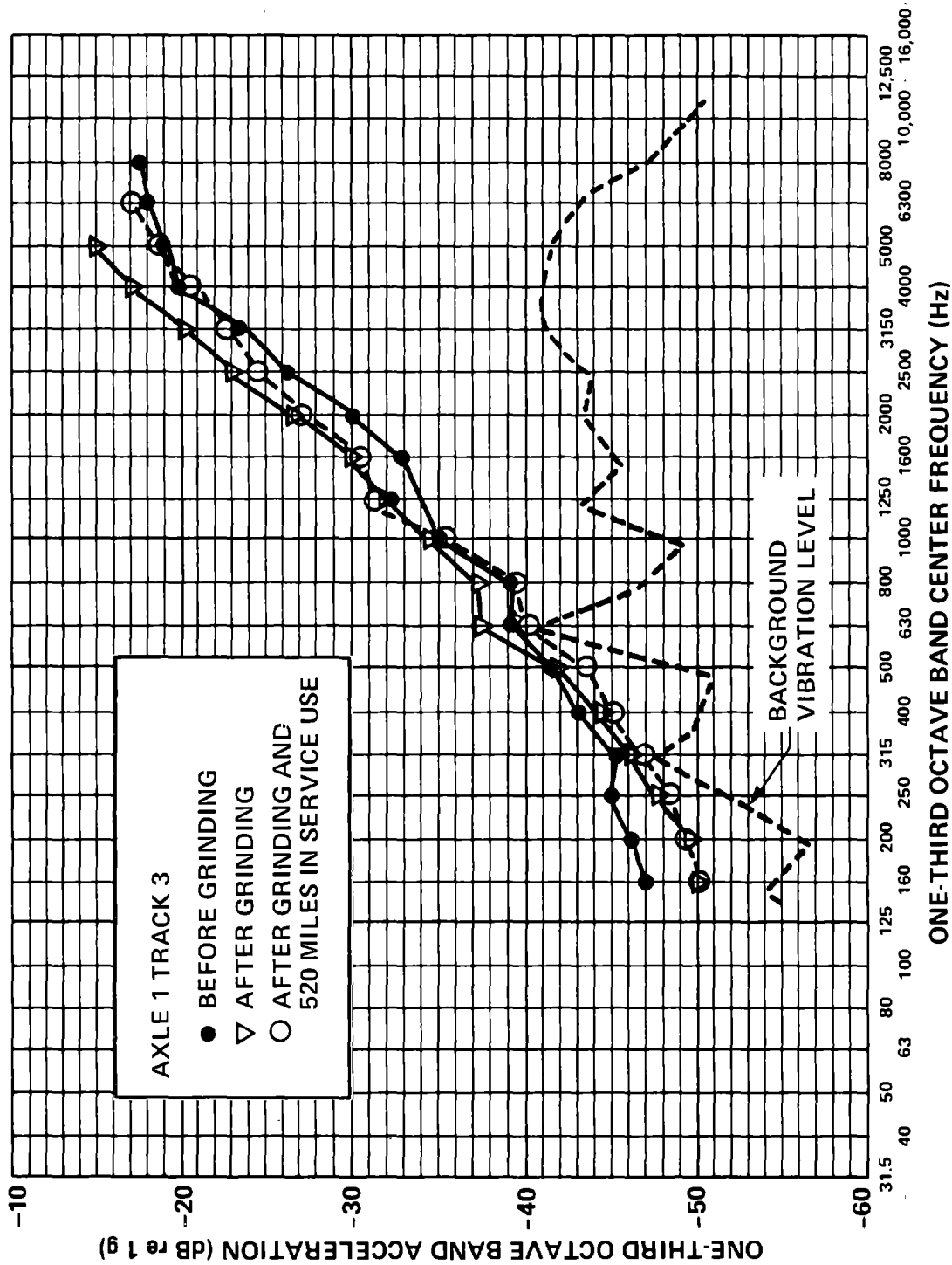


FIG. 131. ONE-THIRD OCTAVE BAND ACCELERATION LEVEL OBTAINED FROM SURFACE ROUGHNESS PROBE BEFORE AND AFTER BELT GRINDING. (WHEEL AXLE 1, TRACK 3; WHEEL SURFACE SPEED = 22.7 in./sec.)

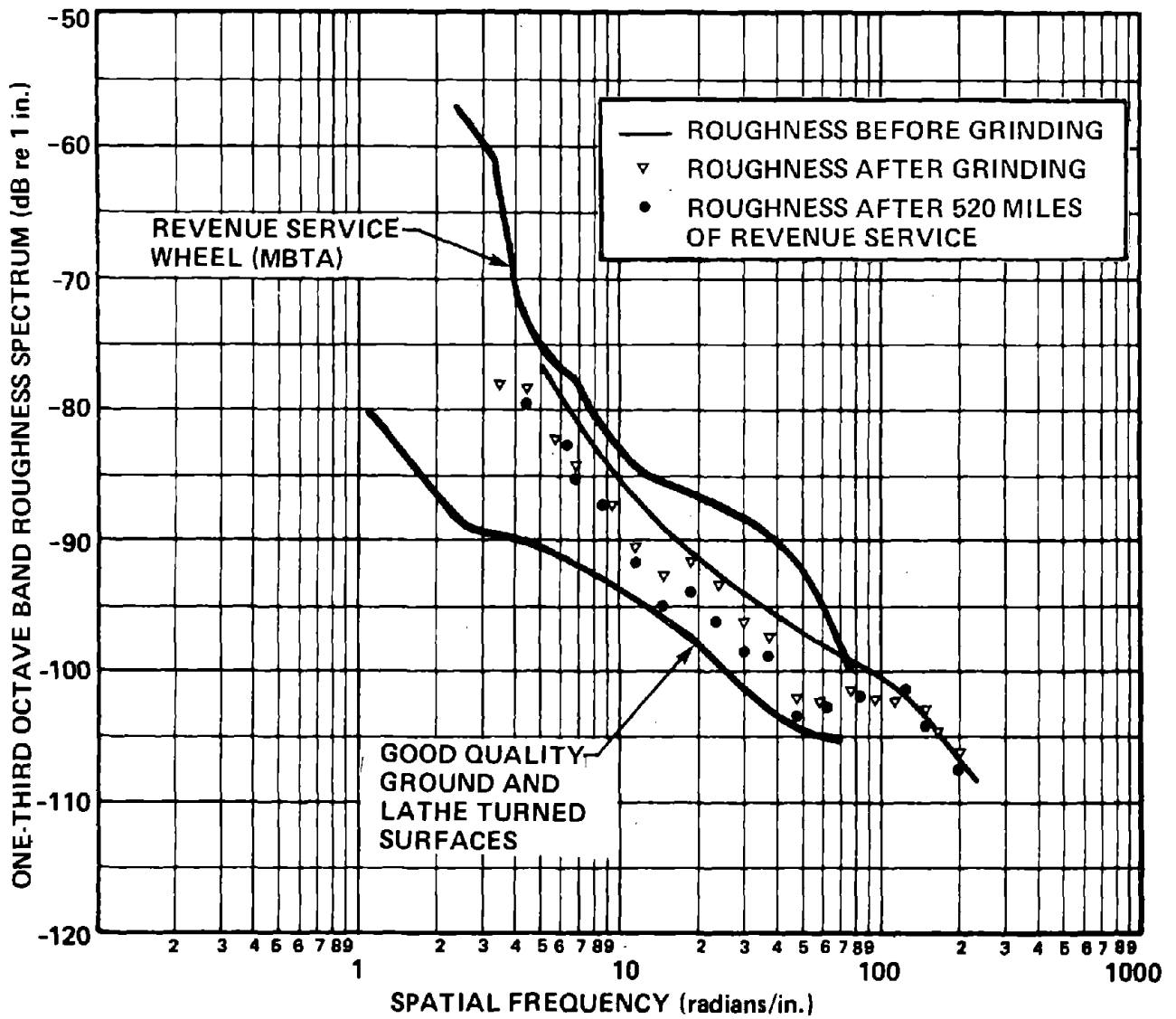


FIG. 132. WHEEL ROUGHNESS BEFORE BELT GRINDING, AFTER BELT GRINDING, AND AFTER 520 MILES OF SERVICE.

limit on roughness at the higher spatial frequencies and represents a slight improvement over the undercar milling machine.

Vertical Axis Rail Grinder

A vertical axis rail grinder is commonly used to reprofile the head of the rail. Figure 133 shows one machine of this type made by Speno and presently in use on SEPTA. It consists of a number of short cars, each carrying two sets of grinding wheels, one set over each rail, with their axes oriented vertically. Each grinding wheel is spun at high speed pressed against the rail head, and the whole train of cars is pulled along the track by a locomotive. By orienting the axes of the grinders at various angles off of vertical but perpendicular to the rail axis, one can shape the rail head to nearly any contour desired. At TTC (Pueblo), a vertical axis rail grinder made by Fairmont was used to grind the screech loop during the time that we were carrying out our field measurements. We used that opportunity to measure the rail roughness after grinding. Figure 134 shows the roughness measuring device in use on the screech loop. After the loop was ground, grinding marks could be clearly seen on the rail head as well as the worn path of the point of contact between the wheel and the rail. Figure 135 shows the roughness spectrum for that portion of the rail head where the grinding mark could be clearly seen. If we compare Fig. 135 with Fig. 74, we find that at high spatial frequencies the rail roughness is higher after grinding than it was on the tangent track section where we made our rolling noise tests. We believe that this higher roughness is caused by the machinery marks left on the rail by the grinder. With time, those marks will wear away and the rail roughness should then become very similar to that in Fig. 74.



FIG. 133. SPENO VERTICAL AXIS RAIL GRINDER AT SEPTA.

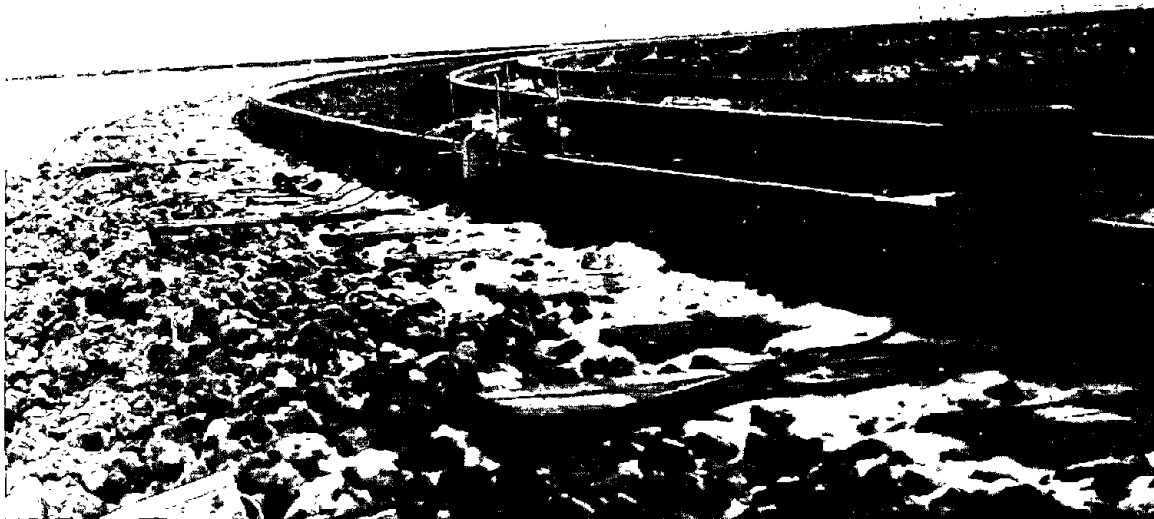


FIG. 134. THE RAIL ROUGHNESS MEASURING DEVICE IN USE ON THE SCREECH LOOP AT TTC (PUEBLO).

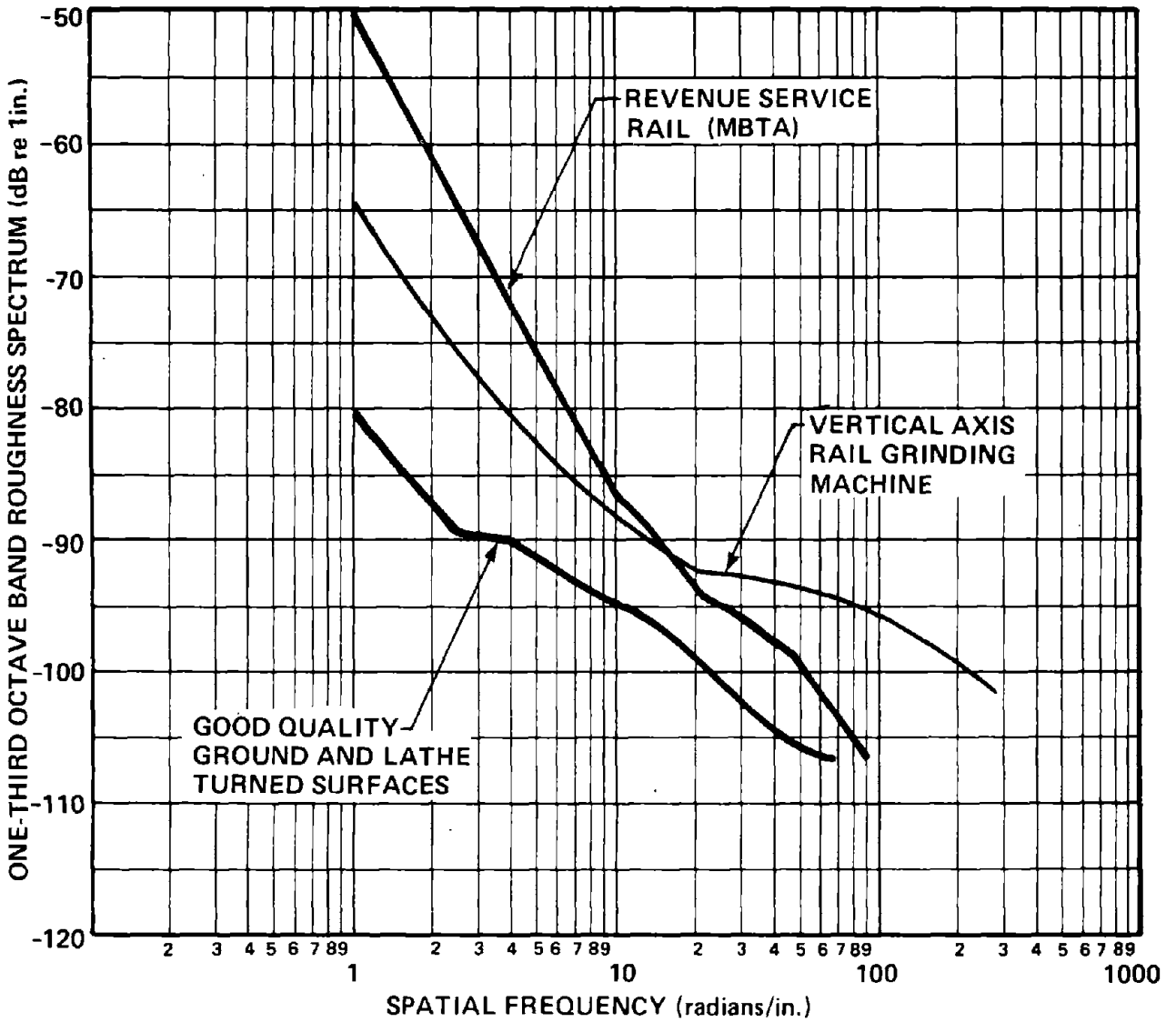


FIG. 135. RAIL ROUGHNESS AFTER USE OF THE VERTICAL AXIS RAIL GRINDER AT TTC (PUEBLO).

Grinding Block Machine

The CTA and TTC (Toronto) both use a rail grinder consisting of a rail car with grinding blocks mounted beneath the trucks. As the rail car is pulled along, the grinding blocks are pressed against the rails. After many passes, irregularities in the rail running surface are ground away. Figure 136 shows the CTA rail grinding car, and Fig. 137 shows the grinding block arrangement under the similar TTC (Toronto) rail grinding car.

To assess the ability of this technique to smooth the rails, we worked with the CTA to select a test site and measure the rail roughness before and after grinding. The test site was a section of the Evanston line on Track 4 North, adjacent to Loyola Station. Figure 138 shows a number of views of the test site. The track was in good condition because it was only five years old and its use is limited to the rush-hour period, Monday to Friday.

We chose a test section 16 ft long and made roughness measurements on both the outside and inside rails. The section of track around Loyola was relatively free from surface corrugations, so that it was not possible to obtain data on rail with and without corrugations. The initial measurements were made before any surface grinding was started. Next, we made intermediate measurements after 7 and 8 passes of the grinding machine. In a second trip to Chicago two weeks later, we measured the roughness after a total of 54 grinding passes. Usually, the grinding machine makes a total of approximately 80 grinding passes before the final finish is achieved. However, the track at Loyola was initially in good condition, so fewer passes were considered necessary.

The roughness measurements were made using the BBN roughness measuring device described in Sec. 3.2.3. Acceleration levels



FIG. 136. THE CTA RAIL GRINDING CAR.

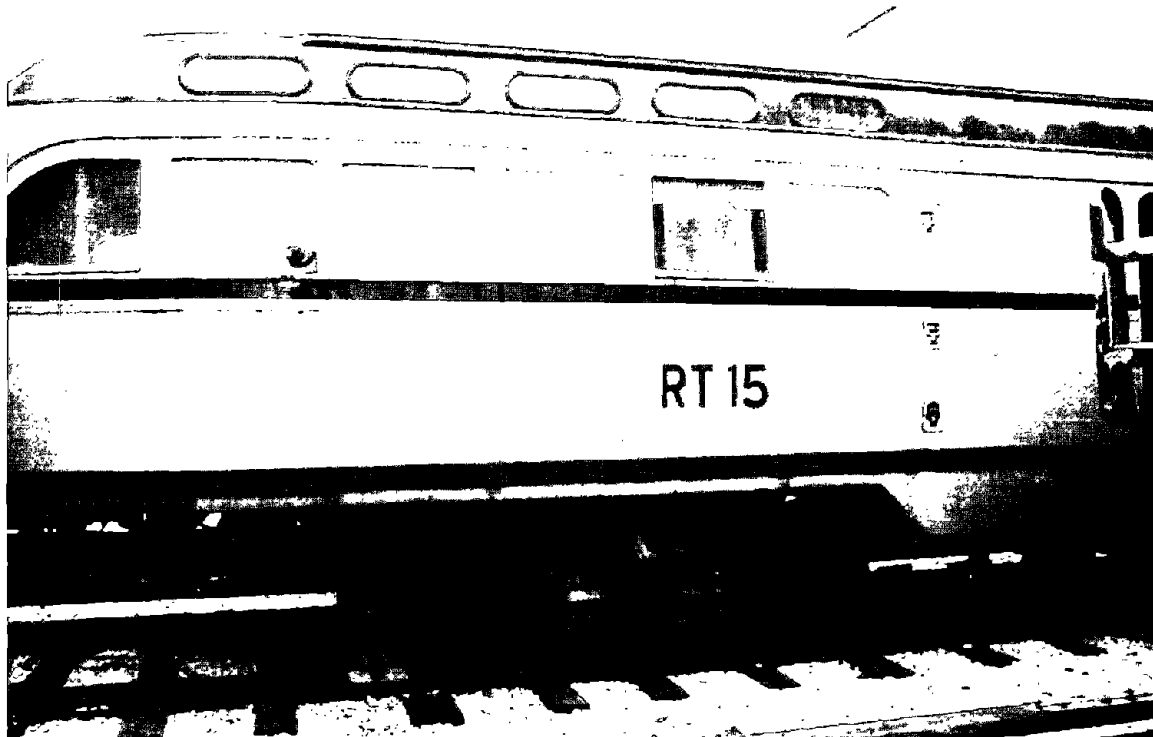
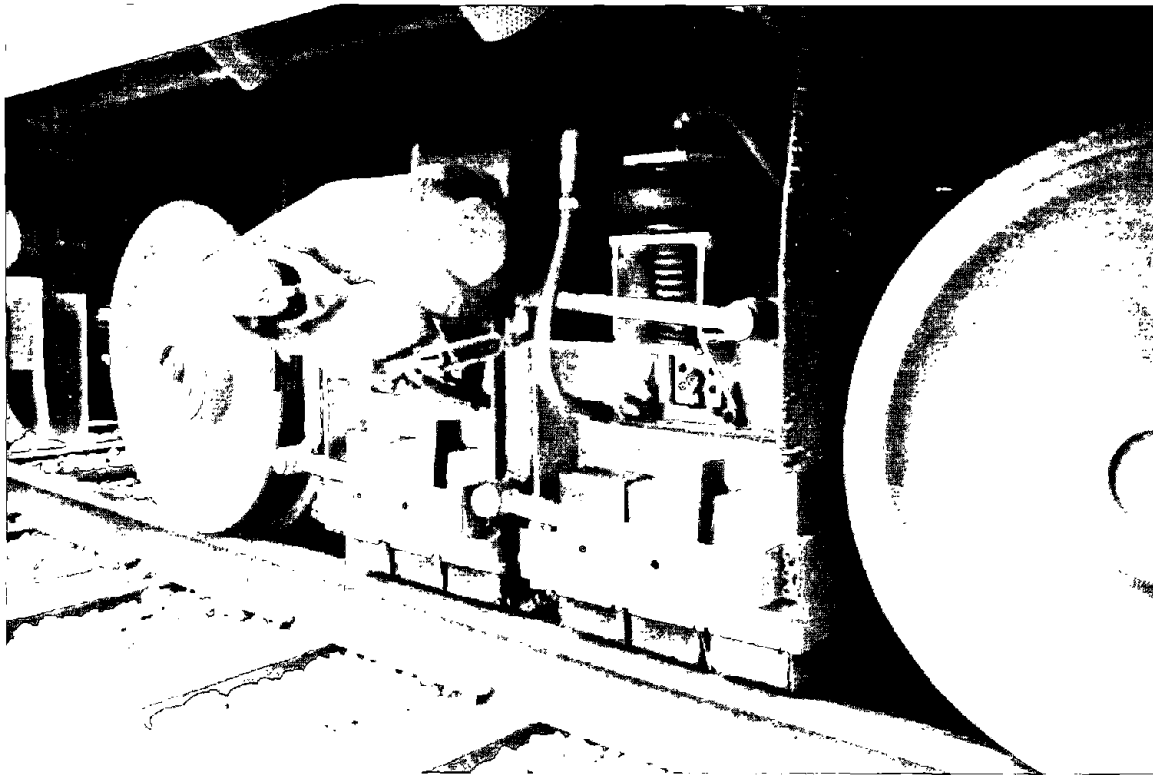


FIG. 137. THE GRINDING BLOCK ARRANGEMENT UNDER THE TRUCKS OF THE TTC (TORONTO) RAIL GRINDING CAR.



FIG. 138. THE CTA TEST SITE AT LOYOLA STATION ON THE EVANSTON LINE.

from the probe were recorded on an FM tape recorder and later analyzed in the lab to obtain the roughness spectrum as a function of wave number. The results are discussed below.

Figure 139 shows the roughness spectrum measured on the outside rail before any surface grinding had been made (runs 6,7). This measurement is compared with our previous data obtained from the welded rail at the test track at Transportation Test Center (TTC), Pueblo, Colorado. The two rails show very similar roughness levels, and it is apparent that the rail at CTA is indeed in good condition, even before surface grinding. The other data points shown in Fig. 139 were taken after 7 and 8 grinding passes. Very little difference is seen in the data after only a few passes. In fact, at small wave numbers (long wavelengths), the roughness appears to be slightly higher after these passes than before grinding took place. The increased roughness probably occurs because only the high spots on the rail are touched by the first few grinding passes, leaving a rougher truncated rail surface.

The finish roughness (54 passes) for the outside rail is compared with the initial roughness in Fig. 140. The solid line shows the average roughness levels taken from runs 6 and 7, while the points represent finish grinding measured at three different probe cart speeds. At wave numbers below $k = 4$ (wavelengths $\lambda > 1.57$ in.), there is very little reduction in surface roughness from the grinding. However, at wave numbers above $k = 4$, there is a 2- to 5-dB reduction in roughness level. This reduction represents a significant improvement in the rail roughness and brings the spectrum level close to the lower limits of achievable smoothness.

The corresponding roughness spectra for the inside rail are shown in Fig. 141. The improvement in rail roughness at high

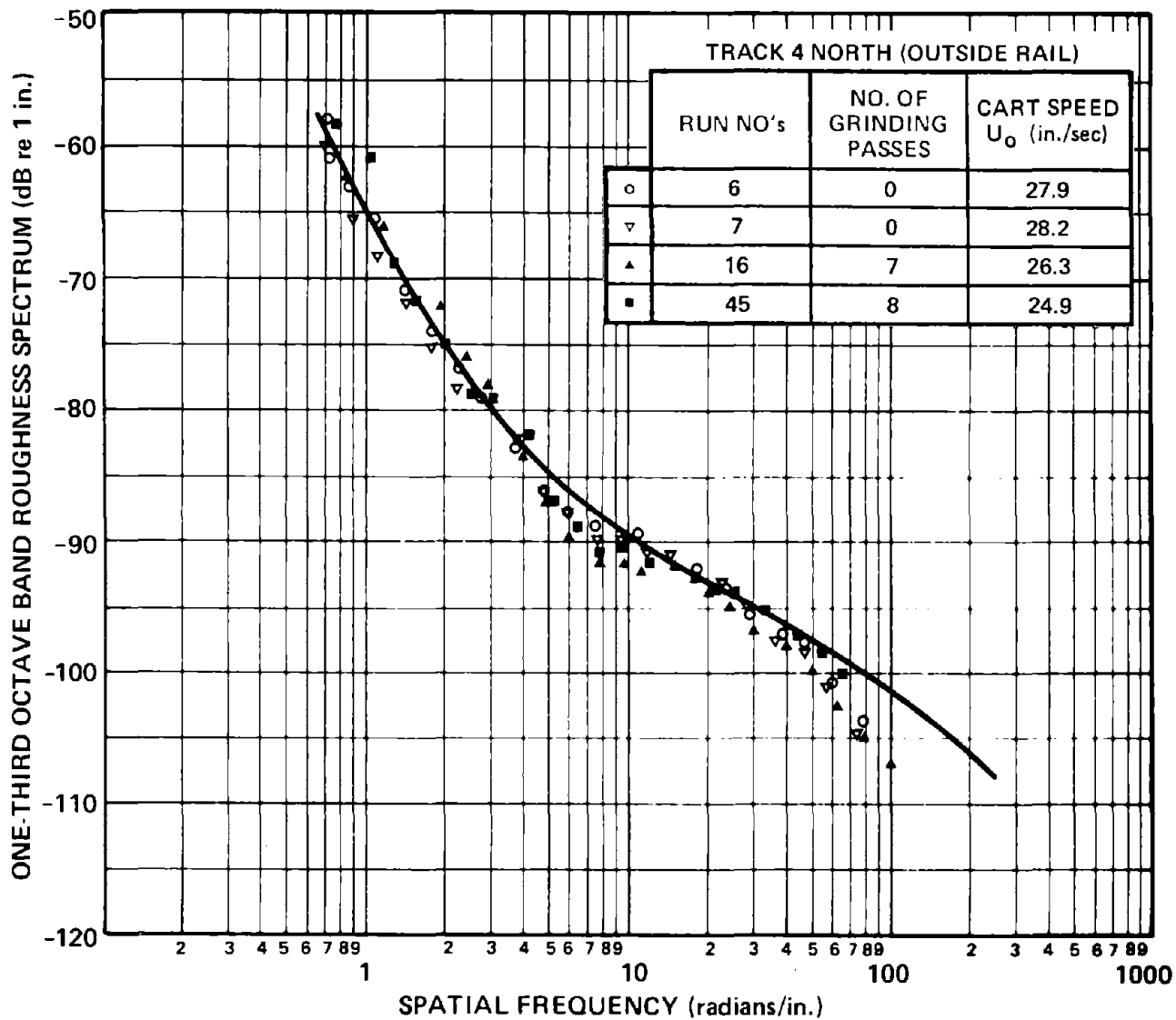


FIG. 139. CTA (LOYOLA STATION) RAIL ROUGHNESS BEFORE GRINDING AND AFTER 7 TO 8 PASSES.

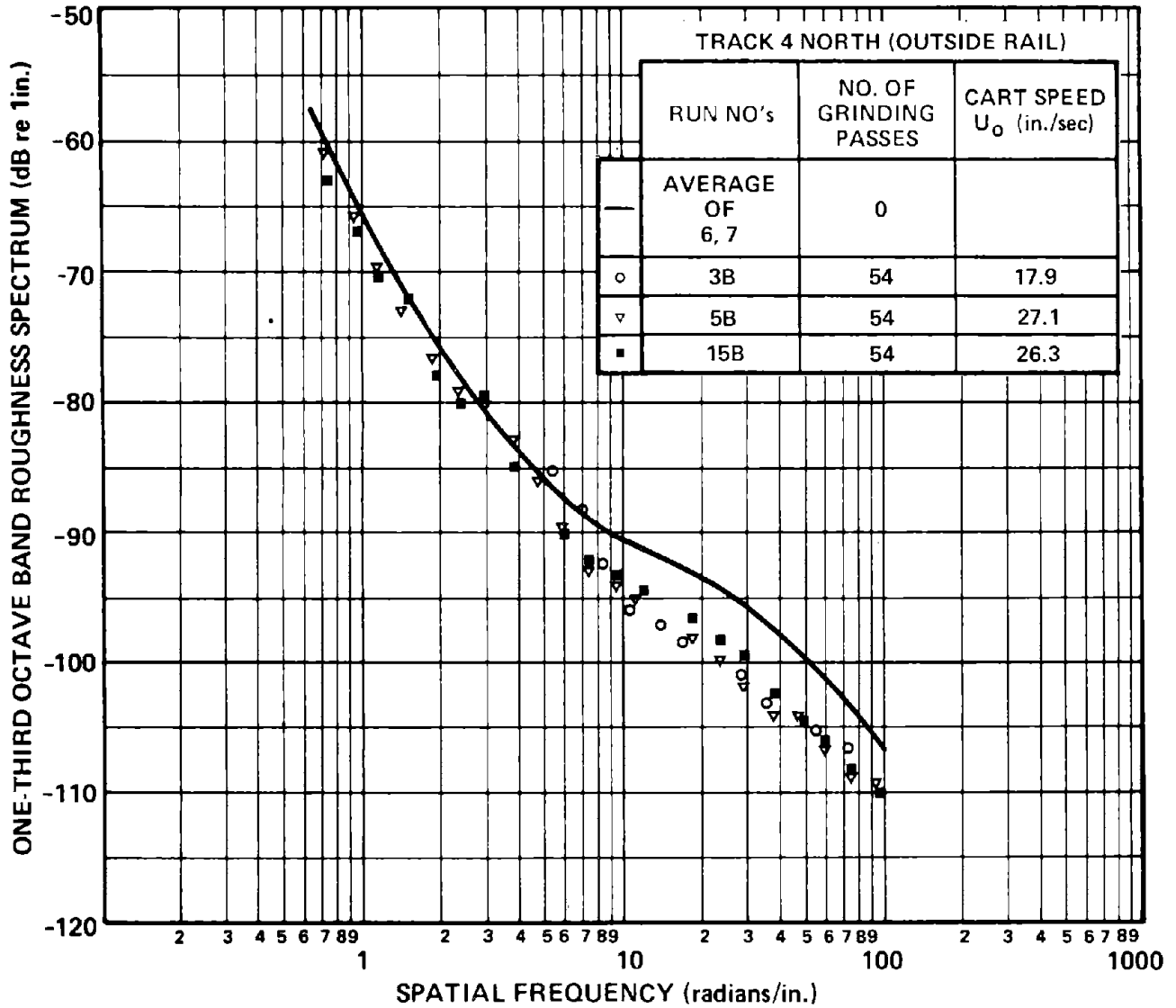


FIG. 140. COMPARISON OF RAIL ROUGHNESS AT CTA (LOYOLA STATION) BEFORE AND AFTER RAIL GRINDING. (OUTSIDE RAIL.)

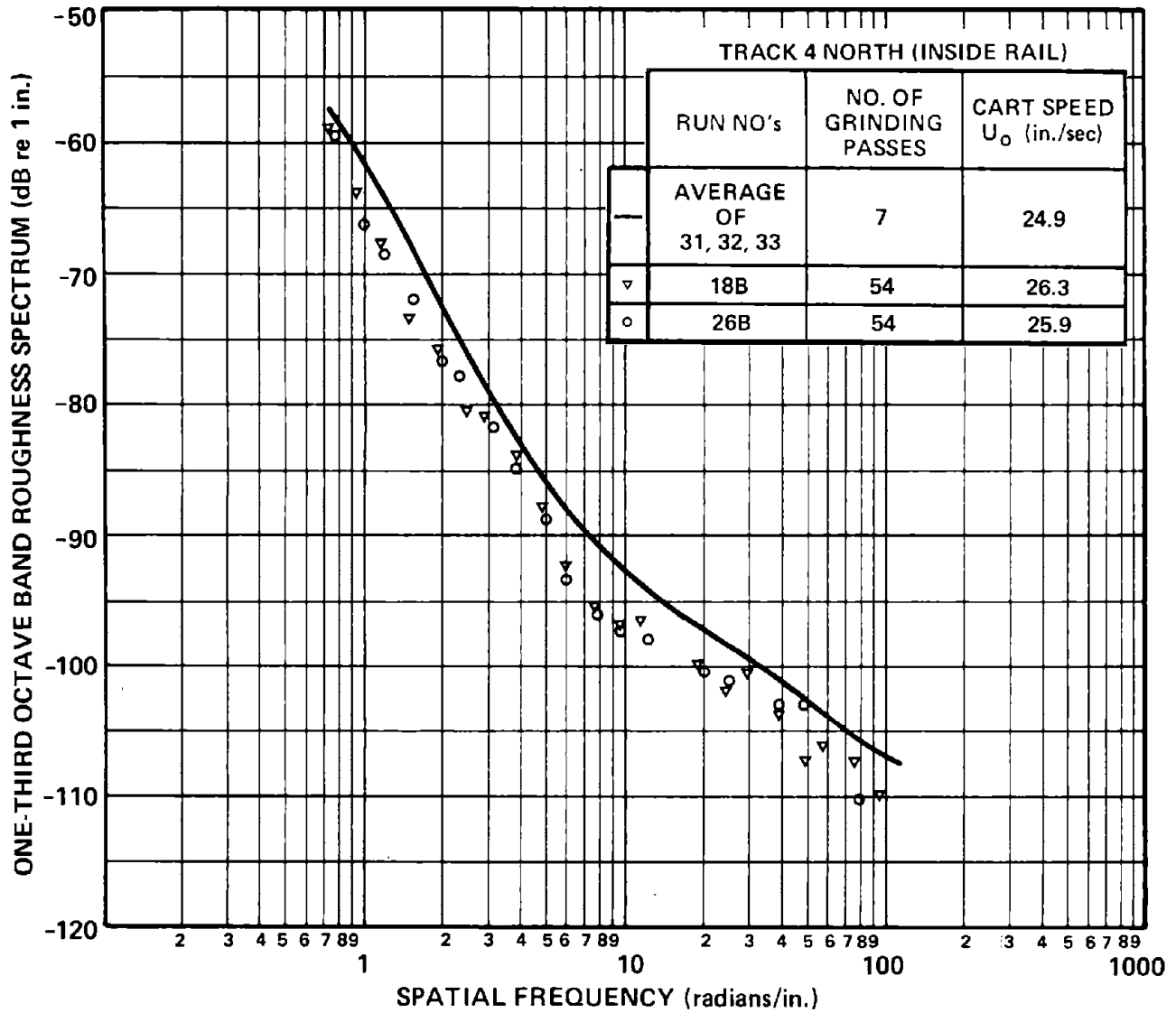


FIG. 141. COMPARISON OF RAIL ROUGHNESS AT CTA (LOYALA STATION) BEFORE AND AFTER RAIL GRINDING. (INSIDE RAIL.)

wave numbers is only 2 to 3 dB after 54 grinding passes. However, note that the initial rail roughness for the inside rail was lower by 1 to 3 dB (at high wave numbers) than that measured on the outside rail. The final roughness levels after grinding for both inside and outside rails are very similar (within ± 1 dB for most wave numbers). Also, the grinding on the inside rail (see Fig. 141) appears to have improved the low wavenumber roughness by 1 or 2 dB).

Figure 142 compares the rail roughness after grinding with the estimated lower bound and with rail roughness on the MBTA. Except for spatial frequencies below 5 rad/in., the CTA rail grinder produces a surface finish that we consider the best achievable. Possibly, with some redesign of the grinding block support, improved performance could be obtained even at the lower spatial frequencies (wavelengths from 1 to 6 in.). However, as we shall see later, such redesign does not seem necessary to achieve the full noise reduction benefits.

Noise Reduction

Using the baseline system configuration of Sec. 4 and the analytical model of Sec. 2, we have estimated the wayside noise that would result after applying the various wheel and rail smoothing techniques discussed above. Figure 143 shows the estimated wayside noise 25 ft from the track centerline caused by the passage of a two-car train at 30 mph on welded rail with no wheel flats. In the figure, the terms "smooth wheels" on "smooth rails" mean wheels or rails with a roughness on their running surfaces equal to the lower bound roughness of Fig. 116.

Each wheel smoothing technique is shown in combination with the smoothest possible rails, and each rail smoothing technique is in combination with the smoothest wheels. These combinations show the greatest possible noise reduction achievable with each technique.

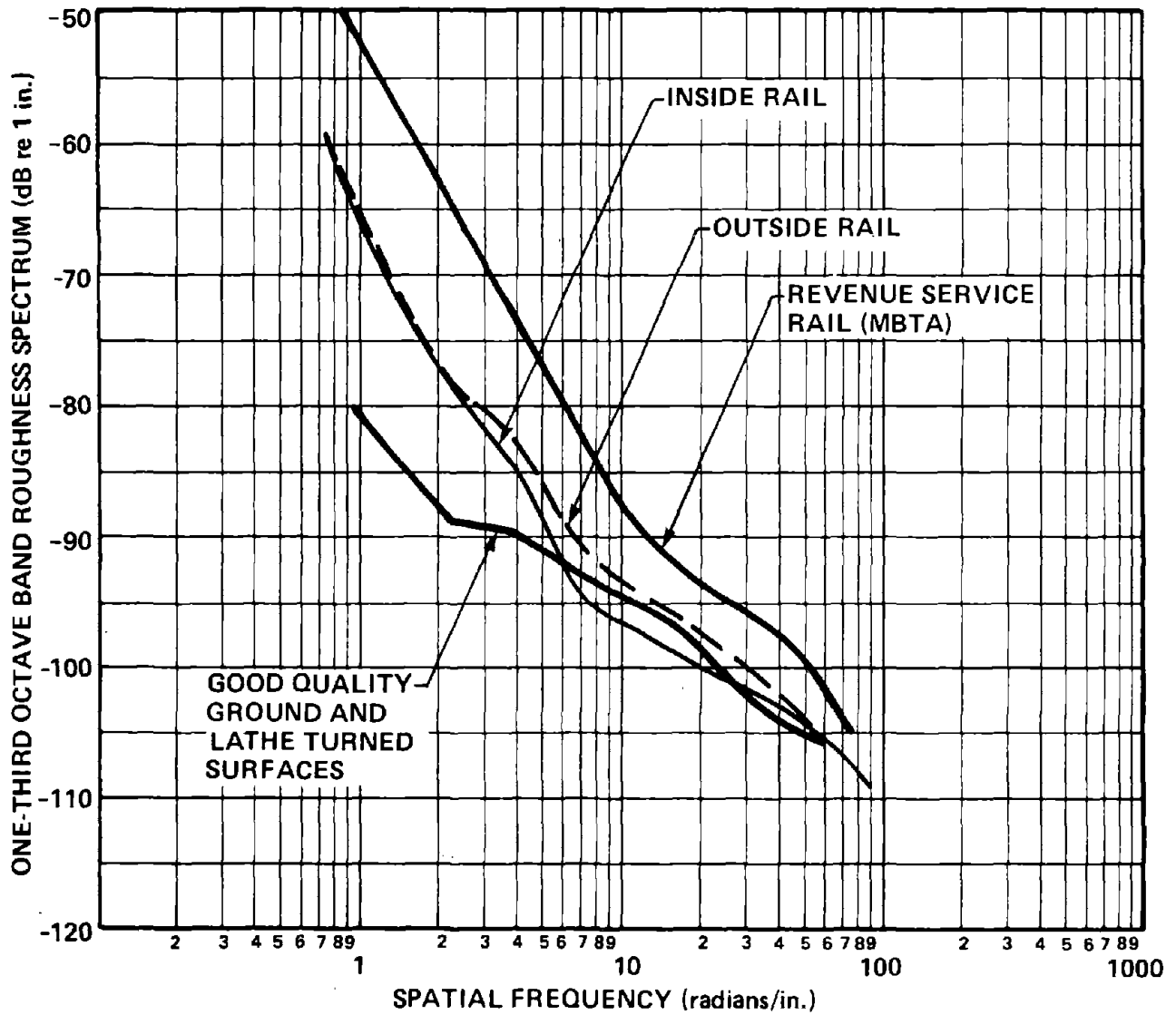


FIG. 142. PERFORMANCE OF THE CTA RAIL GRINDER.

SUMMARY WHEEL/RAIL SMOOTHING TECHNIQUES

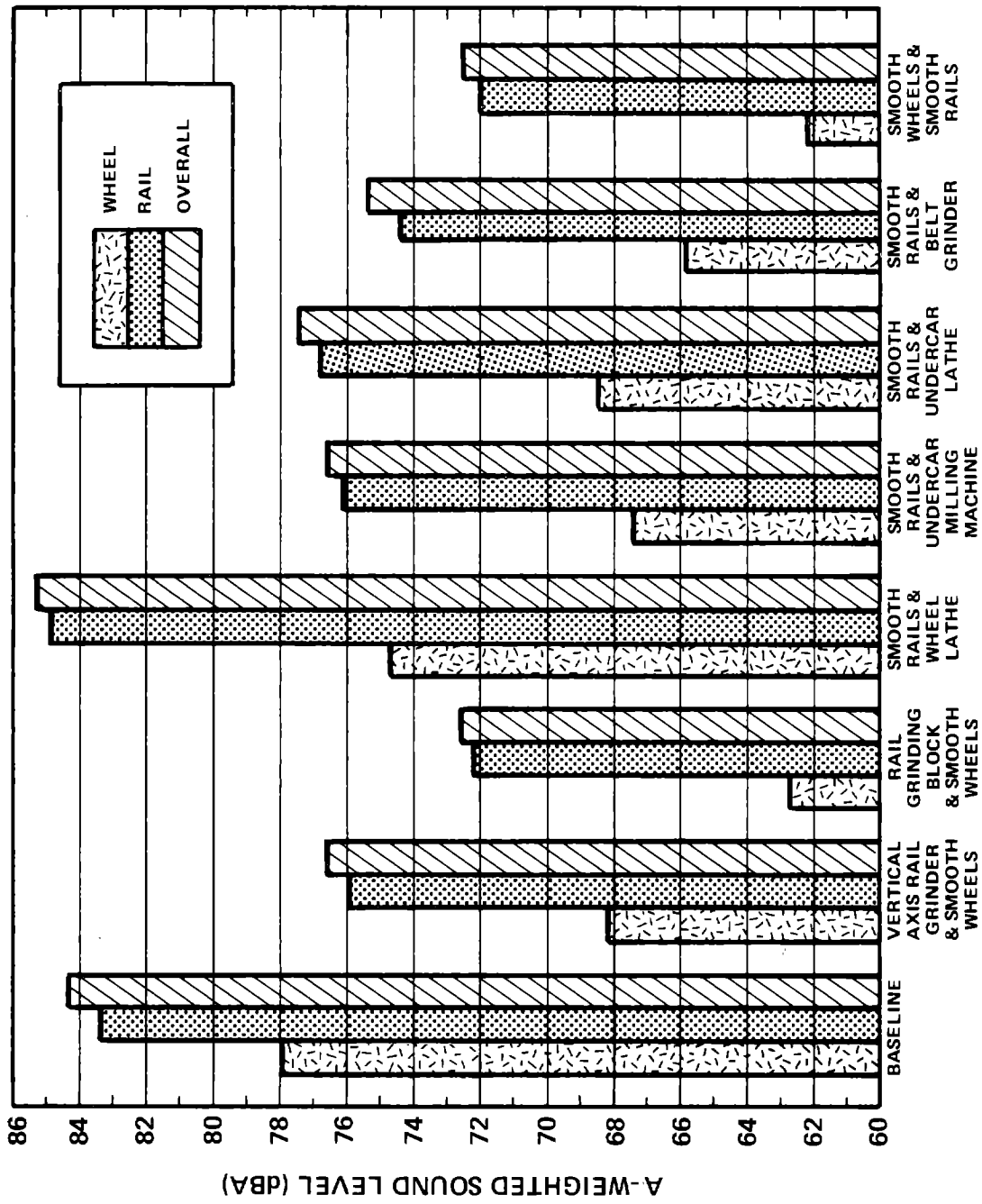


FIG. 143. THE ESTIMATED REDUCTION IN NOISE FROM A TWO-CAR TRAIN AT 25 FT, BECAUSE OF WHEEL TRUING AND RAIL GRINDING.

The rail grinding block machine gives by far the greatest noise reduction of the two rail grinding techniques examined. In fact, the combination of CTA rail grinding and smooth wheels produces little more noise than the combination of smooth wheels and the best achievable rail surface finish (smooth wheels and smooth rails). The best wheel smoothing technique is the TTC (Toronto) belt grinder, although it does not produce a surface finish nearly as good for noise reduction as the CTA rail grinder.

Figure 144 shows the reduction in noise achievable with the CTA rail grinder and the TTC (Toronto) belt grinder. Nearly 10 dBA of noise reduction can be achieved. Another 3-dBA reduction appears possible if improved wheel smoothing techniques can be found.

The above discussion indicates that dramatic reductions in wheel/rail rolling noise are achievable through the proper selection of wheel and rail smoothing techniques. Of course, how long the smooth running surfaces will last in revenue service is an important question that we have made no attempt to address in this study. If both wheels and rails are kept smooth, the running surfaces may remain smooth for some time. On the CTA, we found that the rails were remarkably smooth before grinding. In fact, they were as smooth as the rails on TTC (Pueblo) test track, even though two years had passed since the last grinding. Additional grinding did smooth the rails further, indicating that some roughening had occurred in the intervening two years. However, the rails were still noticeably smoother than revenue service rails on the MBTA, for example.

The results here clearly indicate the value of using the rail grinding block technique - as on the CTA and TTC (Toronto) - for rail smoothing where noise is the primary concern. Where the

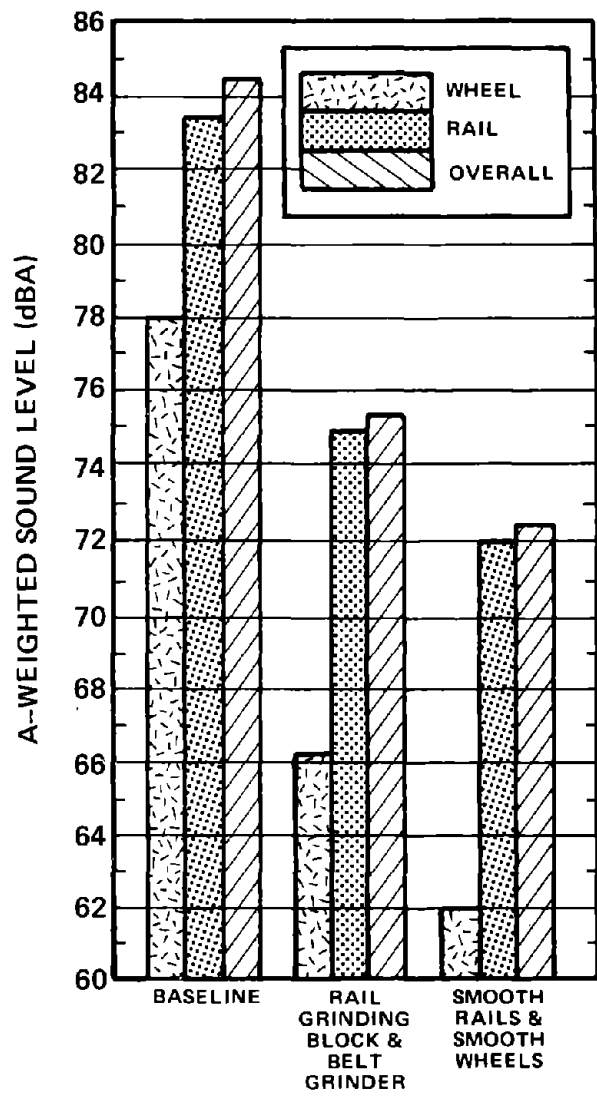


FIG. 144. THE ESTIMATED REDUCTION IN NOISE ACHIEVABLE WITH THE BEST WHEEL-TRUING AND RAIL GRINDING TECHNIQUES.

rails must also be reprofiled, a vertical axis rail grinder can first be used and then the rail grinding block technique can be applied to further smooth rail for noise control.

Although the belt grinder used at TTC (Toronto) does seem to be the best wheel smoothing technique available, an additional 3 dBA of noise reduction should be possible. A smoother wheel finish might be achieved by using different belt speeds, wheel rotation rates, or less abrasive belts. Such a finish might approach the limits of surface finish that the rail grinding block technique has already achieved.

5.2.2 Resiliently treaded wheels

The results of Sec. 4 showed that increasing the contact area and reducing the contact stiffness between wheel and rail can cause significant reductions in wheel/rail noise. Wheel designs that use both increased contact area and reduced contact stiffness have come to be called resiliently treaded wheels. These are distinct from resilient wheels such as the Penn Cushion Wheel or SAB wheel, in which a very thick and heavy tread ring is simply isolated from the rest of the wheel through the use of elastomeric elements. The resiliently treaded wheel uses a thin, light tread ring (or a special tread material) that is sufficiently compliant to deform around irregularities on its own or on the rail's running surface and to contact the rail over a larger area.

As part of this program we examined the noise-reducing capability of two resiliently treaded wheel designs. The first, a nickel titanium treaded (nitinol) wheel was designed and developed by Raychem Corp. as a railroad wheel to provide improved adhesion. It was felt that the nickel titanium alloy in the tread, because it is more compliant than steel, might provide some noise reduction as a resiliently treaded wheel. Therefore,

as part of this program, a number of laboratory tests were performed on two scale model nitinol wheels to determine their acoustic performance. A second wheel was designed, built, and tested in the laboratory by BBN to study a design in which the tread was made resilient by allowing a thin tread ring to deform in bending. In this section, we discuss the laboratory tests carried out on each type of wheel.

Nitinol Wheels

Nitinol or tinel is a general term for a broad class of nickel titanium alloys first exploited for their "shape memory" properties. If cooled to below what is called the transformation temperature, nitinol requires less stress to deform it than it requires at room temperature. If after deformation the material is warmed to above its transformation temperature, it will return to its shape before deformation. When run against steel, nitinol also has special friction properties that result in improved adhesion under certain contaminated conditions; these properties also prevent nitinol-treaded railroad wheels from squealing on short-radius curves.

In the series of tests described here, we examined the ability of a nitinol-treaded railroad wheel to reduce rolling noise. We used the roller rig at Raychem Corp. described in Sec. 2 that was used to obtain lateral friction vs creep data for our squeal studies. For these tests, the rig used a small (approximately 7 1/2-in.-diameter) wheel to simulate a continuous rail. larger (30-in.-diameter) wheel to simulate a continuous rail. This larger wheel (rail wheel) is driven by an ac motor and can operate at speeds in excess of 90 km/hr. The train wheel is brought into contact with the rail wheel and rolls freely with it. Radial loads, which simulate the transit car, are applied to the test wheel. For an earlier, unrelated program, the rig was

scaled to simulate an 18-in. wheel rolling on a rail with a radius of curvature of 14 in. in the plane perpendicular to the rail axis. As shown in Fig. 145, this results in a radius of curvature on the simulated rail head of 5.83 in. If we wish the 7.5-in. test wheels to simulate 30-in. rapid transit wheels, the radius of curvature of the rail head would scale up to 23 in. The radius of curvature of standard rail profiles is 10 in. or 14 in.; therefore, the simulated rail head does not scale properly. However, since we will be comparing simulated nitinol and a simulated standard wheel, we do not consider the discrepancy in rail head radius of curvature too serious.

Of somewhat more concern, however, is the impedance of the rail wheel, which does not properly simulate the impedance of a rail. To make it properly simulate a rail would have required a major development effort involving significant modification of the existing roller rig. We decided to test the nitinol wheel and the resiliently treaded wheel described later in this section on the unmodified roller rig to obtain a preliminary indicating of their performance. Later testing, if justified, should be carried out on an actual rail vehicle.

Tests were carried out for a steel wheel and two nitinol wheels, all provided by Raychem. The geometry of the three test wheels is shown in Fig. 146. The two nitinol wheels are marked "A" and "C," indicating that each was fabricated from slightly different alloys. In addition, the nitinol C wheel was composed of a thin ring of nitinol on a steel wheel, whereas the nitinol A wheel was solid nitinol. Although the composition of the nitinol A and C alloys is considered proprietary by Raychem, Table 10 gives the approximate transition temperatures and elastic moduli of each.

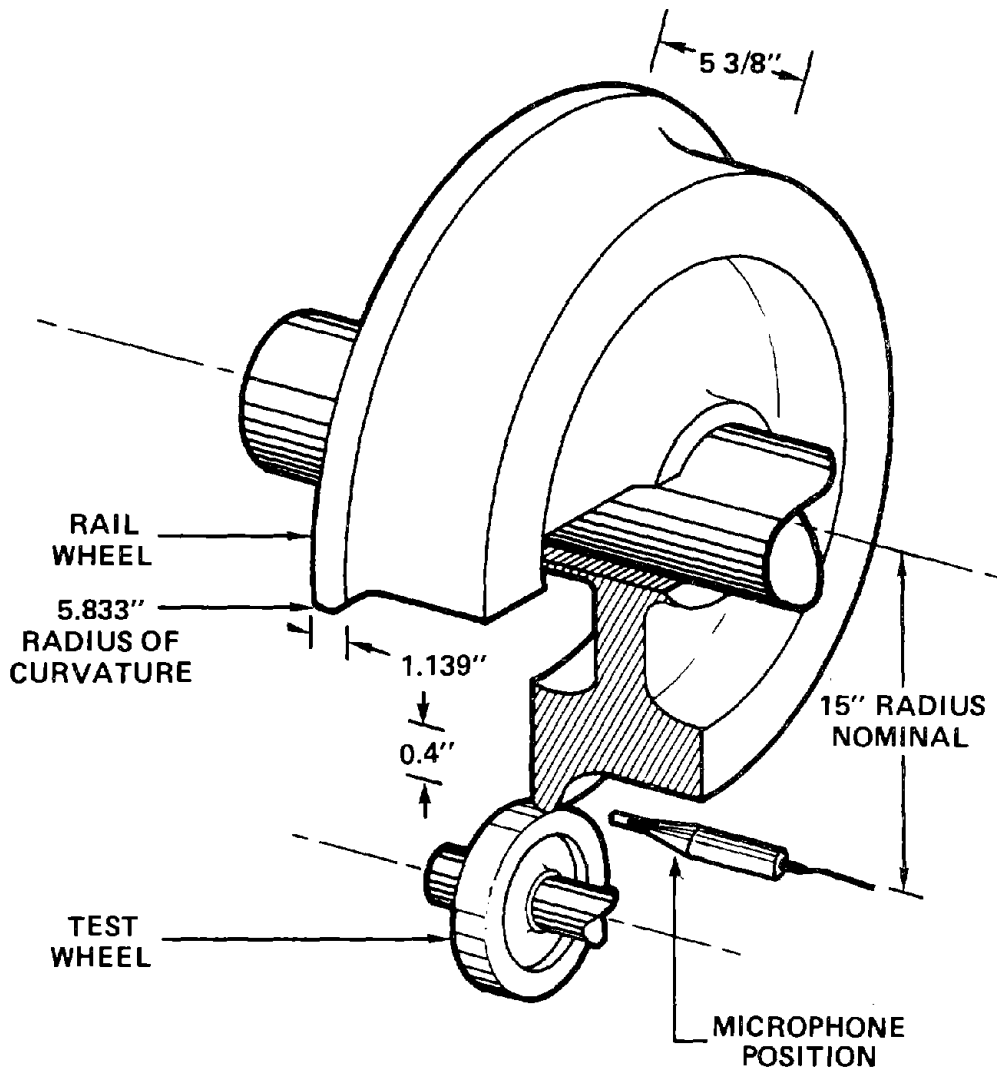


FIG. 145. RAIL WHEEL GEOMETRY.

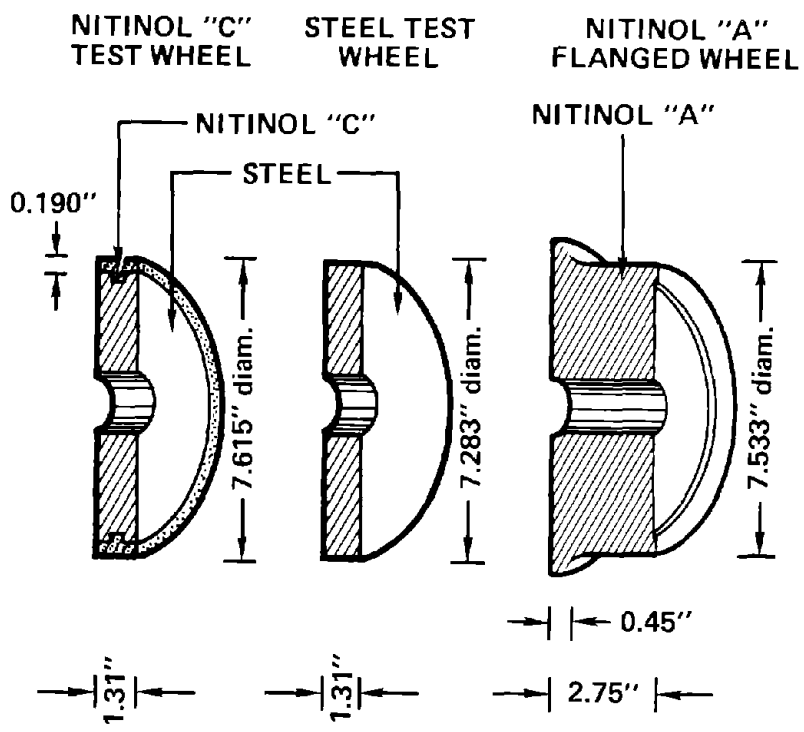


FIG. 146. DIMENSIONS OF THE THREE TEST WHEELS.

TABLE 10. NITINOL ALLOY PROPERTIES.

	Transformation Temperature (°F)	Elastic Moduli (psi)
Nitinol A Alloy	-125°C	1.25·10 ⁷
Nitinol C Alloy	- 70°C	1.1·10 ⁷

Before the test, each of the three test wheels was machined on a lathe and buffed to a high surface finish. The surface roughness of each test wheel was measured using the BBN roughness measuring device. Figure 147 shows the roughness measuring device mounted on the roller rig, and Fig. 148 shows the roughness spectra of the three test wheels and the rail wheel. The circles and triangles show the steel wheel roughness for two different speeds, whereas the nitinol C and nitinol A wheels were measured at only one speed. Figure 148 shows the steel wheel to be smoother than both the nitinol C and the nitinol A wheels. The rail wheel is of comparable roughness to the nitinol wheels. In the generation of rolling noise, the combination of the rail wheel roughness and the test wheel roughness generates the rolling noise. Consequently, when one compares the summation of the steel wheel and the rail wheel roughness with the nickel titanium C wheel and the rail wheel roughness, the difference between these two combinations is small for most of the range of wave numbers.

The area of contact between the rail wheel and the test wheels was measured for both steel and nitinol wheels. These contact patch areas were obtained using the SEM replicating tape described in Sec. 3. The tape was inserted between the wheel and rail and the load applied. Figure 149 shows the two contact patches for 625 lb and 990 lb for the steel and nitinol C wheels. Using the Hertzian theory of Sec. 2, we find that the

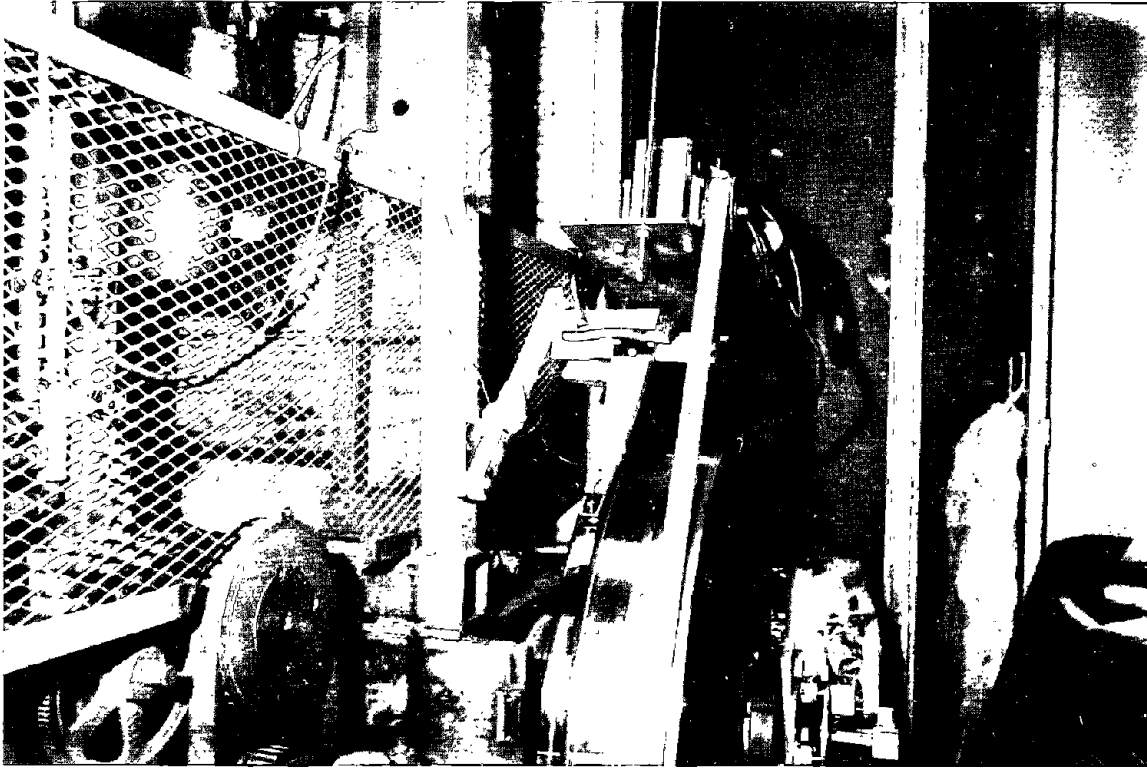


FIG. 147. BBN ROUGHNESS MEASURING PROBE MOUNTED ON ROLLER RIG.

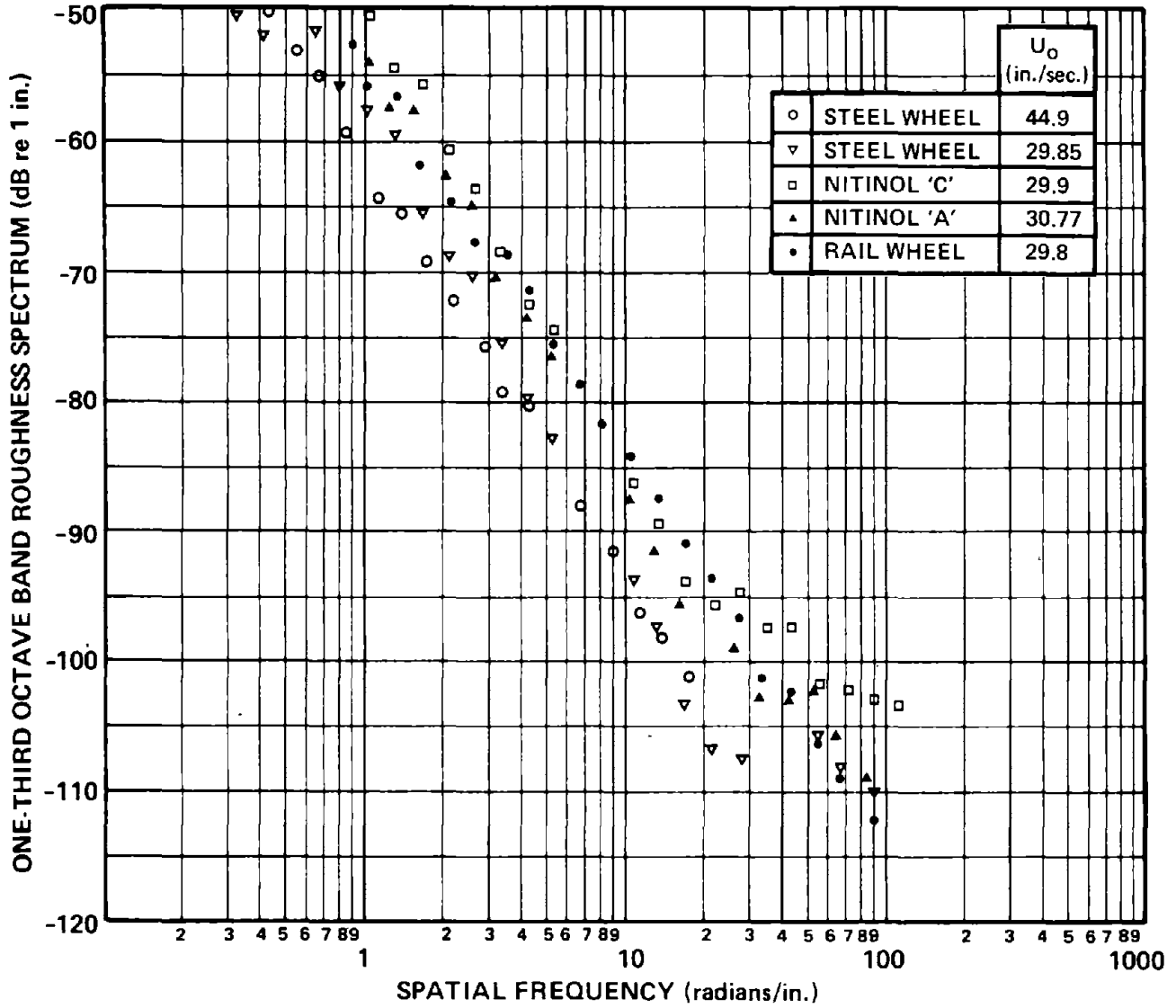


FIG. 148. ROUGHNESS SPECTRA MEASURED ON ROLLER RIG.

No. 1 STEEL WHEEL
625 lbs LOAD



$a/b = 1.56$
AREA = 12.6 sq mm.

No. 2 STEEL WHEEL
990 lbs LOAD



$a/b = 1.58$
AREA = 17.9 sq mm.

No. 3 NITINOL 'C'
625 lbs LOAD



$a/b = 1.63$
AREA = 20.4 sq mm.

No. 4 NITINOL 'C'
990 lbs LOAD



$a/b = 1.60$
AREA = 31.4 sq mm.

FIG. 149. CONTACT PATCH AREAS FOR STEEL NITINOL C WHEELS
(SHOWN ACTUAL SIZE).

theoretical contact areas for the steel wheel and the nitinol wheel at 625 lb load are 10 mm² and 16 mm², respectively. The areas in Fig. 149 measured using the SEM tape are uncorrected. In fact, as we discuss further in Sec. 3, those areas must be reduced by about 24% to account for the thickness of the tape and other factors. Since the uncorrected measured areas are about 20% larger than the theoretical predictions, theory and measurement agree quite well. For the ratio of the two axes of the ellipse the theoretical prediction gives a/b = 1.18. The measured eccentricity of the ellipse is higher, on the order of 1.5 to 1.6.

Noise measurements were made with a 1/4-in. condensor microphone located 1/4 in. from the wheel/rail interface. Figure 150 shows the associated instrumentation. Acceleration measurements were made at two positions on the rail wheel. Accelerometer No. 2 was located axially on the steel rim of the rail wheel, and accelerometer No. 3 was mounted on the center of the aluminum hub. The slip ring system was mounted on the axle of the rail wheel to bring the acceleration signals out to the tape recorder, as shown in Fig. 151. The accelerometers were calibrated and epoxied to the rail wheel with an electrical isolator between the wheel and accelerometer body.

In order to run these scale model tests in a meaningful way, we had to determine how to scale speed and load. If we want the contact patch filtering to be the same in the model and the full scale, then

$$(kb)_m = (kb)_{FS} \quad , \quad (112)$$

where k is the roughness wave number, b is the wheel/rail contact patch radius, the subscript m means model, and the subscript FS means full scale. If the model and full-scale wheel are

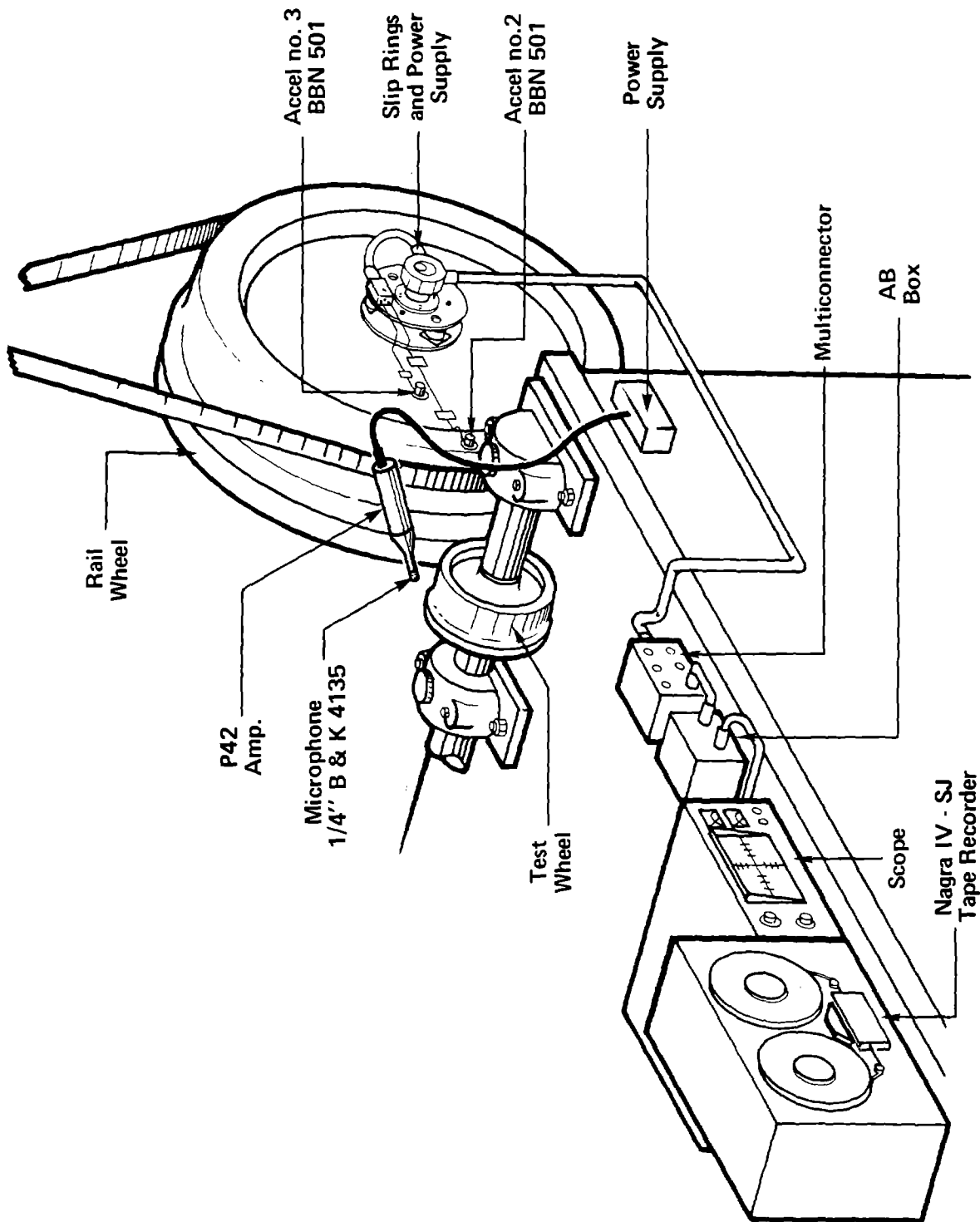


FIG. 150. NOISE AND VIBRATION INSTRUMENTATION.



FIG. 151. SLIP RING ASSEMBLY MOUNTED ON RAIL WHEEL (TTC PHOTO).

geometrically similar, the model and full-scale frequencies are related by

$$\omega_m = \alpha \omega_{FS} \quad , \quad (113)$$

where α is the scale factor or the ratio of full scale to model dimensions. Recalling that $k = \omega/V$, where V is the train speed, we can rewrite Eq. (112) as

$$\frac{\omega_m b_m}{V_m} = \alpha \frac{\omega_{FS} b_m}{V_m} = \frac{\omega_{FS} b_{FS}}{V_{FS}} \quad ,$$

or

$$\alpha \frac{b_m}{V_m} = \frac{b_{FS}}{V_{FS}} \quad .$$

If we require that

$$V_m = V_{FS} \quad ,$$

then the contact patch dimensions must scale with other wheel dimensions.

Using Hertzian contact theory, we can show that

$$\frac{b_m}{b_{FS}} = \left\{ \frac{P_m D_m}{P_{FS} D_{FS}} \right\}^{1/2} \quad , \quad (114)$$

where D is the wheel diameter and P is the load between wheel and rail. Substituting the scale factor α for the ratios of full scale to model wheel diameter and contact patch radius, we obtain

$$\frac{P_{FS}}{P_m} = \alpha^2 \quad .$$

For a 30-in., full-scale wheel, our nominal 7.5-in. scale model wheel implies a scale factor of four, and our scaling laws become

$$\omega_m = 4 \omega_{FS}$$

$$V_m = V_{FS}$$

$$P_m = \frac{P_{FS}}{16} \quad . \quad (115)$$

For example, to simulate a full-scale wheel running with a 10,000-lb wheel load at 60 km/hr at 100 Hz, we must load our model wheel with 625 lb, run it at the full-scale speed of 60 km/hr, and analyze the data at 400 Hz.

The rolling noise for the nitinol C wheel was measured under tangent running conditions for two different speeds, 60 kilometers per hour and 88 kilometers per hour. The noise spectrum measured under these two conditions, shown in Figs. 152 and 153, are compared with the noise under comparable conditions from the steel wheel. Also shown is the background noise. This last was fairly high; we believe it was caused by a cooling fan in the large electric motor that drives the rail wheel. The data above 315 Hz, however, are minimally contaminated with background noise. This frequency in the scale model tests corresponds to about 80 Hz for the full scale. Being able to simulate only those frequencies above 80 Hz is adequate for our purposes here.

If we scale the frequencies in Figs. 152 and 153 to full scale (i.e., divide by 4); apply the proper A-weighting at the full-scale frequencies; and calculate the overall A-weighted sound levels, we find the results shown in Table 11. There is a clear reduction in noise of 5 to 6 dBA at these two speeds. Figure 154 shows the vibration of the rail wheel (for comparable load and speed conditions to those in Fig. 153) measured at accelerometer position No. 2 for both the steel and nitinol C test wheels. The difference between steel and nitinol wheels is considerably larger in the acceleration spectra than in the noise

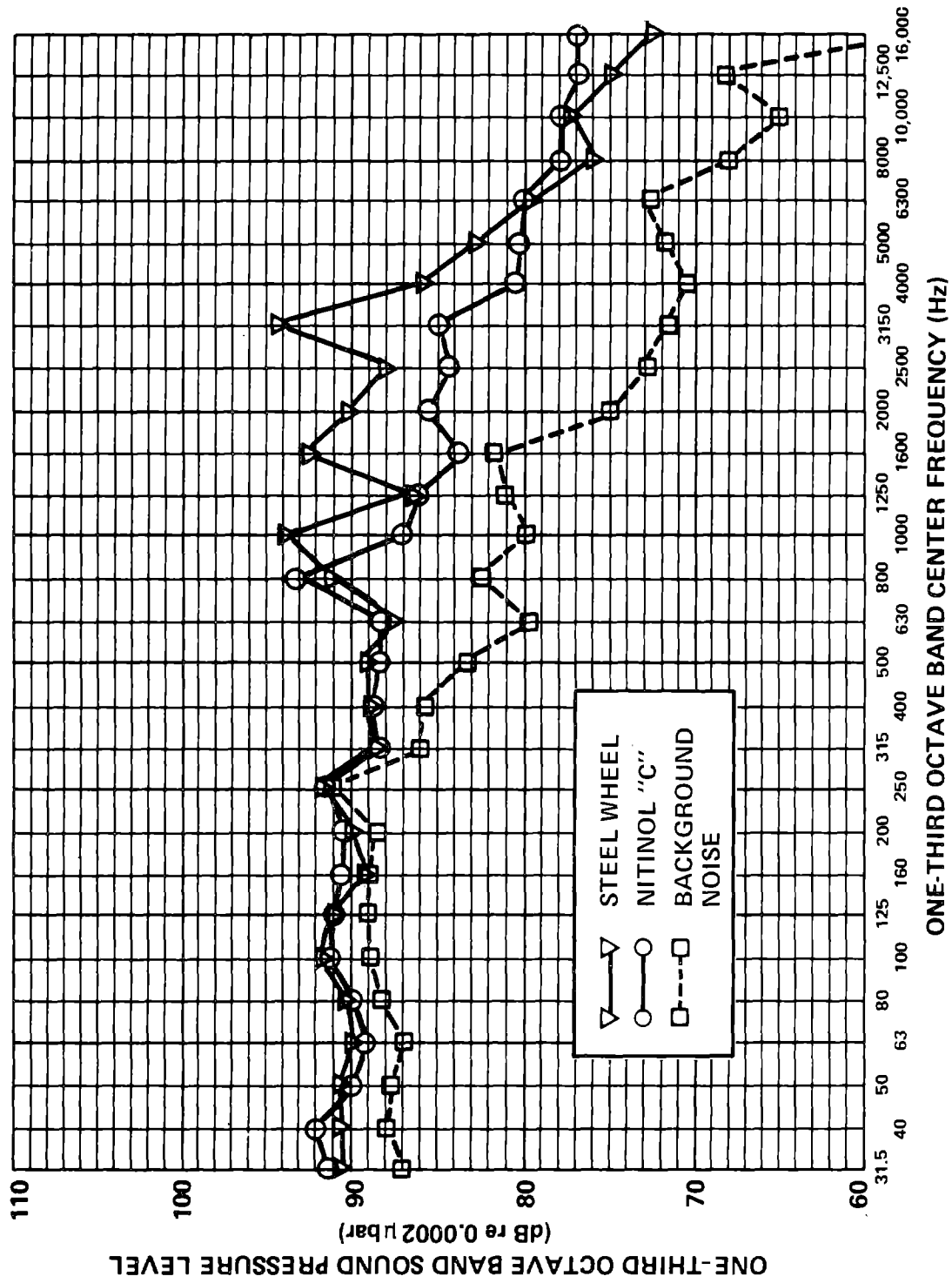


FIG. 152. COMPARISON OF ROLLING NOISE FOR STEEL AND NITINOL C WHEELS. (RAYCHEM ROLLER RIG; LOAD = 625 lb AT 60 km/hr.)

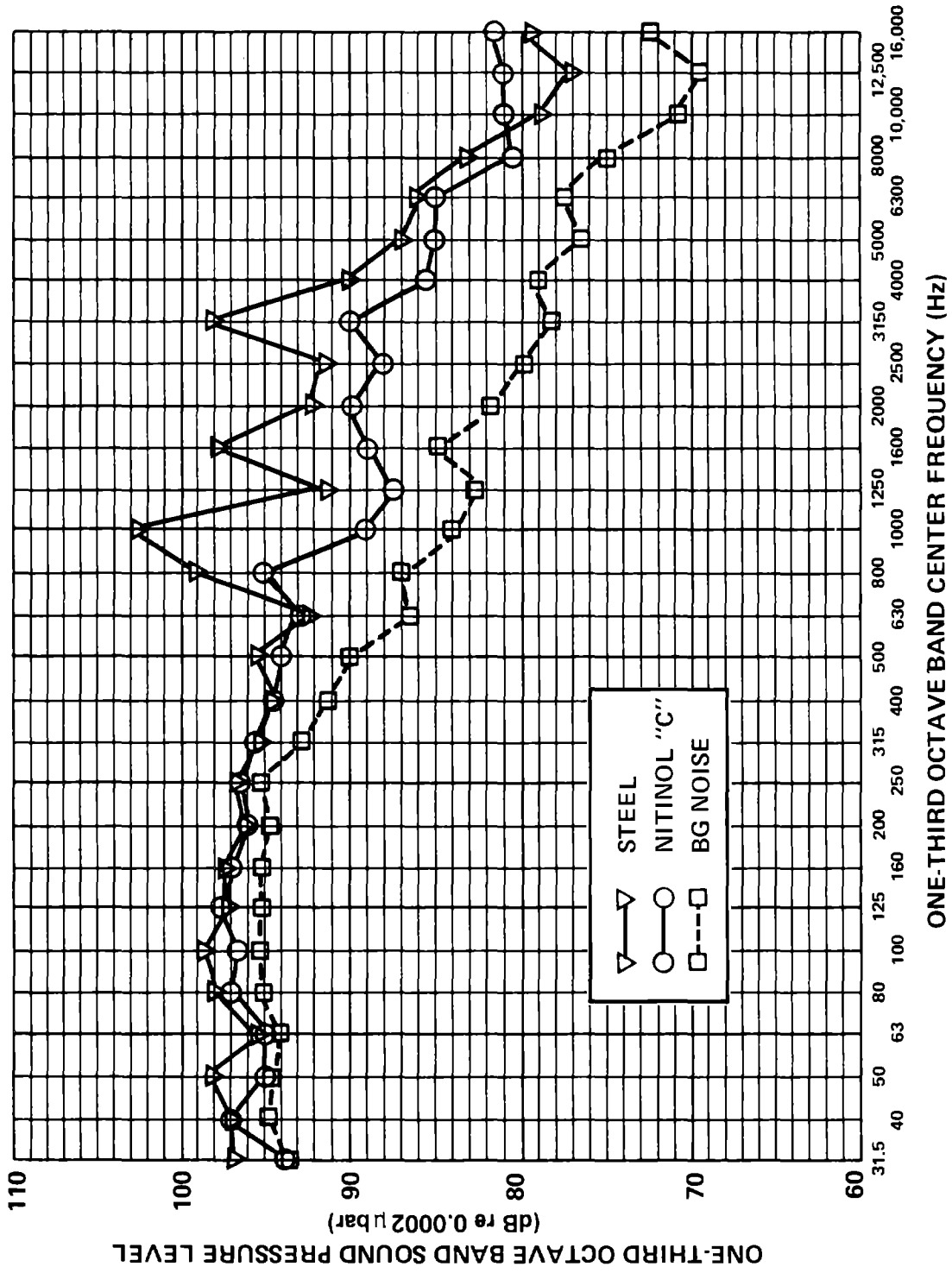


FIG. 153. COMPARISON OF ROLLING NOISE FOR STEEL AND NITINOL C WHEELS.
 (RAYCHEM ROLLER RIG; LOAD = 625 lb AT 88 km/hr.)

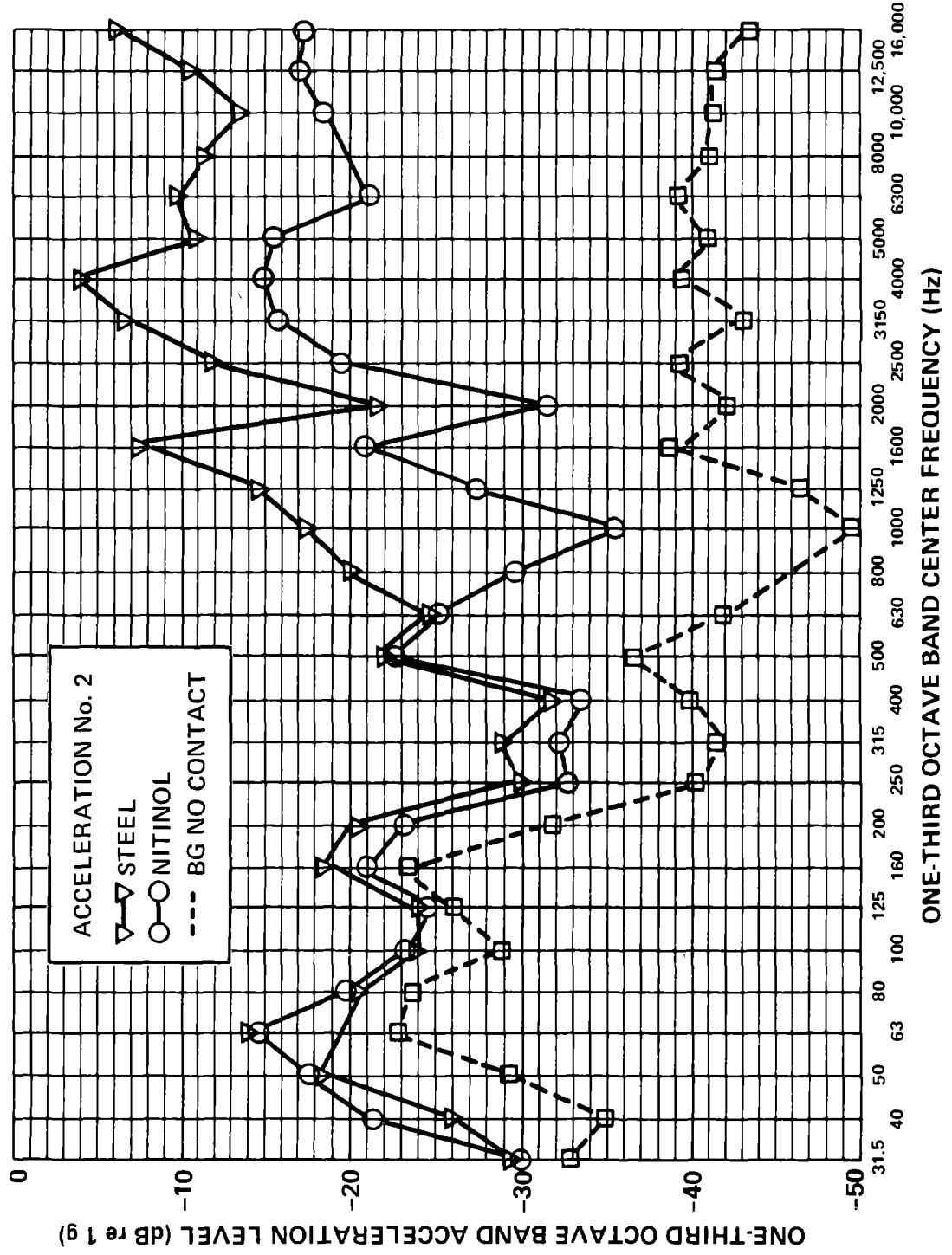


FIG. 154. ROLLING VIBRATION FOR RAIL WHEEL. (LOAD = 625 lb AT 88 km/hr.)

TABLE 11. SUMMARY OF NITINOL C WHEEL TEST RESULTS SCALED UP TO A 30-IN. WHEEL.

Wheel Type	Speed	
	60 km/hr	88 km/hr
Nitinol Wheel	92 dBA	96 dBA
Steel Wheel	97 dBA	102 dBA

spectra. The nitinol C wheel provides considerable reduction in vibration levels above 800 Hz or above 200 Hz when scaled to full size.

The rolling noise for the solid nitinol A test wheel was also measured under rolling noise conditions. Figure 155, however, shows that the noise measured from the nitinol A wheel was in fact louder than the standard steel test wheel. Why this solid nitinol wheel did not show the same reduction as the banded nitinol C wheel is presently a mystery. Since the elastic modulus of the two alloys is nominally the same, one would expect the two wheels to perform the same way. The source of the strong 800-Hz resonance in the noise from this wheel is also a puzzle.

The 5- to 6-dBA reduction in noise from the nitinol C wheel is larger than anticipated. The reduced elastic modulus of the nitinol would be expected to reduce the contact stiffness for nitinol on steel to about 61% of that stiffness for steel on steel. Similarly, the dimensions of the contact area would increase about 27%. For the baseline system of Sec. 3, the analytical model would predict only 1 to 2.5 dBA of noise reduction for these changes in contact area and contact stiffness.

No matter what the source of the discrepancy, the nitinol C wheel shows a significant reduction in rolling noise. Even allowing for the fact that one must exercise some caution in

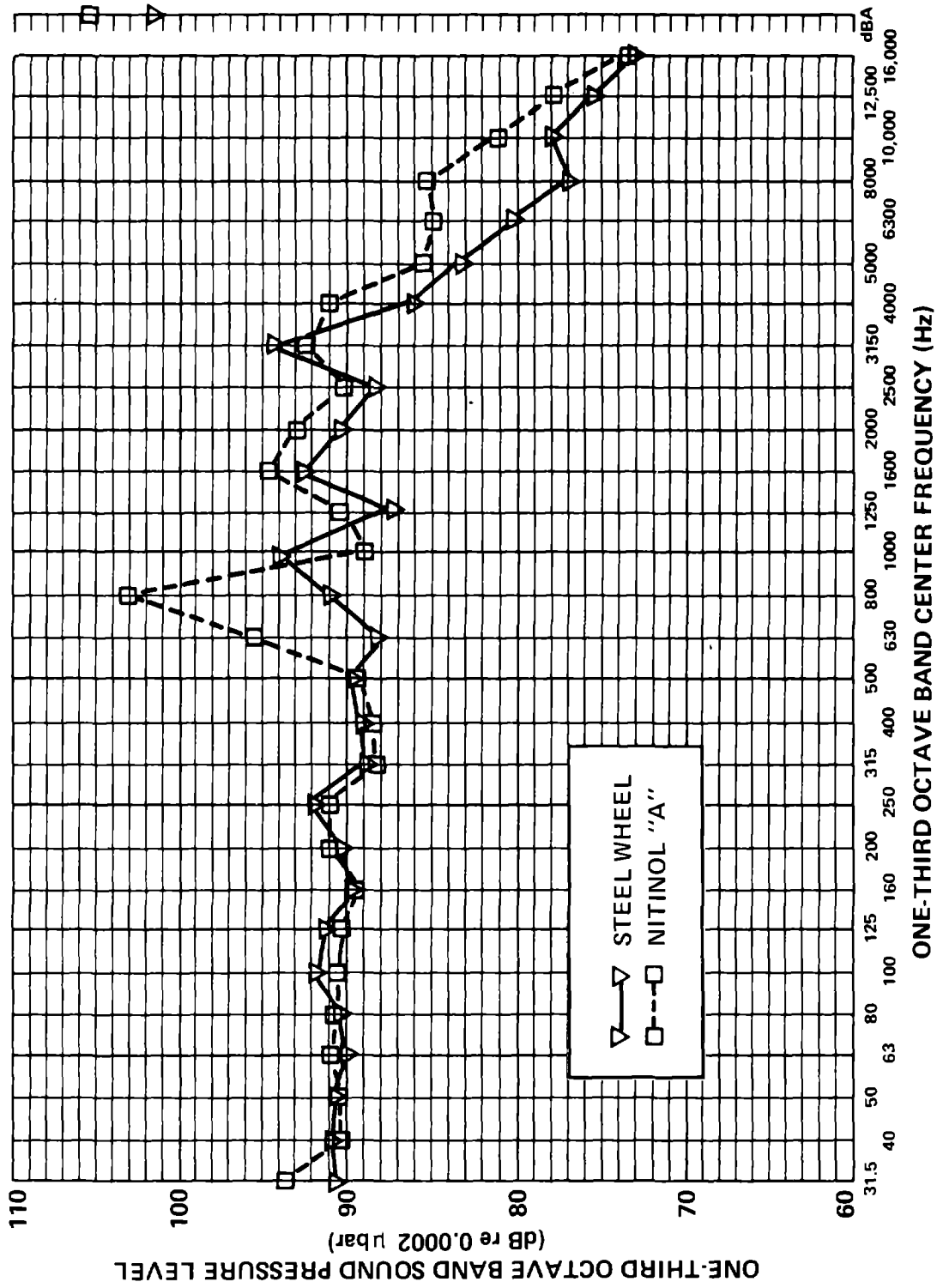


FIG. 155. COMPARISON OF STEEL VS NITINOL A ROLLING NOISE. (RAYCHEM ROLLER RIG; 625 lb AT 60 km/hr.)

extrapolating these results to the case of a wheel rolling on a rail, since our rail wheel does not have the properly scaled impedance, the observed 5 to 6 dBA of noise reduction is significant. Unfortunately, however, nitinol does have a number of properties that might make it unacceptable for use in rapid transit systems. First, the material is very costly and second, it would be expected to exhibit high wear on curves, since the wear rate of nitinol when sliding on steel appears to be quite high. For these reasons, we decided to examine a resiliently treaded wheel design that incorporates only steel in its design and relies on the bending deflection of the tread to introduce resiliency.

Resiliently Treaded Wheel with Mechanical Resilience

The nitinol wheel is a resiliently treaded wheel that uses a special material to introduce compliance at the wheel/rail interface. Because of some of the drawbacks of using this unusual material, we wanted to examine the possibility of introducing tread compliance through purely mechanical means. Figure 156 is a schematic of a concept that we decided to examine. The body of the wheel and the tread are two separate pieces. The tread is a ring supported continuously along its two edges - edge by the body of the wheel and the other edge by a second, removable retaining ring that bolts to the body of the wheel to allow for easy changing of the tread ring. The tread ring is otherwise free to deform in bending in the radial direction. This bending of the tread ring produces the compliant tread.

To ensure that the tread ring will not slip, there is a slight taper at the points where the tread ring joins the body of the wheel and the retaining ring. When the retaining ring bolts are tightened, the tread ring sits firmly against the body of the wheel and the retaining ring. Although there are many possible

THIN TREAD WHEEL

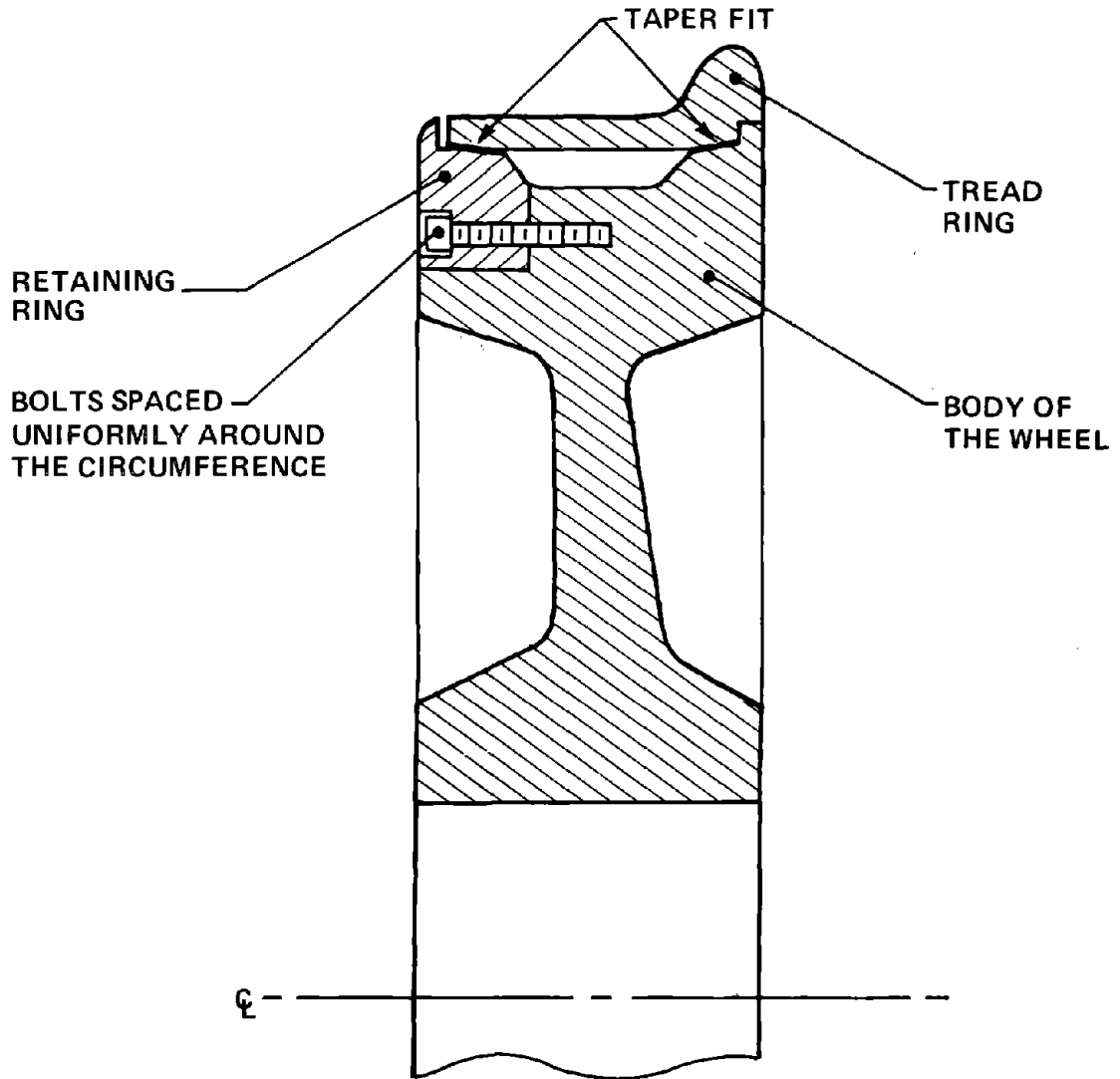


FIG. 156. SCHEMATIC OF A CONCEPT FOR A RESILIENTLY TREADED WHEEL.

techniques for introducing mechanical resilience into the tread, the concept shown in Fig. 156 is mechanically simple, provides for easy tread removal in case of damage (at least for inboard bearing trucks), and is fairly safe. That is, if the tread breaks, it remains on the wheel.

An issue of major concern is whether the tread is durable enough for use on train wheels, i.e., will the tread have a long enough fatigue life and will it be able to handle the loads from the rail without failing? To learn more about the tread's durability, we modeled it as a long, thin, flat strip simply supported at its edges, with a force F applied at the center and distributed over a circle of radius b , as shown in Fig. 157. The stiffness was estimated using formulas by denHartog [8], and the stress was estimated using formulas by Roark and Young [28]. The proper calculation of the dimensions of the area of contact is very difficult. Here we make only a first estimate of the semi-axes of the contact area by ignoring the bending of the tread, ignoring the deformation of the rail head, and assuming that the tread conforms to the rail head as the wheel and rail are brought into contact. The resulting equations are given by:

$$K_c = \frac{Et^3}{0.185 W^2}$$

$$\sigma = \frac{3F}{2\pi t^2} \left[(1+\nu) \ln \left(\frac{2W}{\pi r_o'} \right) + 1 \right]$$

$$r_o' = (1.6 b^2 + t^2)^{1/2} - 0.675 t$$

$$b = \left(\frac{2FR_R}{K_c} \right)^{1/2} \quad a = \left(\frac{2FR_W}{K_c} \right)^{1/2} \quad , \quad (116)$$

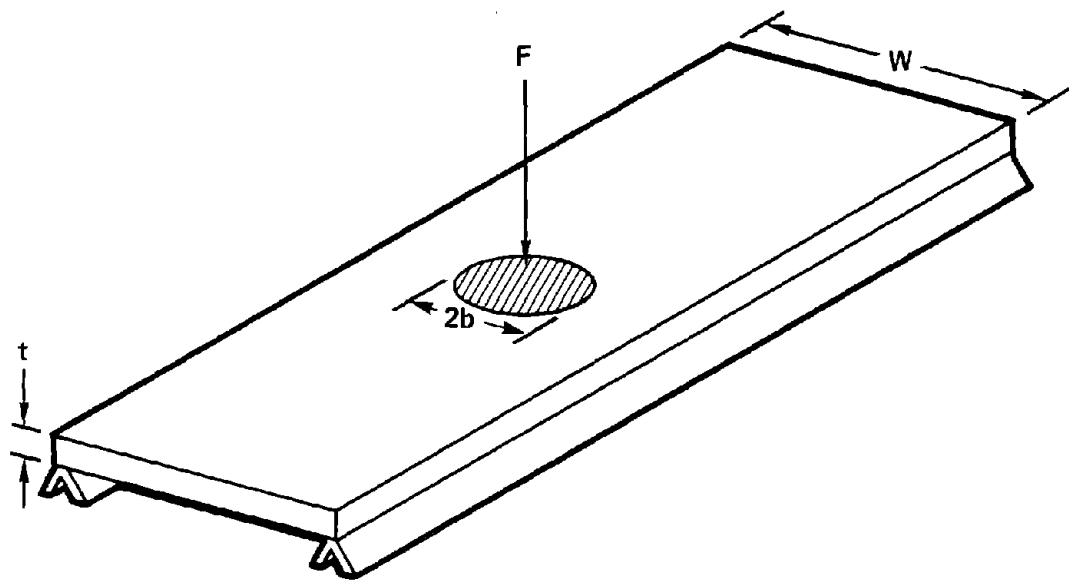


FIG. 157. PRELIMINARY DESIGN.

where E is the elastic modulus of steel; a and b are the semi-axis of the area of contact parallel and perpendicular to the wheel axis, respectively; R_R and R_W are the rail and wheel radii, respectively; σ is the maximum stress in the tread; and the other variables are defined in Fig. 157. Although the above equations are very approximate, they will suffice for our purposes here.

Table 12 uses Eq. (116) to predict stresses, contact patch dimensions, and contact stiffness for various tread thicknesses. For a regular steel wheel,

$$K_c = 1.2 \cdot 10^7 \text{ lb/in.}$$

$$a = b = 0.19 \text{ in.}$$

TABLE 12. PRELIMINARY DESIGN ESTIMATES FOR THE RESILIENTLY TREADED WHEEL.

t (in.)	K_c (lb/in.)	a, b (in.)	σ (lb/m ²)	
1.0	10^7	0.173	$1.71 \cdot 10^4$	$W = 4 \text{ in.}$
0.9	$7.36 \cdot 10^6$	0.20	$2.16 \cdot 10^4$	$R_W = R_R = 14 \text{ in.}$
0.8	$5.19 \cdot 10^6$	0.24	$2.7 \cdot 10^4$	$F = 10,000 \text{ lb}$
0.7	$3.48 \cdot 10^6$	0.29	$3.6 \cdot 10^4$	
0.6	$2.19 \cdot 10^6$	0.37	$4.74 \cdot 10^4$	
0.5	$1.27 \cdot 10^6$	0.49	$6.17 \cdot 10^4$	

The table shows that little benefit in terms of increased contact area or decreased contact stiffness will result unless the tread is thinner than 0.9 in. On the other hand, a tread thickness of less than 1/2 in. will cause stresses that will be difficult to manage. However, if the 1/2-in.-thick tread were manufactured from 4340 alloy steel and heat treated to 150,000 psi

ultimate tensile strength, the maximum stress of 60,000 psi should be manageable, and the fatigue life should be in excess of 10^7 cycles.

We have used the contact stiffnesses and contact areas in Table 12 in the analytical model for the baseline system of Sec. 4 to estimate the performance of the resiliently treaded wheel for various tread thicknesses. Figure 158 shows that a 6.5-dBA noise reduction would be expected for a 1/2-in.-thick tread.

On the basis of these preliminary considerations, we fabricated the 9-in.-diameter scale model test wheels shown in Fig. 159 - one standard wheel and one resiliently treaded wheel with two thicknesses of tread. The wheels were designed to simulate a 28-in.-diameter wheel like the one used by the CTA. Consequently, the scale factor is 3.11, making the 0.16-in. tread a 1/2-in.-thick tread in full scale and the 0.23-in. tread a 3/4-in.-thick tread in full scale. The scaling laws are the same as for the nitinol wheel tests.

The tread rings of the two test wheels were fabricated from 4340 alloy steel, heat treated to 150,000 psi ultimate tensile strength. The solid steel wheel was made from standard cold rolled steel and was not heat treated.

All three wheels were tested on the Raychem Roller Rig for these tests, as were the nitinol wheels. However, the radius of curvature on the rail wheel axis was changed from 5.83 in. to 4.5 in.* so as to scale properly with the 9-in.-diameter test wheels.

*With the scale factor of 3.11, this radius corresponds to 14 in. in the full scale, which is the head radius of 100 lb/yd RE rail section.

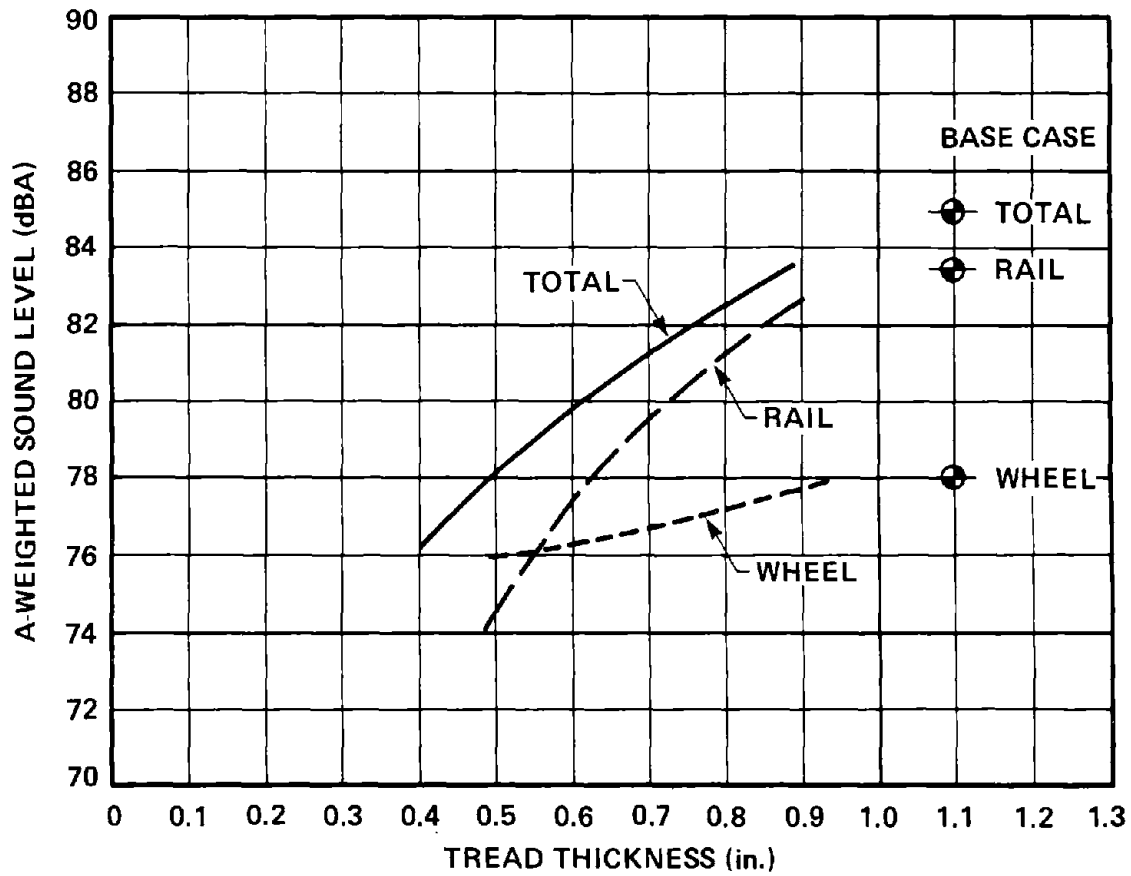
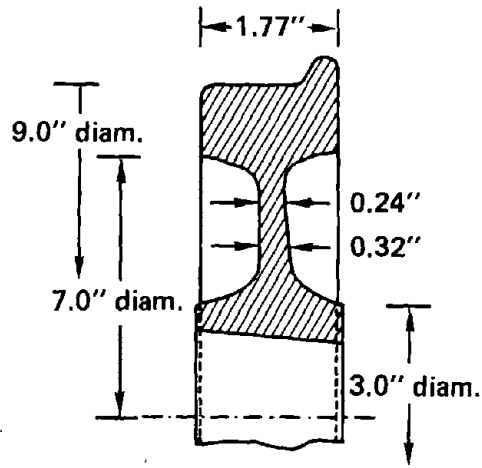
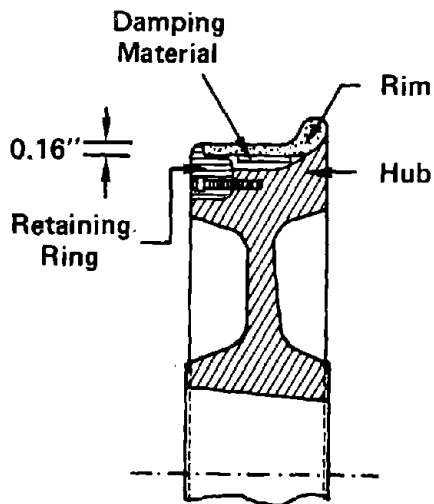


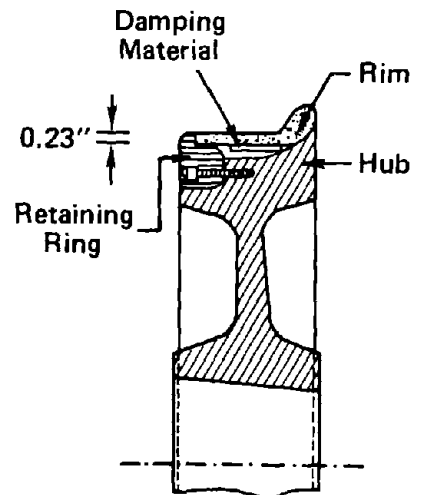
FIG. 158. ESTIMATED ACOUSTIC PERFORMANCE OF THE RESILIENTLY TREADED WHEEL.



STANDARD STEEL
TEST WHEEL



RESILIENT TREAD
4340 STEEL THIN RIM



RESILIENT TREAD
4340 STEEL THICK RIM

FIG. 159. TEST WHEELS USED ON RAYCHEM ROLLER RIG, SCALED FROM CTA 28-in. ROLLED STEEL WHEEL.

Before beginning the noise tests, we performed a series of tests to measure the properties of the test wheels. In particular, we measured

- Wheel roughness
- Contact stiffness
- Contact area
- Tread ring stresses.

The surface roughness of the test wheels was measured before the roller rig tests. Figure 160 shows the standard and the resiliently treaded wheels to have very similar surface roughness after their manufacture. However, during the roller rig tests, at the higher wheel loads, the surface of the standard wheel became very worn, and it is likely that the roughness changed considerably during the course of the roller rig measurements. This roughening and wearing of the surface was a consequence of our not hardening the standard wheel. The high contact stresses at the higher wheel loads probably exceeded the ultimate stress of the material in the contact area and led to the surface deterioration.

The contact stiffness of each wheel was obtained by measuring the deflection of the wheel tread under known applied loads. The static load was applied through the vertical force balance with the test wheel pressed against the rail wheel. The deflection of the test wheel tread was measured by attaching a dial gauge to the tread, with the base of the gauge attached to the rail wheel. Any displacement of the rail wheel under the applied load was eliminated, since the gauge was referenced to the rail wheel. Figure 161 shows the applied load vs the tread deflection for each wheel. During the tests, a certain amount of slack in the bearings of the roller rig had to be taken up at low

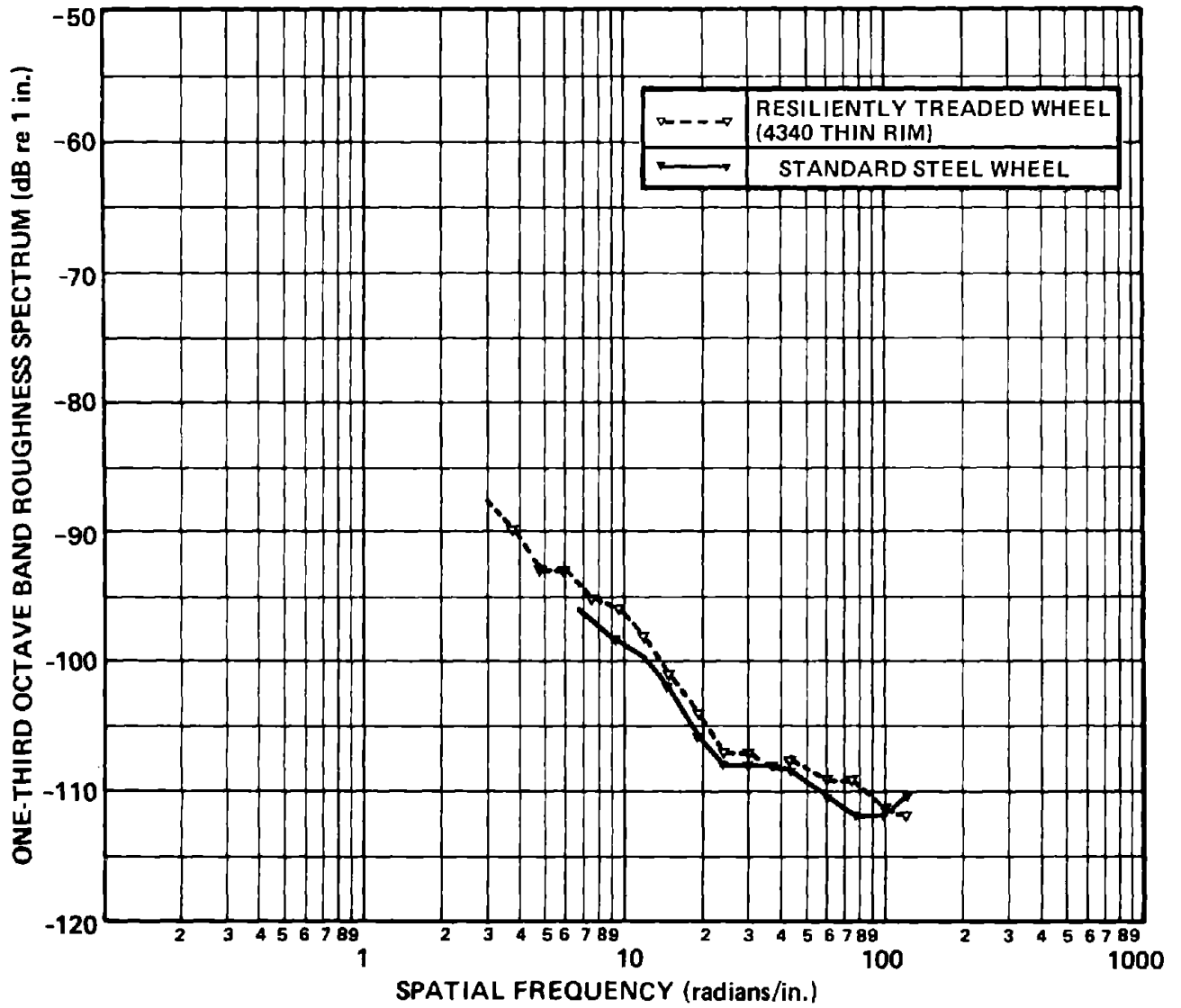


FIG. 160. SURFACE ROUGHNESS OF TEST WHEEL AFTER MANUFACTURE.

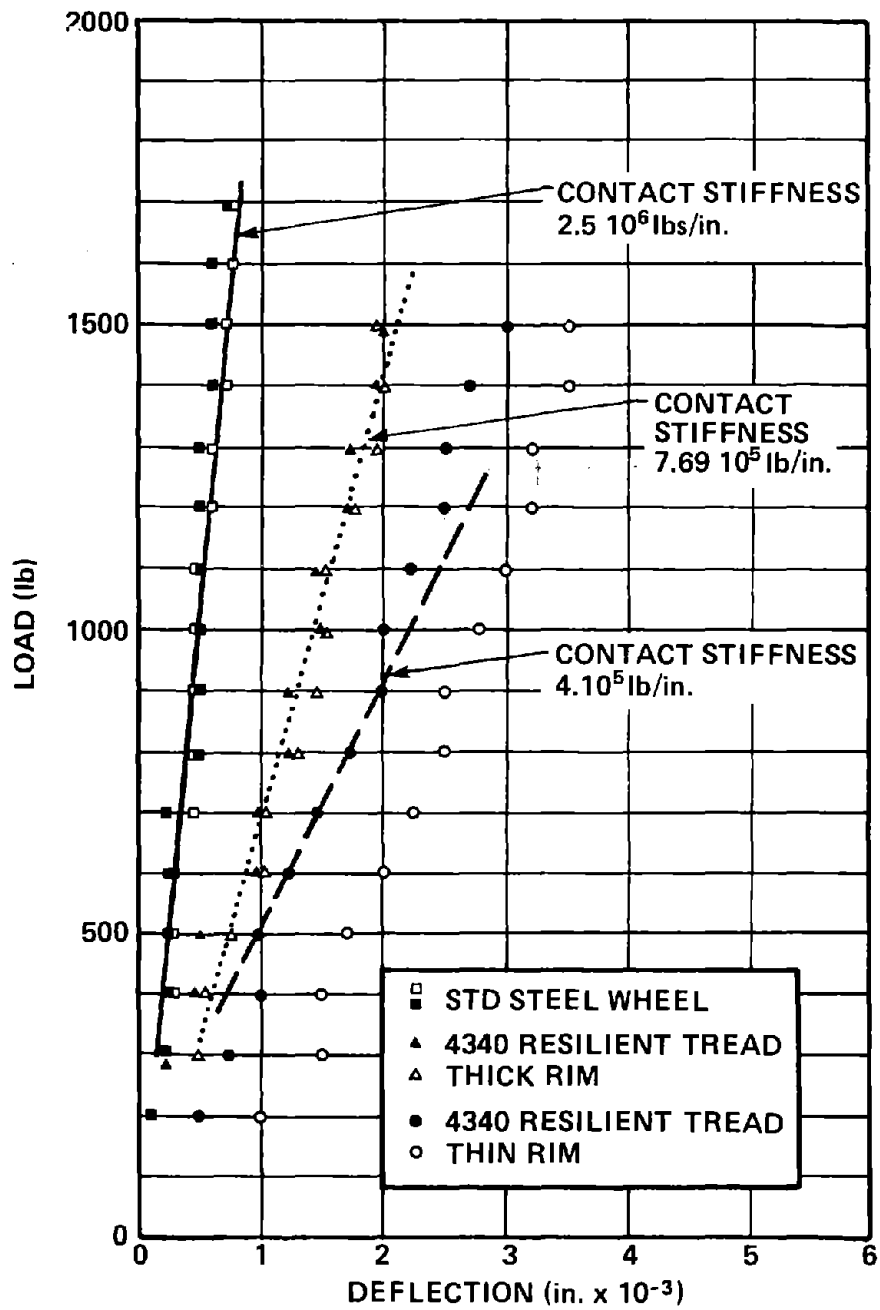


FIG. 161. CONTACT STIFFNESS FOR STANDARD AND RESILIENT TEST WHEELS.

loads. Consequently, some of the first few data points were ignored in drawing the best fit through the data. The slopes of the best fit line through these points are the contact stiffnesses for each wheel.

Table 13 gives the full-scale equivalent contact stiffnesses and compares them with the estimated stiffness from Table 12. Considering the approximate nature of our original estimates, the agreement between the estimated stiffness and the stiffness that we actually achieved is not bad. The close agreement between estimated and measured stiffness for the 0.16-in. tread thickness is probably fortuitous. The disagreement between measured and predicted stiffnesses for the standard wheel may be a consequence of the wear on the standard wheel changing the contact geometry, or it may be due to inaccuracies in the measurement because of the very small deflections with this test wheel.

TABLE 13. CONTACT STIFFNESSES (lb/in.).

Wheel Type	Scale Model	Full Scale	Estimated Full Scale Stiffness
Standard	$2.5 \cdot 10^6$	$7.78 \cdot 10^6$	$1.2 \cdot 10^7$
0.23-in. tread	$7.69 \cdot 10^5$	$2.39 \cdot 10^6$	$4.34 \cdot 10^6$
0.16-in. tread	$4 \cdot 10^5$	$1.24 \cdot 10^6$	$1.27 \cdot 10^6$

The contact area between the test wheels and the rail wheel was measured for three loads and for each of the three test wheels. The SEM replicating tape was again used, and the profiles are shown in Fig. 162, traced directly from the replicating tape image. The long dimension is parallel to the test wheel axis. The standard wheel contact patches are almost rectangular. Rectangular contact areas are typical of worn wheels and probably reflect the wear that occurred on that wheel because

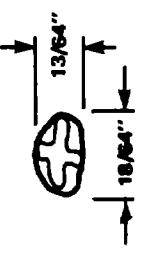
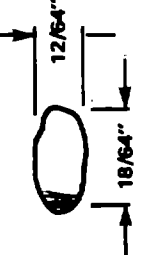
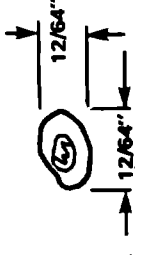
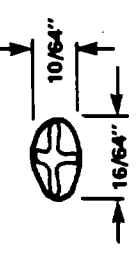
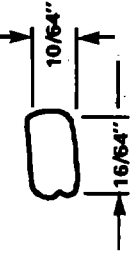
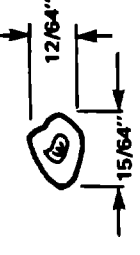
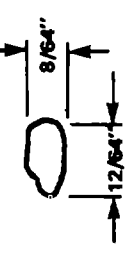
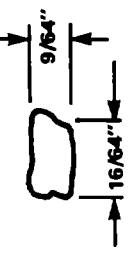
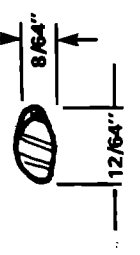
14,500	1500			
9,700	1000			
4,800	500			
FULL SCALE LOAD (lbs)	ACTUAL LOAD ON TEST WHEELS (lbs)	RESILIENTLY TREADED WHEEL 4340 THIN RIM	STANDARD STEEL WHEEL	RESILIENTLY TREADED WHEEL 4340 THICK RIM

FIG. 162. APPROXIMATE CONTACT PATCH SIZES MEASURED ON THE TEST WHEELS FOR DIFFERENT LOADS.

it was not hardened. All wheels have nearly the same contact patch dimensions for the same load, a result that was not expected. Table 14 summarizes the contact patch dimension data in Fig. 162 for the 1000-lb load condition (9700-lb full scale) and compares those dimensions with the estimates in Table 12.

TABLE 14. CONTACT PATCH DIMENSIONS FOR THE 1000-lb SCALED WHEEL LOAD (9700-lb FULL SCALE).

Wheel Type	Scale Model		Full Scale		Estimated Full Scale	
	a	b	a	b	a	b
Standard	8/64	5/64	0.39	0.24	0.18	0.18
0.23-in. wheel tread	7/64	6/64	0.34	0.29	0.26	0.26
0.16-in. wheel tread	8/64	5/64	0.39	0.24	0.49	0.49

The standard wheel contact patch dimensions are nearly twice what Hertzian theory would predict, probably because of the worn track on the standard wheel. For the two test wheels, the correspondence between the estimated and measured contact area dimensions is poor, indicating that a more accurate means for making design estimates is required.

Static stress measurements were obtained on the resiliently treaded wheel using a number of strain gauge rosettes and single gauges. The primary rosette was applied on the center of the resilient tread (see Fig. 163). A single gauge was applied at the edge of the tread, near the support. For each test, the wheel was placed in contact with the rail wheel, the load was

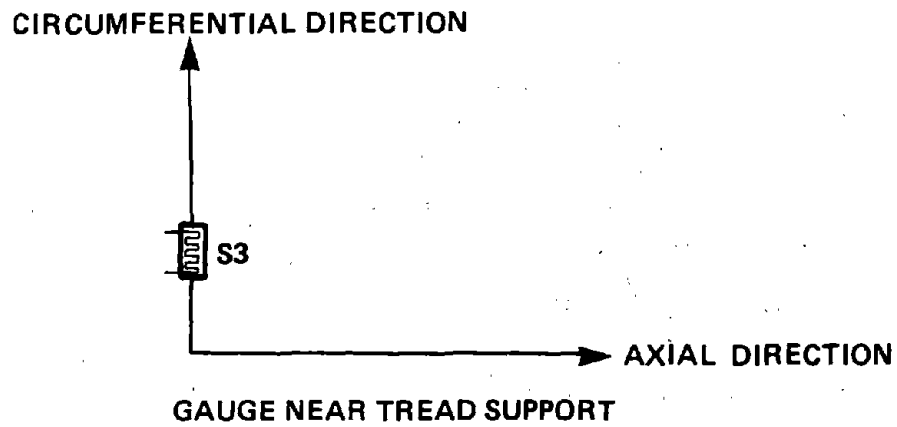
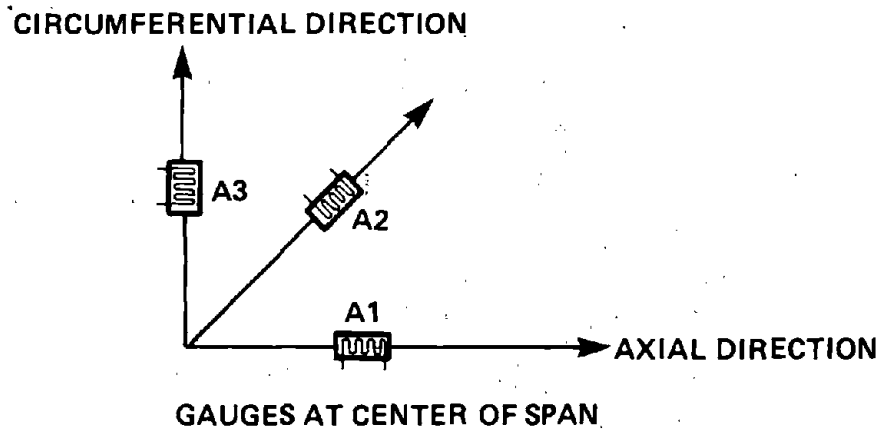


FIG. 164. ORIENTATION OF THE STRAIN GAUGES.

TABLE 15. PRINCIPAL STRESSES AT THE CENTER OF THE 0.16-in.-THICK TREAD.

Position No.	Load (lb)	σ_1 (psi)	σ_2 (psi)	θ (degrees)
1	500	19,500	1,270	22.5
1	1,000	34,690	4,490	22.5
1	1,500	49,400	9,400	18.1
2	500	7,720	-7,720	-16.5
3	500	12,100	-6,340	-270

TABLE 16. STRESSES IN THE TREAD NEAR THE TREAD SUPPORT FOR THE 0.16-in.-THICK TREAD.

Position No.	Load (lb)	σ (psi)
1	500	16,500
1	1,000	34,650
1	1,500	52,800

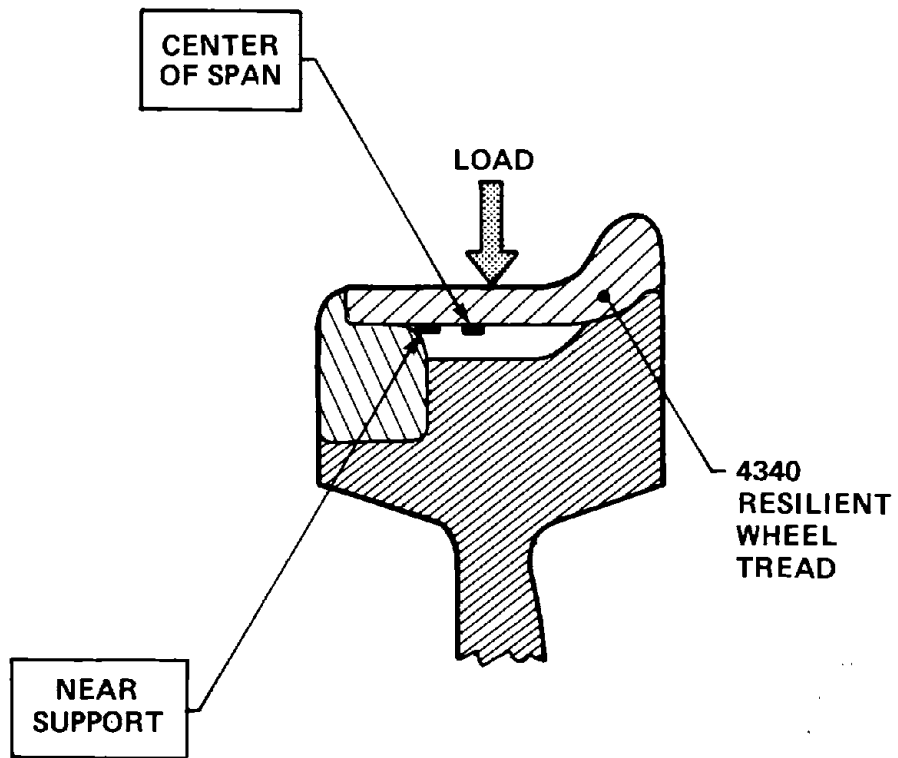


FIG. 163. THE TWO SETS OF STRAIN GAUGES ON THE WHEEL TREAD.

applied, and then the wheel was slowly rotated until the maximum strain position was obtained.

Figure 164 shows the gauge alignment, and typical traces of strain vs circumferential position are shown in Fig. 165. Gauge A1 measures strain in the tread in the circumferential direction, A3 in the axial direction, and S3 in the axial direction. The principal orthogonal stresses and their orientation are shown in Table 15 for the wheel with the thinnest tread. The position numbers refer to the positions in Fig. 165. The stress σ_1 in the table is oriented at angle θ clockwise from the axial direction, and σ_2 is perpendicular to σ_1 . Stresses at the support point are shown in Table 16. In general, the stresses are less than anticipated. The test load of 1000 lb corresponds in the full scale to 9700 lb. For that load, the maximum stresses are only about 35,000 psi. Nearly twice this stress level could be managed with 4340 alloy steel tread, indicating that a still thinner tread ring could be used.

To examine the noise reduction capabilities of this wheel design, we mounted the standard wheel in the roller rig as shown in Fig. 166; ran the wheel at speeds from 10 to 80 km/hr; applied loads from 500 to 1500 lb; and measured the noise with a 1/4-in. microphone at 1/4 in. from the contact point between the test wheel and rail wheel. The mounted microphone is shown in Fig. 166. Subsequent tests were carried out after mounting the resiliently treaded wheel in the roller rig as shown in Fig. 167.

Figure 168 shows typical uncorrected one-third octave band spectra for the standard wheel, the resilient wheel (thin rim), and the rig background noise level (no contact between rotating wheels). The background noise level from the rig was a problem throughout the tests. Figure 169 shows the background noise for each of the wheels turning separately and for them both turning

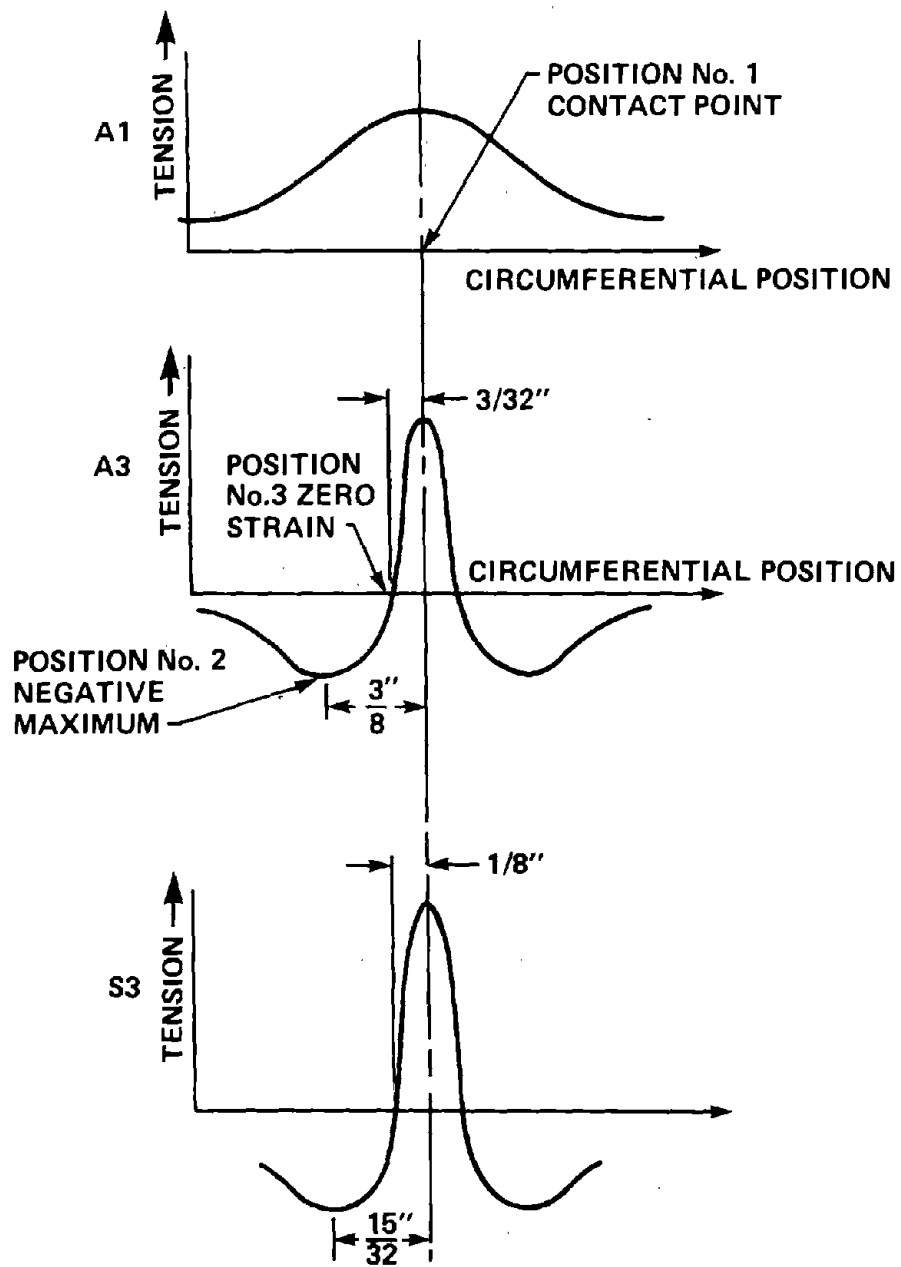


FIG. 165. TYPICAL TRACES OF STRAIN VS CIRCUMFERENTIAL POSITION.

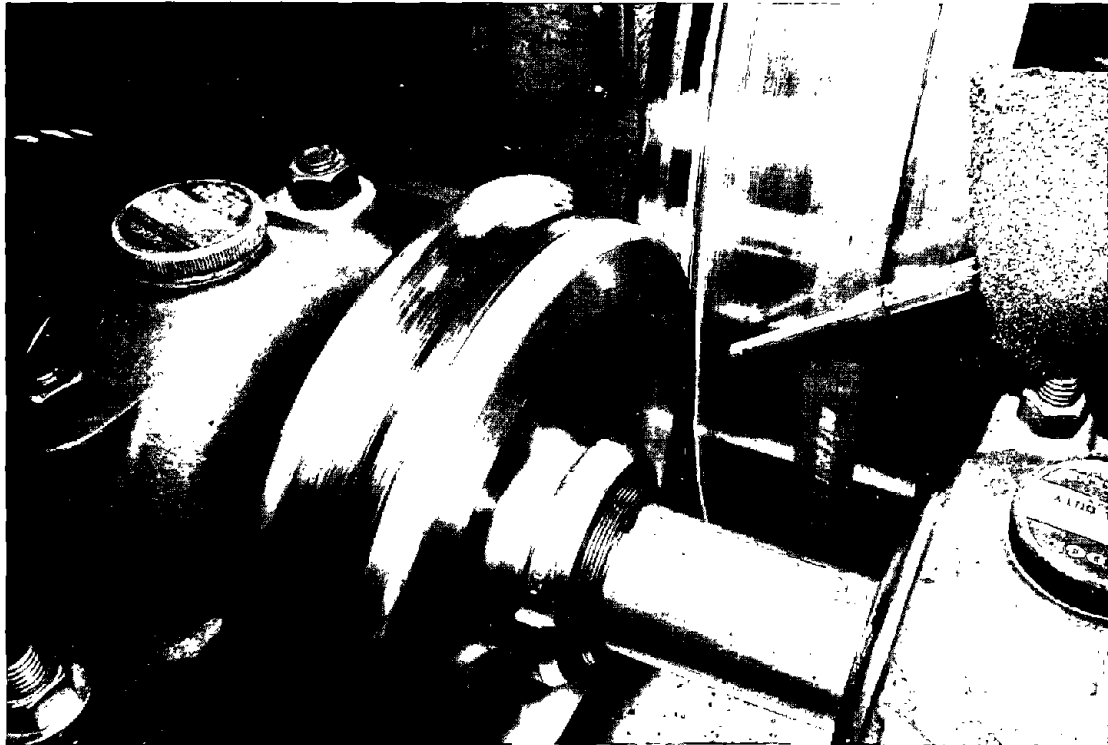


FIG. 166. THE STANDARD STEEL WHEEL MOUNTED IN THE RAYCHEM ROLLER RIG.

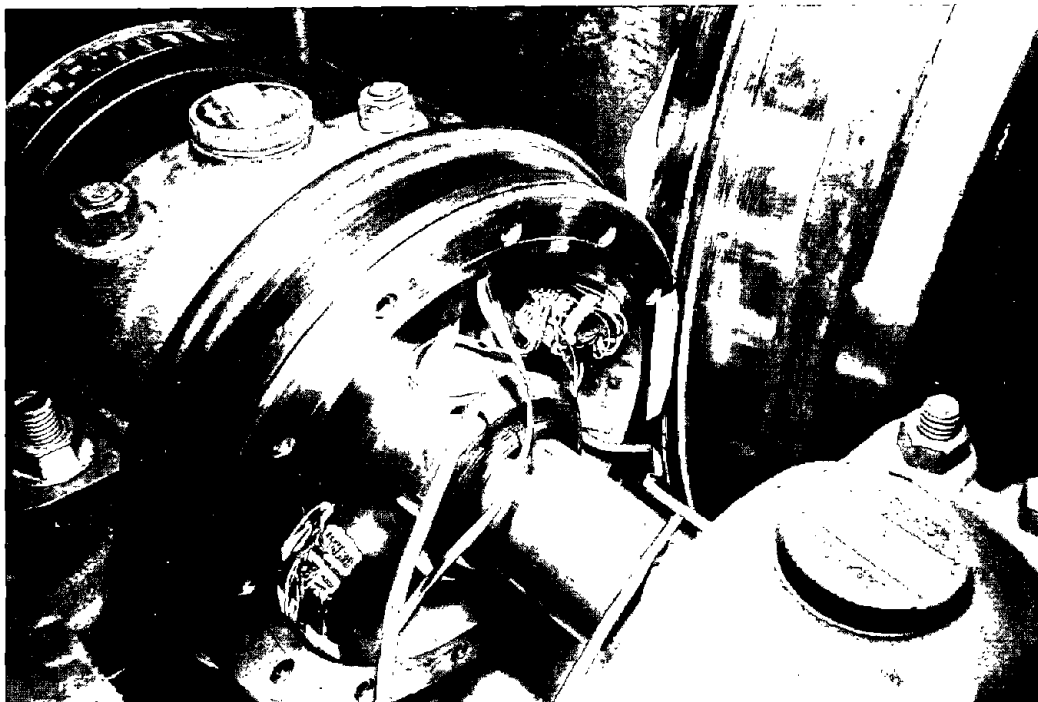


FIG. 167. THE RESILIENTLY TREADED WHEEL MOUNTED IN THE RAYCHEM ROLLER RIG.

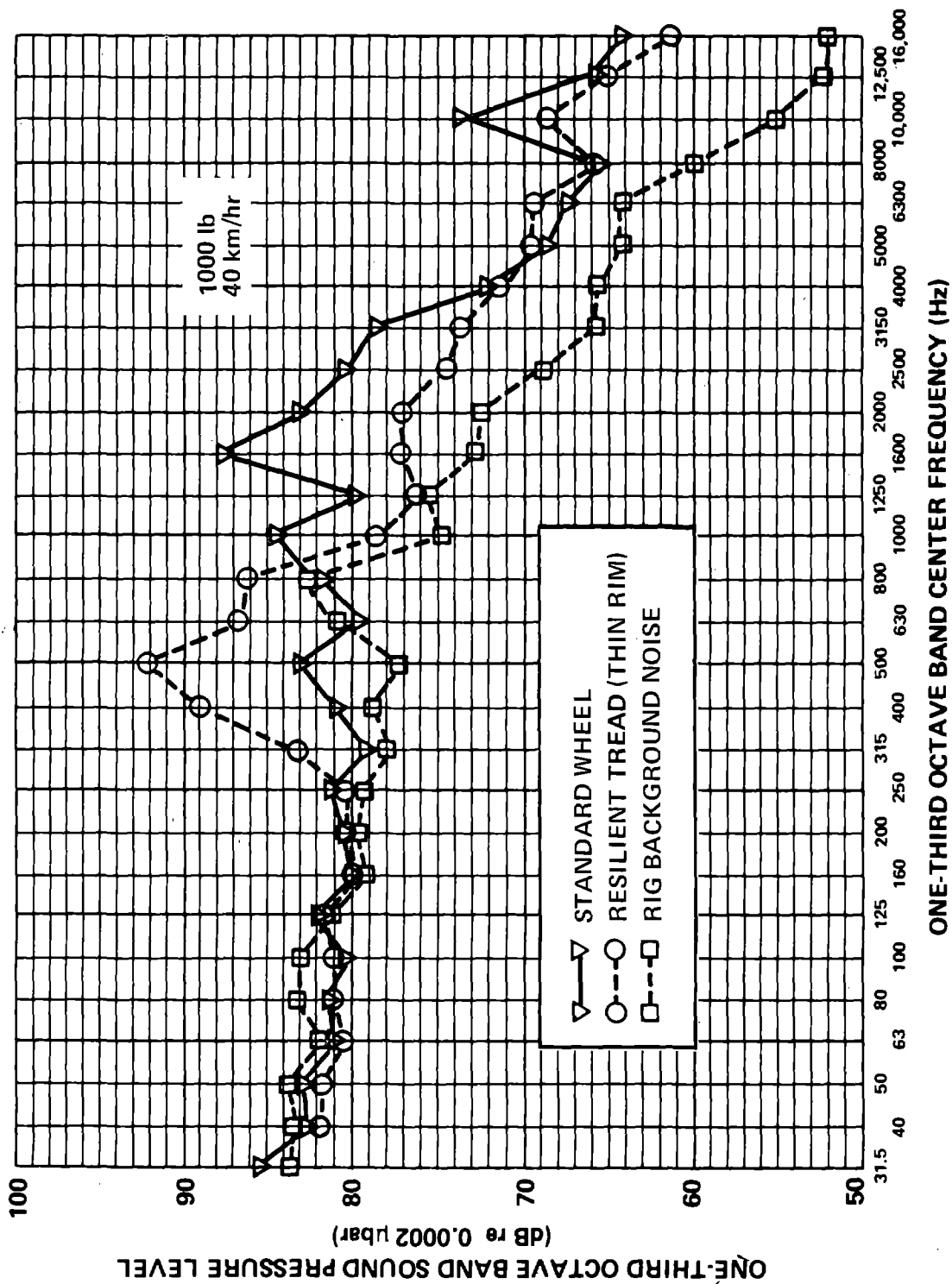


FIG. 168. BASIC, UNCORRECTED DATA ONE-THIRD OCTAVE BAND SPECTRA OF STANDARD WHEEL AND RESILIENTLY TREADED (THIN RIM) WHEEL. (SPEED = 40 km/hr; LOAD = 1000 lb.)

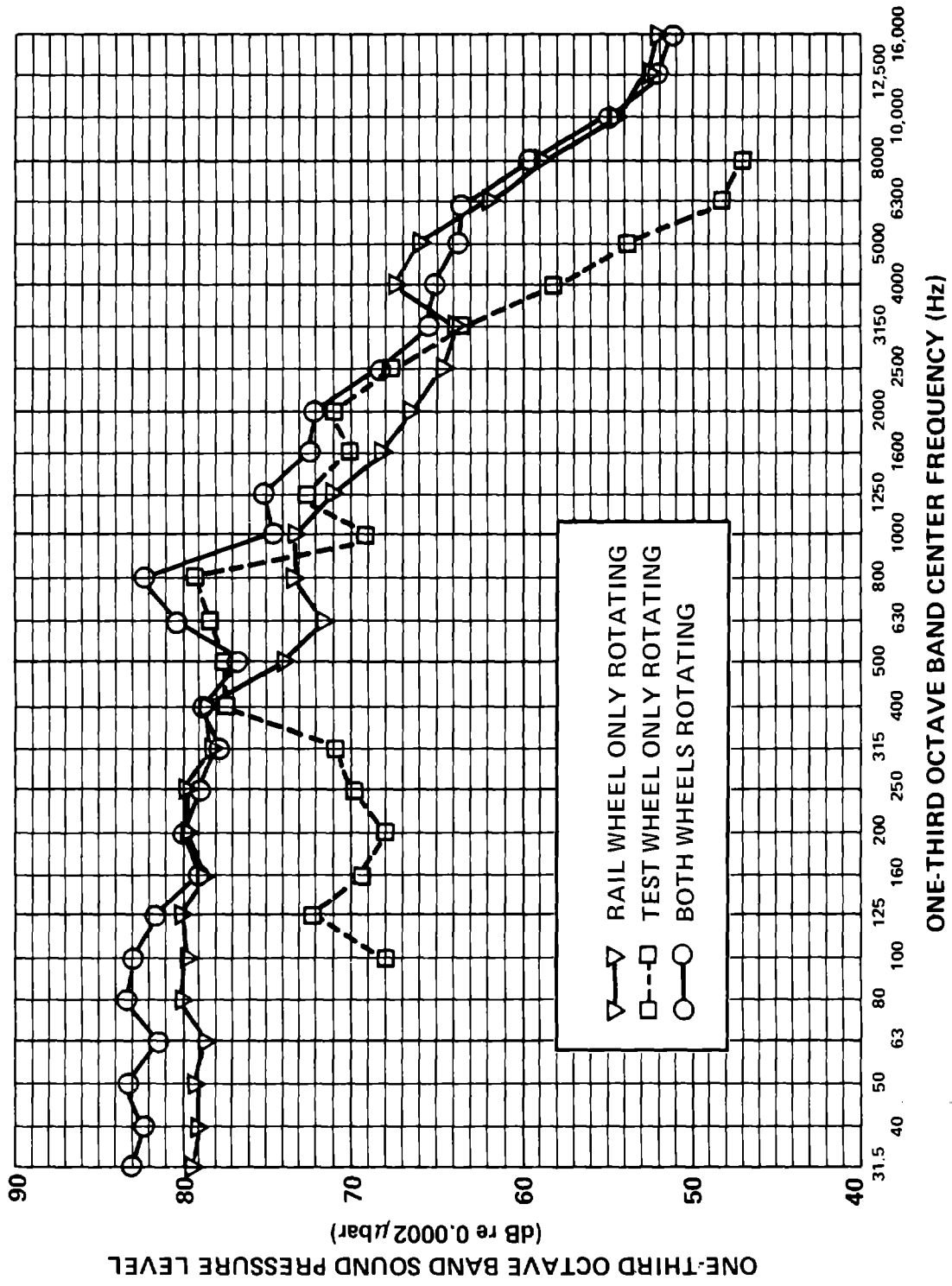


FIG. 169. BACKGROUND NOISE OF ROLLING RIG. (SPEED = 40 km/hr; NO CONTACT BETWEEN RAIL WHEEL AND TEST WHEEL.)

together but not in contact. The noise from the drive motor for the rail wheel dominated at low frequencies, while noise from mechanical devices and bearings of the small wheel dominated the mid range.

Detailed octave and one-third octave band spectra comparing the standard wheel and the resiliently treaded wheel with the thinner rim are shown in Figs. 170 through 173. For both wheels, background noise levels have been subtracted from the spectra, and the spectra have been plotted against the "full-scale frequency," i.e., the measured frequency divided by the scale factor, 3.11. The spectra then correspond in frequency to what one would expect to measure if the 9-in.-diameter test wheels were in fact 28-in.-diameter. We have made this transformation in frequency so that the spectra can be properly A-weighted and overall levels calculated for easy comparison. Table 17 summarizes the results obtained with the resiliently treaded wheel with the thinner tread ring.

The data at 60 km/hr show the greatest noise reduction between the standard and the resilient wheel. The octave band data for the standard wheel at this speed were taken very early in the tests, possibly before the standard wheel had time to wear in and form a larger contact patch. Note that the overall level is also the highest at 60 km/hr.

Data were also obtained for two other microphone positions, close to the large rail wheel and close to the small test wheel. However, the signal-to-noise ratio between the rig noise and the data was worse than at 1/4 in. from the contact patch. Figure 174 shows a comparison of the standard wheel one-third octave band spectra with the thick rim resiliently treaded wheel. These data are uncorrected for background noise, and the frequency scale has not been corrected to the full scale.

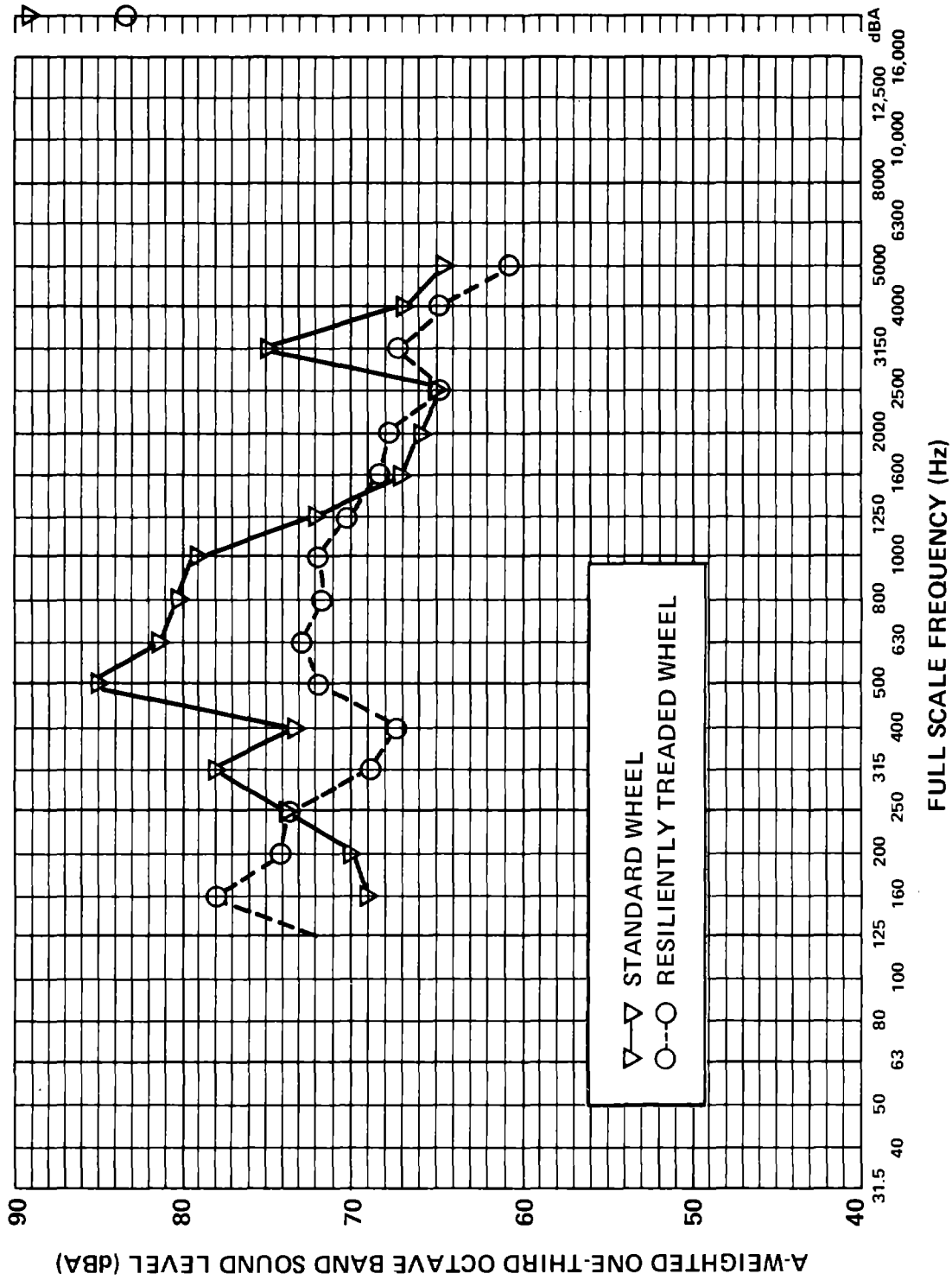


FIG. 170. COMPARISON BETWEEN THE STANDARD WHEEL AND THE RESILIENTLY TREADED WHEEL. (SPEED = 40 km/hr; LOAD = 1000 lb; TREAD RING THICKNESS = 0.16 in.)

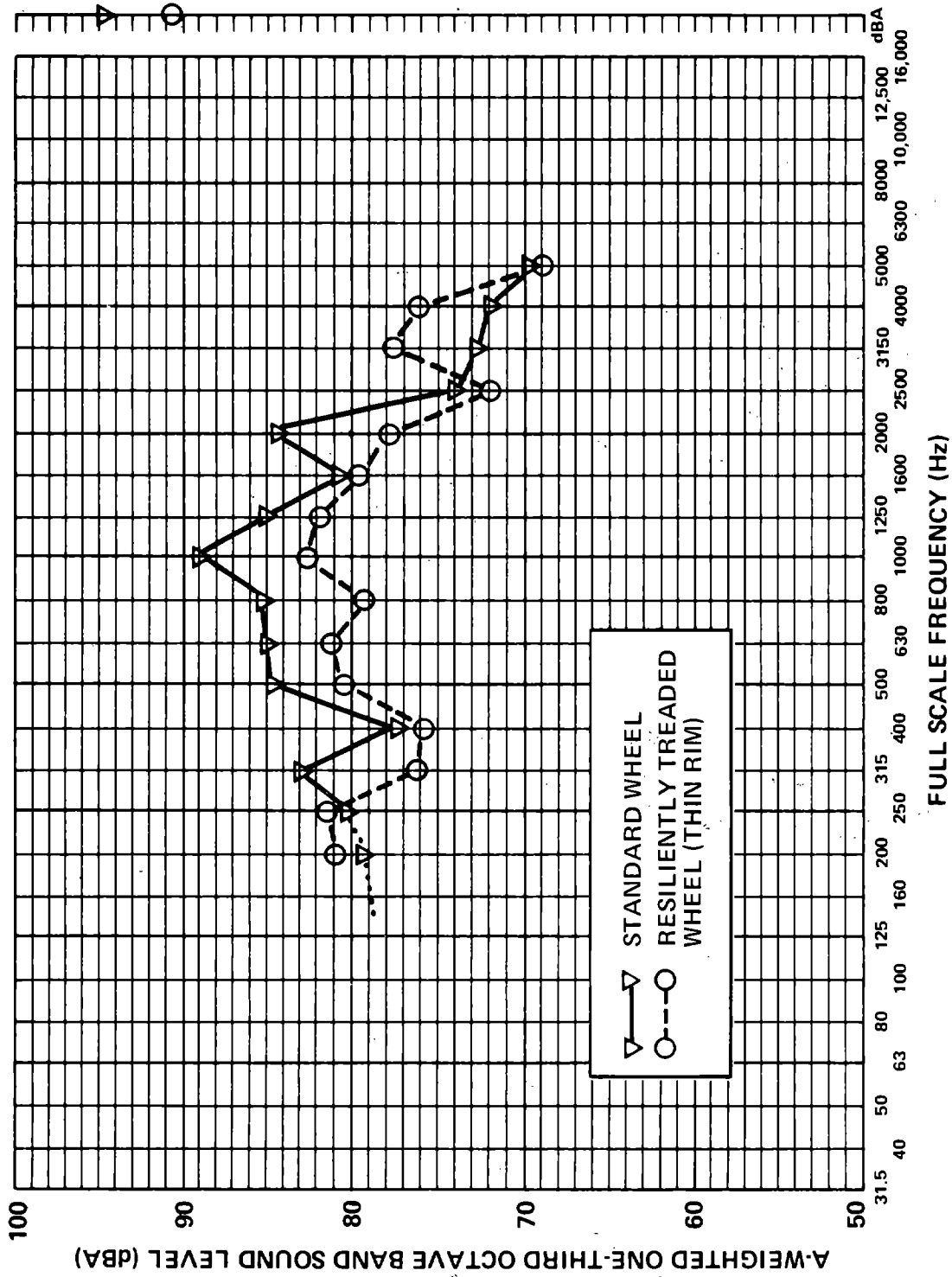


FIG. 171. COMPARISON BETWEEN THE STANDARD WHEEL, AND THE RESILIENTLY TREADED WHEEL. (SPEED = 80 km/hr; LOAD = 1000 lb; TREAD RING THICKNESS = 0.16 in.)

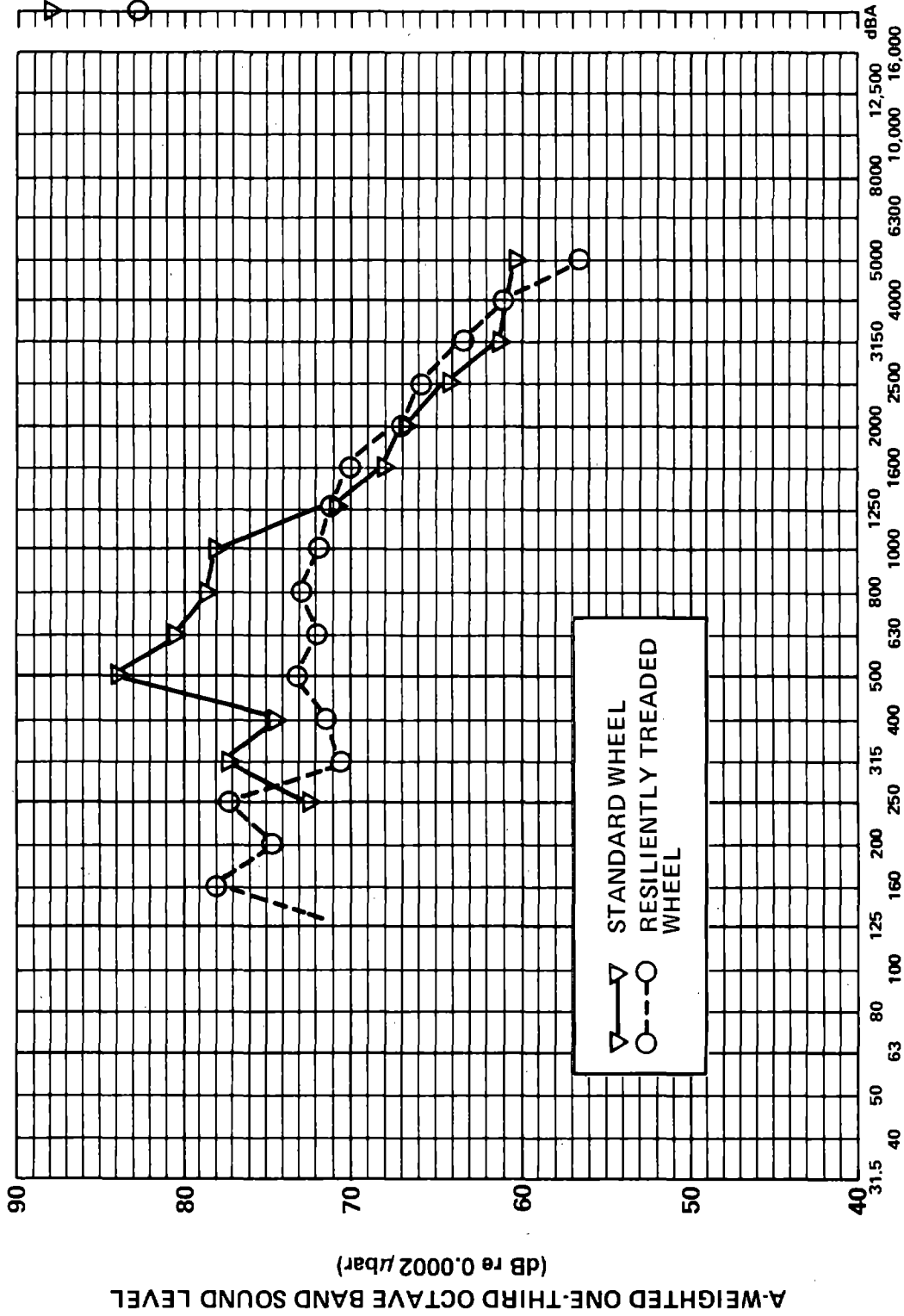


FIG. 172. COMPARISON BETWEEN THE STANDARD WHEEL AND THE RESILIENTLY TREADED WHEEL. (SPEED = 40 km/hr; LOAD = 1500 lb; TREAD RING THICKNESS = 0.16 in.)

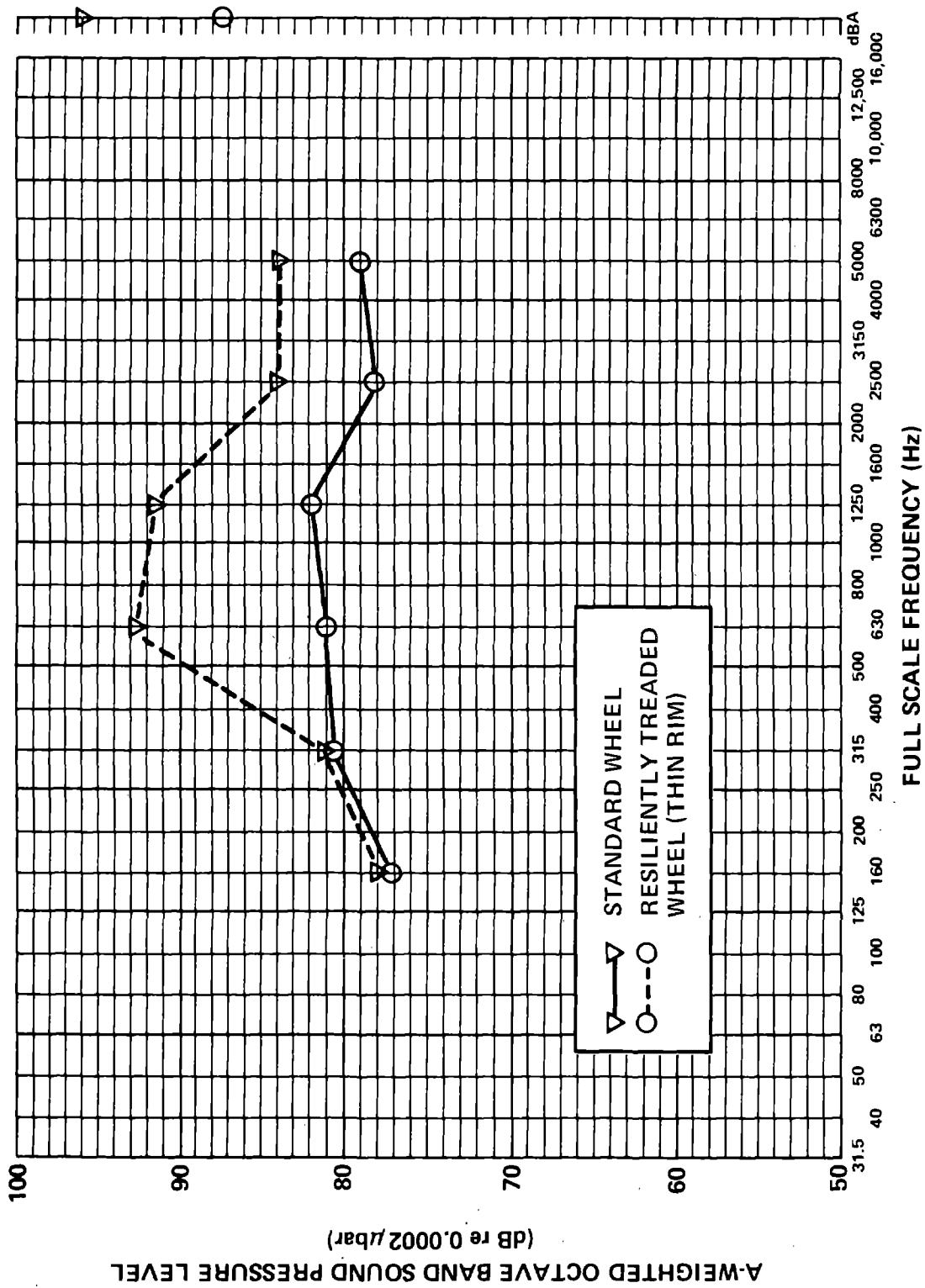


FIG. 173. COMPARISON BETWEEN THE STANDARD WHEEL AND THE RESILIENTLY TREADED WHEEL. (SPEED = 60 km/hr; LOAD = 500 lb; TREAD RING THICKNESS = 0.16 in.)

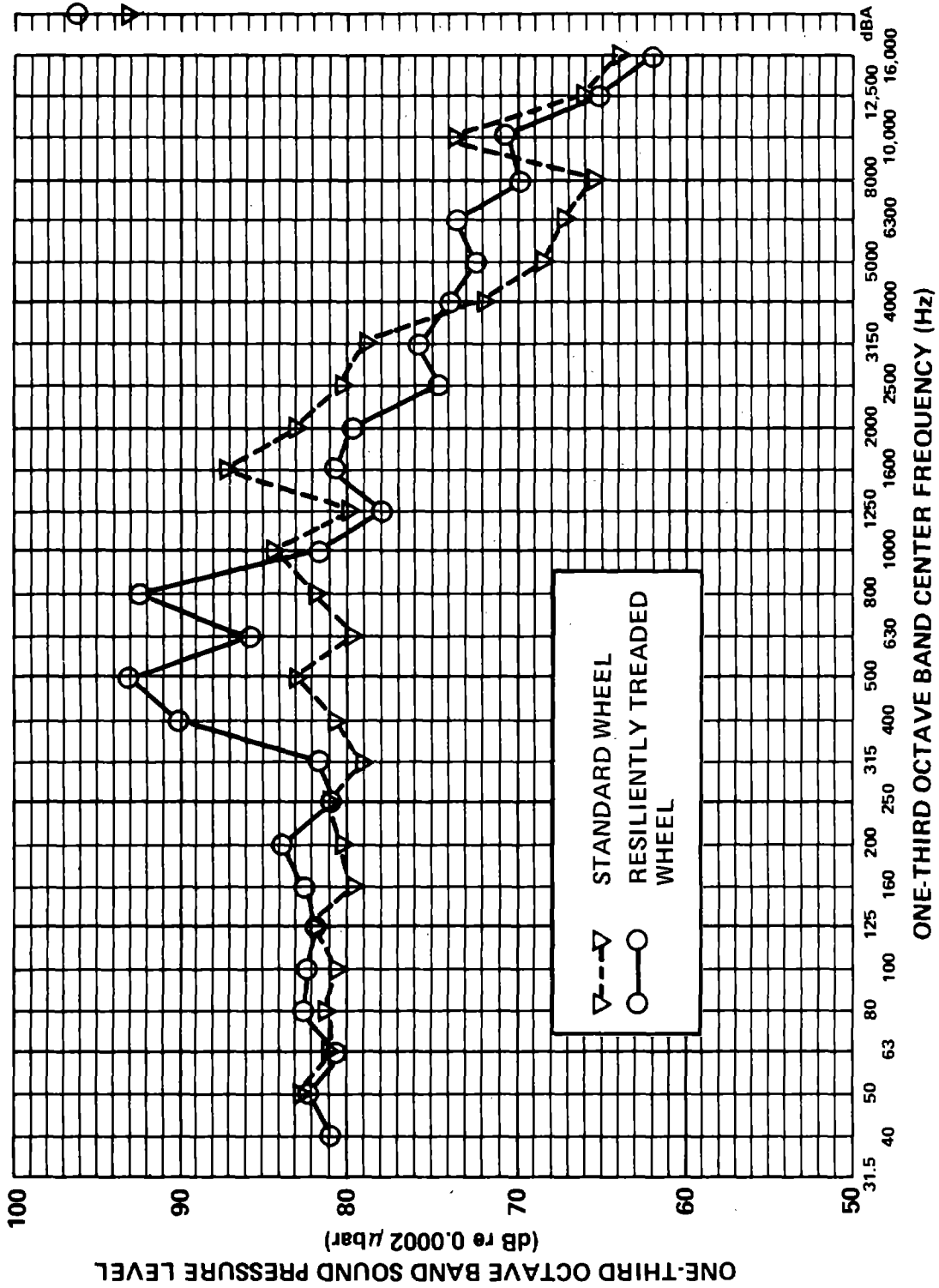


FIG. 174. COMPARISON OF STEEL WHEEL WITH THE RESILIENTLY TREADED WHEEL WITH THE 0.23-in. TREAD RING. (SPEED = 40 km/hr; LOAD = 1000 lb.)

TABLE 17. SUMMARY OF FULL-SCALE NOISE REDUCTIONS ACHIEVED WITH RESILIENTLY TREADED WHEEL WITH 0.16-in. TREAD RING.

Load					
Speed km/hr	Test Condition (lb)	Full Scale (lb)	Standard Wheel (dBA)	Resiliently Treaded Wheel (dBA)	Noise Reduction (dBA)
40	1,000	9,800	89.2	83.4	5.8
40	1,500	14,700	88.0	82.8	5.2
80	1,000	9,800	94.8	90.9	3.9
60	500	4,900	96.0	87.8	8.2

This wheel exhibited strong peaks in the noise spectrum in the 400- to 800-Hz range. We believe these peaks are associated with a contact resonance. Properly shifted in frequency to correspond to full-scale conditions and A-weighted, the 3-dBA increase in noise shown in Fig. 174 from the resiliently treaded wheel will be changed to a slight decrease in noise.

Overall, the performance of the resiliently treaded wheel with the thinner tread is encouraging enough to justify further development. The noise reduction of nearly 8 dBA at 60 km/hr, the one test condition before the standard wheel running surface began to deteriorate, suggests the possibility of substantial noise reduction. In addition, the stress measurements indicate that the tread can easily support loads typical of transit service. In fact, additional noise reduction may be achievable through the use of an even thinner tread ring.



6. CONCLUSIONS AND RECOMMENDATIONS

6.1 Conclusions

6.1.1 Analytical modeling

The improved analytical model developed under this program has been shown to agree reasonably well with field measurements of wheel/rail noise. Where discrepancies have arisen, they have been mostly due to the special testing conditions at the Transportation Test Center. Although the model could be improved even further, it appears at this stage to be a reasonable tool for the design and assessment of new noise control treatments. Further improvements should focus on the application of the model to specialized noise control designs. For example, the very sophisticated wheel response model could be used to examine more fully the use of damping to suppress wheel squeal. An improved rail impedance model that takes into account the periodic support of the ties might also be useful. It could be used to examine the noise reduction achievable from the increased vibration attenuation in the rail resulting from this periodic support.

6.1.2 Noise control

For the suppression of squeal noise, the use of hard-faced rails is a promising site-specific treatment. Preliminary indications are that these rails will suppress squeal, but operating experience in the United States is lacking. This treatment would be especially useful where a transit property has only a few troublesome curves and desires to treat only those curves rather than use wheel damping treatments on their whole fleet of cars.

Measurements of squeal noise on the MBTA have shown that the original rule of thumb, that squeal will occur if the ratio of curve radius to the truck wheelbase is less than 100, is generally a reasonable guideline. Of course, such guidance is useful

only for new construction, since relocating the right-of-way to change curve radii in existing systems is usually out of the question.

The suppression of rolling noise has been a problem for many years; the sensitivity analysis of Sec. 4 discusses this problem. Rolling noise is very insensitive to changes in any of the parameter values defining the wheel/rail system. Although the resiliently treaded wheel concept was shown to provide significant reductions in rolling noise, in the short term rolling noise reduction seems to be best handled by keeping the running surfaces of the wheels and rails as smooth as possible. The rail grinding block technique used by the CTA and TTC (Toronto) is the best rail smoothing technique available for noise suppression, and the belt grinder used by TTC (Toronto) is the best wheel smoothing technique. However, it does appear to be possible to improve the belt grinder somewhat.

6.2 Recommendations

6.2.1 Field testing

Hard-Faced Rails

The installation and test of hard-faced rails on an operating United States transit property would provide the operating experience with this treatment that is presently lacking. One or more curves where squeal occurs should be equipped with hard-faced rails in four sections, as follows:

- Both rails standard
- Hard-faced rails on only the inner rail

- Hard-faced rails on only the outer rail
- Hard-faced rails on both inner and outer rails.

Testing for squeal suppression, rail wear, and other operating problems should be carried out periodically over at least one year.

Improved TTC (Toronto) Belt Grinder

The belt grinding machine at TTC (Toronto) produced the best wheel surface finish of the treatments tested. Some improvement in the surface finish that would result directly in increased noise reduction does appear possible. Changes in operating procedure (wheel speed, belt speed, wheel-to-belt pressure, etc.) and belt grit might result in a surface finish as good as that provided for rails by the rail grinding block technique. The roughness spectrum should be measured after each change in the grinding technique, and the best operating procedure should be defined.

Belt Grinder and Rail Grinding Block Field Evaluation

Noise and vibration measurements should be made with test cars with wheels smoothed using the belt-grinding technique, at a site with rails smoothed by the rail grinding block technique. TTC (Toronto) is a likely site for these measurements, since both techniques are commonly used there. Measurements of wheel and rail roughness should be made in conjunction with the noise and vibration measurements. The testing should be carried out before smoothing, immediately after smoothing, and at periodic intervals until the roughness and noise return to the levels before smoothing. The test cars should be run in regular revenue service throughout the testing period and removed only for brief periods to carry out the necessary measurements. Similarly, the rail test section should be in regular revenue service. Some measurements

of propulsion and auxiliary equipment noise will be necessary to ensure that wheel/rail noise dominates during the testing.

The testing outlined here would verify the noise reduction achievable using these smoothing techniques and would provide information on how often the wheels and rails would have to be smoothed to maintain the desired noise reduction.

Resiliently Treaded Wheel

As described earlier, the roller rig test of the noise reduction achieved with the resiliently treaded wheels was at best only an indication of what could be achieved, since the rail wheel did not properly simulate the rail impedance. Consequently, the next logical step is a test using a rail vehicle. Likely candidates for the testing would be the PRT engineering test vehicle and test track at Pullman-Standard, the test vehicle and track at the Urban Transportation Development Corporation (UTDC), or the SOAC at TTC (Pueblo).

The resiliently treaded wheel with thin tread should be fabricated and installed on the appropriate vehicle, and noise, vibration, stress, contact area, contact stiffness, etc. should be measured as in the laboratory testing. The smaller vehicles at Pullman-Standard or UTDC would be the best for this initial test. If these first tests were successful, later testing could be done with the SOAC at TTC Pueblo.

Wheel Flats

As described earlier, wheel flats can cause a significant increase in wheel/rail noise. Their occurrence can be reduced by a slip prevention system in the braking system of a transit car. Once flat spots develop, they can be removed by wheel truing.

The generation and control of wheel flats is a problem that has never been studied in depth and yet wheel flats are a significant problem on United States transit systems.

A study is needed that will examine the severity of the wheel flat problem on United States rapid transit systems. The study should focus on how wheel flats are generated and how the characteristics of the braking system - wheel/rail adhesion, weather, etc. - affect the rate of wheel flat generation. The goal would be an analytical/empirical model of the braking system that would allow for determining the change in wheel flat generation rate with various changes in the brake system, such as use of slip prevention systems, means for making the transition from dynamic to friction braking, and others. The model can then be used to determine the most cost-effective means for reducing the occurrence of wheel flats.

Impact Noise Annoyance

The average noise during the train passby has generally been used to rank the severity of wheel/rail noise. Impact noise from wheel flats and rail joints tends to be deemphasized by this averaging procedure. Studies are needed to determine whether train noise without impact noise is less annoying than train noise of the same average level with audible impacts immersed in it.

6.2.2 Analytical modeling

Improved Wheel Squeal Model

The improved wheel/rail noise analytical model contains a very sophisticated model of the wheel. If that wheel model were combined with the measurements of lateral friction vs creep

obtained during the program, a better understanding of the role of damping in the suppression of squeal could be obtained.

Rail Damping

The field measurements at TTC (Pueblo) showed that the vibration on the concrete tie supported rail decayed much more rapidly than had been observed on other rail systems. This more rapid decay of vibration, which tended to reduce the rail contribution to wayside noise, is a potential noise control technique. Apparently, the periodic support afforded the rail by the massive concrete ties acts to prevent the propagation of vibration at low frequency. An analytical model of the periodically supported rail would be very useful, so that parameter value changes to enhance this effect could be examined. Such a model could determine the optimum combination of the mass, spacing, ballast properties, etc. to reduce the rail contribution to wayside noise. Since the rail tends to be the largest contribution to wheel/rail noise, a study of this type could have immediate payoffs in noise reduction for new construction.

APPENDIX

REPORT OF NEW TECHNOLOGY

The following items represent new technology or new uses of old technology for the control of wheel/rail noise evaluated as part of this program.

Belt Grinder (p.244)

The belt grinder is a device used by the Toronto Transit Commission to smooth transit car wheels. It produces the best wheel finish for noise reduction of any wheel truing device tested.

Rail Grinding Block Car (p.257)

This device is used by the Toronto Transit Commission and the Chicago Transit Authority to remove irregularities from the rail running surfaces. It produces the best surface finish for noise reduction of any device tested.

Nitinol Wheel (Sec. 5.2.2)

This is a wheel with a tread made of nickel titanium, a concept developed by Raychem Corporation of Menlo Park, CA. It reduces wheel/rail noise slightly due to the greater compliance of the nickel titanium when compared to steel.

Resiliently Treaded Wheel (Sec. 5.2.2)

A scale model of this device was built and tested as part of this program. Compliance is introduced into the tread by use of a thin tread ring. Noise and stress measurements were made indicating that approximately 8 dBA of noise reduction is achievable with manageable stresses in the tread.

Roughness Measuring Device (pp. 141-159)

A device for measuring the roughness spectrum on wheels and rails was developed as part of this program.

Analytical Model (Sec. 2)

An analytical model of wheel/rail rolling noise has been developed that predicts wheel and rail noise and vibration and requires only wheel and rail geometry and roughness as inputs.

REFERENCES

1. L.G. Kurzweil and L.E. Wittig, "Wheel/Rail Noise Control - A Critical Evaluation," U.S. Department of Transportation Report No. UMTA-MA-06-0099-81-1, January 1981.
2. P.J. Remington et al., "Wheel/Rail Noise and Vibration Control," U.S. Department of Transportation Report No. UMTA-MA-06-0025-73-15, May 1974.
3. P.J. Remington, M.J. Rudd, and I.L. Ver, "Wheel/Rail Noise and Vibration: Vol. 1: Mechanics of Wheel/Rail Noise Generation and Vol. 2: Applications to Control of Wheel/Rail Noise," U.S. Department of Transportation Report No. UMTA-MA-06-0025-75-10, May 1975.
4. H.L. Whittemore and S.N. Petrenko, "Friction and Carrying Capacity of Ball and Roller Bearings," U.S. Department of Commerce Bureau of Standards Report No. 201, October 1921.
5. P.J. Remington et al., "Prediction of Noise Reduction in Urban Rail Elevated Structures," U.S. Department of Transportation Report (to be published).
6. I.S. Gradshteyn and I.M. Ryzhik, Table of Integrals Series and Products, Academic Press, New York, 1965.
7. A.E.H. Love, A Treatise on the Mathematical Theory of Elasticity, Dover Publications, New York, 1944.
8. J.P. denHartog, Advanced Strength of Materials, McGraw-Hill Book Co., New York, 1952.
9. M.L. Munjal and M. Heckl, "Vibrations of a Periodic Rail Sleeper System" (to be published in the Journal of Sound and Vibration).
10. Personal Communication, Denys Meade, ISVR University of Southampton, Southampton, England, October 1980.
11. H.-J. Naake, "Experimental Investigation of Vibration on Railroad Rails," Acustica 3:139-147, 1953.
12. C.I. Chessel, "Propagation of Noise Along a Finite Impedance Boundary," J. Acoust. Soc. Am. 62:825-834, 1977.
13. U. Ingard, "On the Reflection of a Spherical Sound Wave from an Infinite Plane," J. Acoust. Soc. Am. 23:329-335, 1951.

14. I. Rudnick, "The Propagation of an Acoustic Wave Along a Boundary," J. Acoust. Soc. Am. 19:348-356, 1947.
15. M.E. Delaney and E.N. Bazley, "Acoustical Properties of Fibrous Absorbent Materials," Appl. Acoust. 3:105-116, 1970.
16. J.E. Piercy and T.F.W. Embleton, "Excess Attenuation or Impedance of Common Ground Surfaces Characterized by Flow Resistance," Paper presented at the 97th Meeting of the Acoustical Society of America, 11-15 June 1979.
17. S. Bolourchi, "Noise Reduction by Ballast in Rail Vehicle Track Structures," MSC Thesis, Massachusetts Institute of Technology, July 1973.
18. J.E. Manning et al., "Noise Prediction Models for Elevated Rail Transit Structures," U.S. Department of Transportation Report No. UMTA-MA-06-0024-75-12, August 1975.
19. I.L. Ver, C.S. Ventres, and M.M. Myles, "Wheel/Rail Noise Part III: Impact Noise Generation by Wheel and Rail Discontinuities," J. Sound and Vibration 46:395-417, 1976.
20. J.H. Laning and R.H. Battin, Random Processes in Automatic Control, McGraw-Hill Book Co., New York, 1956.
21. R.B. Blackman and J.W. Tukey, The Measurement of Power Spectra, Dover Publications Inc., New York, 1959.
22. M.J. Rudd, "Wheel/Rail Noise II: Wheel Squeal," J. Sound and Vibration 46:381-394, 1976.
23. H.J. Saurenman, "In-Service Performance and Costs of Methods to Control Urban Rail Systems Noise: Second Test Series Report," U.S. Department of Transportation Report No. UMTA-06-0099-79-4, October 1979.
24. S. Kumar and B.R. Rajkumar, "Laboratory Investigation of Wheel/Rail Contact Stresses for U.S. Freight Cars Railroad Engineering Laboratory," Illinois Institute of Technology, Chicago, IL.
25. S. Kumar, "Analysis and Measurements of Contact Areas and Stresses Between Wheel and Rail for the State-of-the-Art Car," Railroad Engineering Laboratory, Illinois Institute of Technology, Chicago, IL, April 1980.

26. C.G. Gray and K.J. Johnsen, "The Dynamic Response of Elastic Bodies in Rolling Contact to Random Roughness of Their Surface," J. Sound and Vibration 22:323-342, 1972.
27. M.L. Silver, R.C. Bachus, and R. Priemer, "Noise Assessment of the Chicago Transit Authority Rail Rapid Transit System," U.S. Department of Transportation Report No. UMTA-MA-06-0025-79-8, January 1979.
28. R.J. Roark and W.C. Young, Formulas for Stress and Strain, McGraw-Hill Book Co., New York, 1975.

